

**MODAL IDENTIFICATION OF STRUCTURES BY  
USING BAYESIAN STATISTICS**

**A Thesis Submitted to  
The Graduate School of Engineering and Sciences of  
İzmir Institute of Technology  
in Partial Fulfillment of the Requirements for the Degree of**

**DOCTOR OF PHILOSOPHY**


**in Civil Engineering**

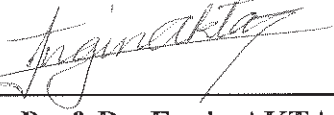
**by  
Çağlayan HIZAL**


**July 2019  
İZMİR**

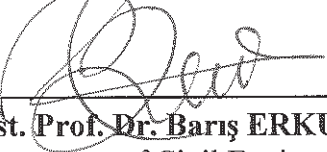
We approve the thesis of **Çağlayan HIZAL**

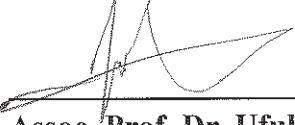
**Examining Committee Members:**

  
\_\_\_\_\_  
**Assoc. Prof. Dr. Gürsoy TURAN**  
Department of Civil Engineering, İzmir Institute of Technology


  
\_\_\_\_\_  
**Assoc. Prof. Dr. Engin AKTAŞ**  
Department of Civil Engineering, İzmir Institute of Technology

  
\_\_\_\_\_  
**Prof. Dr. Hilmi LUŞ**  
Department of Civil Engineering, Boğaziçi University

  
\_\_\_\_\_  
**Asst. Prof. Dr. Barış ERKUŞ**  
Department of Civil Engineering, İstanbul Technical University

  
\_\_\_\_\_  
**Assoc. Prof. Dr. Ufuk YAZGAN**  
Earthquake Engineering and Disaster Management Institute, İstanbul Technical University

18 July 2019

  
\_\_\_\_\_  
**Assoc. Prof. Dr. Gürsoy TURAN**  
Supervisor, Department of Civil Engineering,  
İzmir İnstitute of Technology

\_\_\_\_\_  
**Prof. Dr. Şebnem ELÇİ**  
Head of the Department of Civil  
Engineering

\_\_\_\_\_  
**Prof. Dr. Aysun SOFUOĞLU**  
Dean of the Graduate School of  
Engineering and Sciences

## ACKNOWLEDGEMENTS

First, I would like to express my profound gratitude to my supervisor, Assoc. Prof. Dr. Gürsoy Turan, for his continuous guidance and support during this study. I would also like to thank him for his patience, motivation, friendly attitude throughout my PhD education. Second, I would like to present my sincere thanks to Assoc. Prof. Dr. Engin AKTAŞ, who is a member of my examining committee, for his significant contribution, support, and excitement to improve the scientific quality of this research.

My examining committee members, Prof. Dr. Hilmi LUŞ, Asst. Prof. Dr. Barış ERKUŞ, and Assoc. Prof. Dr. Ufuk YAZGAN deserves my special appreciation for their significant contribution, precious critics and recommendations for my PhD thesis.

I would like to thank KU LEUVEN Structural mechanics for sharing the all measurement data of the Z24 Bridge.

I would also like to present my heartfelt and deepest love and appreciation to my beloved parents, to my beloved mother, my beloved father, and to my very precious brother.

Finally, I wish to present my all deepest appreciation to my wife, who was always beside me during my happy and hard moments, for her continuous support and encouragement not only during my PhD study but also throughout my life. My beloved little daughter also deserves my endless love and gratitude. Words are certainly not enough to express how much I love both of you.

# ABSTRACT

## MODAL IDENTIFICATION OF STRUCTURES BY USING BAYESIAN STATISTICS

Bayesian Probabilistic approaches in the health monitoring of civil engineering structures has gained remarkable interest during past decades. When compared to the available Operational Modal Analysis (OMA) methods, Bayesian Operational Modal Analysis (BAYOMA) determines a probabilistic range with a most probable value and uncertainty instead of a certain result. For this reason, the most important difference of BAYOMA lies in its capability of uncertainty quantification. Therefore, the modal parameters of a measured structure can be determined based on a probabilistic logic according to various cases (for example single measurement setup, well separated and/or closely spaced modes, multiple measurement setups). Further, the finite element model of the investigated structure can also be updated by a Bayesian approach incorporated with modal identification procedure. Some efficient BAYOMA methods such as Bayesian Spectral Density Approach (BSDA) and Bayesian Fast Fourier Transform Approach (BFFTA) have been presented by various researchers during the past two decades. Despite their efficient and fast solution procedure, the available methods have some critical issues that need to be solved. Most of these problems especially lie in the quantification of posterior uncertainties and some special cases arise in closely spaced modes and/or multiple setup measurement cases. In the literature, solutions for the aforementioned problems have been also presented by various researchers. In the light of the accumulated knowledge in the literature, this study presents a computational framework for BAYOMA and Bayesian Model Updating (BMU). In addition to some improvements to the available methods, new and alternative approaches are presented for BAYOMA and BMU. According to the results, it is seen that the quality of identified modal parameters and updated finite element models increases significantly by the proposed computational procedure.

# ÖZET

## YAPILARIN BAYEZYAN İSTATİSTİKLERİ İLE MODAL TANILAMASI

Bayezyan olasılıksal yaklaşımları, inşaat mühendisliği yapılarının sağlığının izlemesinde, geçen on yıllar boyunca kayda değer bir ilgi kazanmıştır. Mevcut Operasyonel Modal Analiz (OMA) yöntemleriyle karşılaştırıldığında Bayezyan Operasyonel Modal Analiz (BAYOMA) yöntemleri, belirli bir sonuç yerine en olası değer ve bu değer belirsizliğini içeren olasılıksal bir aralık belirler. Bu nedenle, BAYOMA'nın en önemli farkı belirsizlikleri tanımlama kabiliyetinde yatmaktadır. Böylece, ölçülen bir yapının modal parametreleri, çeşitli durumlara göre (örneğin tekil ölçüm grubu, iyi ayrılmış ve/veya çakışan modlar, çoklu ölçüm grupları gibi) bir olasılık temelinde belirlenebilir. Ayrıca, incelenen yapının sonlu eleman modeli, modal tanımlama prosedüründen elde edilen sonuçlar kullanılarak, bir Bayezyan yaklaşımıyla da güncellenebilir. Bayezyan Spektral Yoğunluk Yaklaşımı (BSDA) ve Bayezyan Hızlı Fourier Dönüşüm Yaklaşımı (BFFTA) gibi bazı etkili BAYOMA yöntemleri, son yirmi yıl boyunca çeşitli araştırmacılar tarafından sunulmuştur. Etkili ve hızlı çözüm prosedürlerine rağmen, mevcut yöntemlerde üstesinden gelinmesi gereken bazı kritik sorunlar da mevcuttur. Bu sorunların birçoğu, özellikle sonsal (posterior) belirsizliklerin belirlenmesinde yatmakta veya çakışan modlar ya da çoklu ölçüm grupları bulunması gibi bazı özel durumlarda ortaya çıkmaktadır. Literatürde, yukarıda belirtilen sorunlara yönelik çözümler çeşitli araştırmacılar tarafından sunulmuştur. Mevcut bilgiler ışığında, bu çalışma BAYOMA ve Bayezyan Model Güncelleme (BMU) için bir hesap çerçevesi sunmaktadır. Mevcut yöntemlerde bazı iyileştirmelere ek olarak, BAYOMA ve BMU için yeni ve alternatif yaklaşımlar sunulmaktadır. Elde edilen sonuçlara göre, tanımlanan modal parametrelerin ve güncellenmiş sonlu eleman modellerinin kalitesinin, önerilen hesap prosedürü ile önemli ölçüde arttığı görülmektedir.

# TABLE OF CONTENTS

LIST OF FIGURES .....	x
LIST OF TABLES .....	xiv
CHAPTER 1. INTRODUCTION .....	1
1.1. Motivation of Study .....	1
1.2. Literature Review .....	2
1.2.1. Non-Bayesian Methods .....	3
1.2.2. BAYOMA Methods .....	4
1.3. Objectives of the study .....	6
1.4. Outlines .....	7
CHAPTER 2. BAYESIAN OPERATIONAL MODAL ANALYSIS IN FREQUENCY DOMAIN: WELL SEPARATED MODES .....	9
2.1. Introduction.....	9
2.2. Dynamic Response Analysis in Frequency Domain.....	10
2.3. BAYOMA Methods.....	11
2.3.1. Bayesian Spectral Density Approach (BSDA) .....	11
2.3.2. Bayesian Fast Fourier Transform Approach (BFFTA).....	14
2.3.3. Bayesian Spectral Trace Approach (BSTA) .....	15
2.4. Computational Procedure for BAYOMA .....	16
2.4.1. Fast Computational Procedure for Well Separated Modes .....	16
2.4.2. Two-stage Solution for NLLF .....	17
2.4.3. Determination of Most Probable Spectral Parameters .....	18
2.4.4. Asymptotic Behavior Under Large Signal-to-Noise Ratio .....	19
2.4.5. Summary of Overall Computational Procedure .....	21
2.5. Posterior Uncertainties of Optimal Modal Parameters .....	21
2.5.1. Calculation of Hessian Matrix Under Constraints .....	23
2.5.2. An Alternative Method for Calculation of Posterior Covariance Matrix by Two-stage BFFTA.....	24
2.5.3. Posterior Uncertainty of Modal Shape Vector .....	27

2.6. Uncertainty Laws .....	30
2.7. Numerical and Experimental Analysis .....	31
2.7.1. Numerical Analysis I: Ten Story Shear Frame .....	31
2.7.2. Numerical Analysis II: A Comparison for Posterior Uncertainty Quantification.....	37
2.7.3. Experimental Analysis: Three-story Shear Frame .....	38
2.7.4. Field Data Example: 58 Story Building .....	41
2.7.5. Field Data Example: One Rincon Tower .....	46
2.8. Concluding Remarks.....	54
CHAPTER 3. COMPUTATIONAL ISSUES IN BAYOMA .....	55
3.1. Introduction.....	55
3.2. Closely Spaced Modes.....	56
3.3. Effect of Modelling Error .....	58
3.4. Buried Mode Case .....	60
3.4.1. Special Case I: Burying Mode on the Left Side.....	62
3.4.2. Special Case II: Burying Mode on the Right Side .....	62
3.4.3. Special Case III: Burying Mode on Both Sides .....	63
3.5. Summary of Procedures.....	63
3.6. Numerical Analysis.....	65
3.6.1. Closely Spaced Modes .....	65
3.6.2. Effect of Modelling Error.....	67
3.6.3. Buried Mode Case.....	68
3.7. Concluding Remarks.....	71
CHAPTER 4. TWO-STAGE BAYESIAN MODE SHAPE ASSEMBLY TECHNIQUE FOR MULTIPLE SETUPS .....	73
4.1. Introduction.....	73
4.2. Non-Bayesian Methods.....	75
4.2.1. Local Least Squares Approach.....	75
4.2.2. Global Least Squares Approach.....	76
4.3. Bayesian Methods.....	78
4.3.1. Bayesian Global Mode Shape Identification Technique.....	78
4.3.2. Bayesian Mode Shape Assembly .....	81

4.4. Proposed Bayesian Algorithm .....	82
4.4.1. Two-Stage BFFTA for Mode Shape Assembly .....	82
4.4.2. Alternative Solution by Gaussian Approximation .....	85
4.4.3. Estimation of the Weights for Individual Setups .....	87
4.4.4. Posterior Uncertainty .....	88
4.4.5. Summary of Procedure.....	89
4.5. Experimental and Numerical Analysis .....	91
4.5.1. Experimental analysis: Laboratory shear frame.....	91
4.5.2. Benchmark study: Z24 Bridge .....	98
4.5.3. Application for Closely Spaced Modes: One Rincon Tower.....	105
4.5.4. Numerical Analysis: A Comparison for Posterior Uncertainty Quantification.....	108
4.6. Concluding Remarks.....	109

CHAPTER 5. A TWO-STAGE BAYESIAN APPROACH FOR FINITE ELEMENT  
MODEL UPDATING BY USING ACCELERATION RESPONSE

DATA FROM MULTIPLE SETUP MEASUREMENTS.....	110
5.1. Introduction.....	110
5.2. Stage I: Modal Identification .....	113
5.3. Stage II: Model Updating .....	114
5.3.1. Prior Probability Distributions of Eigenvalues and Eigenvectors .....	115
5.3.2. Estimation of Prior Stiffness and Mass Distributions .....	115
5.3.3. Prior Probability Distribution for Modelling Error .....	116
5.3.4. Posterior Probability Distribution for System Parameters .....	117
5.3.4.1. MPV of Modal Parameters .....	118
5.3.4.2. MPV of Model Parameters .....	119
5.4. Summary of Procedures.....	120
5.5. Posterior Uncertainty .....	121
5.6. Probabilistic Damage Detection .....	122
5.7. Numerical and Experimental Analysis .....	122
5.7.1. Numerical analysis: Torsional Shear Frame .....	123
5.7.2. Experimental analysis: Ten story shear frame .....	133



CHAPTER 6. CONCLUSIONS .....	137
6.1. Summary of Results and General Conclusions.....	137
6.2. Recommendations for Future Works.....	139
APPENDICES	
APPENDIX A. DERIVATIVES OF NEGATIVE-LOGARITHM LIKELIHOOD FUNCTION.....	141
APPENDIX B. SCALING OF NEGATIVE LOG-LIKELIHOOD FUNCTION FOR UNIT NORM OF MODE SHAPE VECTOR.....	144
APPENDIX C. DERIVATION OF COHERENCE BETWEEN TWO DIFFERENT SIGNALS AND CAYLEY TRANSFORMATION .....	146
APPENDIX D. DERIVATION OF POSTERIOR COVARIANCE MATRIX FOR CLOSELY SPACED MODES.....	148
APPENDIX E. DERIVATION OF HESSIAN MATRIX FOR MODEL PARAMETERS .....	153
REFERENCES .....	155

# LIST OF FIGURES

<b><u>Figure</u></b>	<b><u>Page</u></b>
Figure 1.1. Flowchart for the proposed computational framework .....	7
Figure 2.1. Vectoral representation of exact and most probable mode shapes.....	27
Figure 2.2. Convergence of exact and approximate EMAC values (solid line: exact, dashed line: approximate) .....	29
Figure 2.3. Root singular value spectrum and possible modes with selected bandwidths .....	32
Figure 2.4. Identified and analytical mode shape vectors.....	33
Figure 2.5. Effect of signal-to-noise ratio on the posterior c.o.v. of spectral parameters .....	34
Figure 2.6. Effect of signal-to-noise ratio on the posterior c.o.v. of first mode shape ...	35
Figure 2.7. Effect of signal-to-noise ratio on the MPVs and posterior standard deviations .....	35
Figure 2.8. Comparison of the computational time required for the calculation of posterior covariance matrix.....	38
Figure 2.9. Schematic view of laboratory frame and measured acceleration responses .....	38
Figure 2.10. Root singular value spectrum and possible modes with selected bandwidths .....	39
Figure 2.11. Root singular value spectrum and possible modes with selected bandwidths .....	40
Figure 2.12. Comparison of exact and approximate marginal distributions.....	41
Figure 2.13. Schematic view of 58-Story Building and sensor locations (Source: Center of Engineering Strong Motion Data).....	42
Figure 2.14. Maximum root singular value spectrum and possible modes .....	43
Figure 2.15. Identified mode shapes in EW direction .....	44
Figure 2.16. Identified mode shapes in NS direction .....	44
Figure 2.17. Identified torsional mode shapes .....	45
Figure 2.18. Elevation view of One Rincon Tower and sensor locations (Source: Center of Engineering Strong Motion Data).....	46

<b><u>Figure</u></b>	<b><u>Page</u></b>
Figure 2.19. Plan views and sensor locations (Source: Center of Engineering Strong Motion Data) .....	47
Figure 2.20. Root singular value spectrum and possible modes.....	48
Figure 2.21. 3D view of the identified mode shapes .....	50
Figure 2.22. EMAC values with $\pm$ standard deviations .....	50
Figure 2.23. Comparison of exact c.o.v. values with uncertainty laws .....	51
Figure 2.24. Identified mode shapes by using NS data .....	52
Figure 2.25. Identified mode shapes by using EW1 data .....	52
Figure 2.26. Identified mode shapes by using EW2 data .....	53
Figure 2.27. Identified torsional mode shapes by using EW1 and EW2 data .....	53
Figure 3.1. Effect of modelling error on the SV spectrum .....	60
Figure 3.2. Possible scenarios for buried mode case .....	61
Figure 3.3 Flowchart for the solution procedure of multiple and buried modes .....	64
Figure 3.4. Maximum singular value spectrum and selected frequency band.....	65
Figure 3.5. Identified mode shapes and their analytical values .....	66
Figure 3.6. Variations in identified modal parameters versus modelling error ratio (with $\pm$ standard deviations) .....	67
Figure 3.7. Variations in MAC values with respect to the modelling error ratio .....	68
Figure 3.8. Identified mode shapes and their analytical values for Case-I, II and III ....	69
Figure 3.9. Identified mode shapes and their analytical values for Case-I, II and III ....	70
Figure 4.1. Flow chart for the proposed algorithm .....	90
Figure 4.2. Ten story shear frame structure .....	92
Figure 4.3. Maximum root singular value spectra .....	92
Figure 4.4. Variations in the estimated signal-to-noise ratios .....	94
Figure 4.5. Assembled mode shapes for Case-I.....	95
Figure 4.6. Assembled mode shapes for Case-II .....	95
Figure 4.7. Variations in MAC values with respect to reference mode shapes versus the number of iterations .....	96
Figure 4.8. Calculated setup weights for Case-I.....	97
Figure 4.9. Calculated setup weights for Case-II.....	98
Figure 4.10. Schematic representation of Z24 Bridge and sensor layouts (Reynders et al, 2012; Reynders and Roeck, 2008) .....	99

<b><u>Figure</u></b>	<b><u>Page</u></b>
Figure 4.11. Root singular value spectrum for all setups .....	100
Figure 4.12. Identified frequencies with representative statistics.....	101
Figure 4.13. Identified damping ratios with representative statistics .....	101
Figure 4.14. Variations in the identified signal-to-noise ratios among different setups.....	102
Figure 4.15. Identified mode shapes by the proposed modified algorithm .....	103
Figure 4.16. Variations in $MAC_{i,0}$ values with respect to number of iterations .....	104
Figure 4.17. Variations in calculated setup weights .....	104
Figure 4.18. Identified natural frequencies and damping ratios with standard deviations .....	106
Figure 4.19. Identified mode shapes .....	107
Figure 4.20. Comparison of the computational time required for the calculation of posterior covariance matrix.....	108
Figure 5.1. Flow chart for the proposed algorithm .....	121
Figure 5.2. Plan view of fifteen story torsional shear frame structure.....	123
Figure 5.3. Selected distributions for prior estimation of stiffness and mass parameters .....	126
Figure 5.4. Cumulative probability of damage for the stiffness parameters (blue line: $x$ - $x$ direction, red line: $y$ - $y$ direction).....	129
Figure 5.5. Variation of the estimated $\theta_{x1}$ versus the number of considered modes (red circle: rigid constraint, blue square: soft constraint for eigenvalues) .....	129
Figure 5.6. Variation of the posterior c.o.v. of $\theta_{x1}$ versus the number of considered modes (red circle: rigid constraint, blue square: soft constraint for eigenvalues) .....	130
Figure 5.7. Variation of the estimated $\theta_{y1}$ versus the number of considered modes (red circle: rigid constraint, blue square: soft constraint for modelling and prediction error) .....	130
Figure 5.8. Variation of the posterior c.o.v. of $\theta_{y1}$ versus the number of considered modes (red circle: rigid constraint, blue square: soft constraint for modelling and prediction error) .....	131

<b><u>Figure</u></b>	<b><u>Page</u></b>
Figure 5.9. Updated mode shapes (blue squares) and analytical values (red line) for undamaged case .....	131
Figure 5.10. Updated mode shapes (blue squares) and analytical values (red line) for damaged case.....	132
Figure 5.11. Updated mode shapes for considered scenarios .....	134

## LIST OF TABLES

<b><u>Table</u></b>	<b><u>Page</u></b>
Table 2.1. Iterative algorithm by Au (2011a) .....	21
Table 2.2. Non-iterative algorithm by Au (2011a) .....	21
Table 2.3. Exact solution algorithm by Monte Carlo Technique.....	29
Table 2.4. Identification results for frequency and damping ratios .....	32
Table 2.5. Identification results for the spectral density of modal excitation and prediction error, and root signal-to-noise ratio .....	32
Table 2.6. Comparison of MAC values of identified mode shapes ( $n$ : mode number) ..	36
Table 2.7. Comparison of identified frequencies ( $Hz$ ) for first mode.....	37
Table 2.8. Comparison of identified damping ratios (%) for first mode .....	37
Table 2.9. Identification results for the spectral density of modal excitation and prediction error, and root signal-to-noise ratio .....	40
Table 2.10. Identified natural frequencies and damping ratios.....	43
Table 2.11. Identification results for the spectral density of modal excitation and prediction error, and root signal-to-noise ratio .....	48
Table 2.12. Identification results for the spectral density of modal excitation and prediction error, and root signal-to-noise ratio .....	49
Table 3.1. Identified frequencies and damping ratios.....	66
Table 3.2. PSD of modal excitations and prediction error.....	67
Table 3.3. Free parameter, $u_{ij}$ for cross PSD of modal excitation .....	67
Table 3.4. Identified frequencies and damping ratios for burying modes .....	69
Table 3.5. Identified modal parameters for buried modes .....	70
Table 4.1. Iterative algorithm for the global least square approach .....	78
Table 4.2. Setup configurations for Case-I and Case-II .....	92
Table 4.3. Average MPVs and representative statistics for $f_i$ and $\zeta_i$ .....	93
Table 4.4. Calculated MAC values for Case I and II.....	96
Table 4.5. Calculated frequencies and damping ratios .....	101
Table 4.6. MAC values for the estimated mode shapes.....	102
Table 4.7. Sensor placements for measurement setups .....	106
Table 5.1. Multiple setup configuration.....	123

<b><u>Table</u></b>	<b><u>Page</u></b>
Table 5.2. Actual and updated natural frequencies with posterior c.o.v.....	127
Table 5.3. Actual and updated stiffness parameters in the $x$ - $x$ direction .....	127
Table 5.4. Actual and updated stiffness parameters in the $y$ - $y$ direction .....	128
Table 5.5. Posterior c.o.v. values for mode shapes ( $\times 10^{-12}$ ) .....	132
Table 5.6. Sensor placement configuration for considered measurement scenarios ....	133
Table 5.7. MPVs and posterior c.o.v. for natural frequencies (“*” denotes the MPVs that are identified from the measurements) .....	133
Table 5.8. Identified stiffness parameters for considered cases .....	134

# CHAPTER 1

## INTRODUCTION

### 1.1. Motivation of Study

Structural Health Monitoring (SHM) applications have an important role to determine the dynamic characteristics of structures which are designed to resist extreme events such as earthquakes, wind loads. The modal properties of the structures including natural frequencies, damping ratios, and modal shape vector have a prominent role in the structural design procedure. However, those design characteristics may show significant deviations from the actual values due to the non-linear effects such as possible variance in the material properties, and small differences in the geometrical configuration during the construction phase. In addition, when structures are subject to extreme events such as earthquakes, they might have been subjected to damage which can also cause a significant change in the dynamic characteristics. For this reason, monitoring the variations in the modal properties become prominent to identify the current state of a structure.

To provide a useful solution for the problems that are mentioned above, Operational Modal Analysis (OMA) methods presents efficient tools to identify modal properties of structures by using acceleration, velocity or displacement response measurements. The most important advantage of OMA methods is that it does not need any information for the input motion. Various OMA methods are available in the literature based on the physical, statistical or probabilistic interpretation of the measured response. In this context, Bayesian Operation Modal Analysis (BAYOMA) presents a framework to identify the modal properties based on a probabilistic logic. According to this framework, the most probable value (MPV) for each modal parameter are quantified with their uncertainties. Different from other OMA methods, BAYOMA defines a probabilistic range with an MPV rather than a certain identified parameter.

As a next step, the finite element model of the measured system may be updated by using a Bayesian probabilistic approach. A posterior probability distribution for model (stiffness and mass components) and modal parameters can be obtained by using the



outputs of any OMA method. In addition, a more reasonable probabilistic model may be obtained when the prior distribution of modal parameters is modeled by BAYOMA.

## 1.2. Literature Review

Modal analysis techniques in the literature can be classified as experimental and operational modal analysis methods due to the requirement of input motion information. Experimental modal analysis (EMA) which utilizes input-output techniques might be more feasible for laboratory studies or some special cases in which the input motion can be controlled by shakers or impact loading. However, the application of EMA is quite limited due to insufficient information available for input motion in most cases (Orlowitz & Brandt, 2017). In this context, OMA presents more feasible techniques to extract the dynamic characteristics of the investigated structure since it utilizes the ambient vibration data without resorting to information of input data. OMA considers a randomly distributed input excitation in stochastic manner. Therefore, it assumes that large number of vibration modes are excited by ambient loading effects.

Various methods are available in the literature for damage detection based on updating the finite element models by using the modal parameters that are identified by OMA or EMA methods. The most generic form of these updating procedures are based on the minimization of discrepancy between the identified eigenvalues, eigenvectors and model eigenvalues and eigenvectors (Yuen, 2010; Touat et al, 2014). Bayesian approaches for finite element model updating are also available in the literature. These approaches are generally a combination of two stages. At first stage, the modal parameters are identified by using the acceleration response measurements, and a proper prior distribution is assigned for modal (eigenvalues and eigenvectors) and model (stiffness or mass scaling factors) parameters (Ching et al, 2006). The main difference between the available Bayesian methods lies in the selection of prior distributions for model parameters. Generally, truncated normal (Yuen and Kuok, 2011; Yan and Katafygiotis, 2015c) or lognormal (Das and Debnath, 2018) distributions or their combinations are selected to represent the prior distribution of model parameters. Another difference lies in the consideration of multiple setup measurements in the Bayesian finite element model updating procedure. Here, two different approaches are available based on generation of prior distribution of measured modal parameters: (i) using the global values obtained by

assembling the local ones from each setup (Yuen and Kuok, 2011), or (ii) using the local identified parameters directly (Yan and Katafygiotis, 2015c; Au and Zhang, 2016; Zhang and Au, 2016; Zhang et al, 2017).

A brief literature review is presented for non-Bayesian and Bayesian OMA methods in the following two subsections. In addition, detailed literature reviews for specific fields that are investigated in this thesis are provided in the corresponding chapters.

### **1.2.1. Non-Bayesian Methods**

Various OMA methods have been presented to the literature based on the time or frequency domain analysis of measured response. Among these, Ibrahim Time-domain Identification, Natural Excitation Technique and Eigensystem Realization Algorithm (NExT-ERA), Stochastic Subspace Identification (SSI), and Frequency Domain Decomposition (FDD) come forward as most conventional and well-known time or frequency domain techniques in the literature.

Ibrahim Time-domain Identification is based on the theory that the output of the ambient excitation can be reduced to an equivalent free vibration response or correlation functions by a random decrement transformation. Finally, the modal parameters are obtained by the solution of an eigenvalue problem that is constructed from the reduced time-domain data (Ibrahim, 1999; Malekjafarian et al, 2012). Another time-domain method, NExT-ERA is a combination of two-different techniques and works in two steps. First, the measured ambient vibration data is processed and transformed by NExT to an equivalent free-vibration response data. Second, the modal properties are extracted by ERA which constructs a linear state-space dynamical model based on the modal characteristics of the measured system (Caicedo, 2011). SSI presents an efficient statistical framework for system identification based on the state-space representation of a linear dynamic model that is excited by a White Noise excitation. First, the state of the system is predicted by a Kalman filter based on the outputs of the Hankel matrix which is a special form of the collected response data (data driven) or its covariance (covariance driven). Second, the optimal prediction is obtained for the state vector by the projection of the outputs of the Kalman filter and the available system matrices. Third, the system matrices are obtained by linear regression of Kalman state sequences. Finally, the

covariances for the measurement noise and modelling error are recovered (Overschee and Moor, 1993; Peeters and De Roeck, 2000). Although SSI is an efficient OMA method and it is widely used in the civil engineering community, computational efforts in the analysis procedure may increase due to possible problems in the selection of a proper model order for the Hankel matrix. If the number of modes to be identified increases, the model order may need to be increased as well. Thus, the dimension of the Hankel matrix will inevitably increase. This problem is also widely seen in the application of NExT-ERA.

A frequency domain identification technique: Frequency Domain Decomposition (FDD) has been presented by Brincker et al (2001). This method first transforms the measured data to frequency-domain by using Fast Fourier Transformation (FFT). Second, the possible modes are detected from the Singular Value (SV) spectrum of the FFT data, and the eigenfrequencies are determined from the dominant frequency band of the corresponding mode(s) by peak-picking. Damping ratios are determined by using the decay of motion of the time-domain response of equivalent single degree of freedom (SDOF) system. This time-domain response is obtained by inverse FFT of the frequency-domain response within the dominant frequency band of the corresponding mode(s). Finally, the mode shapes are obtained by the singular value decomposition of the power spectral density (PSD) matrix of the measured response. The FDD method presents a fast and efficient scheme for frequency domain OMA. However, the method does not consider the modelling error and measurement/environmental noise effects.

### **1.2.2. BAYOMA Methods**

Different from the non-Bayesian methods, BAYOMA presents a probabilistic framework to determine the modal parameters in terms of MPV. Some Non-Bayesian methods also provide statistical information about the identified data in terms of expected value, standard deviation and/or covariance (i.e. SSI, FDD). These methods consider statistical parameters for identified values by a frequentist approach (Au, 2012a). According to these frequentist approaches, the statistical parameters are directly obtained from the sample. For example, the expected value is obtained as the sample mean, and the other parameters are obtained as sample standard deviation, covariance of different trials. Probabilistic approaches, however, defines these parameters in terms of MPV and

uncertainty. In a probabilistic approach, the MPV and uncertainty of the modal parameters are estimated by using a proper probability distribution for the available data. In this context, BAYOMA presents an efficient tool for modal parameter identification and uncertainty quantification by using Bayesian statistics. First, a prior probability distribution function correlated with the measured data is constructed. This function directly depends on the statistical properties of the measured data and it is conditional to the expectation of the set of modal parameters to be identified. Second, a “posterior distribution” for the set of modal parameters are obtained by using Bayes’ theorem.

Basic concept of the BAYOMA was first presented by Katafygiotis and Yuen (2001a) based on the probabilistic distribution of the statistical expectation of sample spectral density matrix. The theory is based on the approximation that the expected spectral density matrix of the measured data follows a complex “Wishart Distribution”. Therefore, the first BAYOMA method is called “Bayesian Spectral Density Approach (BSDA)”. Second, a time-domain approach is presented by Yuen and Katafygiotis (2001b) based on the assumption that the measured response data follows a zero-mean Gaussian distribution. Third, a different BAYOMA method that is referred as “Bayesian Fast Fourier Transform approach” is presented by Yuen and Katafygiotis (2003). This approach assumes that the real and imaginary part of the FFT of measured data follows a zero mean Gaussian distribution. These BAYOMA methods construct a negative-logarithm likelihood function of posterior probability distribution of the set of modal parameters. Minimization of the negative-logarithm likelihood function with respect to the parameters to be identified gives MPVs. However, the computational effort becomes remarkably high due to the increasing number of parameters to be identified as depending on the number of considered modes within a wide frequency band. For this reason, two fast-computational procedures were presented by Au (2011a), (2012b) and (2012c) for well separated and closely spaced modes. These approaches consider a narrow band in which the mode(s) of interest dominates the total response and turns the negative-logarithm likelihood function into a more manageable form.

Yan and Katafygiotis (2015a) presented a two-stage Bayesian approach for ambient system identification. At the first stage, the mode shapes, and spectrum parameters (natural frequency, damping ratio, spectral density of modal excitation, and the spectral density of prediction error) are separated into two parts and MPV of spectrum parameters are determined by employing a “Bayesian Spectral Trace Approach (BSTA)”.

Second, the mode shapes are identified by BSDA substituting spectrum parameters that are determined in the first stage, into the negative-logarithm likelihood function.

In BAYOMA, the posterior probability density function (PDF) of the set of modal parameters can be well-estimated by the Gaussian approximation in case of the sufficiently large amount of measured data (F. Zhang, 2012). Here, a Gaussian PDF is obtained in terms of the MPV and posterior covariance matrix of the modal parameters by using the first order Taylor series expansion of the negative-logarithm likelihood function. Thus, the posterior uncertainties are obtained by the posterior covariance matrix which is derived as a Hessian matrix which basically contains the second order derivatives of the negative-logarithm likelihood function.

### **1.3. Objectives of the study**

The theoretical background of BAYOMA has been well established and numerous theoretical and experimental studies have been presented on this topic by various researchers. In the light of the literature, this study aims to present a wide-range computational framework from modal identification to finite element model updating and damage detection procedure for structures by using Bayesian statistics. For this purpose, new or modified solutions for the problems that are addressed in the literature are aimed to be developed.

One of the most important problems in BAYOMA has been reported as the calculation of the posterior covariance matrix under equality constraints. To solve this problem, a solution procedure was previously presented by Au and Xie (2017). This study presents an alternative solution which results in a block diagonal posterior covariance matrix, and it is derived that the modal shape vector and spectrum parameters have zero correlation. In addition, some improvements for the solution procedure of closely spaced modes are presented.

This study also presents alternative/new algorithms for mode shape assembly and finite element model updating procedure to reduce the computational time/effort and posterior uncertainties of the identified/updated parameters.

A flowchart for the computational framework that is aimed to be developed in this study is presented in Figure 1.1. In this computational framework, Bayesian modal identification procedure takes a very important role. According to this procedure, first,

the most probable modal properties of the measured structure are determined for the cases of single or multiple setups. At second stage, the posterior probability distributions of the identified modal parameters are obtained. At third stage, the prior distributions for modal and model parameters are defined and the finite element model (FEM) of the structure is updated by employing the Bayes' Theorem. At the final stage, the level of the possible damage and its location are determined.

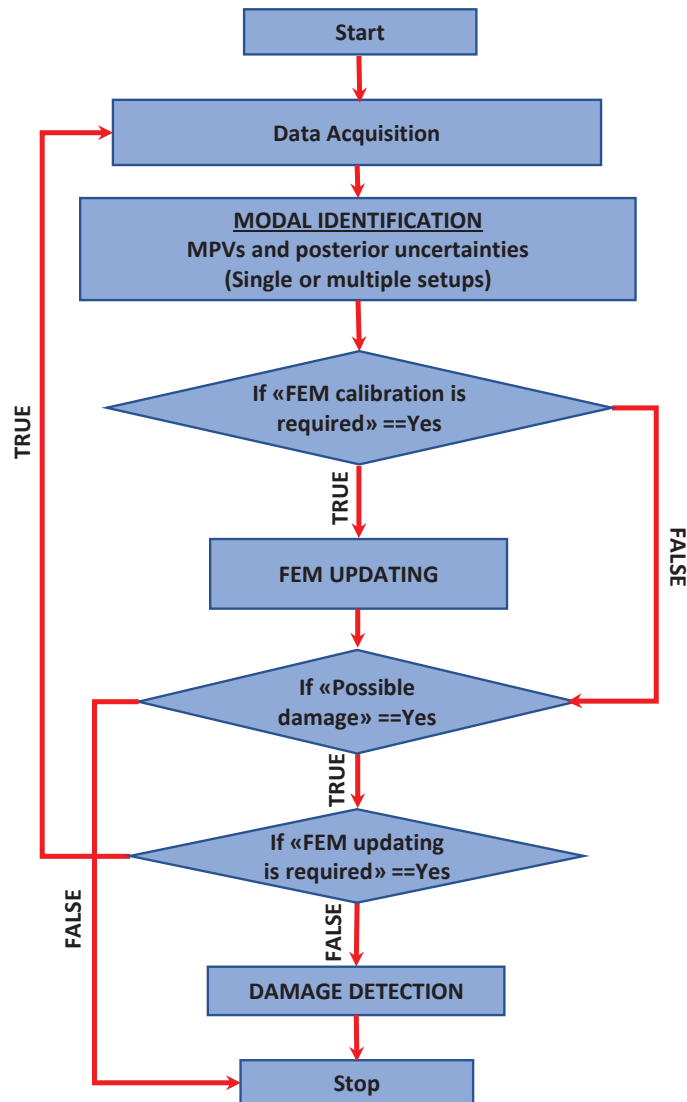


Figure 1.1. Flowchart for the proposed computational framework

## 1.4. Outlines

Based on the main objectives of the presented research, this study is composed by four main chapters.

- Chapter 2 reviews the theoretical background of available BAYOMA methods. An alternative solution for the consideration of equality constraints in the posterior uncertainty quantification is presented. The capabilities and limits of BAYOMA are investigated.
- Chapter 3 reviews some computational issues that are addressed in the literature. The problems of multiple (closely spaced) and buried modes are investigated. A modification is proposed for the solution of multiple mode problems. Effect of modelling error on the identification quality is investigated. Finally, a general solution procedure for buried mode case is presented.
- In Chapter 4, first, the available mode shape assembly algorithms for multiple measurement setups are reviewed. Second, an alternative mode shape assembly technique by two-stage Bayesian Fast Fourier Transform approach is presented. The presented methodology is compared to the available Bayesian method via numerical and experimental analysis.
- Chapter 5 presents a Bayesian finite element model updating procedure including the multiple setup problem and missing data case based on the two-stage Bayesian Fast Fourier Transform approach. The effect of the presented methodology on the identification (or updating) quality and their posterior uncertainties are investigated by numerical and experimental analysis.

## CHAPTER 2

# BAYESIAN OPERATIONAL MODAL ANALYSIS IN FREQUENCY DOMAIN: WELL SEPARATED MODES

### 2.1. Introduction

In frequency domain modal identification, statistical properties of FFT data obtained from measured acceleration responses present a point of view for the estimation of most probable modal parameters including natural frequencies, damping ratios and modal shape vectors. The physical meaning and the statistical properties of FFT data is prominence to construct a probabilistic framework for the expected modal parameters. In addition to these, spectral density level of excitation and possible measurement errors might be important in the identification process. In this context, Bayesian operational modal analysis (BAYOMA) in frequency domain proposes simple and fast algorithms based on the statistical properties of measured data. Katafygiotis and Yuen (2001a) first proposed the Bayesian Spectral Density Approach (BSDA) based on the statistical properties of spectral density matrix. A Bayesian Fast Fourier Transform approach (BFFTA) was proposed by Yuen and Katafygiotis (2003) to estimate the most probable modal parameters by using the Fast Fourier Transform (FFT) data. Au (2011a) proposed a fast algorithm for BFFTA for systems with well separated modes and reformulated the general methodology presented by Yuen and Katafygiotis (2003). In past decade, numerous studies concerning the general computational process and application of Bayesian Spectral Density and Fast Fourier Transform Approach have been presented (Au et al, 2013; Lam et al, 2017; Ni and Zhang, 2015; Ni et al, 2015; Ni et al, 2016; Au, 2016a, 2016b). In addition, Yan and Katafygiotis (2015a) presented a two stage BSDA that separates the modal parameters to be identified into two components: (i) spectrum variables including frequency, damping ratio, and spectral density of modal excitation and prediction error, (ii) spatial parameters including the modal shape components. Although BSDA and BFFTA are motivated by different statistical properties of measured data, they result in similar estimators.



In this chapter, first, the general formulation and derivation of the available BAYOMA methods are presented. Second, the fast-computational procedure that is available in the literature is reviewed for the implementation of BAYOMA methods. Finally, an alternative method for the calculation of posterior covariance matrix is presented as a contribution to the literature. Using the proposed methodology, a block diagonal covariance matrix is obtained, and its validity is verified by the conventional method.

## 2.2. Dynamic Response Analysis in Frequency Domain

System identification of engineering structures with output only identification requires an appropriate mathematical representation of dynamic response in frequency domain. The most prominent problem in output only identification is that the excitation is an unknown parameter. For this reason, the excitation level that enforce the structure to vibrate must be defined as a modal parameter to be identified. In frequency domain, the dynamic equation of motion of a multi degree of freedom (MDOF) system can be written as;

$$M\ddot{U}_k + C\dot{U}_k + KU_k = P_k \quad (2.1)$$

where  $M$ ,  $C$ , and  $K$  are  $n \times n$  sized mass, damping and stiffness matrix, and  $P_k$ ,  $U_k$  denote  $n \times N_t$  sized frequency depended external load and displacement response functions. In addition,  $n$  = number of total degrees of freedom (DOFs), and  $N_t$  = number of acceleration data in time domain. Modal decomposition of the frequency depended displacement, velocity and acceleration responses can be written as below.

$$\begin{aligned} U_k &= \sum_{i=1}^n q_{ki} \varphi_i \\ \dot{U}_k &= \mathbf{i} 2\pi f_k \sum_{i=1}^n q_{ki} \varphi_i \\ \ddot{U}_k &= \mathbf{i}^2 4\pi^2 f_k^2 \sum_{i=1}^n q_{ki} \varphi_i \end{aligned} \quad (2.2)$$

in which  $f_k$  = excitation frequency,  $q_{ki}$ ,  $\varphi_i$  = normal coordinate function and modal shape vector for  $i^{th}$  mode. Thus, the uncoupled equation of motion is written as below by substituting Eq. (2.2) into (2.1) and pre-multiplying by  $\varphi_i^T$ .

$$4\pi^2 f_k^2 q_k (1 + \mathbf{i}2\zeta_i \beta_{ki} + \mathbf{i}^2 \beta_{ki}^2) = \frac{\varphi_i^T P_k}{\varphi_i^T M \varphi_i}; \quad \beta_{ki} = \frac{f_i}{f_k} \quad (2.3)$$

Here,  $f_i$ ,  $\zeta_i$  = natural frequency and damping ratio, and  $\beta_{ki}$  = frequency ratio. Thus, the displacement, velocity, and acceleration responses are obtained as

$$\begin{aligned} U_k &= \sum_{i=1}^n U_{ki}; & U_{ki} &= (4\pi^2 f_k^2)^{-1} p_{ki} h_{ki} \\ \dot{U}_k &= \sum_{i=1}^n \dot{U}_{ki}; & \dot{U}_{ki} &= (2\pi f_k)^{-1} p_{ki} h_{ki} \\ \ddot{U}_k &= \sum_{i=1}^n \ddot{U}_{ki}; & \ddot{U}_{ki} &= p_{ki} h_{ki} \end{aligned} \quad (2.4)$$

where  $h_{ki}$  = transfer function from modal excitation,  $p_{ki}$ , to modal acceleration response,  $\ddot{U}_{ki}$ , for the  $i^{\text{th}}$  mode.

$$p_{ki} = \frac{\varphi_i^T P_k}{\varphi_i^T M \varphi_i}; \quad h_{ki} = \left[ (1 - \beta_{ki}^2) + \mathbf{i}(2\zeta_i \beta_{ki}) \right]^{-1} \quad (2.5)$$

If a frequency band is selected such that a single mode dominates the total response, the spectral density of acceleration response is obtained as;

$$H_k = \ddot{U}_k \ddot{U}_k^* = S_k D_k \varphi \varphi^T; \quad S_k = p_k p_k^*; \quad D_k = h_k h_k^* \quad (2.6)$$

In Eq. (2.6),  $S_k$  = spectral density of modal excitation.  $S_k$  is an unknown spectral parameter, and its expected value should be determined in addition to the expected value of  $f_i$ ,  $\zeta_i$ , and  $\varphi_i$ .

## 2.3. BAYOMA Methods

In this section, first, BAYOMA methods in the literature are introduced. Then, the efficiency of those methods is critically discussed.

### 2.3.1. Bayesian Spectral Density Approach (BSDA)

The statistical expectation for the spectral density matrix of measured response can be defined by its posterior probability distribution. This probabilistic distribution may be used as an estimator to identify the set of modal parameters,  $\theta = [f, \zeta, S, S_e, \varphi^T]$ . Here,  $f$ ,  $\zeta$ ,  $S$ ,  $S_e$ , and  $\varphi$  denote the expected value of natural frequency, damping ratio, spectral density of modal excitation, spectral density of prediction error, and modal shape vector

within the resonant frequency band of a single mode, respectively. The expected value of the spectral density matrix of measured response can be defined as (Yuen, 2010);

$$E[S_{pk}] = E_k = SD_k \varphi \varphi^T + S_e I_N \quad (2.7)$$

in which  $S_{pk} = F_k F_k^*$  and  $F_k = \dot{U}_k + e_k$ . Here,  $F_k$  = scaled FFT of measured acceleration response that includes the error term,  $e_k$ . The spectral density of prediction error includes both the channel noise and the modelling error and can be defined as a diagonal matrix (Yuen and Katafygiotis, 2003).

$$E[e_k e_k^*] = S_e I_N \quad (2.8)$$

in which  $N$  = number of measured DOF. The scaled discrete Fast Fourier Transform (FFT) of the measured response,  $\ddot{y}(t)$ , can be written as below (Au, 2011a).

$$F_k = \sqrt{\frac{2\Delta t}{N_t}} \sum_{s=1}^{N_t} \ddot{y}_s \times e^{-\frac{2\pi i(k-1)(s-1)}{N}} \quad (2.9)$$

where  $k = \{1, \dots, N_t\}$ , and  $\Delta t$  = sampling time interval. Probability distribution of modal parameters depends on the statistical properties of FFT. In this context, a conditional joint probability function of modal parameters (posterior probability density function),  $p(\theta | S_{pk})$ , can be defined for a certain excitation frequency by using Bayes' theorem,

$$p(\theta | S_{pk}) = \frac{p(S_{pk} | \theta) p(\theta)}{p(S_{pk})} \quad (2.10)$$

where  $p(S_{pk} | \theta)$  = likelihood function (or spectral density estimator),  $p(\theta)$  = prior probability distribution of modal parameters,  $p(S_{pk})$  = scaling factor (independent from  $\theta$ ). According to the literature, it is well-known that  $p(S_{pk} | \theta)$  varies much faster than  $p(\theta)$  with respect to  $\theta$  (Yuen and Katafygiotis 2002, Zhang 2011). Therefore, the posterior probability density function,  $p(\theta | S_{pk})$ , can be assumed to be proportional to  $p(S_{pk} | \theta)$ . Yuen (2010) states that spectral density matrix follows the complex Wishart Distribution of dimension  $N$  with  $N_s$  degrees of freedom under ambient excitation. Here  $N_s$  = size of the windowed part of FFT if an average spectral density matrix is used. Thus,  $p(S_{pk} | \theta)$  is written as below (Yuen, 2010).

$$p(S_{pk} | \theta) = \frac{\pi^{-\frac{N(N-1)}{2}} N_s^{N(N_s-N)} |S_{pk}^{avg}|^{N_s-N}}{\prod_{s=1}^{N_s} (N_s - s)! |E_k|^{N_s}} \exp\left(-N_s \text{tr}\left[E_k^{-1} F_k F_k^*\right]\right) \quad (2.11)$$

where  $S_{pk}^{avg}$  = average spectral density matrix.

$$S_{pk}^{avg} = \frac{1}{N_s} \sum_{k=1}^{N_s} F_k F_k^* \quad (2.12)$$

Since the modal parameters are assumed to be linearly independent, the posterior probability density function can be defined as follows in a selected frequency band.

$$\prod_k p(\theta|S_k) \propto \prod_k \frac{\pi^{\frac{N(N-1)}{2}} N_s^{N(N_s-N)} |S_{pk}^{avg}|^{N_s-N}}{\prod_{s=1}^{N_s} (N_s - s)! |E_k|^{N_s}} \exp\left(-N_s \text{tr}\left[E_k^{-1} F_k F_k^*\right]\right) \quad (2.13)$$

Using the negative-logarithm likelihood function of  $p(S_k|\theta)$  might be more practical because the product definition turns to a summation series.

$$L(\theta) = -\ln\left[\prod_k p(\theta|S_k)\right] \propto -\ln\left[\prod_k p(S_{pk}|\theta)\right] \quad (2.14)$$

By using Eq. (2.11), the negative logarithm-likelihood function is arranged as

$$L(\theta) = C + N_s \sum_k \ln|E_k| + N_s \sum_k \text{tr}\left[E_k^{-1} S_{pk}^{avg}\right] \quad (2.15)$$

where  $C$  denotes the constant terms, and does not vary with respect to  $\theta$ .

$$C = -\frac{N_f N(N-1)}{2} \ln \pi + N_f N(N_s - N) \ln N_s + N_f (N_s - N) \ln |S_{pk}^{avg}| + N_f \left(\sum_{s=1}^{N_s} \ln((N_s - s)!) \right)^{-1} \quad (2.16)$$

Using the  $S_{pk}^{avg}$  in the analysis procedure is not necessary, but it provides a reduction in computational time and effort. Instead, the spectral density matrix  $S_{pk}$  can be used in the formulation. In that case,  $N_s$  will be equal to 1, and the negative log-likelihood function is obtained as;

$$L(\theta) = C + \sum_k \ln|E_k| + \sum_k \text{tr}\left[E_k^{-1} F_k F_k^*\right] \quad (2.17)$$

The second term at right hand side can be arranged to a useful form by using an algebraic transformation for the trace of the product.

$$\text{tr}\left[E_k^{-1} F_k F_k^*\right] = F_k^* E_k^{-1} F_k \quad (2.18)$$

Thus, the negative log-likelihood function turns into the following form by substituting Eq. (2.18) into Eq. (2.17).

$$L(\theta) = C + \sum_k \ln|E_k| + \sum_k F_k^* E_k^{-1} F_k \quad (2.19)$$

### 2.3.2. Bayesian Fast Fourier Transform Approach (BFFTA)

The statistical properties of FFT data presents an alternative way to obtain a likelihood estimator. In this context, the posterior PDF for  $\theta$  can be written as below by using the Bayes' theorem.

$$p(\theta|Z_k) = \frac{p(Z_k|\theta)p(\theta)}{p(Z_k)} \quad (2.20)$$

Here,  $Z_k$  = augmented vector that contains the real and imaginary part of scaled FFT.

$$Z_k = \begin{bmatrix} \text{Re}(F_k)^T & \text{Im}(F_k)^T \end{bmatrix}^T \quad (2.21)$$

Under ambient excitation, it is assumed that the real and imaginary part of FFT follows a zero mean Gaussian distribution (Yuen and Katafygiotis, 2003). Thus, the posterior PDF of  $\theta$  can be defined as;

$$\prod_k p(\theta|Z_k) \propto \frac{2\pi^{-(N_f-1)/2}}{\prod_k |C_k|} \exp\left(-\frac{1}{2} \sum_k Z_k^T C_k^{-1} Z_k\right) \quad (2.22)$$

where  $C_k$  = covariance matrix of  $Z_k$ , and it is defined as below (Au, 2011a).

$$C_k = \begin{bmatrix} \text{Re}(E_k) & \text{Im}(E_k) \\ -\text{Im}(E_k)^T & \text{Re}(E_k) \end{bmatrix} \quad (2.23)$$

where,  $\text{Im}(E_k) = -\text{Im}(E_k)^T = 0$ , for well-separated modes (Au, 2011a). Thus, the negative logarithm-likelihood function is obtained as;

$$L(\theta) = -\frac{1}{2}(N_f - 1) \ln 2\pi + \frac{1}{2} \sum_k \ln |C_k| + \frac{1}{2} \sum_k Z_k^T C_k^{-1} Z_k \quad (2.24)$$

As it is seen in Eq. (2.23),  $C_k$  is a  $2N \times 2N$  size band matrix, and its determinant and inverse can be written as below.

$$|C_k| = |E_k|^2; \quad C_k^{-1} = \begin{bmatrix} E_k^{-1} & \\ & E_k^{-1} \end{bmatrix} \quad (2.25)$$

By substituting Eq. (2.25) into Eq. (2.24), the negative logarithm-likelihood function turns into a similar form as given in Eq. (2.19).

### 2.3.3. Bayesian Spectral Trace Approach (BSTA)

BSTA defines the probability distribution of spectrum variables, only. Whereas BSDA and BFFTA formulate the negative-likelihood function depending on the spectrum variables and mode shapes. According to BSTA, it is assumed that  $\{tr[Re(F_k F_k^*)] - tr(E_k)\} / \sqrt{2tr(E_k^2)}$  follows a standard normal distribution (Yan and Katafygiotis, 2015a).

$$p\left(tr(F_k F_k^*) \mid \theta\right) = \left\{4\pi^2 \mid tr(E_k^2)\right\}^{-1/2} \exp\left[-\frac{\{F_k^* F_k - tr(E_k)\}^2}{4tr(E_k^2)}\right] \quad (2.26)$$

Due to the mode shape norm constraint of  $\varphi^T \varphi = 1$ , trace of  $E_k$  and  $E_k^2$  are obtained for well separated modes as below.

$$\begin{aligned} tr(E_k) &= tr(SD_k \varphi \varphi^T + S_e I_N) = SD_k + nS_e \\ tr(E_k^2) &= tr(S^2 D_k^2 \varphi \varphi^T \varphi \varphi^T + 2S_e SD_k \varphi \varphi^T + S_e^2 I_N) \\ &= (SD_k + S_e)^2 + 2S_e SD_k + (n-1)S_e^2 \end{aligned} \quad (2.27)$$

Thus, the negative likelihood function for spectrum variables are obtained as below.

$$\begin{aligned} L(f, \xi, S, S_e) &= N_f \ln 2\pi + \sum_k \ln \left\{ (SD_k + S_e)^2 + 2S_e SD_k + (n-1)S_e^2 \right\} \\ &+ \sum_k \frac{[F_k^* F_k - (SD_k + nS_e)]^2}{4(SD_k + S_e)^2 + 8S_e SD_k + 4(n-1)S_e^2} \end{aligned} \quad (2.28)$$

BSTA is capable of identifying the spectrum parameters as independent from the mode shape vector. For this reason, it is not possible to identify the modal shape vector by BSTA. To solve this problem, Yan and Katafygiotis (2015a) applies a two-stage approach, and calculates the MPV of mode shape vector by using the BSDA. The negative-likelihood function centered at the MPV of spectrum variables that are obtained by BSTA is minimized with respect to mode shape vector. In this study, however, this approach is considered to be inappropriate since the Bayesian nature of the identification process might be deteriorated. Here, MPV of spectrum variables and its uncertainties reflects the results of the probability distribution by BSTA. For this reason, the output of BSTA cannot be directly used in the BSDA, but it can be considered as initial guess (prior most probable value).

## 2.4. Computational Procedure for BAYOMA

Previously introduced methods; BSDA and BFFTA, are motivated by different statistical properties of the FFT data of measured response. However, they result in similar negative logarithm likelihood functions for the estimation of most probable modal parameters. To obtain the MPV of  $\theta$ , an objective function should be defined and minimized with respect to  $f$ ,  $\zeta$ ,  $S$ ,  $S_e$ , and  $\varphi$  under required constraints. In case of well separated modes, the minimization of objective function will require less computational time and effort near the possible modes. A norm constraint is required for mode shape vector in the objective function, because the spectral density of modal excitation depends on the norm of identified most probable  $\varphi$ . This dependence is defined in the following equation.

$$E_k = SD_k \frac{\varphi \varphi^T}{\|\varphi\|^2} + S_e \quad (2.29)$$

where “ $\|\cdot\|$ ” denotes the Euclidian norm of the identified mode shape vector. The remaining parameters ( $f$ ,  $\zeta$ ,  $S_e$ ) do not require an additional constraint in the minimization procedure.

### 2.4.1. Fast Computational Procedure for Well Separated Modes

In the original form of the objective function that is given in Eq. (2.19), the inverse and determinant of  $E_k$  is required to be calculated at each excitation frequency,  $f_k$ . However, the reformulation of objective function in explicit form might be more useful by making some modifications in the calculation of inverse and determinant of the expected spectral density matrix. For this purpose, Au (2011a) defines an orthonormal vector space whose first vector corresponds to mode shape to obtain the inverse and determinant of  $E_k$ . In this study, however, the same result is obtained by using the matrix inversion and determinant lemma (Harville, 1997).

$$\begin{aligned} (ABC + D)^{-1} &= D^{-1} - D^{-1}A(CD^{-1}A + B^{-1})^{-1}CD^{-1} \\ |ABC + D| &= |B^{-1} + CD^{-1}A||B||D| \end{aligned} \quad (2.30)$$

By making use of Eq. (2.30),  $E_k^{-1}$  and  $|E_k|$  are obtained as below.

$$\begin{aligned}
E_k^{-1} &= S_e^{-1} I_N + S_e^{-1} \varphi \left[ \varphi^T S_e^{-1} \varphi + 1 / SD_k \right]^{-1} \varphi^T S_e^{-1} \\
&= S_e^{-1} I_N + \frac{SD_k / S_e}{(SD_k + S_e)} \varphi \varphi^T
\end{aligned} \tag{2.31}$$

$$\begin{aligned}
|E_k| &= \left| 1 / SD_k + \varphi^T S_e^{-1} \varphi \right| |SD_k| |S_e I_N| \\
&= S_e^{N-1} (S_e + SD_k)
\end{aligned} \tag{2.32}$$

where  $|S_e I_N| = S_e^N$ , and  $\varphi^T \varphi = 1$ . Substituting Eqs. (2.29) and (2.32) into Eq. (2.19) and applying the of norm constraint for mode shape leads to

$$\begin{aligned}
J(\theta) &= C + N_f (N-1) \ln S_e + \sum_k \ln (SD_k + S_e) + S_e^{-1} \kappa \\
&\quad - \varphi^T \Delta \varphi + \alpha (\varphi^T \varphi - 1)
\end{aligned} \tag{2.33}$$

where  $N_f =$  number of FFT data within the selected frequency band,  $\alpha =$  Lagrange multiplier that enforces the unit norm of  $\varphi$ , and

$$\kappa = \sum_k F_k^* F_k; \quad \Delta = \sum_k \frac{SD_k / S_e}{(SD_k + S_e)} F_k F_k^* \tag{2.34}$$

In the minimization of Eq. (2.33), two different procedures can be followed. The first procedure is based on an iterative solution to minimize the objective function. The second procedure is composed in two stages, and it leads to a direct solution without iteration (Au, 2017). In this two-stage approach, the modal parameters to be identified can be separated in two parts: (i) first part that includes the spectrum parameters  $f$ ,  $\zeta$ ,  $S$  and  $S_e$ , (ii) second part that includes all modal parameters. Here, the second part can be modified by defining the most probable (optimal) modal shape vector as depending on spectrum parameters.

#### 2.4.2. Two-stage Solution for NLLF

In this section a modified version of the two-stage approach by Au (2011a) is presented. The presented modification is based on the definition of Lagrange multiplier and the procedure for the determination of modal parameters is completely same by Au (2011a). The difference of the presented modification lies in the calculation of posterior covariance matrix for modal parameters. Using the presented modification, the posterior covariance for modal parameters are obtained as a block diagonal matrix by direct differentiation.



Objective function that is given in Eq. (2.33) can be considered with two components; (i) first part that is sensitive to spectrum parameters,  $\theta_s = [f, \zeta, S, S_e]$ , and (ii) second part that is sensitive to  $\theta$ .

$$J(\theta) = C + N_f(N-1)\ln S_e + \underbrace{\sum_k \ln(SD_k + S_e)}_{\text{First Part (Sensitive to } \theta_s)} + S_e^{-1}\kappa - \underbrace{\varphi^T \Delta \varphi + \alpha(\varphi^T \varphi - 1)}_{\text{Second Part (Sensitive to } \theta)} \quad (2.35)$$

The first term is only sensitive to the variation of spectrum parameters while the second term is varying as depending on spectrum parameters as well as mode shape vector. The second term can be reformulated depending on spectrum parameters only. For this purpose, the objective function for  $\varphi$  can be written as follows at the MPV of spectrum parameters

$$J(\theta)|_{\theta_s=\hat{\theta}_s} = L(\hat{\theta}_s) - \varphi^T \Delta(\hat{\theta}_s) \varphi + \alpha(\varphi^T \varphi - 1) \quad (2.36)$$

where “ $\hat{\cdot}$ ” denotes the most probable value. Taking the first order derivative of Eq. (2.36) with respect to  $\varphi$  gives

$$\left. \frac{\partial J}{\partial \varphi} \right|_{\varphi=\hat{\varphi}} = -2\hat{\varphi}^T \Delta(\hat{\theta}_s) + 2\alpha\hat{\varphi}^T = 0 \Rightarrow \Delta(\hat{\theta}_s)\hat{\varphi} = \alpha\hat{\varphi}; \quad \hat{\alpha} = \hat{\varphi}^T \Delta(\hat{\theta}_s)\hat{\varphi} \quad (2.37)$$

It is seen that the optimal mode shape vector can be obtained by solving the standard eigenvalue problem given in Eq. (2.37). Thus, the Lagrange multiplier,  $\hat{\alpha}$  is obtained as the maximum eigenvalue of  $\hat{\Delta}$  and the optimal mode shape vector can be updated as the eigenvector that corresponds to  $\hat{\alpha}$ . However, the optimal spectral parameters need to be obtained before calculation of optimal  $\varphi$ .

### 2.4.3. Determination of Most Probable Spectral Parameters

In the minimization process of objective function with respect to spectral parameters, the most important issue that affect the computational effort is the initial guess. Since, the optimal value of  $\varphi$  depends on the spectral parameters, mode shape remains an unknown in the minimization process. An iterative procedure can be followed at this step in which all modal parameters should be determined simultaneously at each iteration step. A direct solution, however, can be constituted by eliminating the quadratic term in the objective function. This elimination can be done by representing the quadratic term with its optimal value. Hence, the negative logarithm likelihood function can be minimized in two stages: (i) determination of optimal spectral parameters, (ii)

determination of optimal mode shape vector. For this purpose, it can be assumed that the constraint equation is satisfied not only at the MPVs but also within the whole parameter space. Thus, the quadratic term is obtained as a function of spectrum parameters as shown in Eq. (2.38).

$$-\varphi^T \Delta(\theta_s) \varphi + \alpha(\varphi^T \varphi - 1) = \alpha(\theta_s) \quad (2.38)$$

Note that  $\alpha(\theta_s)$  is the function of spectral parameters only. The objective function can be obtained as depending on spectral parameters by substituting Eq. (2.38) into Eq. (2.35) as below.

$$J(\theta_s) = N_f(N-1) \ln S_e + \sum_k \ln(SD_k + S_e)^{-1} + S_e^{-1} \kappa - \alpha(\theta_s) \quad (2.39)$$

Thus, the objective function can be minimized with respect to spectral parameters by unconstrained numerical optimization. This numerical optimization can be done by *fminsearch* or *fminunc* command in MATLAB. The most important issue that affects the computational effort of this minimization process determines the initial guess close to optimal values as much as possible. To determine the initial guess for modal parameters, Au (2011a) proposed the usage of asymptotic behavior of the solution under large-signal-to-noise ratio (*snr*). In case of the large *snr*, optimal modal parameters can be obtained by direct solution of the objective function without any iteration and numerical optimization.

Different from the Au (2011a), this study defines the Lagrange multiplier of  $\alpha$  as a function of spectral parameters not only at MPV but also at the remaining values. Thus, the norm constraint equality will be satisfied at each trial for modal parameters.

#### 2.4.4. Asymptotic Behavior Under Large Signal-to-Noise Ratio

BAYOMA provides an efficient identification procedure by considering the noise effect as a prediction error in the analysis. Depending on the quality of the measured data, the computational effort and posterior uncertainty of estimated optimal values are directly affected in analysis process. The lower *snr* results in larger computational effort and may have an adverse effect on the accuracy of estimated optimal values. Nevertheless, many researchers state that BAYOMA gives reasonable results even for low *snr* (Yuen and Katafygiotis, 2003; Au, 2011a).

The computational difficulties in BAYOMA are removed and the formulation can be defined in more simple form in case of large *snr*. Here, *snr* is defined as below.

$$\gamma_k = \frac{SD_k}{S_e} \quad (2.40)$$

In case of large  $snr$ , the matrix of  $\Delta$  can be rewritten by using the following assumption Au (2011a).

$$\left(1 + \frac{S_e}{SD_k}\right)^{-1} \approx \left(1 - \frac{S_e}{SD_k}\right) \quad (2.41)$$

where Eq. (2.41) is approximately equal to 1. Thus, the matrix of  $\Delta$  can be transformed into the following form

$$\begin{aligned} \Delta &= \sum_k \frac{SD_k/S_e}{(SD_k + S_e)} F_k F_k^* \approx \sum_k \left( S_e^{-1} - \frac{1}{SD_k} \right) F_k F_k^* \\ &= \underbrace{S_e^{-1} \sum_k F_k F_k^*}_{\text{considerably large}} - \underbrace{\sum_k \frac{F_k F_k^*}{SD_k}}_{\text{negligibly small}} \end{aligned} \quad (2.42)$$

By making use of Eqs. (2.41) and (2.42), the objective function given in Eq. (2.39) can be arranged as follows

$$\begin{aligned} J(f, \zeta, S, S_e) &= C + \underbrace{\sum_k \ln D_k}_{\text{Sensitiveto } f \text{ and } \zeta} + \underbrace{\left[ N_f (N-1) \ln S_e + S_e^{-1} (\kappa - \alpha_o) \right]}_{\text{Sensitiveto } S_e} \\ &\quad + \underbrace{\left[ N_f \ln S + S^{-1} \sum_k \alpha_k D_k^{-1} \right]}_{\text{Sensitiveto } f, \zeta, S \text{ and } S_e} \end{aligned} \quad (2.43)$$

where  $\alpha_o = \hat{\varphi}^T \sum_k F_k F_k^* \hat{\varphi}$  (maximum eigenvalue of  $\sum_k F_k F_k^*$ ), and  $\alpha_k = \hat{\varphi}^T F_k F_k^* \hat{\varphi}$  (maximum eigenvalue of  $F_k F_k^*$ ). Minimizing Eq. (2.43) with respect to  $S$  and  $S_e$  gives their optimal values as below.

$$\hat{S}_e = \frac{\sum_k F_k^* F_k - \alpha_o}{N_f (N-1)}; \quad \hat{S} = N_f^{-1} \underbrace{\sum_k \alpha_k D_k^{-1}}_{\text{Sensitiveto } f \text{ and } \zeta} \quad (2.44)$$

In Eq. (2.44), it is seen that optimal  $S$  is sensitive to  $f$  and  $\zeta$ . For this reason, optimal values of  $f$  and  $\zeta$  need to be obtained first. By substituting Eq. (2.44) into Eq. (2.43) and arranging the results leads to

$$J(f, \zeta) = C + \sum_k \ln D_k + N_f \ln \left( \sum_k \alpha_k D_k^{-1} \right) \quad (2.45)$$

To obtain the optimal  $\varphi$ , the matrix of  $\Delta$  can be written as

$$\Delta = S_e^{-1} \sum_k F_k F_k^* \quad (2.46)$$

Thus, optimal mode shape vector can be obtained as the eigenvector that corresponds to the maximum eigenvalue of  $\sum_k F_k F_k^*$ .

### 2.4.5. Summary of Overall Computational Procedure

There are two different algorithms in the literature to obtain MPV of modal parameters by fast computational BAYOMA. First one is an iterative algorithm based on the estimation of optimal modal parameters simultaneously at each step. Second one is a two-stage non-iterative algorithm that estimates the spectral parameters and modal shape vector. The algorithms proposed by Au (2011a) are presented in Table 2.1 and Table 2.2, respectively, with small modifications.

Table 2.1. Iterative algorithm by Au (2011a)

---

Step 1: Set initial guess for $(f, \zeta, S, S_e)$ by using Eq. (2.44) and (2.45)
Step 2: Set initial guess of $\varphi$ as the eigenvector of $\sum_k F_k F_k^*$ .
Step 3: With $\varphi$ being constant, determine optimal $(f, \zeta, S, S_e)$ by minimizing Eq. (2.35)
Step 4: With $(f, \zeta, S, S_e)$ being constant, determine the optimal $\varphi$ as the eigenvector of the maximum eigenvalue of $\Delta$
Repeat Steps 3 to 4 until convergence is reached

---

Table 2.2. Non-iterative algorithm by Au (2011a)

---

Step 1: Set initial guess for $(f, \zeta, S, S_e)$ and by using Eqs. (2.44) and (2.45)
Step 2: Determine optimal $(f, \zeta, S, S_e)$ by minimizing Eq. (2.39)
Step 3: Determine optimal $\varphi$ as the eigenvector of the maximum eigenvalue of $\Delta$

---

## 2.5. Posterior Uncertainties of Optimal Modal Parameters

One of the most prominent advantages of BAYOMA is its capability of determining the posterior uncertainties of identified modal parameters. Determination of the posterior uncertainties of spectrum parameters requires less computational effort when compared to mode shape vector. The posterior uncertainties of spectral parameters can be obtained in terms of coefficient of variation (c.o.v.). Here, c.o.v. is calculated as

the ratio of posterior variance to their MPV's. In addition to posterior c.o.v., the posterior uncertainty of identified mode shape can be defined by the Expected Modal Assurance Criterion (EMAC) value as an estimator to determine the expected discrepancy between exact and identified mode shapes.

The discrepancy between most probable and uncertain values can be well estimated by Gaussian approximation. For this purpose, the objection function can be written by using the second order Taylor series expansion as below.

$$J(\theta) \approx J(\hat{\theta}) + (\theta - \hat{\theta})^T \nabla_{\hat{\theta}} J + \frac{1}{2} (\theta - \hat{\theta})^T \nabla_{\hat{\theta}}^2 J (\theta - \hat{\theta}) \quad (2.47)$$

Here,  $\theta$  and  $\hat{\theta}$  denote uncertain and most probable modal parameters, respectively. In addition,  $\nabla_{\hat{\theta}}^2 J$  = Hessian matrix of  $J(\theta)$  at  $\theta = \hat{\theta}$ . In Eq. (2.47),  $J(\hat{\theta})$  corresponds to a scalar (minimum) and does not affect the variation of  $J(\theta)$  with respect to  $\theta$ . In addition, the first order derivative of  $J(\theta)$  with respect to  $\theta$  will be equal to zero at  $\hat{\theta}$  (at minimum value). Thus, Eq. (2.47) has a relation in the following form which is Gaussian.

$$J(\theta) \approx \frac{1}{2} (\theta - \hat{\theta})^T C_{\hat{\theta}}^{-1} (\theta - \hat{\theta}) \quad (2.48)$$

in which  $(\theta - \hat{\theta})$  = discrepancy between uncertain and most probable modal parameters,  $C_{\hat{\theta}}$  = posterior covariance matrix at  $\theta = \hat{\theta}$ . The posterior covariance matrix can be obtained as the inverse of the second order derivative (Hessian matrix) of  $J(\theta)$  with respect to  $\theta$ . In case of well separated modes, the Hessian matrix within the resonant frequency band of a possible mode is given by

$$H_{\theta} = \begin{bmatrix} J^{(f,f)} & J^{(f,\xi)} & J^{(f,S)} & J^{(f,S_e)} & J^{(f,\varphi)} \\ & J^{(\xi,\xi)} & J^{(\xi,S)} & J^{(\xi,S_e)} & J^{(\xi,\varphi)} \\ & & J^{(S,S)} & J^{(S,S_e)} & J^{(S,\varphi)} \\ \text{Symm.} & & & J^{(S_e,S_e)} & J^{(S_e,\varphi)} \\ & & & & J^{(\varphi,\varphi)} \end{bmatrix}_{(N+4) \times (N+4)} \quad (2.49)$$

where  $J^{(x,y)}$  = derivative of  $J$  with respect to  $x$  and  $y$ , respectively. Posterior uncertainties for identified modal parameters can be obtained by means of posterior covariance matrix. Thus, the posterior covariance matrix is obtained as follows.

$$C_{\theta} = H_{\theta}^{-1} \quad (2.50)$$

### 2.5.1. Calculation of Hessian Matrix Under Constraints

Calculation of the Hessian matrix has difficulties due to the equality constraints defined for the mode shape vector. Conventional methods based on the direct differentiation of the objective function require high computational effort and may not give the exact result due to the norm constraints. In another word, taking the derivatives of the objective function may not be proper way due to the Lagrange multiplier (Au and Xie, 2017). To overcome this problem, a fast-computational procedure was proposed by Au and Xie (2017). In this procedure, a likelihood function,  $L(\theta)$  that minimizes the set of parameters to be identified  $\theta = [\theta_1, \dots, \theta_{nc}]$  under  $n_c$  independent constraints is considered. Thus, the objective function is defined as

$$J(\theta) = L(\theta) + \sum_{j=1}^{n_c} \lambda_j G_j(\theta) \quad (2.51)$$

where  $\lambda_j$  and  $G_j(\theta)$  denote the Lagrange multipliers and equations of equality constraints. The Hessian matrix with respect to  $\theta$  is obtained as below (Au and Xie, 2017).

$$\nabla^2 L_c = \nabla \hat{v}_c^T (\nabla^2 L + \lambda \nabla^2 G) \nabla \hat{v}_c \quad (2.52)$$

Here,  $v_c$  denotes a mapping function that always satisfies the constraint equations. The second order derivative of likelihood function is given by

$$\nabla^2 L = \nabla^2 L(\theta) \Big|_{\theta=v_c(\theta)} = \nabla^2 \begin{bmatrix} L^{(\theta_s, \theta_s)} & L^{(\theta_s, \varphi)} \\ L^{(\varphi, \theta_s)} & L^{(\varphi, \varphi)} \end{bmatrix} \quad (2.53)$$

where,  $v_c$ ,  $G$  and their derivatives are given by

$$\theta = \begin{bmatrix} \theta_s \\ \varphi \end{bmatrix}; \quad v_c(\theta) = \begin{bmatrix} \theta_s \\ \frac{\varphi}{\|\varphi\|} \end{bmatrix}; \quad G = \varphi^T \varphi - 1; \quad (2.54)$$

$$\nabla v_c = \begin{bmatrix} I_{4 \times 4} & \mathbf{0}_{4 \times N} \\ \mathbf{0}_{N \times 4} & I_N - \varphi \varphi^T \end{bmatrix}; \quad \nabla^2 G = \begin{bmatrix} \mathbf{0}_{4 \times 4} & \mathbf{0}_{4 \times N} \\ \mathbf{0}_{N \times 4} & 2I_N \end{bmatrix}$$

Thus, the Hessian matrix under norm constraint is obtained as follows

$$\begin{aligned} \nabla^2 L_c &= \begin{bmatrix} I_{4 \times 4} & \mathbf{0}_{4 \times N} \\ \mathbf{0}_{N \times 4} & I_N - \varphi \varphi^T \end{bmatrix} \nabla^2 \begin{bmatrix} L_{\theta_s \theta_s} & L_{\theta_s \varphi} \\ L_{\varphi \theta_s} & L_{\varphi \varphi} + 2\alpha I_N \end{bmatrix} \begin{bmatrix} I_{4 \times 4} & \mathbf{0}_{4 \times N} \\ \mathbf{0}_{N \times 4} & I_N - \varphi \varphi^T \end{bmatrix} \\ &= \begin{bmatrix} \nabla^2 L_c^{(\theta_s, \theta_s)} & \nabla^2 L_c^{(\theta_s, \varphi)} \\ \nabla^2 L_c^{(\varphi, \theta_s)} & \nabla^2 L_c^{(\varphi, \varphi)} \end{bmatrix} \end{aligned} \quad (2.55)$$

where

$$\begin{aligned}
\nabla^2 L_c^{(\theta_s, \theta_s)} &= \nabla^2 L^{(\theta_s, \theta_s)} \\
\nabla^2 L_c^{(\theta_s, \varphi)} &= L^{(\theta_s, \varphi)} (I_N - \varphi \varphi^T) \\
\nabla^2 L_c^{(\varphi, \theta_s)} &= \left\{ \nabla^2 L_c^{(\theta_s, \varphi)} \right\}^T \\
\nabla^2 L_c^{(\varphi, \varphi)} &= (I_N - \varphi \varphi^T) (L_{\varphi\varphi} + 2\alpha I_N) (I_N - \varphi \varphi^T)
\end{aligned} \tag{2.56}$$

Gradients of  $L(\theta)$  with respect to modal parameters are presented in Appendix A.

## 2.5.2. An Alternative Method for Calculation of Posterior Covariance Matrix by Two-stage BFFTA

In this section, the Hessian matrix is reformulated by applying the two-stage approach that is presented in Section 2.4.2. The possible errors due to the equality constraints are removed in the conventional analytical derivation without resorting a mapping function. Finally, the Hessian is obtained as a block diagonal matrix and it is verified with the procedure by Au and Xie (2017).

In the derivation of negative-likelihood function, the expected spectral density of modal excitation,  $S$ , is scaled so that the mode shape vector has unit norm. The main problem in the calculation of posterior covariance matrix lies in the fact that the unit norm assumption for mode shape is satisfied only at MPV when the Lagrange multiplier method is applied. To solve this problem, Au and Xie (2017) defines a mapping function that always satisfies the equality constraints. When the mode shape is scaled to the unit norm for each trial, this problem can be solved without using the Lagrange multiplier method (see Appendix B). In this study, however, an alternative and simplified method with Lagrange multiplier is presented based on the two-stage BFFTA. For this purpose, the objective function for modal parameters can be rewritten as below.

$$J(\theta_s, \varphi) = L_s(\theta_s) - \varphi^T \left\{ -\Delta(\theta_s) + \alpha(\theta_s) I_N \right\} \varphi - \alpha(\theta_s) \tag{2.57}$$

where  $L_s(\theta_s)$  = likelihood function that depends on spectrum parameters only, and  $\alpha(\theta_s)$  = maximum eigenvalue of  $\Delta(\theta_s)$ ,  $[\alpha(\theta_s) = \varphi^T \Delta(\theta_s) \varphi]$ .

$$\begin{aligned}
L_s(\theta_s) &= C + N_f (N - 1) \ln S_e + \sum_k \ln (S D_k + S_e) + S_e^{-1} \kappa \\
\alpha(\theta_s) &= \varphi^T \Delta(\theta_s) \varphi
\end{aligned} \tag{2.58}$$

Here, the Lagrange multiplier,  $\alpha$  is defined as a function of spectrum parameters so that the norm constraint equality is always satisfied. This assumption may not be considered as a proper usage for Lagrange multiplier. However, it becomes necessary to define this multiplier as a function of  $\theta_s$  in order to satisfy the norm constraints. In addition, it should be noted that  $\alpha$  still corresponds to a scalar value for the marginal distribution of mode shape vector. Under these assumptions, the derivatives of Eq. (2.57) are obtained as follows.

$$J^{(\theta_s, \theta_s)} = \frac{\partial^2 L_s(\theta_s)}{\partial \theta_s^2} - \frac{\partial^2 \alpha(\theta_s)}{\partial \theta_s^2} \quad (2.59)$$

$$J^{(\varphi, \varphi)} = -\Delta(\theta_s) + \alpha(\theta_s) I_N \quad (2.60)$$

$$J^{(\theta_s, \varphi)} = 2\varphi^T \frac{\partial}{\partial \theta_s} \{-\Delta(\theta_s) + \alpha(\theta_s) I_N\} \quad (2.61)$$

At  $\theta = \hat{\theta}$ , the Hessian matrix can be written as

$$H_{\hat{\theta}} = \begin{bmatrix} J^{(\hat{\theta}_s, \hat{\theta}_s)} & J^{(\hat{\theta}_s, \hat{\varphi})} \\ J^{(\hat{\varphi}, \hat{\theta}_s)} & J^{(\hat{\varphi}, \hat{\varphi})} \end{bmatrix} \quad (2.62)$$

where

$$\begin{aligned} J^{(\hat{\theta}_s, \hat{\theta}_s)} &= \frac{\partial^2 L_s(\hat{\theta}_s)}{\partial \hat{\theta}_s^2} \Big|_{\theta_s = \hat{\theta}_s} - \hat{\varphi}^T \left[ \frac{\partial^2 \{-\Delta(\theta_s) + \alpha(\theta_s) I_N\}}{\partial \theta_s^2} \Big|_{\theta_s = \hat{\theta}_s} \hat{\varphi} + \frac{\partial^2 \alpha(\theta_s)}{\partial \theta_s^2} \Big|_{\theta_s = \hat{\theta}_s} \right] \\ &= \frac{\partial^2 L_s(\hat{\theta}_s)}{\partial \hat{\theta}_s^2} \Big|_{\theta_s = \hat{\theta}_s} + \frac{\partial^2 \alpha(\theta_s)}{\partial \theta_s^2} \Big|_{\theta_s = \hat{\theta}_s} \end{aligned} \quad (2.63)$$

$$J^{(\hat{\varphi}, \hat{\varphi})} = -2\Delta(\hat{\theta}_s) + 2\alpha(\hat{\theta}_s) I_N \quad (2.64)$$

$$J^{(\hat{\theta}_s, \hat{\varphi})} = 2\hat{\varphi}^T \frac{\partial \{-\Delta(\theta_s) + \alpha(\theta_s) I_N\}}{\partial \theta_s} \Big|_{\theta_s = \hat{\theta}_s} \quad (2.65)$$

At  $\theta_s = \hat{\theta}_s = \hat{\theta}$ ,  $\partial\{-\Delta(\theta_s) + \alpha(\theta_s)\}/\partial\theta_s$  can be arranged as

$$\frac{\partial}{\partial \theta_s} \{-\Delta(\hat{\theta}_s) + \alpha(\hat{\theta}_s)\} \Big|_{\theta_s = \hat{\theta}_s} = \left[ -\frac{\partial \Delta}{\partial \theta_s} + \hat{\varphi}^T \frac{\partial \Delta}{\partial \theta_s} \hat{\varphi} I_N \right] \Big|_{\theta_s = \hat{\theta}_s} \quad (2.66)$$

Substituting (2.66) into Eq. (2.65) and re-arranging,  $J^{(\hat{\theta}_s, \hat{\varphi})}$  can be written as

$$2\hat{\varphi}^T \frac{\partial \Delta(\theta_s)}{\partial \theta_s} \Big|_{\theta_s = \hat{\theta}_s} (I_N - \hat{\varphi} \hat{\varphi}^T) \quad (2.67)$$



In Eq. (2.67), it is seen that the matrix of  $(I_N - \hat{\varphi}\hat{\varphi}^T)$  is a semi-positive definite matrix whose null vector corresponds to  $\hat{\varphi}$ . Therefore,  $J^{(\hat{\theta}_s, \hat{\varphi})}$  is obtained as below (see Appendix B).

$$J^{(\hat{\theta}_s, \hat{\varphi}_s)} = 2\hat{\varphi}^T \frac{\partial \Delta(\theta_s)}{\partial \theta_s} \Big|_{\theta_s = \hat{\theta}_s} \times \left( 0 \times \hat{\varphi}\hat{\varphi}^T + \sum_{i=2}^N \rho_i \rho_i^T \right) = 0 \quad (2.68)$$

where  $I_N = \sum_{i=1}^N \rho_i \rho_i^T$ ,  $\rho_1 = \varphi$ ,  $\varphi^T \rho_i = 0$  (for  $i=2 \dots N$ ) and  $\rho_i =$  eigenvectors of  $(I_N - \hat{\varphi}\hat{\varphi}^T)$ , respectively. Hence, the Hessian of  $J(\theta)$  is obtained as a block diagonal matrix.

$$H_{\hat{\theta}} = \begin{bmatrix} H_{\hat{\theta}_s} & \mathbf{0}_{4 \times N} \\ \mathbf{0}_{N \times 4} & H_{\hat{\varphi}} \end{bmatrix} \quad (2.69)$$

Here,  $H_{\hat{\theta}_s} = J^{(\hat{\theta}_s, \hat{\theta}_s)}$  and  $H_{\hat{\varphi}_s} = J^{(\hat{\varphi}_s, \hat{\varphi}_s)}$ . Finally, the posterior covariance matrix is obtained as the inverse of  $H_{\hat{\theta}}$ .

$$C_{\hat{\theta}} = \begin{bmatrix} C_{\hat{\theta}_s} & \mathbf{0}_{4 \times N} \\ \mathbf{0}_{N \times 4} & C_{\hat{\varphi}} \end{bmatrix} \quad (2.70)$$

where  $C_{\hat{\theta}_s} = H_{\hat{\theta}_s}^{-1}$  and  $C_{\hat{\varphi}_s} = H_{\hat{\varphi}_s}^{-1}$ . According to Eq. (2.70), it is seen that the posterior covariance of spectrum parameters and mode shapes can be decoupled. Thus, the posterior coefficient of variation (c.o.v.) of spectral parameters are obtained as follows.

$$\begin{aligned} cov(f) &= \frac{C_{\hat{\theta}_s}(f, f)}{\hat{f}}; \quad cov(\xi) = \frac{C_{\hat{\theta}_s}(\xi, \xi)}{\hat{\xi}}; \\ cov(S) &= \frac{C_{\hat{\theta}_s}(\hat{S}, \hat{S})}{\hat{S}}; \quad cov(S_e) = \frac{C_{\hat{\theta}_s}(\hat{S}_e, \hat{S}_e)}{\hat{S}_e} \end{aligned} \quad (2.71)$$

The same result can be obtained by the manipulation of the computation scheme presented by Au an Xie (2017). Here, the derivative of  $\nabla^2 L_c^{(\varphi, \varphi)}$  given in Eq. can be arranged as below at MPV of  $\theta$ .

$$\nabla^2 L_c^{(\hat{\theta}_s, \hat{\varphi})} = \hat{\varphi}^T \times \frac{\partial \Delta}{\partial \theta_s} \Big|_{\theta_s = \hat{\theta}_s} \times (I_N - \hat{\varphi}\hat{\varphi}^T) = 0 \quad (2.72)$$

When compared to the previous calculation procedure, the proposed methodology promises less computational effort for single mode approach since the large sized matrix computations are overpassed.

### 2.5.3. Posterior Uncertainty of Modal Shape Vector

Different from the spectral parameters, the posterior uncertainty of mode shape vector is generally defined by the Expected Modal Assurance Criterion (EMAC) in addition to the c.o.v. Here, EMAC can be estimated by the manipulation of the difference between most probable and uncertain mode shapes (Au, 2017).

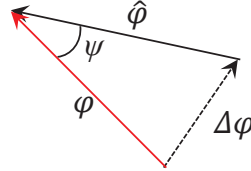


Figure 2.1. Vectoral representation of exact and most probable mode shapes

Figure 2.1 shows the schematic representation of the vectoral difference (uncertainty). Here,  $\hat{\varphi}$  and  $\varphi$  denote the most probable and exact mode shape vectors, respectively. In addition,  $\Delta\varphi$  and  $\psi$  represents the mode shape uncertainty and phase angle between  $\hat{\varphi}$  and  $\varphi$ , respectively. Due to the Hermitian structure of  $H_{\hat{\varphi}}$ , its eigenspace decomposition can be written as follows.

$$H_{\hat{\varphi}} = \sum_{i=1}^N \delta_{\hat{\varphi},i}^{-2} \rho_i \rho_i^T \quad (2.73)$$

where  $\delta_{\hat{\varphi},i}^{-2}$  = eigenvalues, and  $\rho_i$  = eigenvectors of  $H_{\hat{\varphi}}$ . Thus, the eigenspace decomposition of  $H_{\hat{\varphi}}$  is obtained as

$$\begin{aligned} \sum_{i=1}^N \delta_{\hat{\varphi},i}^{-2} \rho_i \rho_i^T &= \underbrace{\left[ -2\hat{\alpha} \times \hat{\varphi} \hat{\varphi}^T - \sum_{i=2}^N 2\lambda_i \times \rho_i \rho_i^T \right]}_{\text{Decomposition of } -2\Delta} + \underbrace{\left[ 2\hat{\alpha} \times \hat{\varphi} \hat{\varphi}^T + \sum_{i=2}^N 2\hat{\alpha} \times \rho_i \rho_i^T \right]}_{\text{Decomposition of } 2\alpha I_N} \\ &= 0 \times \hat{\varphi} \hat{\varphi}^T + \sum_{i=2}^N 2(\hat{\alpha} - \lambda_i) \times \rho_i \rho_i^T \end{aligned} \quad (2.74)$$

It is seen that the minimum eigenvalue corresponding to the most probable mode shape vector of  $H_{\hat{\varphi}}$  is equal to zero, and the remaining eigenvalues are positive definite. Therefore,  $H_{\hat{\varphi}}$  is a semi-positive definite matrix. Thus, the posterior covariance matrix is obtained as follows.

$$C_{\hat{\varphi}} = \sum_{i=1}^N \delta_{\hat{\varphi},i}^2 \rho_i \rho_i^T = \infty \times \hat{\varphi} \hat{\varphi}^T + \frac{1}{2} \sum_{i=2}^N (\hat{\alpha} - \lambda_i)^{-1} \times \rho_i \rho_i^T \quad (2.75)$$

Obtaining the exact  $C_{\hat{\varphi}}$  is not possible since its eigenvalue that corresponds to  $\hat{\varphi}$  is infinite. Instead, the pseudo inverse of  $H_{\hat{\varphi}}$  can be obtained to avoid numerical errors.

Here, the mode shape uncertainty,  $\Delta\varphi$ , is a combination of the eigenvectors of eigenvectors of  $H_{\hat{\varphi}}$ , weighted by the eigenvalues of  $\delta_{\varphi,i}$ . For this reason, the first eigenvector (corresponding to  $\hat{\varphi}$ ) can be neglected, since it does not cause a discrepancy. Thus, the pseudo inverse of  $H_{\hat{\varphi}}$  can be assumed to be equal to the covariance of  $\Delta\varphi$ . The pseudo inverse of  $H_{\hat{\varphi}}$  can be obtained as a semi positive definite Hermitian matrix by neglecting the zero-eigenvalue term of Hessian matrix (Au and Zhang, 2011).

$$C_{\hat{\varphi}} = H_{\hat{\varphi}}^+ = \sum_{i=2}^N \delta_{\varphi,i}^2 \rho_i \rho_i^T \quad (2.76)$$

where “+” denotes the pseudo inverse.

The uncertainty of mode shape,  $\Delta\varphi$ , follows a zero mean Gaussian distribution with covariance matrix,  $C_{\hat{\varphi}}$ , and it is defined by the following equation (Au and Zhang, 2011).

$$\Delta\varphi = \sum_{i=2}^N z_i \delta_{\varphi,i} \rho_i \quad (2.77)$$

where  $z_i$  = independent and identically distributed (*i.i.d.*) Gaussian numbers. Thus, the uncertain mode shape can be written as below.

$$\varphi = \hat{\varphi} + \sum_{i=2}^N z_i \delta_{\varphi,i} \rho_i \quad (2.78)$$

Note that the exact mode shape,  $\varphi$ , should be normalized to unit norm.

$$\|\varphi\| = \left( \|\hat{\varphi}\|^2 + \left\| \sum_{i=2}^N z_i \delta_{\varphi,i} \rho_i \right\|^2 \right)^{1/2} = \left( 1 + \sum_{i=2}^N z_i^2 \delta_{\varphi,i}^2 \right)^{1/2} \quad (2.79)$$

The expected MAC between the uncertain and most probable mode shapes can be obtained as;

$$\begin{aligned} EMAC &= \frac{\varphi^T \hat{\varphi}}{\|\varphi\| \|\hat{\varphi}\|} = \left[ \underbrace{(\hat{\varphi}^T \hat{\varphi})}_{=1} + \sum_{i=2}^N z_i \delta_{\varphi,i} \underbrace{(\hat{\varphi}^T \rho_i)}_{=0} \right] \times \left( 1 + \sum_{i=2}^N z_i^2 \delta_{\varphi,i}^2 \right)^{-1/2} \\ &= \left( 1 + \sum_{i=2}^N z_i^2 \delta_{\varphi,i}^2 \right)^{-1/2} \end{aligned} \quad (2.80)$$

Au and Zhang (2011) state that EMAC can be well estimated by direct Monte Carlo Simulation. However, a direct analytical solution can be obtained by the following assumption.

$$EMAC \approx [1 + (N - 1)\delta_\varphi^2]^{-1/2} \quad (2.81)$$

where  $\delta_\varphi \cong \delta_{\varphi,i}$  (for  $i=1 \dots N$ ). This assumption asymptotically approaches to the exact solution, while  $\delta_{\varphi,i} \rightarrow 0$ , and  $N \rightarrow \infty$  (Au and Zhang, 2011). For comparison purposes, an exact solution is obtained by Monte Carlo Simulation with  $N_s = 500,000$  randomly generated samples. Here, each sample,  $z_i$  is generated as independent and identically distributed (*i.i.d.*) gaussian numbers, and the statistical distribution of EMAC is obtained. Finally, the exact EMAC is calculated as the sample mean of EMACs (see Table 2.3 for overall procedure).

Table 2.3. Exact solution algorithm by Monte Carlo Technique

---

Step 1: Set $z_i$ as a randomly generated ( $N_s \times 1$ ) size <i>i.i.d.</i> normally distributed vector (wgn function can be used for MATLAB)
Step 2: Calculate $[EMAC]_i$ value for each sample by Eq. (2.80)
Step 3: Calculate exact EMAC as the sample mean, $EMAC = 1/N_s \sum [EMAC]_i$

---

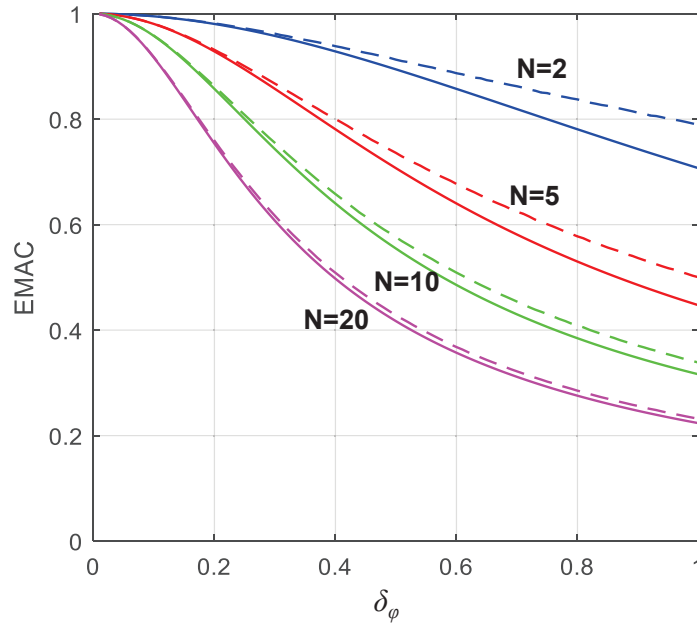


Figure 2.2. Convergence of exact and approximate EMAC values (solid line: exact, dashed line: approximate)

Figure 2.2 shows the convergence of exact and approximate EMAC values that are calculated for  $N=2, 5, 10$  and  $20$ , respectively. At first view, it is seen that the simulated results improve the conclusions of Au and Zhang (2011). As the measured number of DOF ( $N$ ) increases, the exact and approximate solutions match better. It is

worth to note that EMAC value cannot be calculated when  $N$  is smaller than 2. Nevertheless, it is seen that the worst case occurs when  $N=2$  as stated by Au and Zhang (2011). For this case, relative difference between exact and approximate solutions increases up to 10% at  $\delta_\varphi=1.00$ .

The posterior c.o.v. of mode shape can be estimated via the posterior covariance matrix,  $C_\varphi$  (Au 2017). Here, the posterior variance of the mode shape is calculated as

$$\sigma_\varphi^2 = tr[C_\varphi] = tr\left[\sum_{i=2}^N \delta_{\varphi,i}^{-2} \hat{\varphi} \hat{\varphi}^T\right] = \sum_{i=2}^N \delta_{\varphi,i}^{-2} \quad (2.82)$$

Thus, the posterior c.o.v. can be obtained as the posterior standard deviation divided by the norm of the most probable mode shape.

$$cov(\varphi) = \frac{\sigma_\varphi}{\|\hat{\varphi}\|} = \sqrt{\sum_{i=2}^N \delta_{\varphi,i}^{-2}} \quad (2.83)$$

## 2.6. Uncertainty Laws

Managing the uncertainty of modal parameters is a major challenge due to the complexity of the calculation of posterior covariance matrix in BAYOMA. This complexity extremely related with the data duration, selected bandwidth and signal-to-noise ratio (Au, 2014a, 2014b). In case of large data duration with small damping, the uncertainty parameters can be estimated by the following equation (Au, 2014a, 2014b)

$$\delta_x^2 \approx \delta_{x1}^2 = \delta_{x0}^2 \left(1 + \frac{a_x}{\gamma_{k,max}}\right) \quad (2.84)$$

where  $\delta_x$  = c.o.v. of parameter  $x$ ,  $\gamma_{k,max} = S/(4S_e \zeta^2)$ ,  $\delta_{x0}$  and  $\delta_{x1}$  are zeroth and first order term, respectively. In addition,  $a_x$  is a parameter that depends on the bandwidth, data length and period.  $\delta_{x0}$ ,  $\delta_{x1}$  and  $a_x$  is defined by Au (2014a) as follows.

- For frequency

$$\delta_{f0}^2 = \frac{\zeta}{2\pi N_c B_f(\tau)}; \quad B_f(\tau) = \frac{2}{\pi} \left( \tan^{-1} \tau + \frac{\tau}{\tau^2 + 1} \right); \quad a_f = \frac{4(\tau - \tan^{-1} \tau)}{\left( \tan^{-1} \tau + \frac{\tau}{\tau^2 + 1} \right)} \quad (2.85)$$

- For damping ratio

$$\delta_{\xi_0}^2 = \frac{1}{2\pi N_c \hat{\xi} B_f(\tau)}; \quad B_{\xi}(\tau) = \frac{2}{\pi} \left( \tan^{-1} \tau + \frac{\tau}{\tau^2 + 1} - \frac{2(\tan^{-1} \tau)^2}{\tau} \right) \quad (2.86)$$

$$a_{\xi} = \frac{4(\tau^2 + 1)(3 - \tan^{-1} \tau - 3\tau + \tau^2 \tan^{-1} \tau) \tan^{-1} \tau}{3(\tau^2 + 1)(\tau - 2 \tan^{-1} \tau) \tan^{-1} \tau + \tau^2}$$

- For spectral density of modal excitation

$$\delta_{s_0}^2 = \frac{1}{2\pi N_c B_f(\tau)}; \quad B_s(\tau) = 1 - \frac{2}{\tau} (\tan^{-1} \tau)^2 \left( \tan^{-1} \tau + \frac{\tau}{\tau^2 + 1} \right)$$

$$a_s = 2 + \frac{2}{3} \tau^2 - \frac{(\tan^{-1} \tau)^2}{2(\tan^{-1} \tau)^2 - b\tau} \left( \frac{8 \tan^{-1} \tau}{b} - \frac{8}{\tan^{-1} \tau} + \frac{4}{3} \tau^2 + 4 \right) \quad (2.87)$$

$$b = \tan^{-1} \tau + \frac{\tau}{\tau^2 + 1}$$

- For spectral density of prediction error

$$\delta_{s_{e0}}^2 = \frac{1}{(n-1) N_f B_{s_e}(\tau)}; \quad B_{s_e}(\tau) = 1; \quad a_{s_e} = 0 \quad (2.88)$$

- For mode shape vector

$$\delta_{\phi}^2 = \frac{(n-1) \hat{S}_e \hat{\xi}}{\pi \hat{S} N_c B_{\phi}(\tau)}; \quad B_{\phi}(\tau) = \frac{2}{\pi} \tan^{-1} \tau \quad (2.89)$$

Where  $\tau =$  bandwidth factor for the selected frequency band,  $\hat{f}(1 \pm \tau \hat{\xi})$ ,  $N_c = N_f/2\hat{\xi}$ ,  $N_f =$  number of FFT points within  $\hat{f}(1 \pm \tau \hat{\xi})$ .

## 2.7. Numerical and Experimental Analysis

In this section, the effectiveness of the proposed modifications for BAYOMA methods is investigated. For this purpose, numerical/experimental studies and field applications are presented.

### 2.7.1. Numerical Analysis I: Ten Story Shear Frame

A finite element model of a ten-story shear frame is generated with inter-story stiffness, and story mass of 450 kN/m and 250 kg, respectively. An *i.i.d.* synthetic Gaussian white noise is generated as forcing function with PSD of 1  $\mu g^2/Hz$ , 100 Hz sampling rate and 300 sec duration. To obtain a uniform PSD for each modal excitation,

the spatial distribution of the forcing function is arranged as  $s = \Phi^T \Phi^T M \Phi \mathbf{1}$ , where  $\Phi$ = modal shape matrix,  $M$ = mass matrix, and  $\mathbf{1}$ =  $10 \times 1$  size unit vector. In addition, an *i.i.d.* Gaussian white noise with a PSD of  $10 \mu\text{g}^2/\text{Hz}$  is added to the acceleration response of each story.

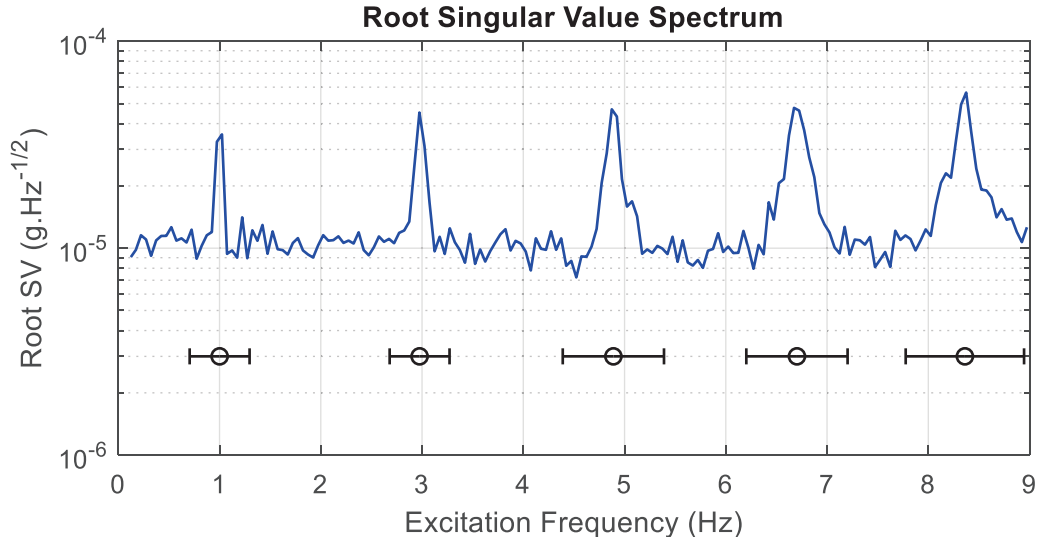


Figure 2.3. Root singular value spectrum and possible modes with selected bandwidths

In Figure 2.3, the average root singular value spectrum of the acceleration responses is presented by 1000 windows. In each window, the average spectral density matrix of 30 data points is obtained, and their maximum singular values are calculated. First five modes are detected at 1.00, 3.00, 4.90, 6.75, and 8.40 Hz, and the corresponding selected frequency bands are as indicated in the Root SV spectrum.

Table 2.4. Identification results for frequency and damping ratios

Mode Number	f (Hz.)			$\xi$ (%)		
	MPV	Exact	c.o.v. (%)	MPV	Exact	c.o.v. (%)
1	1.0187	1.0092	0.12	0.90	1.00	19.76
2	3.0016	3.0051	0.13	1.02	1.00	47.60
3	4.9330	4.9338	0.11	0.97	1.00	11.42
4	6.7569	6.7524	0.10	1.02	1.00	10.01
5	8.4191	8.4201	0.11	0.99	1.00	19.69

Identification results for spectrum parameters are presented in Table 2.4 and Table 2.5. It is seen that the identification results well match with their analytical values.

Posterior coefficient of variations for identified frequencies are less than 0.15 %. The posterior c.o.v for  $S_e$  varies from 2.65 to 8.11%. Identification uncertainties increase for  $S_s$  and  $\zeta$ . Here, the posterior c.o.v. of  $\zeta$  is determined as 47.60 while the MPV is well matched with the exact value. Note that the posterior c.o.v. only shows the identification uncertainty. The fact that the MPV perfectly matches the exact value does not necessarily correspond to low (or zero) uncertainty.

Table 2.5. Identification results for the spectral density of modal excitation and prediction error, and root signal-to-noise ratio

Mode Number	$S$ ( $\mu g^2/Hz$ )			$S_e$ ( $\mu g^2/Hz$ )			$\gamma$	
	MPV	Exact	c.o.v. (%)	MPV	Exact	c.o.v. (%)	MPV	Exact
1	1.01	1.00	13.97	12.63	10.00	3.65	260	250
2	1.04	1.00	17.63	11.51	10.00	8.11	217	250
3	0.94	1.00	12.13	12.20	10.00	2.32	205	250
4	0.91	1.00	10.96	12.81	10.00	2.04	171	250
5	1.01	1.00	32.36	14.40	10.00	2.65	179	250

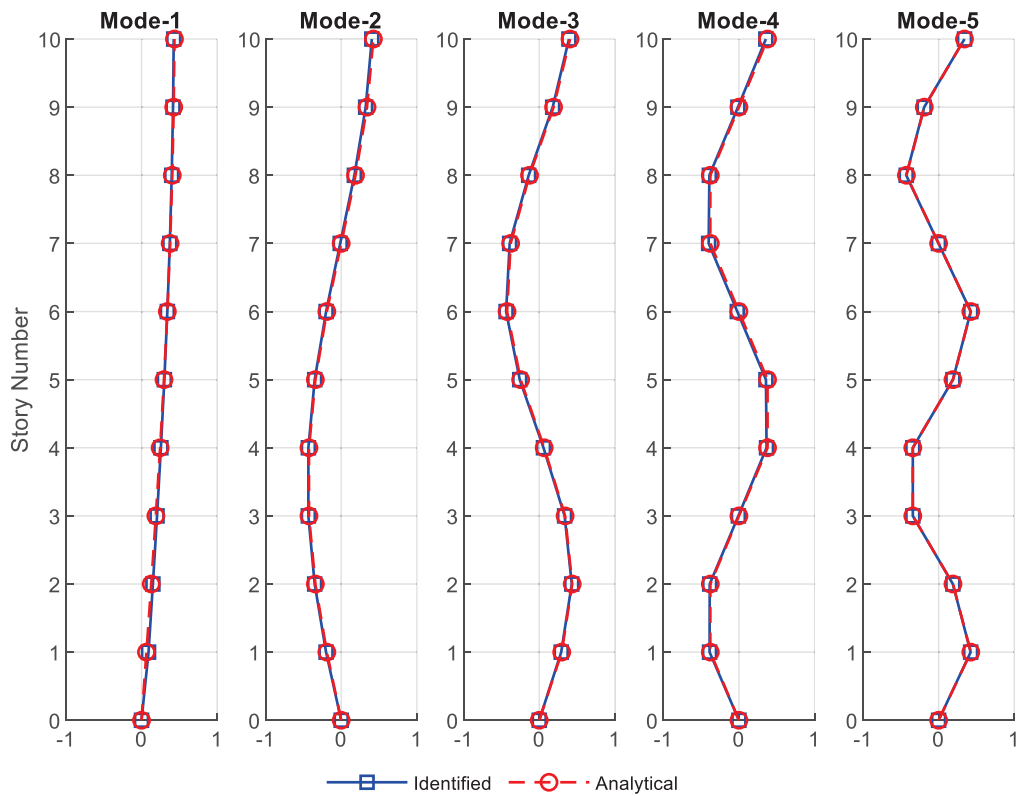


Figure 2.4. Identified and analytical mode shape vectors



Effect of signal-to-noise ratio on the identification uncertainty for the first mode is illustrated in Figure 2.5 and Figure 2.6. At first view, it is observed that the uncertainty is not affected by the signal-to-noise ratio for the spectral density of prediction error,  $S_e$  while it shows significant variation for the natural frequency, damping ratio and the spectral density of modal excitation. Identification uncertainty decreases as the signal-to-noise ratio increases, and it converges to a constant value. This case shows that the uncertainty cannot be reduced to zero even for significantly large values of signal-to-noise ratio. This observation is compatible with the results reported by Au (2017). Additionally, it is seen that the uncertainty laws give reasonable results for posterior coefficient of variations of identified values. A gradually decreasing divergence from the exact value is observed from  $\gamma_k = 10$  to 100 for c.o.v. of frequency and damping ratios. The maximum divergence is observed to be 50% and 15% for the c.o.v. of frequency and damping ratio, respectively. The c.o.v. for the spectral density of modal excitation,  $S$ , spectral density of prediction error,  $S_e$ , and the modal shape vector,  $\varphi$ , well match with the exact values.

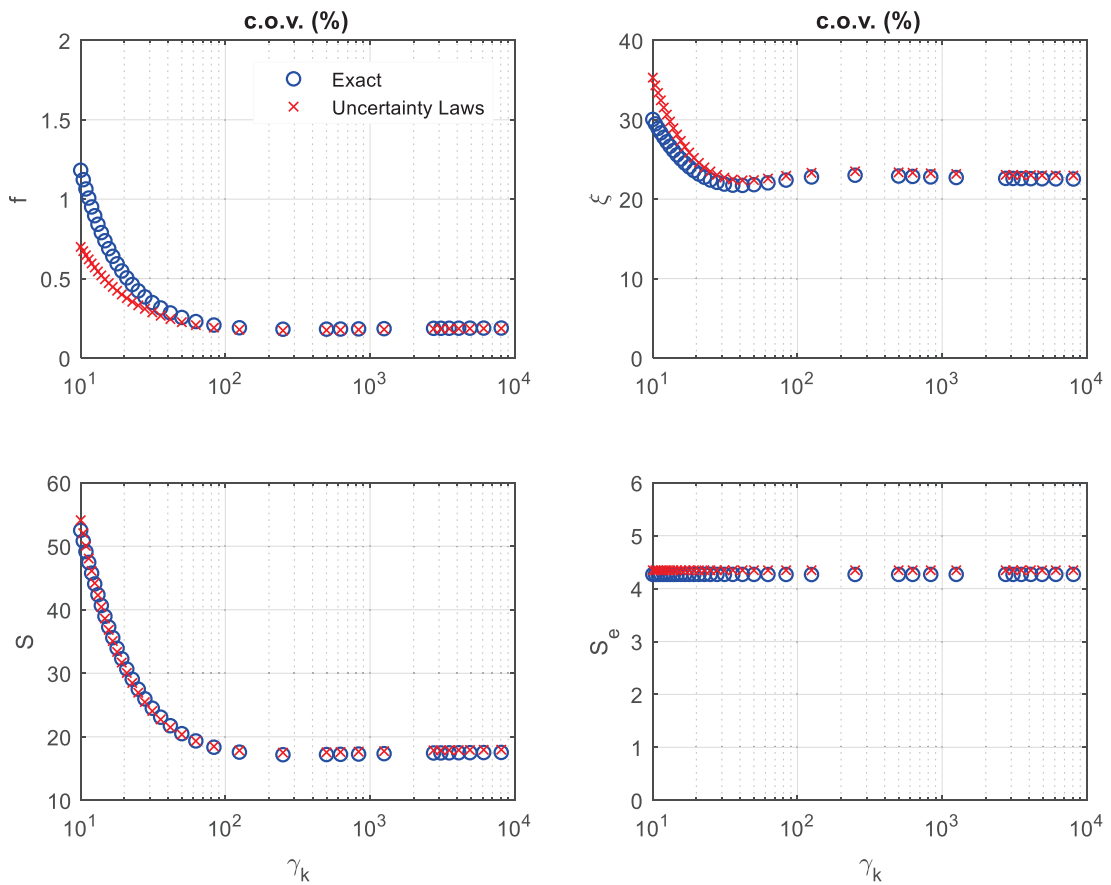


Figure 2.5. Effect of signal-to-noise ratio on the posterior c.o.v. of spectral parameters

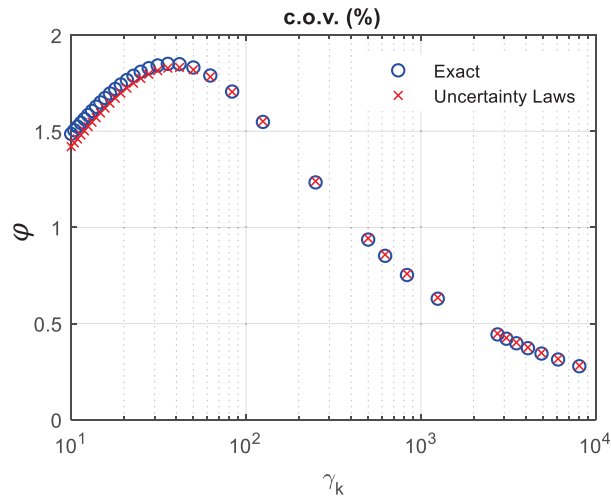


Figure 2.6. Effect of signal-to-noise ratio on the posterior c.o.v. of first mode shape

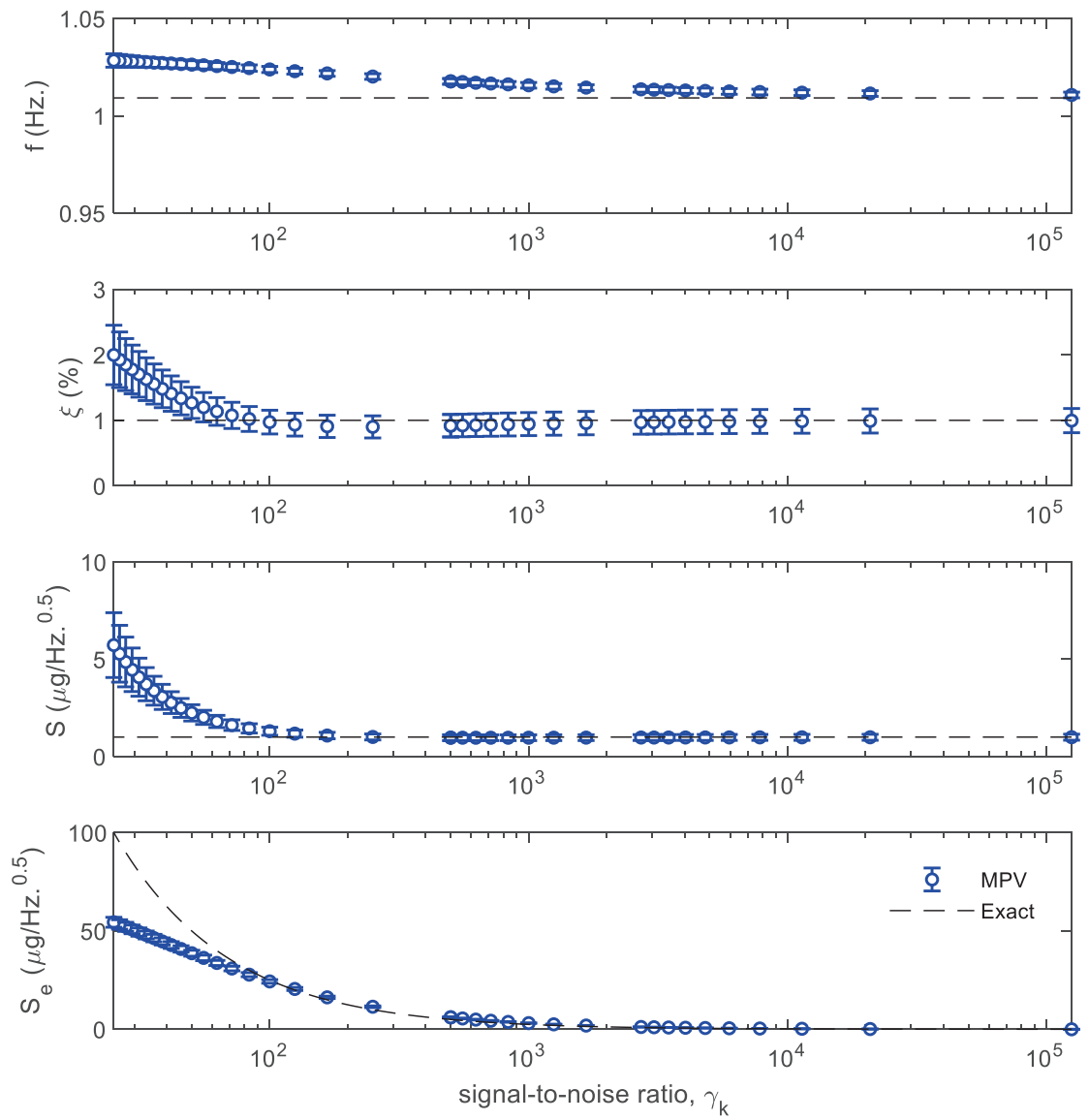


Figure 2.7. Effect of signal-to-noise ratio on the MPVs and posterior standard deviations

Figure 2.7 presents the variations in the identified MPVs of spectrum parameters as well as their uncertainties in terms of standard deviations. It is seen that MPVs converge to exact values with decreasing posterior standard deviations while the modal signal-to-noise ratio increases. Here, most dramatical difference is observed in prediction error for  $\gamma_k < 100$ . This difference seems reasonable since the prediction error does not only reflect the pure noise effect, but also contains a combined effect of single-mode modelling assumption and large level of noise. For this reason, the decrease in the identification quality for the smaller values of signal-to-noise ratio is considered to be correlated with the combined effect of measurement noise and modelling error.

For comparison purposes, the considered shear frame is investigated by using two different identification techniques: covariance driven SSI (SSI-COV) and FDD. The results obtained for  $\gamma_k=1250, 250$  and  $50$  are presented below. Here, Table 2.6, Table 2.7 and Table 2.8 present the MAC values of mode shapes, natural frequencies and damping ratios identified by BAYOMA, FDD and SSI, respectively. Although the result show that BAYOMA gives relatively better convergence to the exact values, a reasonable difference is not observed among different techniques. The largest difference is observed in mode shapes and damping ratios for  $\gamma_k=50$ . In fact, each identification technique can give reasonable results when the data quality is good. Here, the main difference of BAYOMA lies in providing the uncertainty information for the identified values. In addition, BAYOMA does not require any signal processing procedure such as resampling, high or low pass filtering. However, the results by SSI could be obtained for resampling of data to  $25 \text{ Hz}$  sampling frequency to reduce the noise effects. Otherwise, the lower modes cannot be identified even for the large model orders.

Table 2.6. Comparison of MAC values of identified mode shapes ( $n$ : mode number)

$n$	$\gamma_k=1250$			$\gamma_k=250$			$\gamma_k=50$		
	BAYOMA	FDD	SSI	BAYOMA	FDD	SSI	BAYOMA	FDD	SSI
1	1.0000	1.0000	0.9969	0.9996	0.9978	0.9921	0.9955	0.9895	0.9810
2	0.9999	0.9999	0.9996	0.9998	0.9978	0.9956	0.9967	0.9905	0.9904
3	0.9999	0.9999	0.9999	0.9999	0.9993	0.9996	0.9956	0.9927	0.9904
4	0.9999	0.9997	1.0000	0.9998	0.9989	0.9992	0.9970	0.9915	0.9906
5	1.0000	0.9984	1.0000	0.9999	0.9994	0.9990	0.9962	0.9870	0.9912

Table 2.7. Comparison of identified frequencies ( $Hz$ ) for first mode

$n$	<i>Actual</i>	$\gamma_k=1250$			$\gamma_k=250$			$\gamma_k=50$		
		BAYOMA	FDD	SSI	BAYOMA	FDD	SSI	BAYOMA	FDD	SSI
1	1.01	1.01	1.01	1.01	1.02	1.01	0.99	1.02	1.04	1.03
2	3.00	3.00	3.01	3.01	3.01	3.01	2.99	3.01	3.03	3.05
3	4.93	4.93	4.93	4.92	4.94	4.95	4.97	4.94	4.89	4.91
4	6.76	6.76	6.76	6.74	6.76	6.78	6.74	6.76	6.71	6.78
5	8.42	8.42	8.42	8.42	8.42	8.40	8.41	8.42	8.44	8.43

Table 2.8. Comparison of identified damping ratios (%) for first mode

$n$	<i>Actual</i>	$\gamma_k=1250$			$\gamma_k=250$			$\gamma_k=50$		
		BAYOMA	FDD	SSI	BAYOMA	FDD	SSI	BAYOMA	FDD	SSI
1	1.00	0.95	1.17	1.23	0.90	1.32	1.15	1.27	1.52	0.71
2	1.00	0.99	0.90	0.97	1.13	0.74	0.89	1.13	1.56	0.84
3	1.00	0.98	1.01	0.85	1.05	1.13	1.01	1.11	0.88	0.84
4	1.00	1.02	0.85	0.92	1.05	0.51	0.83	1.07	1.18	0.94
5	1.00	0.98	0.81	1.14	0.93	0.52	0.93	0.81	0.65	0.72

### 2.7.2. Numerical Analysis II: A Comparison for Posterior Uncertainty Quantification

In this section, the computational time required by the proposed methodology for the calculation of posterior covariance matrix is compared to the method by Au and Xie (2017) by using a small illustrative example. Here, an analytical shear frame model is considered whose fundamental frequency and damping ratio are set to 1 Hz, and 1%, respectively. The number of DOF of the considered model varies from 2 to 1000. An *i.i.d.* Gaussian excitation with modal PSD of  $10 \mu g^2/Hz$  is generated as ambient loading with 100 Hz sampling ratio and 300 sec duration. The measured response is contaminated by a Gaussian white noise with PSD of  $1 \mu g^2/Hz$ . Calculations are carried out by MATLAB 2018b, and ASUS notebook computer with i7 6700HQ 2.60 GHz processor and 16 GB RAM.

Figure 2.8 presents a comparison of the required computational time for the proposed methodology and the method by Au and Xie (2017). It is seen that the proposed

methodology requires less computational time. However, no significant difference is observed while the number of DOF is smaller than 500.

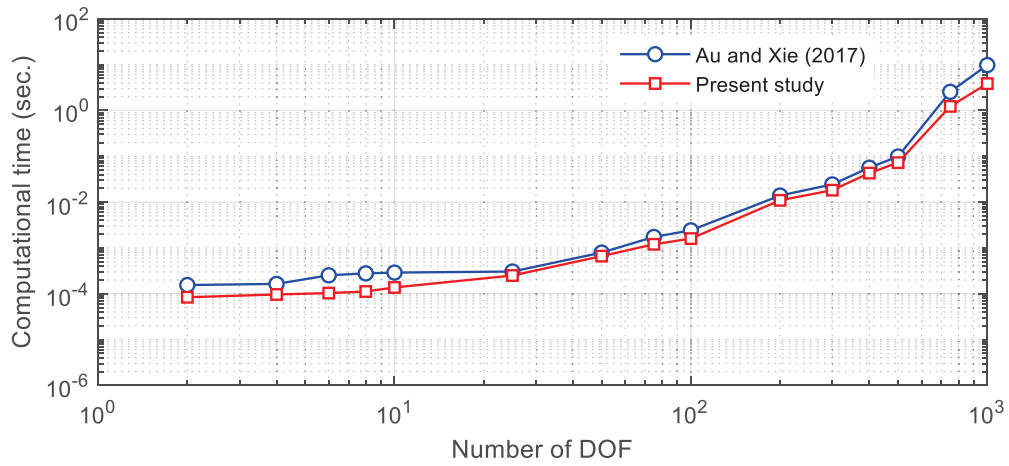


Figure 2.8. Comparison of the computational time required for the calculation of posterior covariance matrix

### 2.7.3. Experimental Analysis: Three-story Shear Frame

A three-story laboratory shear frame is shown in Figure 2.9. It is investigated under ambient excitation with 250 Hz sampling rate. Three piezo-electric accelerometers are used which are defined with 1000 mV/g sensitivity and  $11.4 \mu\text{g}/(\text{Hz.})^{0.5}$  spectral noise density.

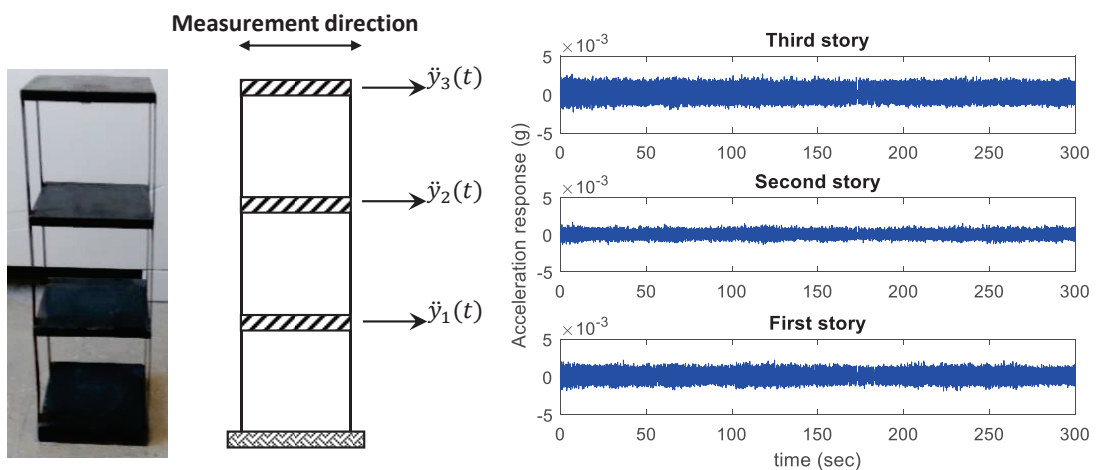


Figure 2.9. Schematic view of laboratory frame and measured acceleration responses

The measurement system consists of a laptop computer with a 1.5 GHz single CPU, Linux operating system, and 16 channel USB DUX-Sigma data acquisition box with

24 bit analog to digital conversion, A first order analog lowpass filter with a cut-off frequency at 120 Hz for each channel, and a constant current supply for the accelerometers.

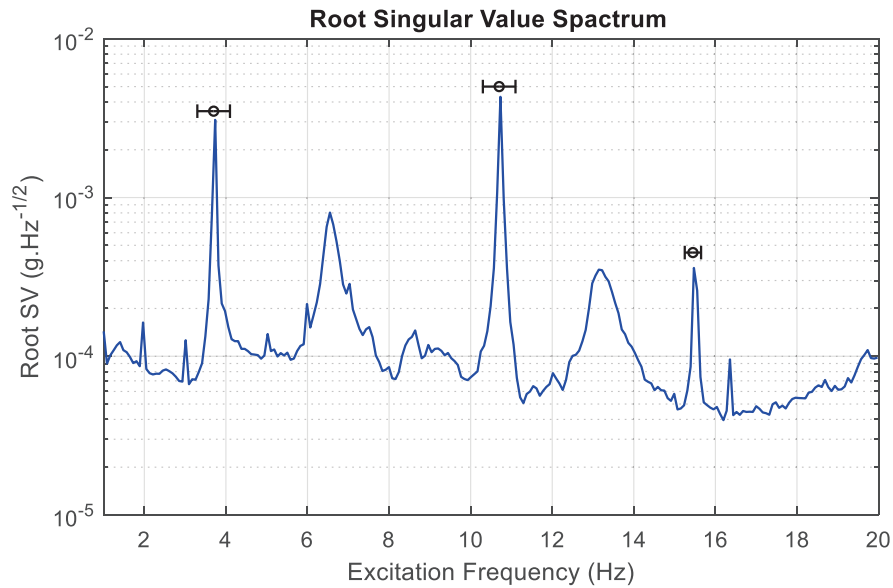


Figure 2.10. Root singular value spectrum and possible modes with selected bandwidths

Root singular value spectrum of acceleration response measurements is presented in Figure 2.10. For a smooth spectrum, a hamming window is applied by using 75 data points (with 1000 windows) and without overlapping. This is sufficient in order to obtain a smooth singular value spectrum for the estimation of possible modal frequencies.

According to Figure 2.10, one is tempted to include the frequencies around 7 Hz and 13 Hz as structural modes. The identified mode shapes at 7 Hz and 13 Hz do not belong to the investigated structure and can be considered as noise or spurious modes. In this particular case, these modal appearances are considered to be modes of the laboratory structure in which the experiment is conducted.

Identified most probable values are presented in Table 2.9. At first view, the signal quality is found to be well for all modes with the minimum signal to noise ratio of approximately 280. In the first and second mode, signal to noise ratio is considerably large (approximately 2250). Despite the large signal to noise ratios, identified spectral densities of prediction error are found to be 90 to 800 folds when compared with the identified spectral density of modal excitations. This case is considered to be the result of very small modal damping.

Table 2.9. Identification results for the spectral density of modal excitation and prediction error, and root signal-to-noise ratio

Mode Number	$f$		$\xi$		$S$		$S_e$		$\gamma$
	MPV (Hz.)	c.o.v. (%)	MPV (%)	c.o.v. (%)	MPV ( $\mu\text{g}/\text{Hz.}$ )	c.o.v. (%)	MPV ( $\mu\text{g}/\text{Hz.}$ )	c.o.v. (%)	
1	3.7194	0.02	0.1113	11.12	19.93	3.94	1788.60	2.39	2247
2	10.7277	0.01	0.0885	7.34	12.97	3.61	1969.92	2.48	2049
3	15.5025	0.01	0.1023	5.75	1.29	4.96	1082.45	3.39	284

Identified mode shapes are presented in Figure 2.11. At first view, it is seen that the identified mode shapes are compatible with the general expected mode shapes for a shear frame with uniform story stiffness and mass. EMAC values are obtained as [1.000 1.000 1.000] for the three modes. In addition, posterior c.o.v. are calculated as 0.34, 0.23 and 0.53%.

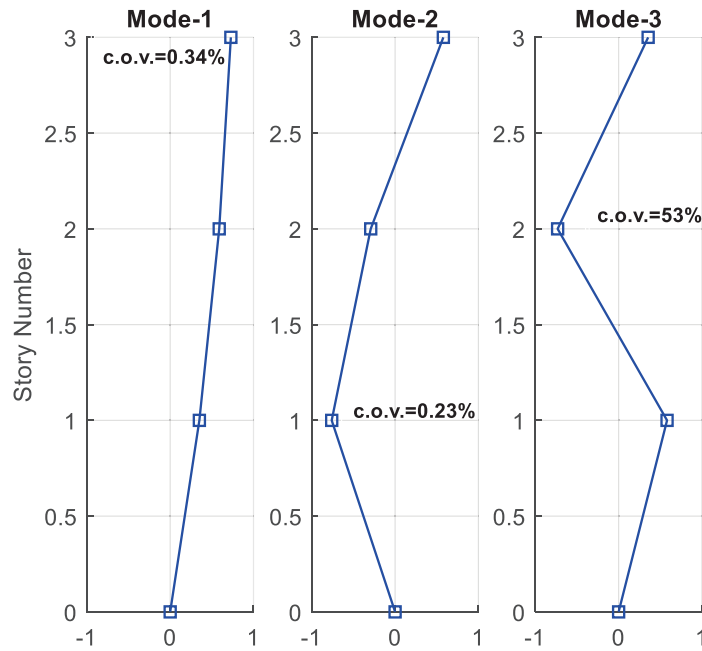


Figure 2.11. Root singular value spectrum and possible modes with selected bandwidths

The exact marginal pdf for a modal parameter can be obtained by direct integration of multivariate probability density function with respect to remaining parameters. Thus, the exact marginal PDFs are obtained as below.

$$\begin{aligned}
 p(f) &= -\int \int \int \exp[L(\theta)] d\zeta dS dS_e; & p(\xi) &= -\int \int \int \exp[L(\theta)] df dS dS_e \\
 p(S) &= -\int \int \int \exp[L(\theta)] df d\zeta dS_e; & p(S_e) &= -\int \int \int \exp[L(\theta)] df d\zeta dS
 \end{aligned}
 \tag{2.90}$$

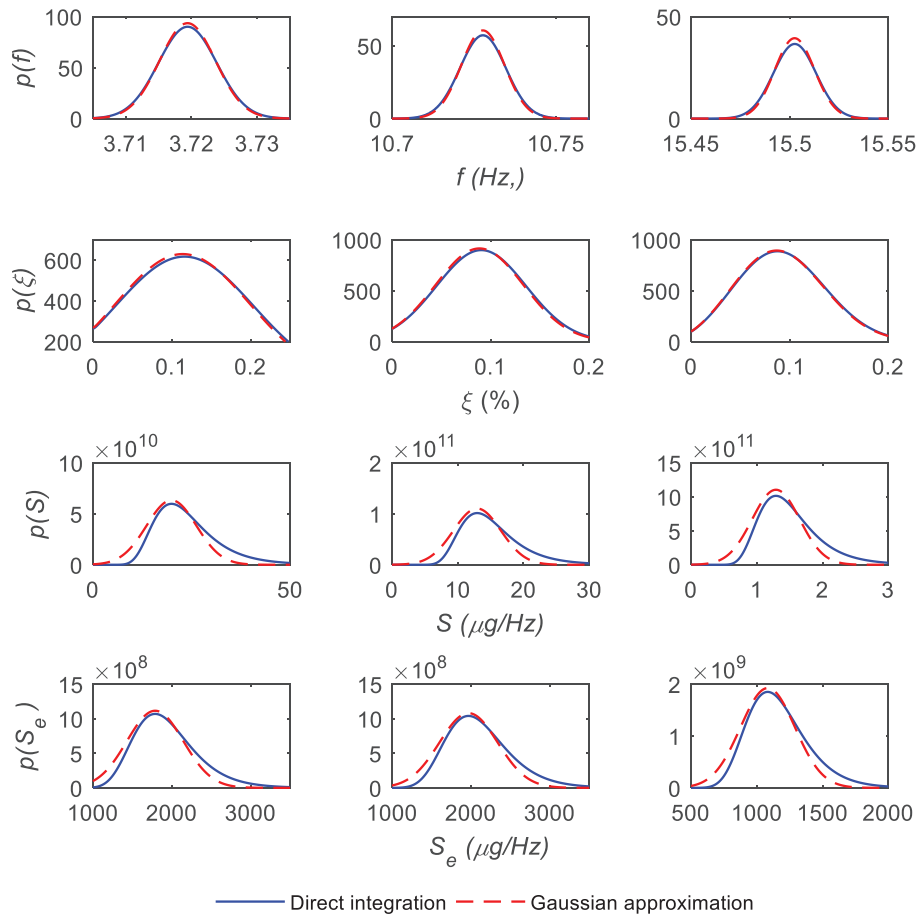


Figure 2.12. Comparison of exact and approximate marginal distributions

As an alternative, gaussian approximation can be used to obtain the marginal PDFs. For this purpose, the marginal likelihood function of a modal parameter can be constructed by setting the remaining parameters to be equal to their MPVs. Here, likelihood function is constructed by Eq. (2.48). The final form of marginal PDFs should be normalized so that the cumulative probability density is 1 for both methods.

Marginal probability density functions that are obtained by Gaussian approximation and by direct numerical integration (exact) are presented in Figure 2.12. It is seen that Gaussian approximation converges to exact values. However, the direct integration is expensive in terms of computational time and effort. Instead, Gaussian approximation may be the best alternative in terms of computational time and effort.

#### 2.7.4. Field Data Example: 58 Story Building

In this section, the modal properties a 58-story building, located in San Francisco, is investigated by using BAYOMA and FDD identification techniques. The building was



designed by a dual core shear walls and outrigger frames to decrease its displacement demand in the lateral directions (Çelebi et al., 2016). The ambient acceleration records were acquired by California Strong Motion Instrumentation Program (CSMIP) of the California Geological Survey (CGS) by using a 32-channel measurement system. The schematic view of the building and sensor placement configurations are presented in Figure 2.13. The measure acceleration responses are divided in North-South (NS) and East-West (EW) components and the modal properties in the lateral directions are obtained separately. For torsional modes, the records in the NS directions are utilized only. Due the lack of the measurement points, only the results for the first three torsional modes are presented.

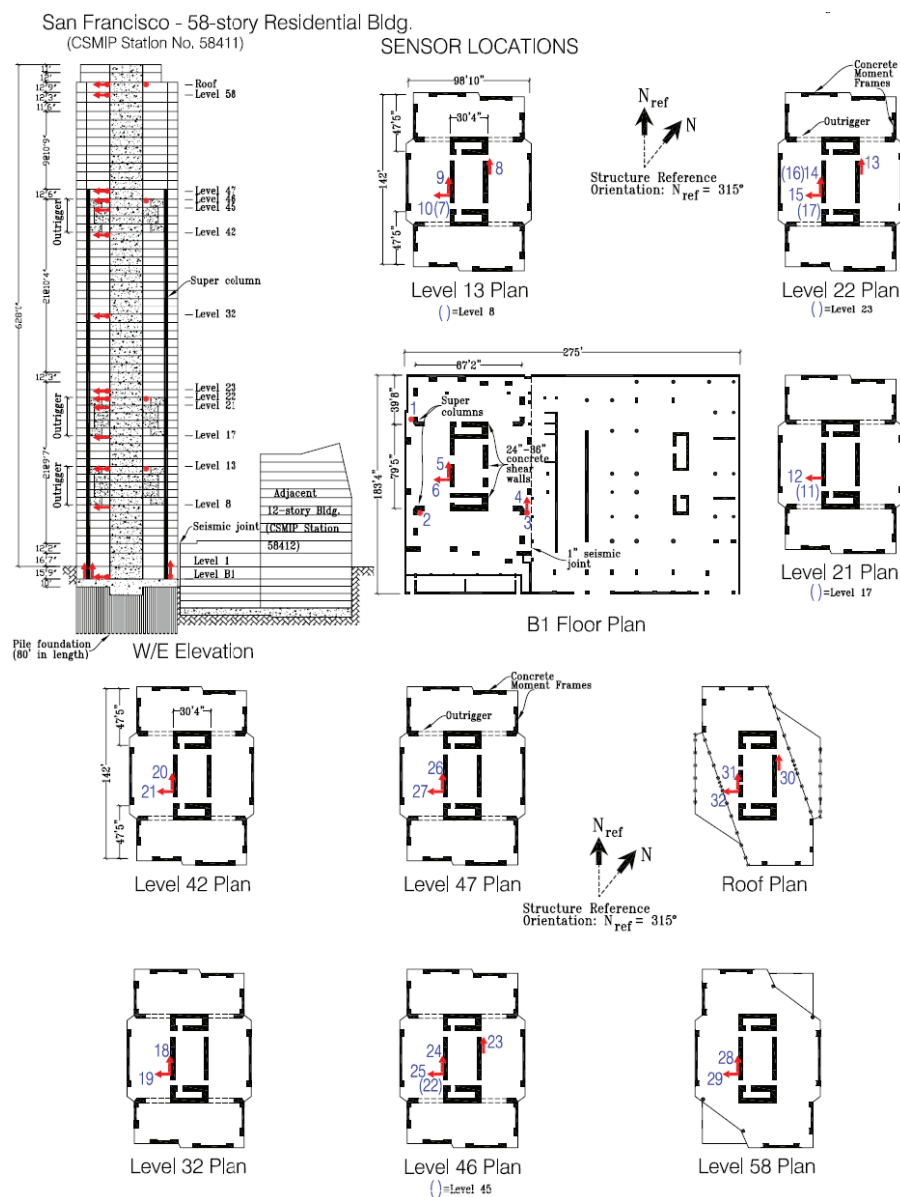


Figure 2.13. Schematic view of 58-Story Building and sensor locations (Source: Center of Engineering Strong Motion Data)

Maximum root singular value spectrum of the records in the NS and EW directions and possible modes are presented in Figure 2.14. According to this spectrum, five lateral modes in the NS and EW directions, and three torsional modes are detected and identified by using two different techniques.

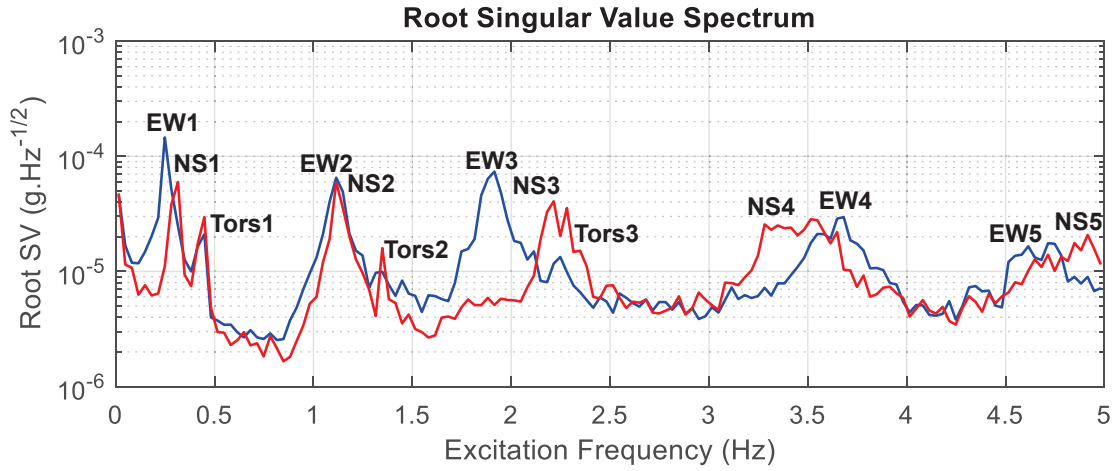


Figure 2.14. Maximum root singular value spectrum and possible modes

Table 2.10. Identified natural frequencies and damping ratios

<i>Mode Number</i>	<i>f (Hz.)</i>			<i>ξ (%)</i>		
	<i>BAYOMA</i>		<i>FDD</i>	<i>BAYOMA</i>		<i>FDD</i>
	<i>MPV</i>	<i>c.o.v. (%)</i>		<i>MPV</i>	<i>c.o.v. (%)</i>	
EW1	0.26	0.74	0.26	1.94	37.34	4.91
NS1	0.30	0.61	0.29	1.60	38.10	4.79
Tors1	0.44	0.54	0.44	0.47	60.60	2.73
EW2	1.12	0.36	1.12	1.83	22.29	1.85
NS2	1.13	0.25	1.12	1.00	25.88	1.45
Tors2	1.36	0.19	1.37	0.55	37.79	1.59
EW3	1.90	0.47	1.90	2.03	42.13	1.42
NS3	2.19	0.41	2.19	0.90	27.31	1.55
Tors3	2.28	0.31	2.29	1.30	32.37	1.37
NS4	3.35	0.49	3.34	2.87	37.04	2.72
EW4	3.66	0.36	3.66	2.17	30.99	1.89
EW5	4.61	0.40	4.61	2.19	38.85	2.19
NS5	4.90	0.21	4.90	1.36	27.85	2.57

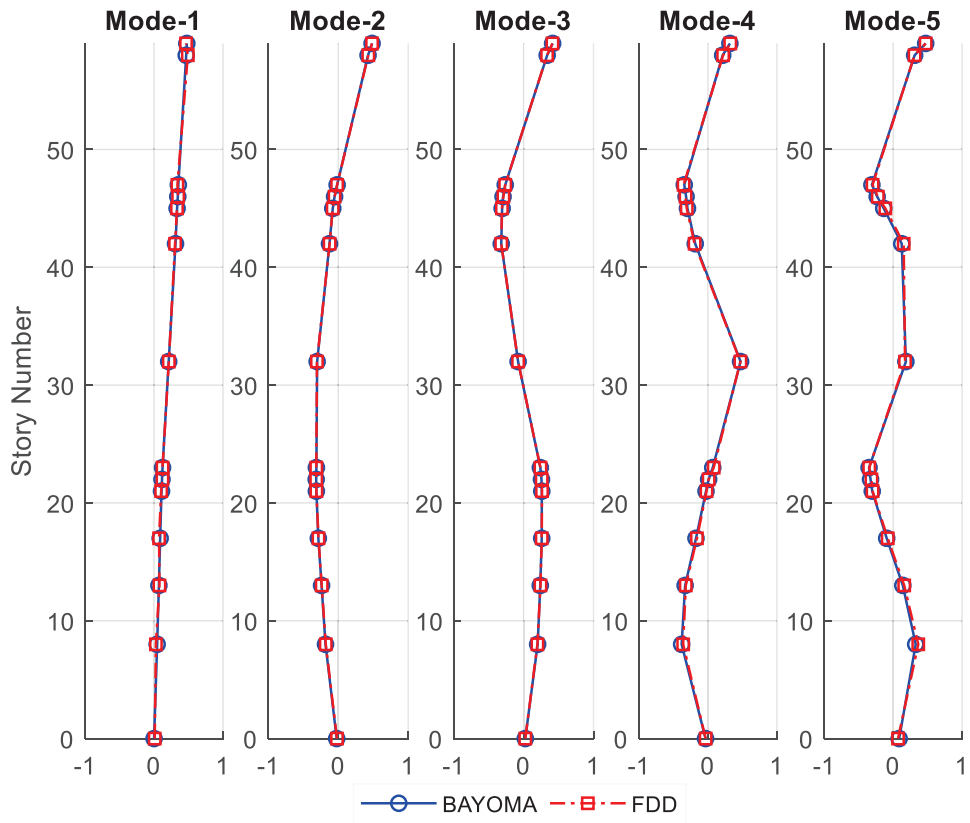


Figure 2.15. Identified mode shapes in EW direction

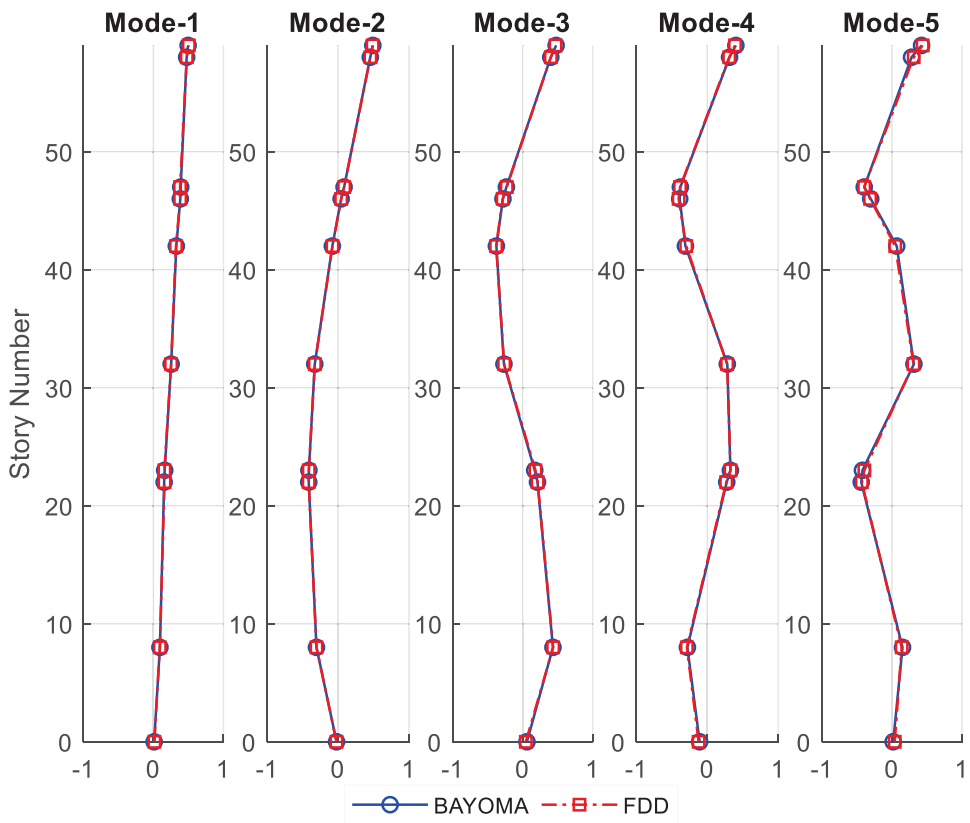


Figure 2.16. Identified mode shapes in NS direction

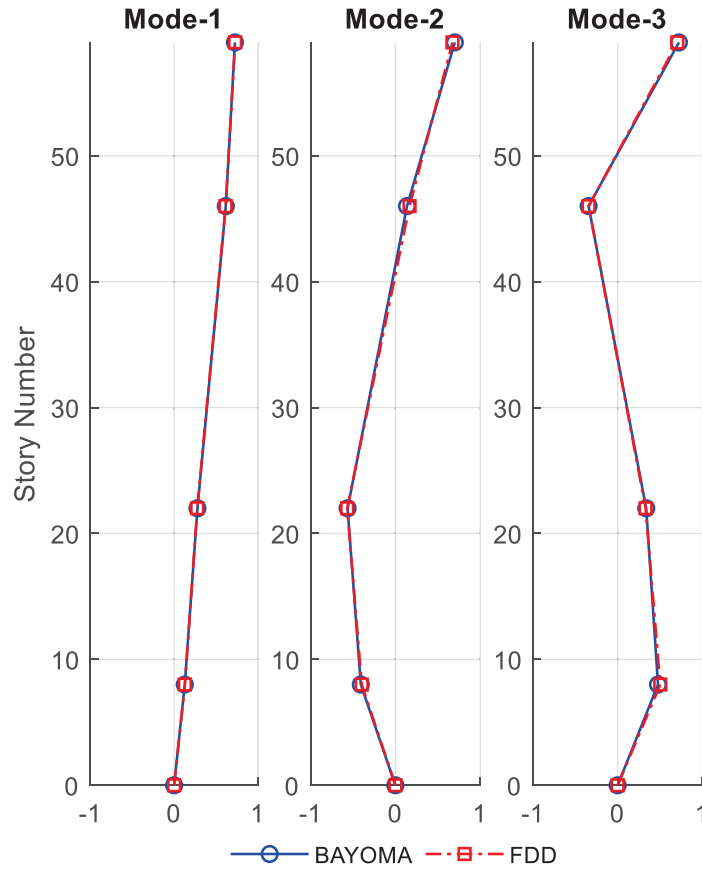


Figure 2.17. Identified torsional mode shapes

Most probable natural frequencies, damping ratios and their identification uncertainties in terms of c.o.v. are presented in Table 2.10. For comparison purposes, the results are verified by FDD identification technique. According to the obtained results, a good agreement is observed between the applied techniques. For damping ratio, however, a reasonable convergence is not observed. The difference in the identified damping ratios is considered to be induced by the applied robust methodology in FDD. It should be noted that the FDD identifies the damping ratio by using the logarithmic decrement obtained the inverse FFT of the band limited frequency response data, and this methodology may cause large modelling errors due to the omission of the prediction error. In addition, the identified mode shapes in the EW, NS and torsional directions are presented in Figure 2.15, Figure 2.16, and Figure 2.17, respectively. Again, a good agreement is observed between the results obtained by BAYOMA and FDD.

### 2.7.5. Field Data Example: One Rincon Tower

Modal parameters of a 64-story building, One Rincon Tower, is investigated in this section by using BAYOMA. The structural system of the building consists of a dual core wall and outriggers. A 72-channel acceleration response monitoring system was installed in the context of a project by the California Strong Motion Instrumentation Program (CSMIP) of the California Geological Survey and the National Strong Motion Project (NSMP) of the California Geological Survey and the National Strong Motion Project (NSMP) under the Advanced National Seismic Systems managed by the United States Geological Survey (USGS). The ambient response data that is investigated in this study is provided by the Center of Engineering Strong Motion Data (CESMD). The schematic view of the building and sensor locations are illustrated in Figure 2.18 and Figure 2.19, respectively.

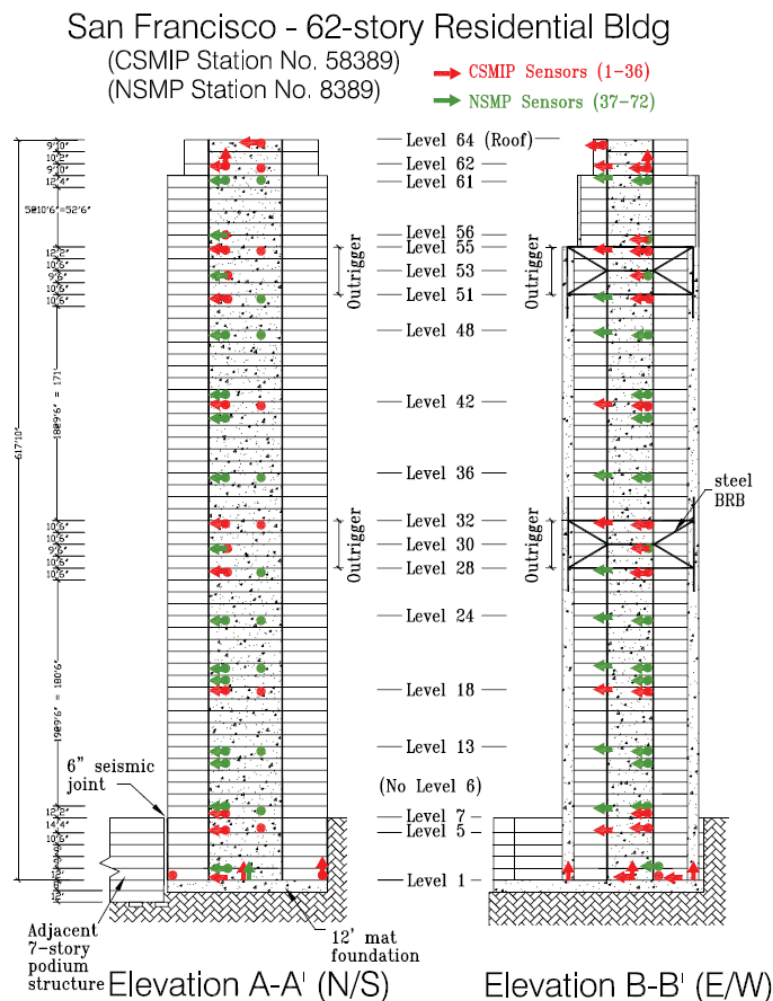


Figure 2.18. Elevation view of One Rincon Tower and sensor locations (Source: Center of Engineering Strong Motion Data)

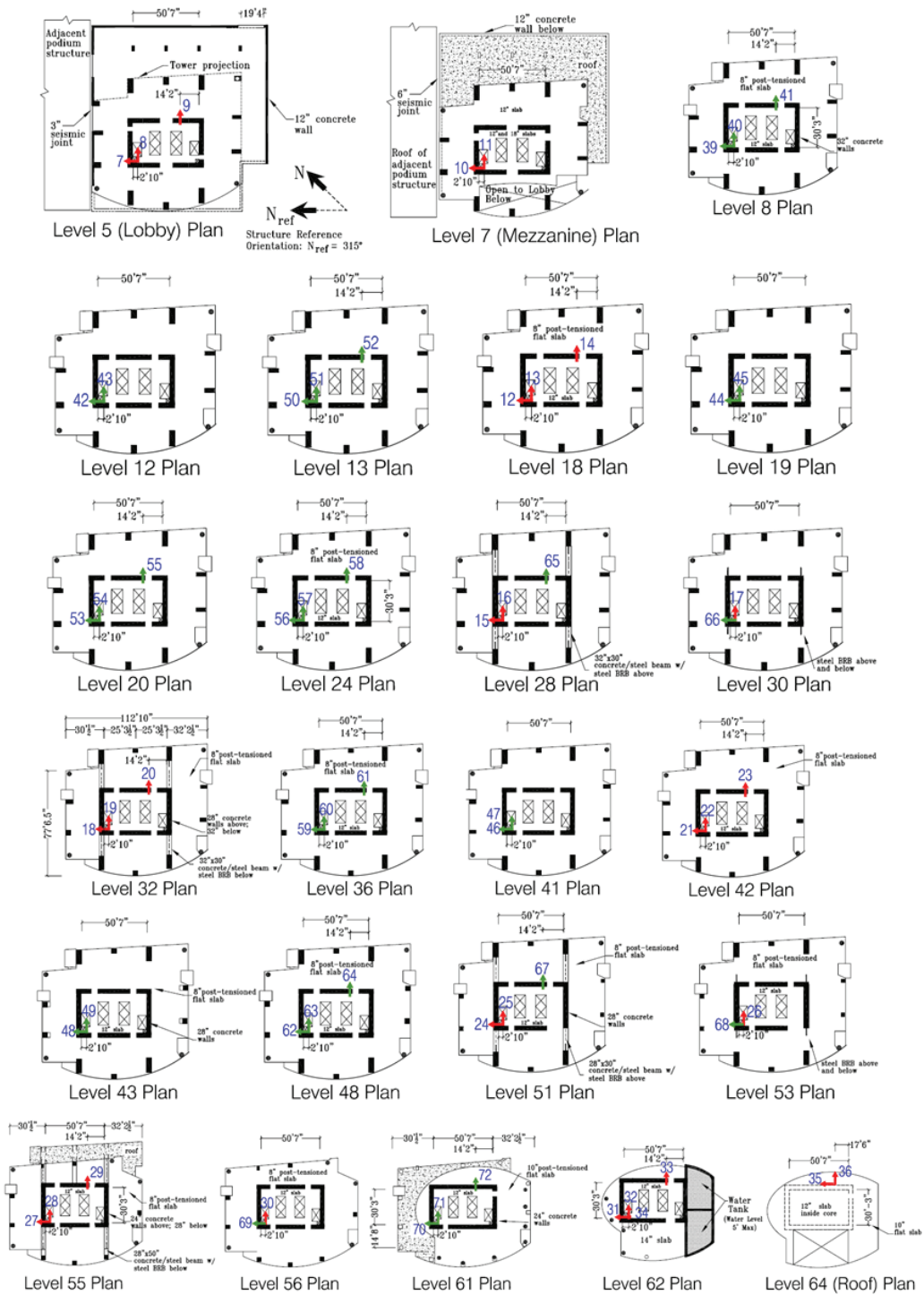


Figure 2.19. Plan views and sensor locations (Source: Center of Engineering Strong Motion Data)

The root singular value spectrum of the ambient response data along the North-South (NS) and East-West (EW) direction is presented in Figure 2.20. Torsional modes are visible at the frequencies around the peak values for both EW and NS directions. Here, translational modes are investigated separately. However, the torsional modes are identified by consideration of all measurement directions.

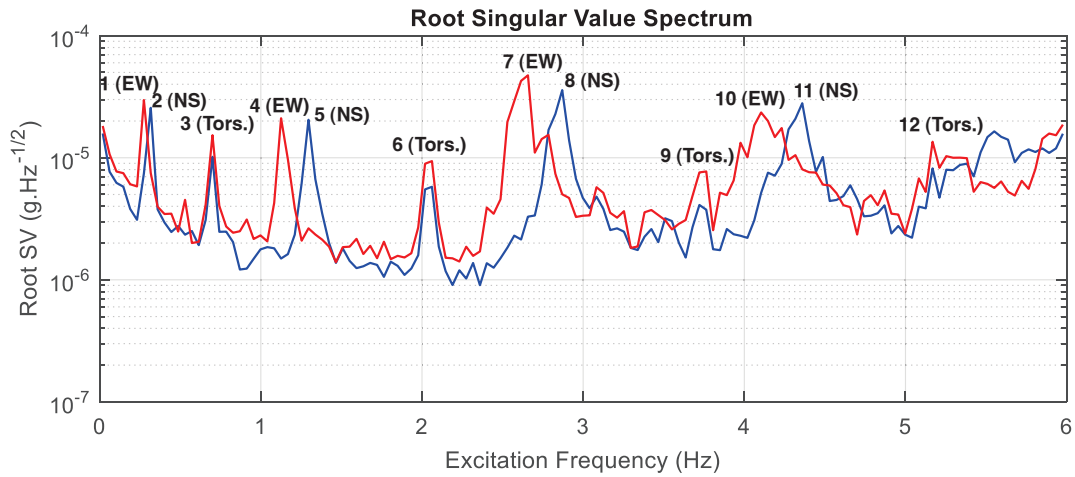


Figure 2.20. Root singular value spectrum and possible modes

Table 2.11. Identification results for the spectral density of modal excitation and prediction error, and root signal-to-noise ratio

Mode Number	$f$ (Hz.)			$\xi$ (%)		
	MPV	c.o.v. (%)	Çelebi et al. (2013)	MPV	c.o.v. (%)	Çelebi et al. (2013)
1 (EW)	0.27	0.75	0.27	1.84	40.51	0.30-0.90
2 (NS)	0.31	1.04	0.30	1.66	41.17	0.90
3 (Torsion)	0.71	0.31	0.70	0.86	35.80	0.40
4 (EW)	1.14	0.19	1.14	0.58	34.35	2.1-4.4
5 (NS)	1.30	0.24	1.30	0.43	47.61	0.50
6 (Torsion)	2.04	0.14	2.04	0.49	29.25	0.48
7 (EW)	2.63	0.16	2.59	0.78	22.87	0.30
8 (NS)	2.86	0.14	2.83	0.68	24.43	0.90-1.30
9 (Torsion)	3.74	0.26	3.72	1.58	21.76	1.30
10 (EW)	4.12	0.23	4.12	1.18	29.33	0.59-0.70
11 (NS)	4.34	0.13	4.34	0.72	22.95	1.70
12 (Torsion)	5.20	0.33	5.17	1.05	23.76	2.60

Identified most probable frequencies and damping ratios, and the previous results obtained by Çelebi et al. (2013) are presented in Table 2.11. In the study by Çelebi et al.

(2013), the frequency and damping values are obtained by SSI-COV using the MATLAB-System Identification Toolbox. They separated the acceleration responses in two parts along the East-West (EW) direction as EW1 and EW2. Here, EW1 and EW2 denote the acceleration responses in the EW direction obtained at the left bottom, and right upper sides of the plan view, respectively. For this reason, two different results are given for damping ratios in the EW direction. Results show that the identified most probable frequencies are similar with Çelebi et al. (2013). However, damping ratios do not match. These results may be considered as reasonable incorporating the larger variations in posterior uncertainty. Here, posterior c.o.v. of frequency values vary from 0.13 to 0.75. However, the c.o.v. increases up to 41.17% for damping ratio. In addition, the identified spectral densities of modal excitation and prediction error, and root modal signal-to-noise ratios are presented in Table 2.12.

Table 2.12. Identification results for the spectral density of modal excitation and prediction error, and root signal-to-noise ratio

Mode Number	$S$		$S_e$		$\sqrt{\gamma}$
	MPV ( $\mu\text{g}^2/\text{Hz.}$ )	c.o.v. (%)	MPV ( $\mu\text{g}^2/\text{Hz.}$ )	c.o.v. (%)	
1 (EW)	3.5908	19.64	1.0730	3.59	50.24
2 (NS)	2.4160	29.54	0.3348	4.51	80.81
3 (Torsion)	0.1436	13.78	0.1112	2.26	66.38
4 (EW)	0.1653	13.35	0.1546	2.54	88.64
5 (NS)	0.0915	37.97	0.1553	5.75	89.11
6 (Torsion)	0.0210	14.17	0.0772	2.26	53.50
7 (EW)	0.9776	15.50	0.2250	2.56	133.14
8 (NS)	0.3370	17.45	0.0989	2.82	136.11
9 (Torsion)	0.0340	24.95	0.5061	2.18	8.19
10 (EW)	0.3483	36.88	0.2123	3.42	54.20
11 (NS)	0.1938	20.81	0.1145	2.86	90.74
12 (Torsion)	0.0560	35.18	0.4808	2.71	16.28



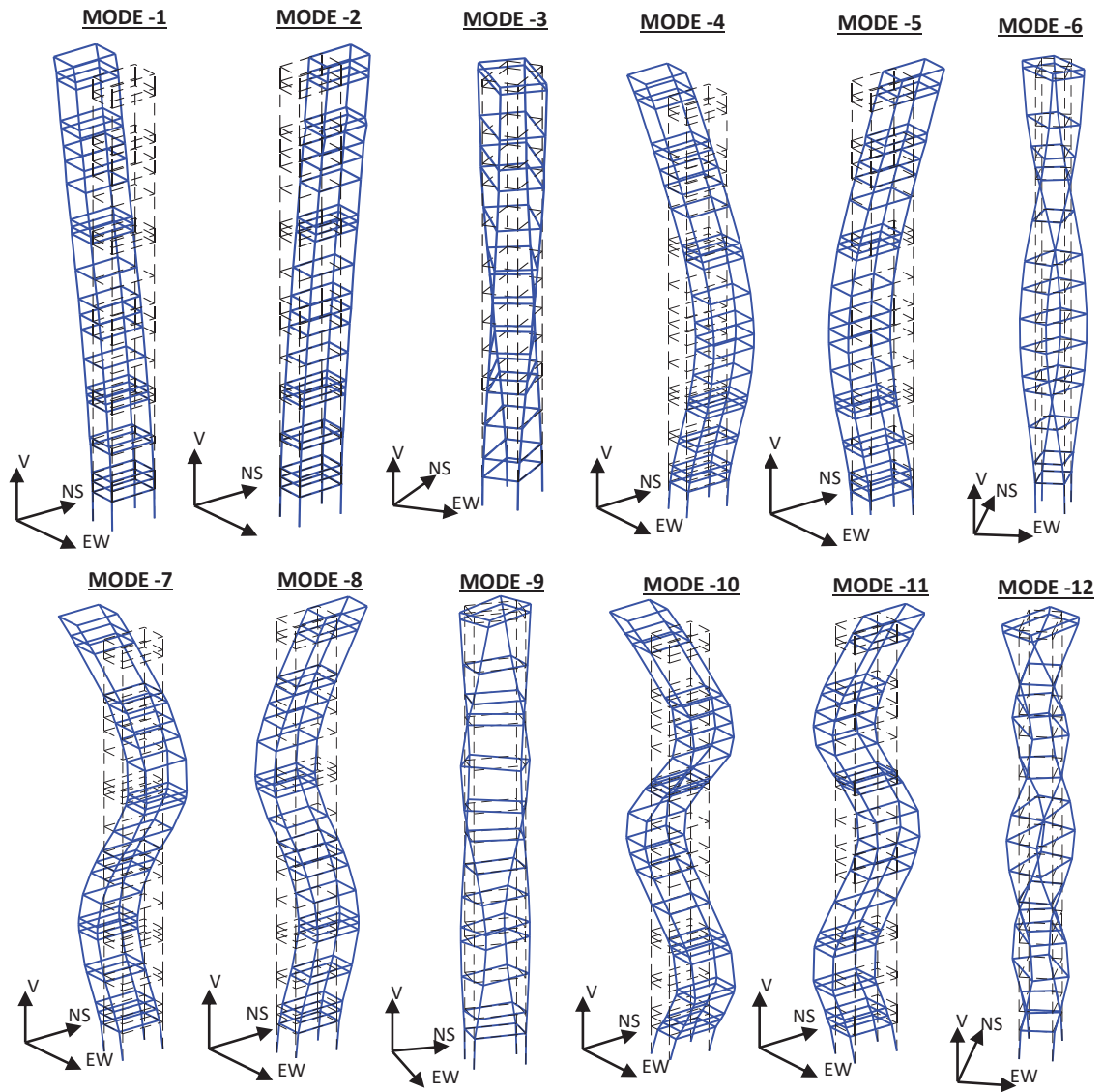


Figure 2.21. 3D view of the identified mode shapes

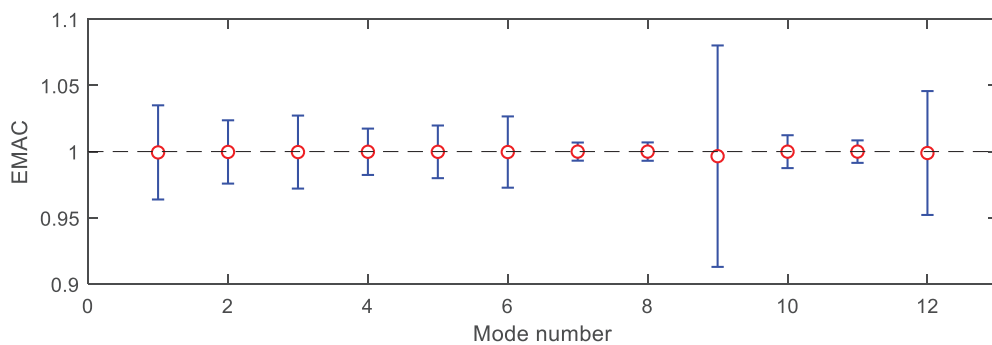


Figure 2.22. EMAC values with  $\pm$  standard deviations

Figure 2.21 shows the 3D view of the identified mode shapes. In addition, the EMAC values, and calculated posterior standard deviations are presented in Figure 2.22. Calculated EMAC values that are close to 1 show that the quality of identified mode

shapes is good. A direct relation is not observed between the EMAC and posterior standard deviation. The larger uncertainty arises in the 9<sup>th</sup> mode with the EMAC value of 0.9986. However, the remaining ones do not show a proportional relation.

Figure 2.23 presents exact posterior coefficient of variation values by the proposed methodology versus the values obtained by using the uncertainty laws. Results show that the exact values well matched with the results obtained by uncertainty laws. Due to the quality of data (large signal-to-noise ratio) the observed convergence is considered to be reasonable.

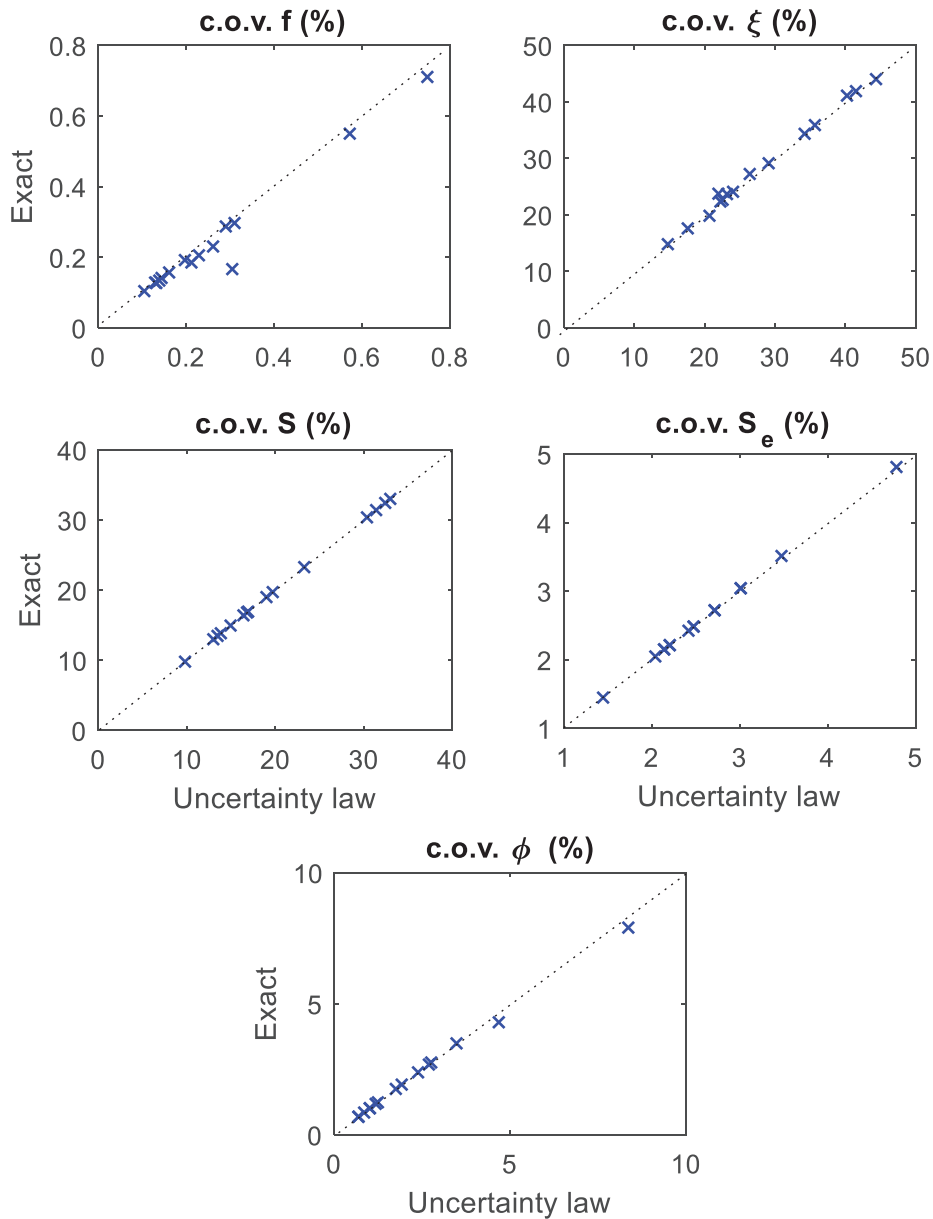


Figure 2.23. Comparison of exact c.o.v. values with uncertainty laws

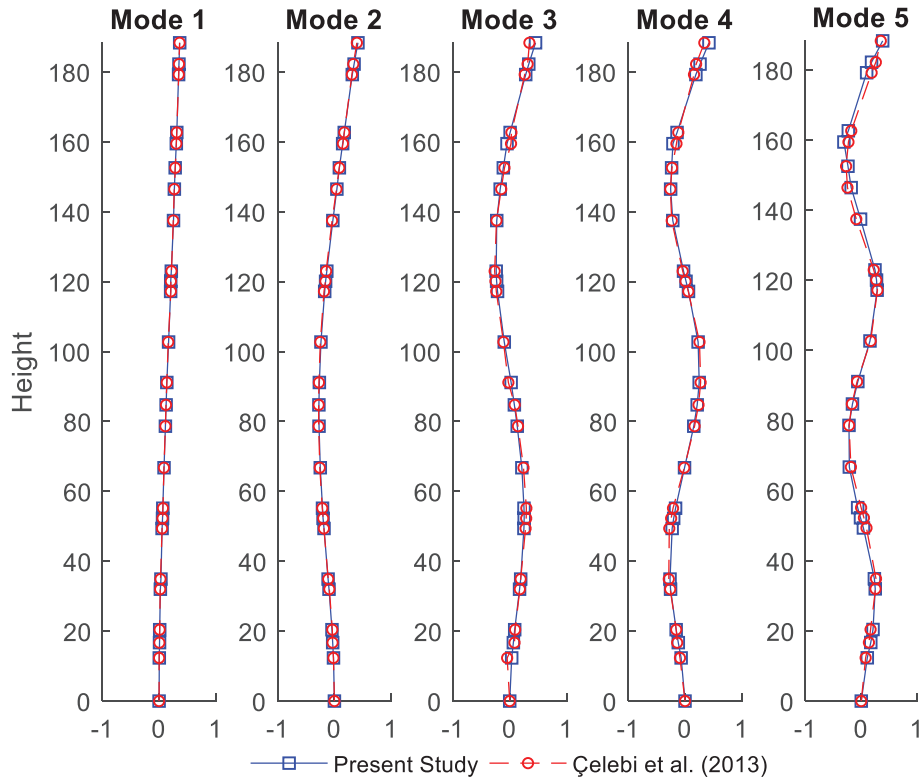


Figure 2.24. Identified mode shapes by using NS data

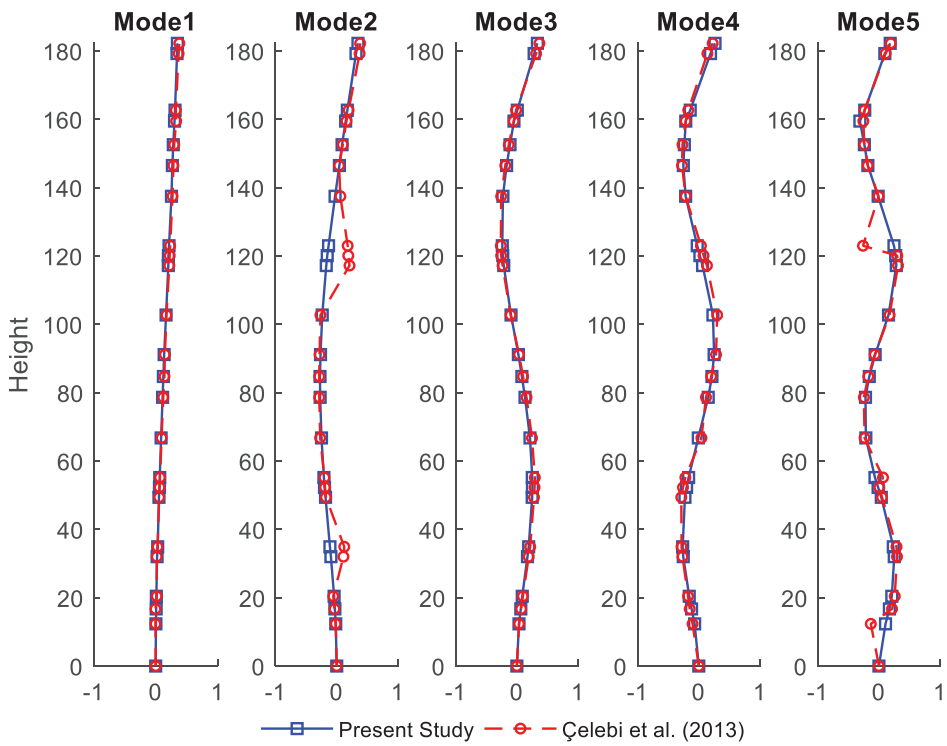


Figure 2.25. Identified mode shapes by using EW1 data

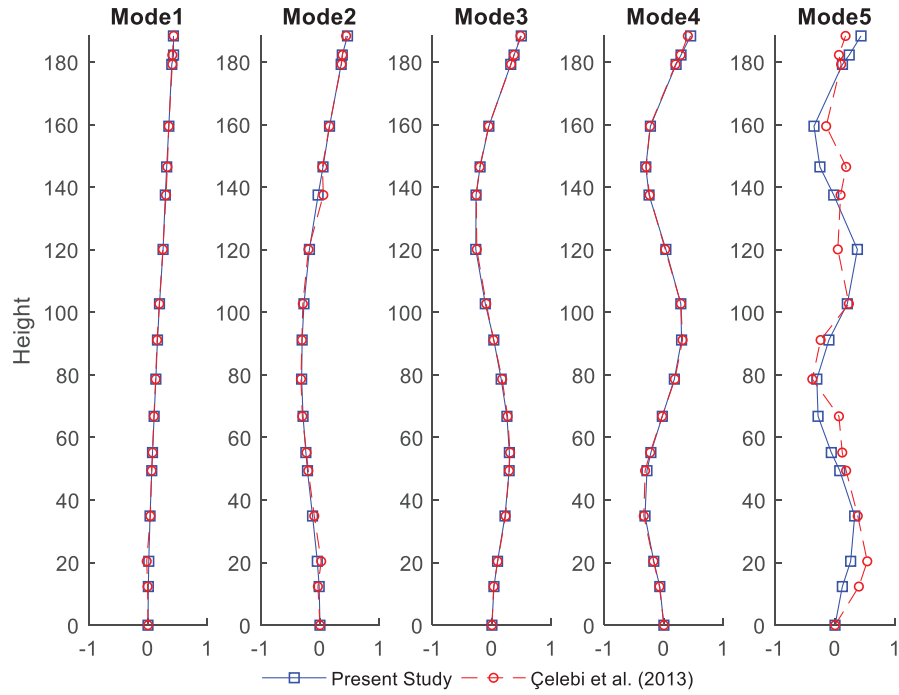


Figure 2.26. Identified mode shapes by using EW2 data

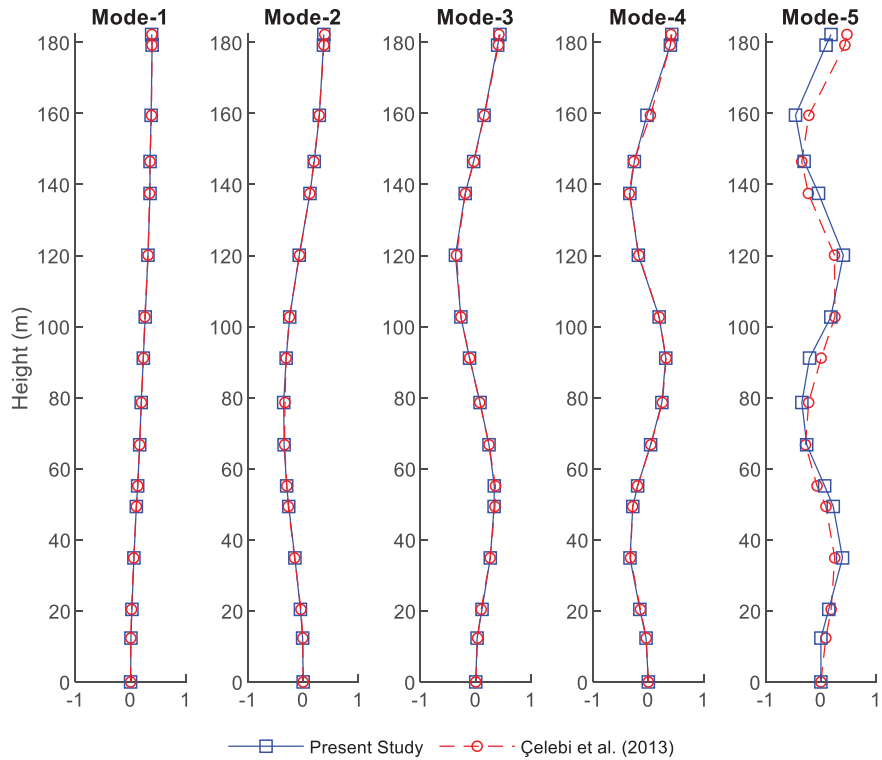


Figure 2.27. Identified torsional mode shapes by using EW1 and EW2 data

For comparison purposes, 2D view of the calculated modes shapes in this study and by Çelebi et al. (2013) are presented in Figure 2.24, Figure 2.25, Figure 2.26 and

Figure 2.27. The mode shapes in the EW direction are separated as EW1 and EW2 to be comparable to the study by Çelebi et al. (2013). In the global sense, the presented mode shapes match well, except for EW1 and EW2. At the second and fifth modes for EW1, and fifth mode for EW2, the results by Çelebi et al. (2013) show some distortions which are not compatible with the expectation of the general mode shapes.

## 2.8. Concluding Remarks

In this chapter, a review for the theoretical background of frequency based BAYOMA methods and available algorithms for well separated modes are presented. For posterior uncertainty quantification, an alternative method for the calculation of posterior covariance matrix is proposed. Numerical and experimental analysis are presented to illustrate the advantages and disadvantages of BAYOMA. The results are summarized below.

- Although BSDA and BFFTA are motivated from different statistical properties of measured data, it is seen that the final form of objective functions obtained for both methods are same. The solution of the objective function in its original form requires too much computational effort due to very small signal-to-noise ratio without the dominant frequency band. For this reason, working on a selected frequency band becomes useful much more.
- In case of well separated modes, the solution procedure can be simplified. In this procedure, a two-stage approach can be applied. At first stage, only spectral parameters are identified via condensed objective function. At second stage, the optimal mode shape vector can be obtained by minimizing the likelihood function centered at the MPV of spectral parameters identified. The most critical point in this two-stage approach is to effect of norm constraints on the singularity of posterior covariance matrix
- One of the most prominent advantages of BAYAMO is to provide an estimation for posterior uncertainty. In the calculations for posterior statistics, the two-stage approach can also be applied. Based on this idea, an alternative methodology is presented in this study. Numerical results indicate that the proposed methodology requires less computational time when compared to the fast calculation scheme by Au and Xie (2017).

## CHAPTER 3

### COMPUTATIONAL ISSUES IN BAYOMA

#### 3.1. Introduction

Frequency domain BAYOMA provides an efficient methodology to determine the most probable modal parameters as well as their uncertainties. In case of well-separated modes, BAYOMA can be modified to a fast algorithm which assumes that only a single mode is available within a selected frequency band. Thus, the considered system is modeled as an equivalent single mode system. This assumption has a modelling error due to the contribution of unmodeled modes within the selected band. BAYOMA is also capable of identifying the level of this modelling error together with instrumental and environmental noise effect.

The effect of modelling error results in an ill-conditioned fast BAYOMA algorithm in case of closely spaced modes. Therefore, a different algorithm is needed to model this type of problem. Au (2012b) and (2012c) presented an efficient method to identify the most probable modal parameters and posterior uncertainties for closely spaced modes. This algorithm revises the expected covariance matrix of measured response so that it comprises the possible modes within a selected frequency band. In addition, the modelling error may cause significant discrepancy between the identified MPVs and their actual values even for the well-separated modes. This problem is widely seen in case of the mode of interest being buried by unmodeled mode(s). A solution procedure for this problem is presented by Zhu et al. (2019) for a special case in which the burying mode appears at a lower frequency than the buried mode.

This chapter presents a revisit for the possible computational issues in regard to the modelling errors. First, the closely spaced mode algorithm that is proposed by Au (2012b) and (2012c) is reviewed, and a modified algorithm is presented to reduce the computational effort. Second, the effect of modelling error is investigated. Third, the problem of buried mode case and their solution procedure are investigated. Finally, three numerical examples are presented that addresses all these problems, and the results are discussed.

### 3.2. Closely Spaced Modes

The fast algorithm presented by Au (2011a) works well only in the case of well separated modes. If two or more modes are available in the selected frequency band, the previous procedure might not be successful in the determination of most probable modal parameters since the response is dominated by multiple modes. To overcome this problem, an efficient iterative method is presented by Au (2012b). In this method, the expected spectral density of measured response is written as below,

$$E_k = [\Phi]_{N \times N_m} [H_k]_{N_m \times N_m} [\Phi^T]_{N_m \times N} + S_e I_N \quad (3.1)$$

where

$$\Phi = \left[ \begin{array}{c|c|c|c} \{\varphi_1\}_{N \times 1} & & & \{\varphi_{N_m}\}_{N \times 1} \\ \hline & \cdot & \cdot & \\ \hline & & & \end{array} \right]_{N \times N_m}$$

$$H_k = \text{diag} \left( \begin{array}{c} h_{k1} \\ \cdot \\ \cdot \\ \cdot \\ h_{kN_m} \end{array} \right) \times \begin{bmatrix} S_{11} & \cdot & \cdot & \cdot & S_{1N_m} \\ & \cdot & & & \\ & & \cdot & & \\ & & & \cdot & \\ S_{N_m 1} & & & & S_{N_m N_m} \end{bmatrix}_{N_m \times N_m} \times \text{diag} \left( \begin{array}{c} h_{k1}^* \\ \cdot \\ \cdot \\ \cdot \\ h_{kN_m}^* \end{array} \right) \quad (3.2)$$

Here,  $N_m$  = number of modes within the selected band and  $N$  = number of measurement points. The inverse and determinant of  $E_k$  can be obtained as follows by making use of the matrix inversion and determinant lemma.

$$E_k^{-1} = S_e^{-1} I_N - S_e^{-1} \Phi (\Phi^T \Phi + S_e H_k^{-1})^{-1} \Phi^T$$

$$|E_k| = |H_k^{-1} + \Phi^T \Phi S_e^{-1}| |H_k| |S_e I_N| \quad (3.3)$$

$$= |S_e I_{N_m} + \Phi^T \Phi H_k| S_e^{(N-N_m)}$$

The negative-logarithm likelihood function can be obtained by using Eq. (3.3). The main problem in the minimization process arises on the problem that the phase angle between the mode shapes, and the imaginary and real part of the cross spectral densities. To overcome this problem, the mode shape basis can be defined via its singular value decomposition as below.

$$\Phi = U \Sigma V^T$$

$$U = \left[ \begin{array}{c|c} B_{N \times m} & \bar{B}_{N \times (N-m)} \end{array} \right]_{N \times N}; \quad \Sigma V^T = \left[ \begin{array}{c} \alpha_{m \times N_m} \\ \mathbf{0}_{(N-m) \times N_m} \end{array} \right]_{N \times N_m} \quad (3.4)$$

where  $m \leq \min(N, N_m)$ . Hence, the modal shape vector can be written as below (Au, 2012b).

$$\Phi = B\alpha \quad (3.5)$$

Here,  $B$  and  $\alpha$  denote the orthonormal basis within the mode shape subspace, and position of each mode shape vector with respect to  $B$ , respectively (Au, 2012b). Substituting Eq. (3.5) into Eq. (3.3), and after some mathematical manipulations, the inverse and determinant of  $E_k$  can be obtained as below.

$$\begin{aligned} E_k^{-1} &= S_e^{-1}I_N - S_e^{-1}B\alpha_s \left( \alpha_s^T \alpha_s + S_e \bar{H}_k^{-1} \right)^{-1} \alpha_s^T B^T \\ &= S_e^{-1}I_N - S_e^{-1}B\alpha_s \bar{H}_k \alpha_s^T \left( \alpha_s \bar{H}_k \alpha_s^T + S_e \bar{H}_k^{-1} \right)^{-1} B^T \\ &= S_e^{-1}I_N - S_e^{-1}B \left( I_{N_m} - S_e \bar{E}_k^{-1} \right) B^T \\ |E_k| &= \left| S_e I_{N_m} + \alpha_s^T \alpha_s \bar{H}_k \right| S_e^{(N-N_m)} \\ &= \left| \bar{E}_k \right| S_e^{(N-N_m)} \end{aligned} \quad (3.6)$$

where,

$$\bar{E}_k = \alpha_s \bar{H}_k \alpha_s^T + S_e I_m \quad (3.7)$$

and

$$\begin{aligned} \bar{H}_k &= \text{diag} \left( \begin{bmatrix} h_{k1} \\ \vdots \\ h_{km} \end{bmatrix} \right) \times \begin{bmatrix} 1 & \cdot & \cdot & \cdot & \chi_{1N_m} \\ \cdot & \cdot & \cdot & \cdot & \cdot \\ \cdot & \cdot & \cdot & \cdot & \cdot \\ \cdot & \cdot & \cdot & \cdot & \cdot \\ \chi_{N_m 1} & \cdot & \cdot & \cdot & 1 \end{bmatrix}_{N_m \times N_m} \times \text{diag} \left( \begin{bmatrix} h_{k1}^* \\ \vdots \\ h_{kN_m}^* \end{bmatrix} \right) \\ \alpha_s &= \left[ \alpha_1 \sqrt{S_{11}} \quad \cdot \quad \cdot \quad \cdot \quad \alpha_m \sqrt{S_{mm}} \right]_{\bar{m} \times m}; \quad \chi_{ij} = S_{ij} / \sqrt{S_{ii} S_{jj}} \end{aligned} \quad (3.8)$$

Here,  $\chi_{ij}$  = coherence between  $i^{\text{th}}$  and  $j^{\text{th}}$  modal excitations. Substituting Eq. (3.3) into Eq. (2.19) the likelihood function for modal parameters can be arranged as;

$$\begin{aligned} L(\theta) &= NN_f \ln \pi + (N - \bar{m}) N_f S_e + S_e^{-1} \bar{\kappa} + \sum_k \ln \left| \bar{E}_k \right| \\ &\quad + \sum_k \bar{F}_k^* \bar{E}_k^{-1} \bar{F}_k \\ \bar{F}_k &= B^T F_k; \quad \bar{\kappa} = \sum_k \left( F_k^* F_k - \bar{F}_k^* \bar{F}_k \right) \end{aligned} \quad (3.9)$$

subjected to norm constraint,  $B^T B = I_N$ . Eq. (3.9) can be minimized by following a two-stage procedure. Au (2012b) stated that the MPV of spectrum parameters can be determined under the constraint of  $\|\chi_{ij}\| \leq 1$ . To preserve this constraint,  $\chi_{ij}$  can be defined by the following equation (Au, 2012b).



$$\begin{aligned} \chi_{ij} &= \sin(u_{ij}) \times e^{iv_{ij}} \\ u_{ij} &= \sin^{-1}(\|\chi_{ij}\|); \quad v_{ij} = \tan^{-1}(\text{Im}\{\chi_{ij}\} / \text{Re}\{\chi_{ij}\}) \end{aligned} \quad (3.10)$$

In this study, however, it is analytically proved that  $\chi_{ij}$  can be assumed as a real number (see Appendix C). Thus, the coherence can be written according to the free parameter of  $u_{ij}$  without referring to  $v_{ij}$ .

$$\chi_{ij} \approx \sin(u_{ij}) \quad (3.11)$$

At the second step, the mode shape basis,  $B$  can be obtained by minimizing Eq. (3.9). In the conventional Bayesian algorithm by Au (2012b), the equality constraint of  $B^T B = I_N$  is preserved by the hyper-angle representation of  $B$ . Recently, a less time-consuming method by using the Cayley transformation based on the Crank-Nicholson type updating scheme was presented by Zhu et al (2019). According to this scheme,  $B$  is updated as follows (Wen and Yin, 2013).

$$\begin{aligned} B^*(\tau) &= B - \frac{\tau}{2} A [B + B^*(\tau)] \\ A &= GB^T - BG^T \end{aligned} \quad (3.12)$$

where  $\tau$  = step size,  $B^*(\tau)$  = updated value of  $B$ , and  $G$  = the gradient of  $L(\theta)$  with respect to  $B$  (see Appendix B for details).

$$G = \frac{\partial L(\theta)}{\partial B} = -2S_e^{-1} \sum_k \text{Re}(F_k F_k^* B [I_{N_m} - S_e \bar{E}_k^{-1}]) \quad (3.13)$$

Solving Eq. (3.12) for  $B^*(\tau)$  gives

$$B^*(\tau) = \left( I_m + \frac{\tau}{2} A \right)^{-1} \left( I_m - \frac{\tau}{2} A \right) B \quad (3.14)$$

In addition, within a selected band, the number of modal parameters to be identified is obtained as below.

$$\begin{aligned} N_\theta &= \underbrace{N_m}_{\text{frequency}} + \underbrace{N_m}_{\text{damping ratio}} + \underbrace{N_m^2}_{\text{PSD of modal excitation}} + \underbrace{N_m N}_{\text{mode shape coordinate}} + \underbrace{1}_{\text{PSD of prediction error}} \\ &= (N_m + 1)^2 + N_m N + O(N_m^2) \end{aligned} \quad (3.15)$$

### 3.3. Effect of Modelling Error

BAYOMA formulation for well-separated modes assumes that only a single mode is dominant within the selected frequency band. The effects of the remaining modes are

assumed to be very small. Therefore, a single mode system can be modelled in the considered frequency band. If remaining modes have small contributions on the response within the selected band, they might cause an error in the computational procedure. This modelling error needs to be quantified in the analysis process. Au (2017) defines this modelling error as a ratio of the PSD of unmodeled mode(s) to the dominant mode. This ratio can be written as follows when there is only one mode of interest within the selected band.

$$\rho_m = \frac{4\hat{S}_j\hat{\xi}_i^2}{\left(1 - \hat{f}_j^2 / \hat{f}_i^2\right)^2 + 4\hat{\xi}_j^2 \hat{f}_j^2 / \hat{f}_i^2} \quad (3.16)$$

where  $i$  and  $j$  denote the mode of interest and the unmodeled mode, respectively. Eq. (3.16) can be arranged as below in case of small damping ratio.

$$\begin{aligned} \left[ \left(1 - \hat{f}_j^2 / \hat{f}_i^2\right)^2 + 4\hat{\xi}_j^2 \hat{f}_j^2 / \hat{f}_i^2 \right] &\approx \left(1 - \hat{f}_j^2 / \hat{f}_i^2\right)^2 \\ \Rightarrow \rho_m &\cong \frac{4\hat{S}_j\hat{S}_i^{-1}\hat{\xi}_i^2}{\left(1 - \hat{f}_j^2 / \hat{f}_i^2\right)^2} \end{aligned} \quad (3.17)$$

To illustrate the modeling error concept, a simple example is considered. For this purpose, a three degree of freedom system is analytically modelled with the natural frequencies of 1, 3, and 5 Hz, and 1% modal damping ratio. Two different scenarios are considered for modal excitation levels. These are; Scenario I:  $S_1=S_2=S_3=100 \mu\text{g}^2/\text{Hz}$ , and Scenario II:  $S_1=300 \mu\text{g}^2/\text{Hz}$ ,  $S_2=100 \mu\text{g}^2/\text{Hz}$ , and  $S_3=50 \mu\text{g}^2/\text{Hz}$ . In addition, the prediction error is assumed to be zero in order to see the modelling error effect only.

Figure 3.1 presents the SV spectrum of uncoupled modal and total responses obtained for Scenario I and II in frequency domain. It is seen that the spectral density of total response is higher than the individual (uncoupled) modal values. The difference between the total and uncoupled modal responses indicates the modeling error level due to the single mode assumption. In case of uniform modal excitation level for all modes, the spectral density of total response shows an error of about 6 and 14 % for 2<sup>nd</sup> and 3<sup>rd</sup> mode, respectively. In case of non-uniform modal excitation level, however, the increase in the error exceeds to 40% for 3<sup>rd</sup> mode.

A numerical example for a further investigation of the effect of modelling error ratio on the identification quality is presented in Section 3.6.2.

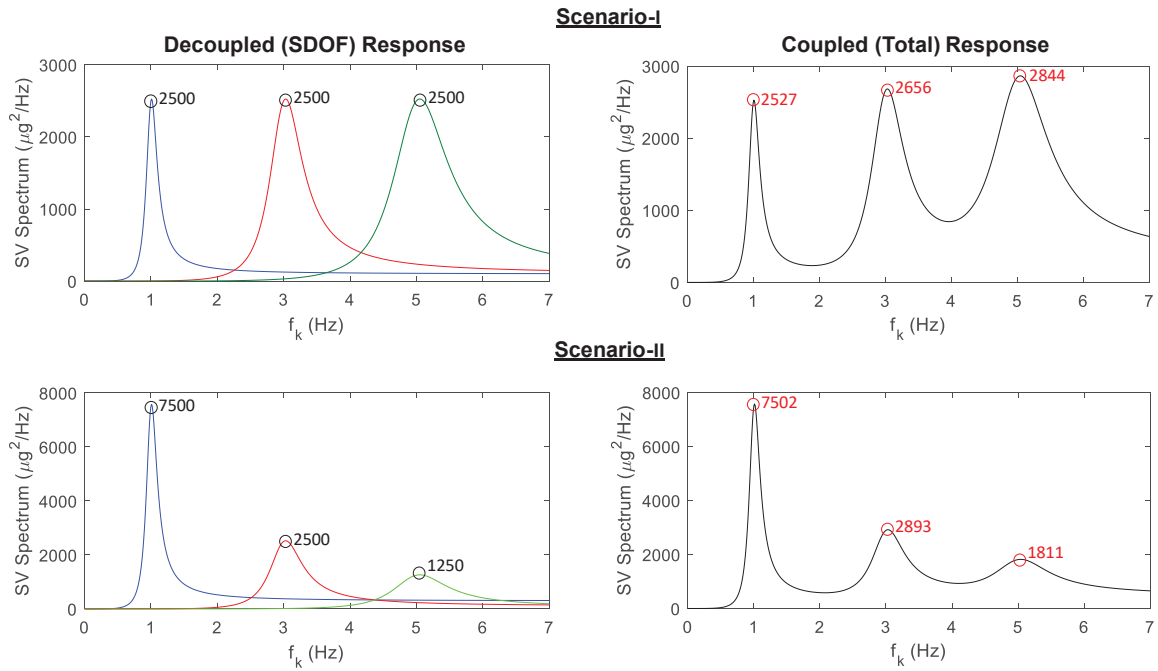


Figure 3.1. Effect of modelling error on the SV spectrum

### 3.4. Buried Mode Case

Modelling error might cause big computational issues when an unmodeled mode is dominant within the select band for the mode of interest. In this case, the response of the mode of interest might not be adequately large and/or cannot be easily perceptible. Figure 3.2 illustrates the burying mode case. Here, it is seen that the mode of interest named as “buried mode” is highly dominated by the burying mode(s) (Zhu et al. 2019).

To overcome this problem, Zhu et al. (2019) presented an algorithm which is a modified form of the procedure for closely spaced modes. In this algorithm, however, only the case of the burying mode being on the left side of the buried mode is considered. In addition, the burying mode should be quite far away from the buried mode. When the buried and buried modes are not enough far away from each other, the problem can also be solved by closely spaced mode algorithm. However, the computational time and posterior uncertainty may increase due to the large bandwidth selection. To overcome this problem, a more general solution for example the case of the burying mode being on the right side and/or on both sides of buried mode can be also modeled by following a similar procedure. For this purpose, a general approach that covers some possible cases is presented in this study. According to this approach, the expected spectral density matrix of the acceleration response is constructed based on the procedure given in Section 3.2.

Here, the transfer function(s) for burying mode(s) are assumed to be initially estimated via the most probable frequency and damping ratios that are determined by using the BAYOMA formulation for single modes.

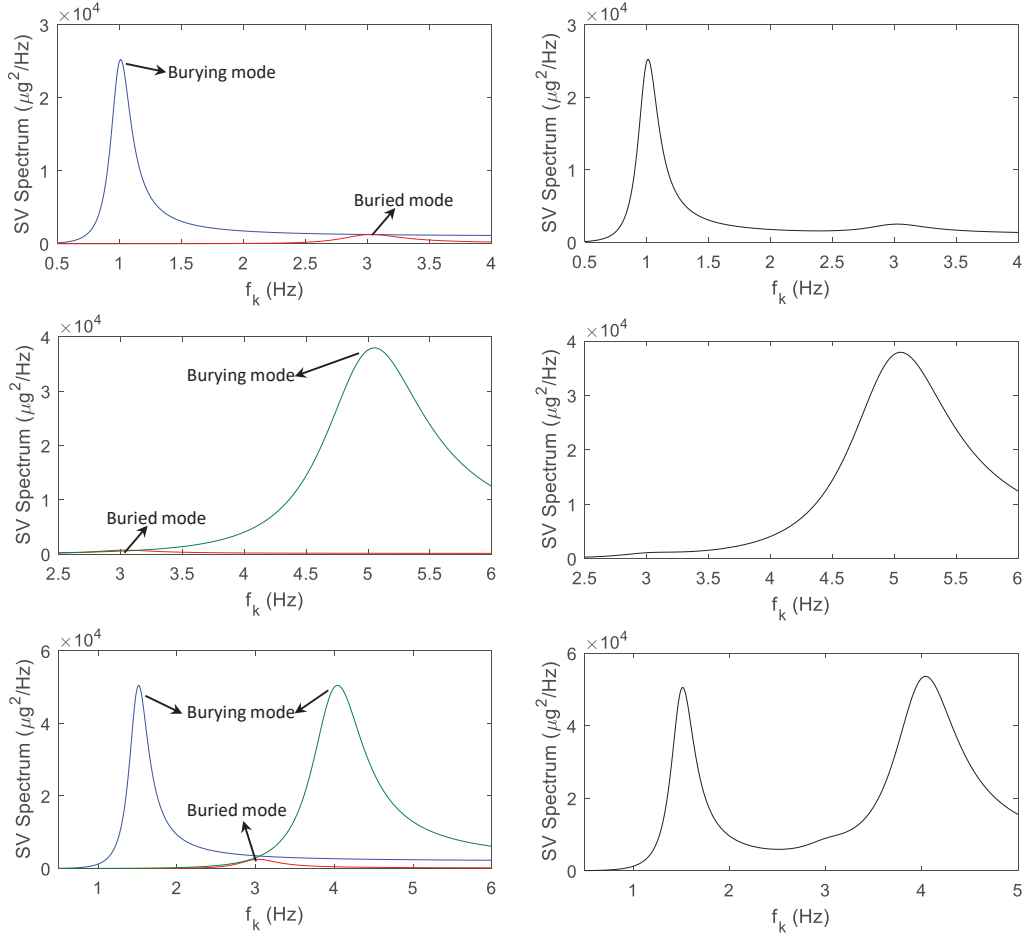


Figure 3.2. Possible scenarios for buried mode case

It can be seen in Eq. (3.2), that the range of the modelling error ratio,  $\rho_m$ , can be as small as zero and may be larger than unity. If the error is close to zero, the single mode identification procedure is used. A buried mode identification approach is necessary, however, for considerably large modelling error ratios. This case will be addressed by using a numerical study in Section 0. For a more general solution, the expected spectral density matrix of the measured response can be written as below.

$$E_k = \Phi \begin{bmatrix} \hat{h}_{ki} & 0 & 0 \\ 0 & h_{kn} & 0 \\ 0 & 0 & \hat{h}_{kj} \end{bmatrix} \begin{bmatrix} S_{ii} & S_{ni} & S_{ji} \\ S_{in} & S_{nn} & S_{jn} \\ S_{ij} & S_{nj} & S_{jj} \end{bmatrix} \begin{bmatrix} \hat{h}_{ki}^* & 0 & 0 \\ 0 & h_{kn}^* & 0 \\ 0 & 0 & \hat{h}_{kj}^* \end{bmatrix} \Phi^T + S_e I_N \quad (3.18)$$

In Eq. (3.18),  $i$  and  $j$  = indices for burying modes,  $n$  denotes the buried mode, and “^” denotes MPV of  $h_{ki}$  and  $h_{kj}$  that are obtained by single mode approach within the resonant frequency band of burying mode. Here, only the spectral densities and mode shapes of

the burying modes need to be determined in addition to the modal parameters of buried mode. Thus, the number of modal parameters to be identified is obtained as;

$$N_{\theta} = \underset{\text{frequency}}{1} + \underset{\text{damping ratio}}{1} + \underset{\text{PSD of modal excitation}}{N_m^2} + \underset{\text{mode shape coordinate}}{N_m N} + \underset{\text{PSD of prediction error}}{1} \quad (3.19)$$

$$= N_m (N_m + N) + 3$$

This approach can be simplified for some special cases in which the burying and buried modes are quite far away from each other (Zhu et al. 2019). These special cases can be classified depending on the location of burying modes.

### 3.4.1. Special Case I: Burying Mode on the Left Side

If it is assumed that only two possible modes are available in the selected frequency band, and the burying mode being on the left side,  $\hat{h}_{kj}$  can be written as;

$$\hat{h}_{ki} = \frac{1}{(1 - \beta_{ki}^2) + i2\zeta_i \beta_{ki}} \approx 1 \quad (3.20)$$

assuming  $\beta_{ki} = f_i/f_k \approx 0$ . Thus, the spectral density matrix within the selected can be written as below.

$$E_k = \Phi \begin{bmatrix} 1 & 0 \\ 0 & h_{kn} \end{bmatrix} \begin{bmatrix} S_{ii} & S_{in} \\ S_{ni} & S_{nn} \end{bmatrix} \begin{bmatrix} 1 & 0 \\ 0 & h_{kn}^* \end{bmatrix} \Phi^T + S_e I_N \quad (3.21)$$

where  $S_{in} = S_{ni}^*$ .

### 3.4.2. Special Case II: Burying Mode on the Right Side

If the burying modes being on the right side of the mode of interest and these modes are quite far away from each other, again two modes will dominate the measured response. In this case, the transfer function can be arranged as below assuming  $\beta_{kj} = f_j/f_k \gg 1$ .

$$h_{kj} = \frac{1}{(1 - \beta_{kj}^2) - i2\zeta_j \beta_{kj}} \approx -\beta_{kj}^{-2} \quad (3.22)$$

Thus, the expected spectral density matrix of the acceleration response can be written as.

$$E_k = \Phi \begin{bmatrix} h_{kn} & 0 \\ 0 & -\beta_{kj}^{-2} \end{bmatrix} \begin{bmatrix} S_{nn} & S_{nj} \\ S_{jn} & S_{jj} \end{bmatrix} \begin{bmatrix} h_{kn}^* & 0 \\ 0 & -\beta_{kj}^{-2} \end{bmatrix} \Phi^T + S_e I_N \quad (3.23)$$

### 3.4.3. Special Case III: Burying Mode on Both Sides

When the possible mode within a selected band is buried by two modes, the three modes, (i) the mode on the left side, (ii) the mode of interest, and (iii) the mode on the right side should be considered in the construction of the expected spectral density matrix. In this case,  $E_k$  is written as below assuming  $\beta_{ki} = f_i/f_k \approx 0$  and  $\beta_{kj} = f_j/f_k \gg 1$ .

$$E_k = \Phi \begin{bmatrix} 1 & 0 & 0 \\ 0 & h_{kn} & 0 \\ 0 & 0 & -\hat{\beta}_{kj}^{-2} \end{bmatrix} \begin{bmatrix} S_{ii} & S_{ni} & S_{ji} \\ S_{in} & S_{nn} & S_{jn} \\ S_{ij} & S_{nj} & S_{jj} \end{bmatrix} \begin{bmatrix} 1 & 0 & 0 \\ 0 & h_{kn}^* & 0 \\ 0 & 0 & -\hat{\beta}_{kj}^{-2} \end{bmatrix} \Phi^T + S_e I_N \quad (3.24)$$

### 3.5. Summary of Procedures

The solution of multiple and buried mode problems can be obtained by following the same computational procedure for closely spaced modes. Here, the number of modal parameters to be identified will only show variance based on the type of problem. The initial guess for frequencies can be set to the excitation frequency at the peak value of singular value spectrum. Damping ratios can be initially chosen as 1% as it is suggested by Au (2012b). Initial guess of  $S$  can be calculated from the corresponding peak value of the singular value spectrum. Au (2012b) suggests the following approach that assumes large signal-to-noise ratio for the initial calculation of  $B$  and  $S_e$ . According to this approach, assuming  $S_{ii}D_{kii}/S_e = S_{jj}D_{kjj}/S_e \approx \infty$  yields

$$S_e B \bar{E}_k^{-1} B^T \approx 0 \Rightarrow |E_k| \approx S_e^{(N-m)}; \quad E_k^{-1} \approx S_e^{-1} (I_N - BB^T) \quad (3.25)$$

Thus, the negative-logarithm likelihood function is obtained as,

$$L(\theta) \approx (N - \bar{m}) N_f S_e + S_e^{-1} \kappa + S_e^{-1} \sum_{i=1}^m B_i^T \Delta B_i \quad (3.26)$$

where

$$\kappa = \sum_k F_k^* F_k; \quad \Delta = \sum_k \text{Re}(F_k F_k^*) \quad (3.27)$$

Thus, the initial guess for  $S_e$  can be obtained as follows by minimizing  $L(\theta)$ .

$$S_e = \frac{\bar{\kappa}}{N_f(N - N_m)} \quad (3.28)$$

$$\bar{\kappa} = \sum_{i=1}^m B_i^T \Delta B_i = \sum_k (F_k^* F_k - F_k^* B^T B F_k)$$

The initial guess for  $B$  can be obtained as the eigenvectors that correspond to the largest  $m$  eigenvalues of  $\Delta$ . Finally, the initial guess for  $\alpha$  can be obtained by a reverse calculation of Eq. (3.5) as below.

$$\alpha = (B^T B)^{-1} B^T \Phi \quad (3.29)$$

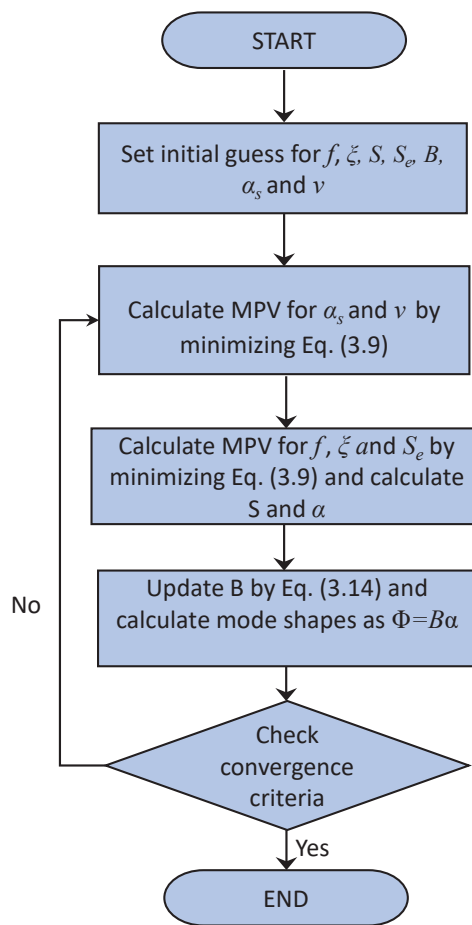


Figure 3.3 Flowchart for the solution procedure of multiple and buried modes

A flowchart for the overall computational procedure is presented in Figure 3.3. The proposed flowchart has a small modification based on the fact that the modelling of coherence,  $\chi_{ij}$ . For buried mode case, different from the closely spaced modes, the frequency and damping values of the burying modes are not considered as the parameters to be identified. These parameters are assumed to be initially estimated and assigned to

the MPVs that are obtained by the single mode approach for the burying modes, separately.

### 3.6. Numerical Analysis

In this section, first, a numerical example is presented to validate proposed modification for closely spaced modes. Second, the effect of modelling error on the parameter estimation quality is investigated. Finally, a numerical example is presented for the considered buried mode cases.

#### 3.6.1. Closely Spaced Modes

A six-story shear frame structure with closely spaced modes is investigated in this section. The natural frequencies of the structure are arranged as 1.00 and 1.03 Hz for first two modes, respectively. Modal damping ratio is set to 1.00 %. Free vibration mode shapes are considered as  $[0.1048, 0.2097, 0.3145, 0.4193, 0.5241, 0.6290]^T$ , and  $[0.3354, 0.5590, 0.4472, 0.1118, -0.2236, -0.5590]^T$  for the first two modes, respectively. Two different *i.i.d.* Gaussian modal excitations are generated with PSD of  $1\mu\text{g}^2/\text{Hz}$ . The acceleration data of each story is acquired in 300 sec duration with 100 Hz sampling frequency. The prediction error for the measured acceleration data is set to have  $1\mu\text{g}^2/\text{Hz}$  spectral density.

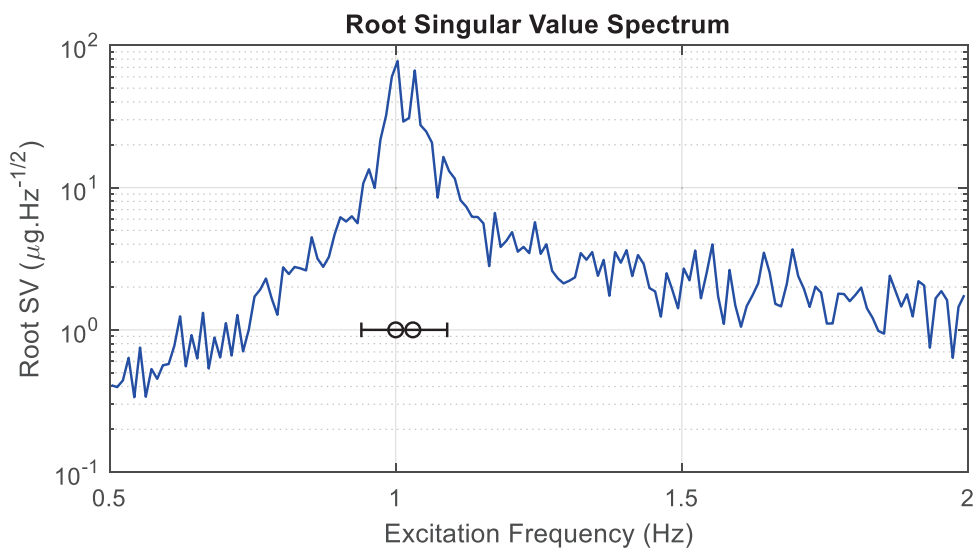


Figure 3.4. Maximum singular value spectrum and selected frequency band



Maximum singular value spectrum of the acceleration response and the selected bandwidth with possible modes are presented in Figure 3.4. Identified mode shapes are presented in Figure 3.5. A reasonable convergence is observed for the mode. In addition, identification results for spectrum parameters are presented in

Table 3.1, 3.2 and 3.3 which show good convergence with the analytical values. Note that this study is based on a single trial with a randomly generated *i.i.d.* Gaussian white noise excitation. The identification uncertainties may undergo variations among different trials.

As a result, the presented modification is verified by the numerical analysis. Hereby, it is shown that the estimation quality is preserved by the proposed modification, while the number of parameters to be identified is reduced.

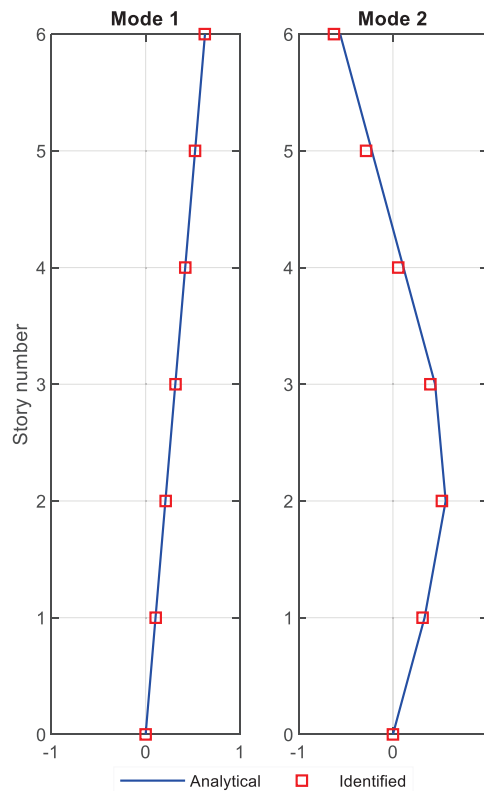


Figure 3.5. Identified mode shapes and their analytical values

Table 3.1. Identified frequencies and damping ratios

<i>Mode number</i>	<i>f (Hz.)</i>			<i>ξ (%)</i>		
	<i>Exact</i>	<i>MPV</i>	<i>c.o.v. (%)</i>	<i>Exact</i>	<i>MPV</i>	<i>c.o.v. (%)</i>
1	1.000	1.002	0.13	1.00	1.08	19.63
2	1.030	1.032	0.18	1.00	1.02	20.71

Table 3.2. PSD of modal excitations and prediction error

<i>Mode number</i>	<i>PSD of modal excitation, <math>S_{ii}</math></i>			<i>PSD of prediction error, <math>S_e</math></i>		
	<i>Exact</i>	<i>MPV</i>	<i>c.o.v. (%)</i>	<i>Exact</i>	<i>MPV</i>	<i>c.o.v. (%)</i>
1	1.00	0.97	44.82	1	1.07	29.46
2	1.00	1.09	49.14			

Table 3.3. Free parameter,  $u_{ij}$  for cross PSD of modal excitation

<i>Exact</i>	<i>MPV</i>	<i>c.o.v. (%)</i>
-0.1297	-0.1579	43.25

### 3.6.2. Effect of Modelling Error

In this section, the six-story structure that is given in the previous numerical example is investigated again by a small modification to show the effect of modelling error on the identification quality. Different from the previous example, the fundamental frequencies for first two modes are considered as  $f_1 = 1$  Hz,  $f_2 = 3$  Hz. The spectral density of modal excitation for the first mode is taken as  $S_1 = 1.00 \mu\text{g}^2/\text{Hz}$ . The spectral density of modal excitation of the second mode is arranged in ascending order so that the modelling error ratio is between  $\rho_m = 0$  and  $\rho_m = 1$ .

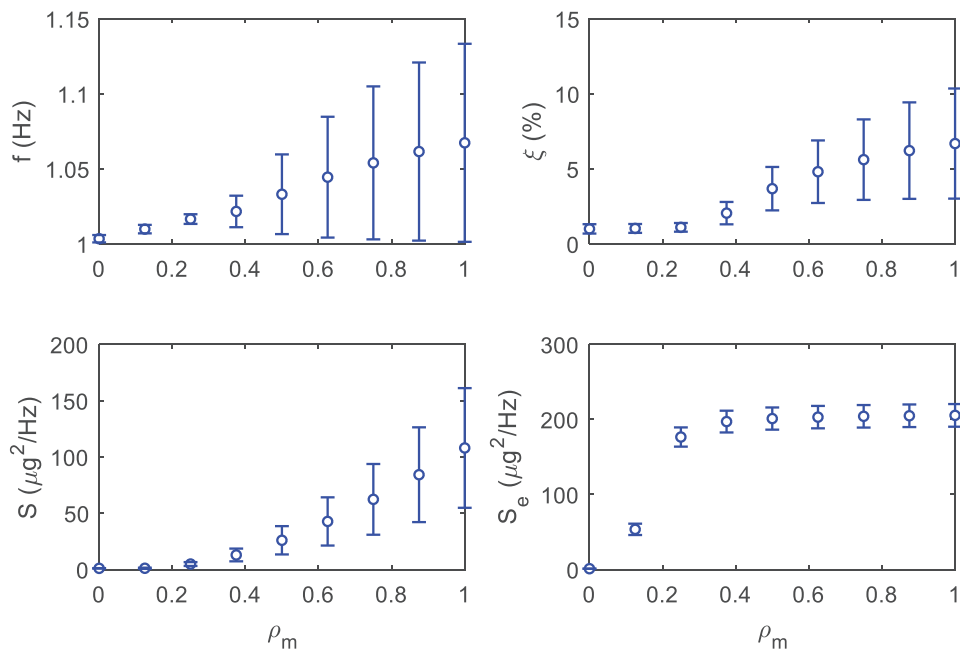


Figure 3.6. Variations in identified modal parameters versus modelling error ratio (with  $\pm$  standard deviations)

Figure 3.6 presents the identified MPV of modal parameters and their posterior standard deviations with respect to the modelling error ratio. Additionally, the MAC values between the identified mode shapes and their analytical values are presented in Figure 3.7. The MAC values are not acceptable for modelling error ratios larger than 0.1. Therefore, it is not reasonable to apply the single mode approximation for the mode of interest. To improve the identification quality, it is suggested to investigate the corresponding mode by the burying mode approach when  $\rho_m > 0.1$ .

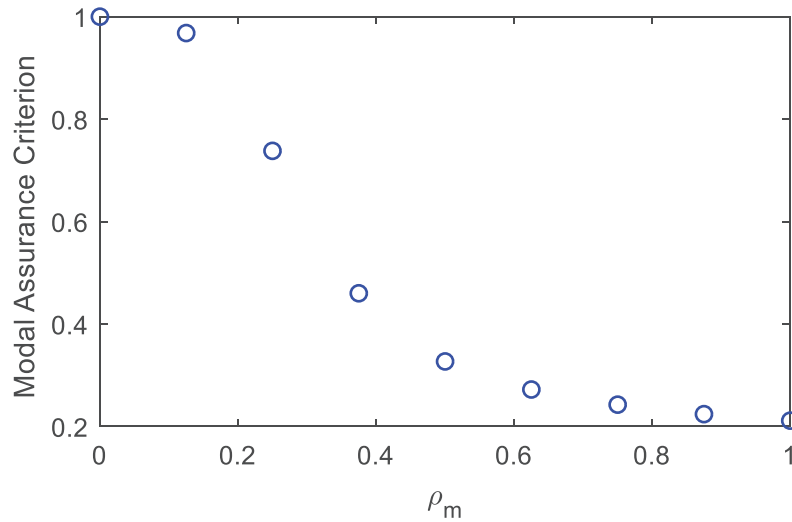


Figure 3.7. Variations in MAC values with respect to the modelling error ratio

### 3.6.3. Buried Mode Case

Again, a six-story shear frame is considered in this example. The first three natural frequencies and damping ratios of the structure is considered as  $f_1=1.00$  Hz,  $f_2=3.00$  Hz and  $f_3=5.00$  Hz,  $\zeta_1=\zeta_2=\zeta_3=1\%$  for the first three modes. The free vibration mode shapes are considered as  $\varphi_1 = [0.1048, 0.2097, 0.3145, 0.4193, 0.5241, 0.6290]^T$ ,  $\varphi_2 = [0.3354, 0.5590, 0.4472, 0.1118, -0.2236, -0.5590]^T$ , and  $\varphi_3 = [0.4170, 0.6255, 0.2085, -0.4170, -0.2085, 0.4170]^T$ . Three different cases are considered: (i) Case-I: burying mode on the left side, (ii) Case-II: burying mode on the right side, (iii) burying modes on both sides. The structure is subjected to *i.i.d.* Gaussian excitations with modal PSD of  $500 \mu g^2/Hz$  for burying modes, and  $1 \mu g^2/Hz$  for buried modes, respectively, for all cases. Similarly, the measured acceleration responses are considered to have a prediction error with  $1 \mu g^2/Hz$ . The maximum singular value spectrums of the acceleration responses are presented below for Case-I, II and III (see Figure 3.8).

Identified fundamental frequencies and damping ratios for burying modes are presented in Table 3.4. Here, the modal parameters of buried modes are obtained by the BFFTA algorithm for well separated modes. At the next step, the modal properties of the buried mode are identified by using the presented algorithm for buried mode case. Identified results for burying and buried modes case are presented in Table 3.4 and Table 3.5. It is seen that the identified parameters well match with the analytical values.

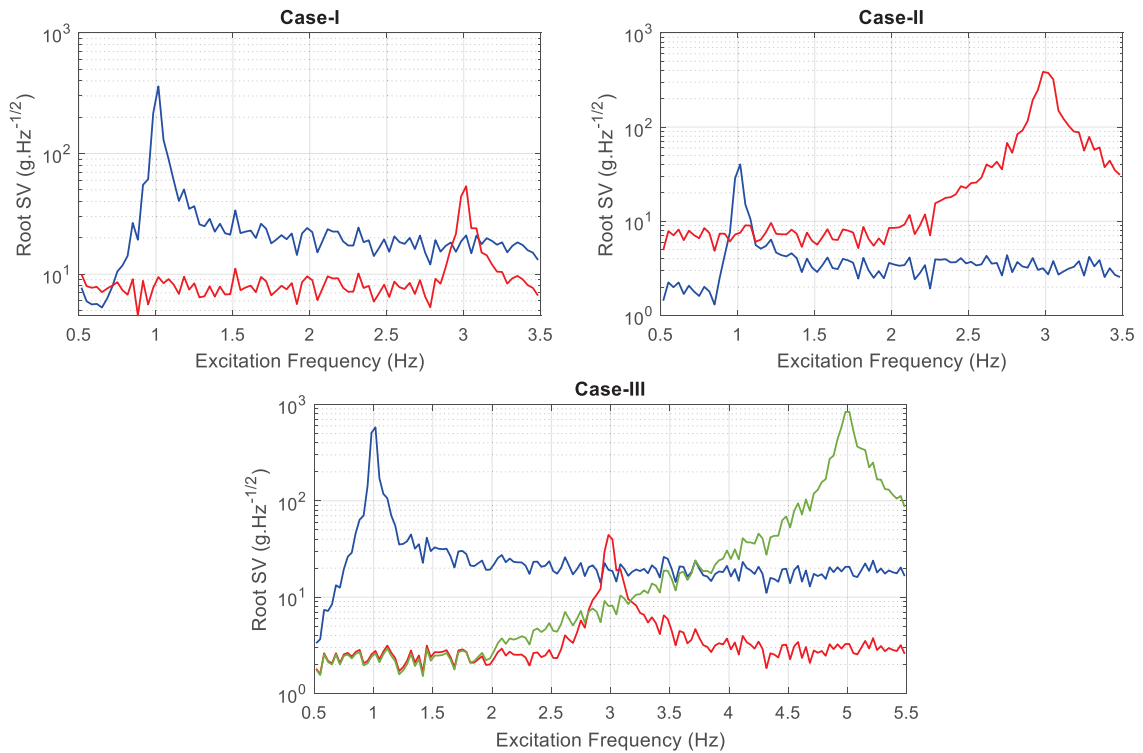


Figure 3.8. Identified mode shapes and their analytical values for Case-I, II and III

Table 3.4. Identified frequencies and damping ratios for burying modes

<i>Burying mode location</i>	<i>Case-I</i>		<i>Case-II</i>		<i>Case-III</i>	
	<i>f (Hz)</i>	<i>ξ (%)</i>	<i>f (Hz)</i>	<i>ξ (%)</i>	<i>f (Hz)</i>	<i>ξ (%)</i>
Left side	1.0015	1.0124	-	-	1.0126	0.9913
Right side	-	-	2.9998	1.0236	5.0183	0.9896

Table 3.5. Identified modal parameters for buried modes

<i>Case</i>	$f$ (Hz)	<i>c.o.v.</i> (%)	$\xi$ (%)	<i>c.o.v.</i> (%)	$S$ ( $\mu\text{g}^2/\text{Hz}$ )	<i>c.o.v.</i> (%)	$S_e$ ( $\mu\text{g}^2/\text{Hz}$ )	<i>c.o.v.</i> (%)
I	2.9956	0.18	1.02	32.74	1.18	66.25	1.21	33.48
II	1.0126	0.22	0.97	29.26	1.18	62.36	1.32	38.66
III	3.0216	0.36	1.03	41.42	1.23	71.21	1.56	45.29

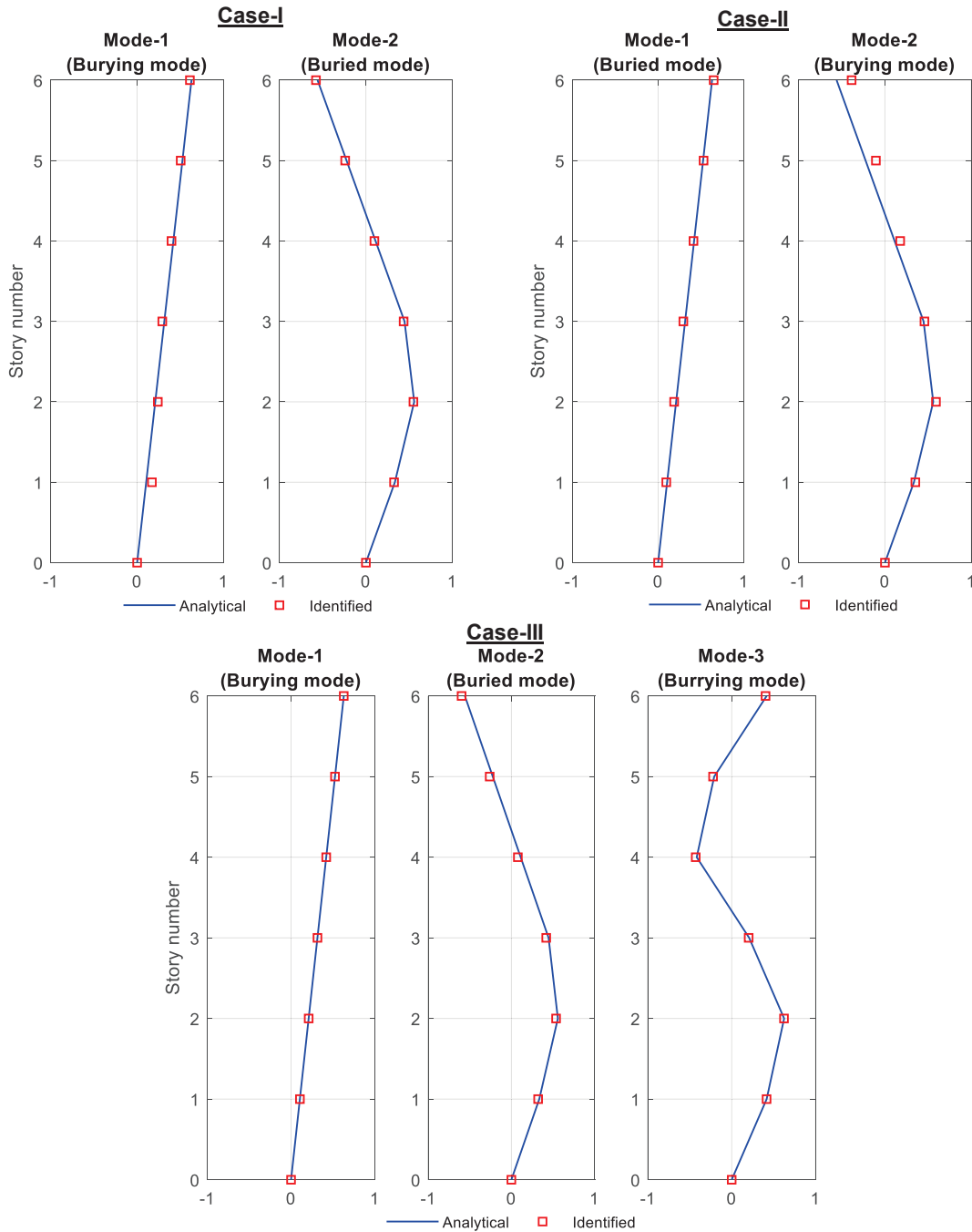


Figure 3.9. Identified mode shapes and their analytical values for Case-I, II and III

Figure 3.9 presents the identified mode shapes and their analytical values. Here, identified mode shapes for burying modes denote the MPVs within the dominant frequency band for buried mode. Note that the modelling error is calculated as 0.158 for all cases. The identified mode shapes for buried modes show good convergence to the analytical values for Case-I, II and III.

### 3.7. Concluding Remarks

This chapter investigates some computational issues in BAYOMA which have been reported previously in the literature. First, the solution procedure that was previously proposed in the literature for the multiple (closely spaced) mode problem is investigated. Here, a small modification is proposed for the computational procedure to decrease the number of parameters to be identified in the analysis. Second, the effect of modelling error on the identification quality is investigated. Finally, the buried mode case is investigated, and a generalized solution is proposed. The analytical derivation of the posterior covariance for multiple mode case is available in the literature (Au 2012c). In this study, similarly, the posterior covariance matrix is obtained by using the fast calculation scheme proposed by Au and Xie (2017). In this calculation, different from Au (2012c), the derivatives of the likelihood function are obtained by reformulation of the expected spectral density matrix of modal excitation (see Appendix C). In addition, the dimension of the Hessian matrix is less than the conventional approach due to the reduced number of modal parameters to be identified.

- It is analytically proven that the coherence between the  $i^{th}$  and  $j^{th}$  modal excitation can be assumed as a real number. Therefore, the free parameter of  $v_{ij}$  becomes unnecessary, and this modification reduces the number of parameters to be updated during the iterations as well as the computational time and effort.
- As it is reported in the literature larger modelling errors makes the single mode assumption unreasonable within the selected frequency band. According to the results of this study, the buried mode case should be considered when the modelling error ratio is significantly large ( $\rho_m > 0.1$ ).
- In the literature, a special case in which the burying mode is located on the left side of the buried mode has been investigated. This study proposes a generalized methodology in which the modal parameters of burying modes are assumed as

partially known. Numerical results show that the proposed procedure gives reasonable results with respect to various scenarios for the location of burying modes.

## CHAPTER 4

# TWO-STAGE BAYESIAN MODE SHAPE ASSEMBLY TECHNIQUE FOR MULTIPLE SETUPS

### 4.1. Introduction

In large scale structures, monitoring of the change in modal parameters has a direct effect to make decisions after extreme events (such as earthquakes, tornadoes, etc.). For this reason, a full scaled monitoring of change in modal parameters becomes necessary. In the literature, it is known that the modal parameter estimation process in large scaled structures requires more computational effort due to the insufficient number of measurement instruments (such as accelerometer, data acquisition devices). This case makes it necessary to use multiple measurement setups in the identification process. Even though the natural frequencies and damping ratios can be obtained via the individual setups, obtaining the global mode shape that covers the all measurement setups arises as an issue. Essentially, there are two different methods in the literature to obtain the global mode shape vector; *(i)* Pre-identification, and *(ii)* Post identification methods. Pre-identification methods are based on various scaling processes for FFTs to obtain a full set of synchronous measured data. In case of constant reference sensor (or sensors) and large signal-to-noise ratio, pre-identification methods are capable of obtaining the global mode shapes with an acceptable accuracy. However, the convergence of those methods reduces in case of roving sensors and/or relatively low signal levels due to the accumulated errors in scaling procedure (Döhler et al. 2011).

Post identification methods are based on the assembly of local mode shapes that are identified in individual setups or direct estimation of global mode shapes incorporated by multiple setups. Here, the local least square approach comes forward as the most conventional one, but the results are highly sensitive to sensor configuration and estimation quality of local mode shapes. More efficient methods have been presented in the current decade for global mode shape assembly or estimation. Au (2011b) presented the Global Least Square Approach for the assembly of local mode shapes with an iterative algorithm. This iterative algorithm is based on the minimization of the equally weighted



discrepancies between the local part of global mode shape and identified local mode shape. In addition, some probabilistic approaches for mode shape assembly have also been developed based on the Bayesian inference. These methods are capable of identifying not only the global mode shapes but also their posterior uncertainties. There are two different approaches in the literature for Bayesian mode shape assembly. First, Au and Zhang (2012) presented a Bayesian approach for direct estimation of global mode shape vector and local spectrum variables incorporating the multiple measurement setups. Au (2017) modified the original algorithm that was presented by Au and Zhang (2012) and proposed a simplified iterative algorithm. In addition, a different Bayesian technique was presented by Yan and Katafygiotis (2015b) that is motivated by the Global Least Square Approach. Their approach is based on the assembling local mode shapes that are weighted by their posterior covariance matrices for local mode shapes at individual setups.

The available Bayesian global mode shape identification methods (Au and Zhang, 2012; Au, 2017; Yan and Katafygiotis, 2015b) are motivated from different approaches (BFFTA and BSDA) and follow different ways to estimate the most probable global mode shape. The basic motivation of this chapter is to develop an alternative mode shape assembly algorithm which results in same eigenvalue equations (for global mode shapes) that can be obtained by the aforementioned procedures. For this purpose, first, the two-stage BFFTA by Au (2017) for single setup problems with well separated modes is adopted to multiple setups and a modified likelihood function for the global mode shape is derived. Second, the same solution is obtained by the Gaussian approximation for the most probable local mode shape vector. Finally, the weights of individual setups in the most probable global mode shape vector is obtained by using the expansion of Hessian matrix for local mode shapes. The final form of the proposed procedure does not need to identify local mode shapes separately. Instead, it utilizes the statistical information of Hessian matrix of the local mode shapes which can be derived by using only the local spectrum variables and FFT of measured data. According to the obtained results, it is seen that the proposed algorithm results in higher convergence speed when compared to the available BFFTA algorithm.

## 4.2. Non-Bayesian Methods

Non-Bayesian mode shape assembly methods are based on scaling procedures for mode shapes in order to obtain the best fit between the reference DOF. Most conventional one is Local Least Square Approach in which all mode shapes are scaled with respect to a selected reference setup. Au (2011b) presented a Global Least Squares Approach which promises less computational effort and error when compared to the local least squares approach. In this section, a revisit for least squares approaches is presented.

### 4.2.1. Local Least Squares Approach

The local least square approach is conventionally used in modal identification with multiple setups. The method is based on the scaling of mode shape coordinates at reference DOFs among different measurement setups. For this purpose, a least squares estimation is applied to determine the scaling factor for the measurement group to be transformed to a selected reference group. This least square estimation can be obtained as below.

$$J(c_{ji}) = (\varphi_i - c_{ji}\varphi_j)^T (\varphi_i - c_{ji}\varphi_j) \quad (4.1)$$

in which  $\varphi_i, \varphi_j$  = coordinates of local mode shape vectors at reference measurement points which belong to the  $i^{th}$  and  $j^{th}$  groups,  $c_{ji}$  = scaling factor between the groups  $i$  and  $j$ .  $\varphi_i, \varphi_j$  will be scalars if there is only a single reference point between the setups  $i$  and  $j$ . In explicit form, Eq. (2.1) can be rewritten as

$$J(c_{ji}) = \varphi_i^T \varphi_j - c_{ji} \varphi_i^T \varphi_j + c_{ji}^2 \varphi_j^T \varphi_j \quad (4.2)$$

Taking the first order derivative of Eq. (4.2) with respect to  $c_{ji}$  gives the optimal value of  $c_{ji}$  as follows.

$$\frac{\partial J}{\partial c_{ji}} = -2c_{ji}\varphi_i^T \varphi_j + 2c_{ji}\varphi_j^T \varphi_j = 0 \quad \Rightarrow c_{ji} = \frac{\varphi_i^T \varphi_j}{\varphi_j^T \varphi_j} \quad (4.3)$$

The local mode shapes identified in each group are scaled by the optimal  $c_{ji}$ . Finally, the global mode shape vector is assembled from the scaled local mode shapes. When the measurement groups have common reference sensors, this method generally gives reasonable results if the data quality is good for each setup. However, the results may be unreasonable in case of roving reference sensors among different setups. The

reason of this fact may be caused by the accumulated error in the scaling process from one group to another.

## 4.2.2. Global Least Squares Approach

A global least square approach is presented by Au (2011b) to mitigate the possible errors in the conventional local least square approach. In the global least square approach, the relative error (discrepancy) between local mode shapes that are identified in each group and the corresponding part of the global mode shape vector is minimized by the least square estimation given in Eq. (4.4).

$$J(\mathbf{L}_i\Phi, \alpha_i) = (\Gamma_i\Phi - r_i\hat{\phi}_i)^T (\Gamma_i\Phi - r_i\hat{\phi}_i) + \alpha_i (\Phi^T \Gamma_i^T \Gamma_i \Phi - r_i^2) \quad (4.4)$$

The least square estimation given in Eq. (4.4) is obtained for  $i^{th}$  measurement group. Here,  $\Phi$  denotes the  $N \times 1$  global mode shape vector ( $N = \#$  of total measured DOFs),  $\hat{\phi}_i$  is  $N_i \times 1$  size identified (MPV) local mode shape vector with unit Euclidian norm ( $N_i = \#$  of measured DOFs at each group), and  $r_i$  is the norm of the local part of global mode shape vector. In addition,  $\Gamma_i$  denotes a  $N_i \times N$  selection matrix for  $i^{th}$  group. Selection matrix comprises the information of local measurement points versus total measured DOF. For example, when  $N=5$ ,  $N_i=3$ , and only the first, second and fifth DOFs are measured in  $i^{th}$  group, the selection matrix is written as

$$\Gamma_i = \begin{bmatrix} 1 & 0 & 0 & 0 & 0 \\ 0 & 1 & 0 & 0 & 0 \\ 0 & 0 & 0 & 0 & 1 \end{bmatrix} \quad (4.5)$$

Hence, the local part of the global mode shape vector and its norm at  $i^{th}$  group is obtained as

$$\begin{aligned} \Phi_i &= \Gamma_i \Phi \\ r_i &= \pm \|\Phi_i\| = \pm (\Phi^T \Gamma_i^T \Gamma_i \Phi)^{1/2} \end{aligned} \quad (4.6)$$

In addition,  $\alpha_i$  denotes the Lagrange multiplier that enforces the norm of the local mode shape to be equal to  $r_i$  in Eq. (4.6). Thus, the first order derivative of Eq. (4.4) with respect to  $\alpha_i$  gives,

$$\begin{aligned} \left. \frac{\partial J_i}{\partial r_i} \right|_{\alpha_i = \hat{\alpha}_i} &= -2\Phi^T \Gamma_i^T \hat{\phi}_i \pm 2r_i \hat{\phi}_i^T \hat{\phi}_i \pm 2\alpha_i r_i = 0 \\ \Rightarrow \hat{\alpha}_i &= \pm r_i^{-1} \Phi^T \Gamma_i^T \hat{\phi}_i - 1 \end{aligned} \quad (4.7)$$

At the MPV of  $\alpha_i$ , the second order derivative of Eq. (4.7) with respect to  $r_i$  should be larger than zero.

$$\begin{aligned} \left. \frac{\partial^2 J_i}{\partial r_i^2} \right|_{\alpha_i = \hat{\alpha}_i} &= 2\hat{\phi}_i^T \hat{\phi}_i + 2\alpha_i > 0 \Rightarrow \alpha_i > -1 \\ \Rightarrow (\pm r_i^{-1} \Phi^T \Gamma_i^T \hat{\phi}_i - 1) > -1 &\Rightarrow \pm r_i^{-1} \Phi^T \Gamma_i^T \hat{\phi}_i > 0 \end{aligned} \quad (4.8)$$

Thus, the optimal  $r_i$  can be determined as follows.

$$\hat{r}_i = \text{sgn}(\Phi^T \Gamma_i^T \hat{\phi}_i) \|\Gamma_i^T \Phi\| \quad (4.9)$$

where “sgn(.)” denotes the signum function. Since, the local mode shapes are considered as statistically independent parameters, the objective function that covers all setups can be written as below.

$$J(\Phi, \beta) = \sum_{i=1}^{N_s} (\Gamma_i \Phi - r_i \hat{\phi}_i)^T (\Gamma_i \Phi - \hat{r}_i \hat{\phi}_i) + \sum_{i=1}^{N_s} \alpha_i (\Phi^T \Gamma_i^T \Gamma_i \Phi - r_i^2) + \beta (1 - \Phi^T \Phi) \quad (4.10)$$

where  $\beta$  and  $N_s$  denotes the Lagrange multiplier that enforces the unit norm of global mode shape vector, and number of setups, respectively. Minimizing Eq. (4.10) with respect to  $\Phi$  gives,

$$\begin{aligned} \sum_{i=1}^{N_s} (2\Phi^T \Gamma_i^T \Gamma_i - 2\hat{r}_i \hat{\phi}_i^T \Gamma_i + 2\hat{\alpha}_i \Phi^T \Gamma_i^T \Gamma_i) - 2\beta \Phi^T &= 0 \\ \Rightarrow A\Phi + b = \beta\Phi \end{aligned} \quad (4.11)$$

in which;

$$A = \left[ \sum_{i=1}^{N_s} \Gamma_i^T (1 + \alpha_i) \Gamma_i \right]; \quad b = \left[ \sum_{i=1}^{N_s} -r_i \Gamma_i^T \hat{\phi}_i \right] \quad (4.12)$$

Eq. (4.11) is a constrained eigenvalue problem and can be solved by using the following augmented matrix (Au, 2011b).

$$D = \begin{bmatrix} A & bb^T \\ I_N & A^T \end{bmatrix} \quad (4.13)$$

The global mode shape vector can be obtained as the lower  $N \times 1$  part of the eigenvector that corresponds to its minimum eigenvalue. It is seen that the solution of Eq. (4.13) requires an iterative procedure. To reduce the computational effort, an initial guess for global mode shape vector can be obtained by assuming that the partial mode shape is perfectly coherent with identified mode shape.

$$r_i = \hat{\phi}_i^T \Gamma_i \Phi \quad (4.14)$$

Thus, the Lagrange multiplier,  $\alpha_i$  will be equal to zero, and the vector of  $b$  can be written as below.

$$b = \left[ \sum_{i=1}^{N_s} -\Gamma_i^T \hat{\phi}_i \hat{\phi}_i^T \Gamma_i \right] \quad (4.15)$$

Substituting Eq. (4.15) into Eq. (4.11) leads to

$$\left[ \sum_{i=1}^{N_s} \Gamma_i^T (I_{N_i} - \hat{\phi}_i \hat{\phi}_i^T) \Gamma_i \right] \Phi = \beta \Phi \quad (4.16)$$

The initial guess for the global mode shape vector can be obtained as the eigenvector that corresponds to the minimum eigenvalue of the following matrix. Overall computational procedure for global least squares approach is presented in Table 4.1.

$$\sum_{i=1}^{N_s} \Gamma_i^T (I_{N_i} - \hat{\phi}_i \hat{\phi}_i^T) \Gamma_i \quad (4.17)$$

Table 4.1. Iterative algorithm for the global least square approach

Step 1: Set the initial guess for $\Phi$ by using Eq. (4.17)
Step 2: Determine $r_i$ and $\alpha_i$ by using Eqs. (4.6) and (4.7)
Step 3: Determine $\Phi$ by using Eq. (4.13)
Repeat Step 2 to 3 until convergence is reached

### 4.3. Bayesian Methods

The most probable value of the global mode shape vector from multiple setups can be estimated by a Bayesian Probabilistic Framework. In the literature, two different iterative methods are available: (i) Bayesian global mode shape estimation technique proposed by Au (2017), and (ii) Bayesian approach for mode shape assembly proposed by Yan and Katafygiotis (2015b).

#### 4.3.1. Bayesian Global Mode Shape Identification Technique

Bayesian probabilistic approach for global mode shape estimation is first proposed by Au and Zhang (2012) as an iterative algorithm and modified by Au (2017). Based on the statistical properties of FFT of the measured acceleration data, the

conditional probability density function for the set of modal parameters in an individual setup,  $i$ , can be written as follows by using the Bayesian Inference.

$$p(\theta_i | Z_{ki}) = \frac{p(Z_{ki} | \theta_i) p(\theta_i)}{p(Z_{ki})} \quad (4.18)$$

Here,  $\theta_i = [f_i, \zeta_i, \bar{S}_i, S_{ei}, \varphi_i]$ , is the set of modal parameters to be identified and comprises the natural frequency, damping ratio, spectral density of modal excitation that is scaled with respect to the unit norm for local mode shape, spectral density of prediction error, and local mode shape vector (with unit norm) at  $i^{th}$  setup, respectively. Here, the local mode shape corresponds to the measured DOF at  $i^{th}$  setup. In addition,  $Z_{ki} = [\text{Re}(F_{ki}); \text{Im}(F_{ki})] \in \mathfrak{R}$  denotes the augmented FFT vector of the measured response at the  $i^{th}$  setup. In case of non-informative prior distribution for  $p(\theta_i)$ ,  $p(\theta_i | Z_{ki})$  can be assumed to be proportional to  $p(Z_{ki} | \theta_i)$ . With a large amount of measured data,  $p(\theta_i | Z_{ki})$  follows a zero mean Gaussian distribution (Au and Zhang, 2012).

$$p(\theta_i | Z_{ki}) \propto (2\pi)^{-N_i} |C_{\theta_i}|^{-1} \exp\left(-\frac{1}{2} Z_{ki}^T C_{\theta_i}^{-1} Z_{ki}\right) \quad (4.19)$$

where  $N_i = \#$  of measured DOF,  $C_{\theta_i} =$  expected value of the covariance matrix,  $E[Z_{ki} Z_{ki}^T]$ .

$$E[Z_{ki} Z_{ki}^T] = \frac{1}{2} \begin{bmatrix} E[\text{Re}(F_{ki} F_{ki}^*)] & 0 \\ 0 & E[\text{Re}(F_{ki} F_{ki}^*)] \end{bmatrix} \quad (4.20)$$

In addition,  $F_{ki} =$  FFT of acceleration response,  $N_{fi} = \#$  of data within the selected frequency band,  $\bar{S}_i =$  scaled PSD of modal excitation, and  $S_{ei} =$  expected PSD of prediction error in the dominant frequency band at  $i^{th}$  setup, respectively. The expected PSD of measured response,  $E_k$ , is written as below.

$$E_k = E[\text{Re}(F_{ki} F_{ki}^*)] = \bar{S}_i D_{ki} \varphi_i \varphi_i^T + S_{ei} I_{N_i}; \quad \bar{S}_i = r_i^2 S_i; \quad r_i = \pm \|\psi_i\|; \quad \psi_i = r_i \varphi_i \quad (4.21)$$

where  $[\cdot]^* =$  conjugate transpose,  $\|\cdot\| =$  Euclidian norm,  $F_{ki} =$  FFT of measured response at  $i^{th}$  setup,  $S_i =$  spectral density of modal excitation that is scaled with respect to the unit norm of global mode shape vector,  $\psi_i =$  local mode shape with norm of  $r_i$ , and  $I_{N_i} = N_i \times N_i$  size identity matrix. In addition,  $D_{ki}$  is written as below.

$$D_{ki} = \left[ (1 - \beta_{ki}^2)^2 + (2\zeta_i \beta_{ki})^2 \right]^{-1}; \quad \beta_{ki} = f_i / f_k \quad (4.22)$$

Thus, the negative log-likelihood function for the  $i^{th}$  setup can be written as below.

$$L_i(\theta_i) = N_i N_{fi} \ln \pi + (N_{fi} - 1) \ln S_{ei} + \sum_k \ln(\bar{S}_i D_{ki} + S_{ei}) + S_{ei}^{-1} \kappa_i - \varphi_i^T \Delta_i \varphi_i \quad (4.23)$$

where

$$\kappa_i = \sum_k F_{ki}^* F_{ki}; \quad \Delta_i = \sum_k \frac{\bar{S}_i D_{ki} S_{ei}^{-1}}{(\bar{S}_i D_{ki} + S_{ei})} \text{Re}(F_{ki} F_{ki}^*) \quad (4.24)$$

The local mode shapes identified in each setup are linearly independent (Au, 2017). Therefore, the objective function for  $\Phi$  can be written as below by using Eq. (4.23).

$$J(\Phi, \alpha, \beta) = \sum_{i=1}^{N_s} \left[ N_i N_{fi} \ln \pi + (N_{fi} - 1) \ln S_e + \sum_k \ln(\bar{S}_i D_{ki} + S_{ei}) \right] \\ + \sum_{i=1}^{N_s} \left[ S_e^{-1} \kappa_i - r_i^2 \Phi^T \Gamma_i^T \Delta_i \Gamma_i \Phi + \alpha_i (\Gamma_i^T \Phi^T \Gamma_i \Phi - r_i^2) \right] + \beta (1 - \Phi^T \Phi) \quad (4.25)$$

Taking the first order derivative of Eq. (4.25) with respect to  $r_i$  gives (Au, 2017)

$$\hat{\alpha}_i = \frac{\Phi^T \Gamma_i^T \Delta_i \Gamma_i \Phi}{S_e r_i^4} \quad (4.26)$$

Taking the first order derivative of Eq. (4.25) with respect to  $\Phi$  results in a standard eigenvalue-eigenvector problem as follows.

$$B\Phi = \beta\Phi \\ B = \sum_{i=1}^{N_s} \hat{\alpha}_i L_i^T L_i - A; \quad A = r_i^{-2} L_i^T \Delta_i L_i \quad (4.27)$$

In case of large  $snr$ ,  $\bar{S}_i$  and  $S_{ei}$  can be obtained in same manner as it is explained in Chapter 2.

$$\frac{\bar{S}_i D_{ki}}{(\bar{S}_i D_{ki} + S_{ei})} \cong 1 - \frac{S_{ei}}{\bar{S}_i D_{ki}} \quad (4.28)$$

$$S_{ei} \cong \frac{\kappa_i - \lambda_i}{(N_i - 1) N_{fi}}; \quad \bar{S}_i \cong \sum_k \lambda_{ki} D_{ki}^{-1} \quad (4.29)$$

where

$$\lambda_{ki} = \frac{\Phi^T \Gamma_i^T \Delta_{ki} \Gamma_i \Phi}{\Phi^T \Gamma_i^T \Gamma_i \Phi}; \quad \lambda_i = \sum_k \lambda_{ki}; \quad \Delta_{ki} \approx \text{Re}(F_k F_k^*) \quad (4.30)$$

Substituting Eqs. (4.28) and (4.29) into Eq. (4.25) and taking the first order derivative with respect to  $\Phi$  leads to the following eigenvalue problem

$$A_0 \Phi = \beta \Phi \\ A_0 = \left[ \sum_{i=1}^{N_s} \Gamma_i^T \left( \sum_k F_{ki} F_{ki}^* - \bar{\lambda}_i \right) \Gamma_i \right]; \quad \bar{\lambda}_i = \max \left[ \text{eig}(F_{ki} F_{ki}^*) \right] \quad (4.31)$$

The high  $snr$  can be used for the initial guess of spectral parameters and global shape vector (Au, 2017).

### 4.3.2. Bayesian Mode Shape Assembly

A Bayesian mode shape assembly method that is motivated from the global least squares approach is presented by Yan and Katafygiotis (2015b). The negative log-likelihood function can be written by Gaussian Approximation as follows.

$$L_i(\varphi_i) = -\ln[p(\varphi_i|Z_{ki})] \propto \frac{1}{2}(\varphi_i - \hat{\varphi}_i)^T C_{\hat{\varphi}_i}^{-1}(\varphi_i - \hat{\varphi}_i) \quad (4.32)$$

where higher order terms can be neglected since the third and higher order derivatives of  $L_i(\hat{\varphi}_i)$  will be equal to zero. Once the MPV of spectral parameters are determined, the objective function can be written to depend on the global mode shape only.

$$J(\Phi, \chi, a, \beta) = \frac{1}{2} \sum_{i=1}^{N_s} (\chi_i \Gamma_i \Phi - \hat{\varphi}_i)^T C_{\hat{\varphi}_i}^{-1} (\chi_i \Gamma_i \Phi - \hat{\varphi}_i) + \sum_{i=1}^{N_s} \alpha_i (\chi_i^2 \Phi^T \Gamma_i^T \Gamma_i \Phi - 1) + \beta (1 - \Phi^T \Phi) \quad (4.33)$$

in which  $\chi_i^{-1} = \pm \|\Gamma_i \Phi\|$ , and  $\alpha_i, \beta$  are the Lagrange multipliers. In addition,  $C_{\hat{\varphi}_i}$  denotes the posterior covariance matrix for  $\hat{\varphi}_i$ . Taking the first order derivative of Eq. (4.33) with respect to  $\chi_i$  and solving for  $\alpha_i$  gives

$$\hat{\alpha}_i = \frac{\Phi^T \Gamma_i^T C_{\hat{\varphi}_i}^{-1} \Gamma_i \Phi}{2\Phi^T \Gamma_i^T \Gamma_i \Phi} \pm \frac{\hat{\varphi}_i^T C_{\hat{\varphi}_i}^{-1} \Gamma_i \Phi}{2\Phi^T \Gamma_i^T \Gamma_i \Phi} \quad (4.34)$$

The minimum value of the objective function occurs when the Hessian of the objective function with respect to  $\chi_i$  is larger than zero (Yan and Katafygiotis 2015b).

$$\left. \frac{\partial^2 J}{\partial \chi_i^2} \right|_{\alpha_i = \hat{\alpha}_i} = \Phi^T \Gamma_i^T C_{\hat{\varphi}_i}^{-1} \Gamma_i \Phi + 2\alpha_i \|\Gamma_i \Phi\|^2 > 0 \quad (4.35)$$

Thus, the optimal values of  $\chi_i$  and  $\alpha_i$  is obtained as (Yan and Katafygiotis 2015b).

$$\hat{\alpha}_i = \frac{\Phi^T \Gamma_i^T C_{\hat{\varphi}_i}^{-1} \Gamma_i \Phi}{2\Phi^T \Gamma_i^T \Gamma_i \Phi} + \left| \frac{\hat{\varphi}_i^T C_{\hat{\varphi}_i}^{-1} \Gamma_i \Phi}{2\Phi^T \Gamma_i^T \Gamma_i \Phi} \right| \quad (4.36)$$

$$\hat{\chi}_i = \text{sgn}(\hat{\varphi}_i^T C_{\hat{\varphi}_i}^{-1} \Gamma_i \Phi) \|\Gamma_i \Phi\|^{-1}$$

Substituting Eq. (4.36) into Eq. (4.33), and taking the first order derivative with respect to  $\Phi$  leads to the following constrained eigenvalue problem.

$$A\Phi + b = \beta\Phi \quad (4.37)$$

where

$$A = \frac{1}{2} \sum_{i=1}^{N_s} \chi_i^2 \Gamma_i^T C_{\hat{\varphi}_i}^{-1} \Gamma_i + \sum_{i=1}^{N_s} \alpha_i \chi_i^2 \Gamma_i^T \Gamma_i; \quad b = \frac{1}{2} \sum_{i=1}^{N_s} \chi_i \Gamma_i^T C_{\hat{\varphi}_i}^{-1} \hat{\varphi}_i \quad (4.38)$$



Thus, the optimal value of  $\Phi$  can be updated as eigenvector of the augmented matrix given in Eq. (4.13).

#### 4.4. Proposed Bayesian Algorithm

In this section, an alternative mode shape assembly algorithm is presented. The two-stage Bayesian approach, which is previously applied for single setup problem by Au (2011a) is adopted to multiple setup case. At first stage of the proposed methodology, the MPV of spectrum variables are obtained by minimizing the local likelihood with respect to local spectrum variables. At second stage, a constrained negative logarithm likelihood function for local mode shape is obtained. Finally, the global mode shape vector is obtained by minimization of assembled local likelihood functions.

##### 4.4.1. Two-Stage BFFTA for Mode Shape Assembly

The negative logarithm-likelihood function for  $p(\theta_i|Z_{ki})$  can be considered in two parts for well separated modes: (i) the first part only is sensitive to  $\theta_{si} = [f_i, \zeta_i, \bar{S}_i, S_{ei}]$ , and (ii) the second part is sensitive to  $\theta_i$  (Au, 2017).

$$L_i(\theta_i) = \underbrace{N_i N_{f_i} \ln \pi + (N_{f_i} - 1) \ln S_{ei} + \sum_k \ln (\bar{S}_i D_{ki} + S_{ei}) + S_{ei}^{-1} \kappa_i}_{\text{First Part (Sensitive to } \theta_{si})} - \underbrace{\varphi_i^T \Delta_i \varphi_i}_{\text{Second Part (Sensitive to } \theta_i)} \quad (4.39)$$

The Most Probable Value (MPV) for each parameter can also be determined by the direct minimization of Eq. (4.39) as similar to the methodology presented in the Section 2.4.2. In this minimization process, the modal parameters including spectral parameters and mode shapes can be decoupled for computational simplicity. For globally identifiable problems, it is known that Eq. (4.39) has a unique minimum at the MPV of  $\theta_i$ . For this reason, when the MPV of the local mode shape is considered, the second part of Eq. (4.39) can be represented as the function of  $\theta_{si}$ .

$$\hat{\varphi}_i^T \Delta_i \hat{\varphi}_i = \ell_i(\theta_{si}) \quad (4.40)$$

Here,  $\hat{\varphi}_i$  = MPV of local mode shape with unit norm (for  $i^{th}$  setup). Thus, the negative logarithm-likelihood function will only depend on the spectral parameters when  $\ell_i$  is substituted into Eq. (4.).

$$L_i(\theta_i) = L_{si}(\theta_{si}) - \ell_i(\theta_{si}) \quad (4.41)$$

$$L_{si}(\theta_{si}) = N_i N_{fi} \ln \pi + (N_{fi} - 1) \ln S_e + \sum_k \ln(\bar{S}_i D_{ki} + S_e) + S_e^{-1} \kappa_i$$

The spectral parameters can be obtained by minimizing Eq. (4.41). It follows that the first part will be constant when the most probable value (MPV) of  $\theta_{si}$  is substituted into Eq.(4.39). An inclusion of a unit norm constraint for  $\varphi_i$  to the likelihood function (centered at the MPV of  $\theta_{si}$ ) results in the following equation.

$$J_i(\varphi_i, \lambda_i, \hat{\theta}_{si}) = L_{si}(\hat{\theta}_{si}) - \varphi_i^T \hat{\Delta}_i \varphi_i + \lambda_i (\varphi_i^T \varphi_i - 1) \quad (4.42)$$

where  $L_{si}(\hat{\theta}_{si})$  = optimal value of first part, and  $\lambda_i$  is the Lagrange multiplier that enforces the unit norm of the local mode shape. Minimization of Eq. (4.42) with respect to  $\varphi_i$  gives,

$$\left. \frac{\partial J_i(\varphi_i, \lambda_i)}{\partial \varphi_i} \right|_{\varphi_i = \hat{\varphi}_i} = -2\hat{\varphi}_i^T \hat{\Delta}_i + 2\lambda_i \hat{\varphi}_i^T = 0 \quad (4.43)$$

Eq. (4.43) can be solved as a standard eigenvalue problem which results in the MPV of  $\varphi_i$ . Further, it is seen that the optimal value of  $\lambda_i$  equals to the optimum  $\ell_i$  which is equal to the maximum eigenvalue of  $\hat{\Delta}_i$ .

$$\hat{\lambda}_i = \hat{\varphi}_i^T \hat{\Delta}_i \hat{\varphi}_i \quad (4.44)$$

At first stage, the most probable spectrum variables can be obtained by minimizing Eq. (4.41) with respect to  $\theta_{si}$ . At the next step, the constrained negative logarithm likelihood function (centered at the MPV of spectrum parameters) for local mode shape at an individual setup, is obtained by arranging Eq. (4.41), as below.

$$J_i(\varphi_i, \lambda_i, \hat{\theta}_{si}) = L_{si}(\hat{\theta}_{si}) - \lambda_i + \varphi_i^T (-\hat{\Delta}_i + \lambda_i) \varphi_i \quad (4.45)$$

Neglecting the constant terms that do not affect the variation of  $\varphi_i$  leads to the following relation.

$$J_i(\varphi_i, \lambda_i, \hat{\theta}_{si}) \propto \frac{1}{2} \varphi_i^T H_{\hat{\varphi}_i} \varphi_i \quad (4.46)$$

where,  $H_{\hat{\varphi}_i}$  = Hessian matrix of  $J_i(\varphi_i, \hat{\lambda}_i, \hat{\theta}_{si})$  with respect to  $\varphi_i$  (with unit norm) at  $\theta_i = \hat{\theta}_i$ .  $H_{\hat{\varphi}_i}$  can be calculated numerically using finite difference method or can be derived analytically. For both procedures, the equality constraints that arises due to the norm of the local mode shape should be considered (Au, 2011a; Au and Xie, 2017). Otherwise,  $H_{\hat{\varphi}_i}$  will be a negative definite matrix, and therefore it will inevitably contradict the minimization nature of the MPV of mode shape (Au, 2011a).  $H_{\hat{\varphi}_i}$  can be analytically

derived by following the methodology that is proposed by Au and Xie (2017) or can be simply obtained by double differentiating of Eq. (4.45) with respect to  $\hat{\varphi}_i$ .

$$H_{\hat{\varphi}_i} = \left. \frac{\partial^2 J_i(\varphi_i, \hat{\lambda}_i, \hat{\theta}_{si})}{\partial \varphi_i^2} \right|_{\varphi_i = \hat{\varphi}_i} = -2\hat{\Delta}_i + 2\hat{\lambda}_i I_{N_i} \quad (4.47)$$

The modal shapes of individual setups are statistically independent (Au and Zhang, 2012). Thus, the objective functions for each setup can be assembled by linear combination, and the resulting objective function for the global mode vector,  $\Phi$ , under norm constraints can be written as follows by substituting  $\varphi_i = r_i^{-1} \Gamma_i \Phi$ , where  $\Gamma_i$  is the selection matrix that extracts the DOFs measured at  $i^{\text{th}}$  setup.

$$J(\Phi, \alpha, \beta, r) = \frac{1}{2} \sum_{i=1}^{N_s} r_i^{-2} \Phi^T \Gamma_i^T H_{\hat{\varphi}_i} \Gamma_i \Phi + \sum_{i=1}^{N_s} \alpha_i (\Phi^T \Gamma_i^T \Gamma_i \Phi - r_i^2) + \beta (1 - \Phi^T \Phi) \quad (4.48)$$

where  $\alpha = [\alpha_1, \dots, \alpha_{N_s}]$ ,  $r = [r_1, \dots, r_{N_s}]$ ,  $\alpha_i$  = Lagrange multiplier for the norm constraint of  $\Gamma_i \Phi = r_i$ , and  $\beta$  = Lagrange multiplier that enforces the unit norm for  $\Phi$ . The Lagrange multiplier  $\alpha_i$  is obtained at the minimum value of Eq. (4.48) with respect to  $r_i$ .

$$\frac{\partial J}{\partial r_i} = -r_i^{-3} \Phi^T \Gamma_i^T H_{\hat{\varphi}_i} \Gamma_i \Phi - 2\alpha_i r_i = 0 \Rightarrow \hat{\alpha}_i = -\frac{r_i^{-4}}{2} \Phi^T \Gamma_i^T H_{\hat{\varphi}_i} \Gamma_i \Phi \quad (4.49)$$

Note that the second order derivative of the objective function with respect to  $r_i$  is a non-negative value since  $H_{\hat{\varphi}_i}$  is semi-positive definite (Au, 2011a).

$$\frac{\partial^2 J}{\partial r_i^2} = 3r_i^{-4} \Phi^T \Gamma_i^T H_{\hat{\varphi}_i} \Gamma_i \Phi - 2\hat{\alpha}_i = 4r_i^{-4} \Phi^T \Gamma_i^T H_{\hat{\varphi}_i} \Gamma_i \Phi \geq 0 \quad (4.50)$$

Minimizing Eq.(4.50) with respect to  $\Phi$  leads to

$$\left. \frac{\partial J}{\partial \Phi} \right|_{\Phi = \hat{\Phi}} = \hat{\Phi}^T \left[ \sum_{i=1}^{N_s} r_i^{-2} \Gamma_i^T H_{\hat{\varphi}_i} \Gamma_i \right] + \hat{\Phi}^T \left[ \sum_{i=1}^{N_s} 2\hat{\alpha}_i \Gamma_i^T \Gamma_i \right] + 2\beta \hat{\Phi}^T = 0 \quad (4.51)$$

Thus, the most probable global mode shape vector is obtained by the solution of the following standard eigenvalue problem.

$$A \hat{\Phi} = \beta \hat{\Phi} \quad (4.52)$$

in which

$$A = \frac{1}{2} \sum_{i=1}^{N_s} \Gamma_i^T (r_i^{-2} H_{\hat{\varphi}_i} + 2\hat{\alpha}_i I_{N_i}) \Gamma_i \quad (4.53)$$

#### 4.4.2. Alternative Solution by Gaussian Approximation

In this section, it is shown that the solution for the global mode shape vector is unique regardless of the implemented assembly methodology. For this purpose, the final solution for the global mode shape in Eq. (4.52) is obtained by following a similar procedure to the method by Yan and Katafygiotis (2015b). Since the problem is globally identifiable, the conditional PDF for  $i^{th}$  local mode shape centered at the MPV for spectrum variables can be estimated by Gaussian approximation. For this purpose, the conditional PDF for global mode shape can be written as below.

$$p(\Phi | [\varphi_1 \dots \varphi_{N_s}]) = \prod_{i=1}^{N_s} p(\Phi | \varphi_i) \quad (4.54)$$

According to the Bayes' theorem, the following equality can be constructed.

$$p(\Phi | \varphi_i) = \frac{p(\varphi_i | \Phi) p(\Phi)}{p(\varphi_i)} \quad (4.55)$$

where,  $p(\Phi)$  and  $p(\varphi_i | \Phi)$  denote the marginal and conditional prior distributions for  $\Phi$  and  $\varphi_i$ , respectively. Again, assuming a noninformative prior distribution for  $p(\Phi)$ ,  $p(\varphi_i | \Phi)$  can be well estimated by Gaussian approximation around the MPV of local mode shape.

$$p(\Phi | \varphi_i) \propto p(\varphi_i | \Phi) = |H_{\hat{\varphi}_i}^{-1}| (2\pi)^{-N/2} \exp\left(\frac{1}{2} (r_i^{-1} \Gamma_i \Phi - \hat{\varphi}_i)^T H_{\hat{\varphi}_i} (r_i^{-1} \Gamma_i \Phi - \hat{\varphi}_i)\right) \quad (4.56)$$

where  $H_{\hat{\varphi}_i}$  is used instead of the inverse of the posterior covariance matrix. Thus, the negative logarithm likelihood function of  $p(\varphi_i | \Phi)$  is written as;

$$\begin{aligned} L_i(\Phi, r_i) &= -\ln[p(\varphi_i | \Phi)] \\ L_i(\Phi, r_i) &= \frac{1}{2} N \ln \pi + \frac{1}{2} \ln |H_{\hat{\varphi}_i}^{-1}| + \frac{1}{2} (r_i^{-1} \Gamma_i \Phi - \hat{\varphi}_i)^T H_{\hat{\varphi}_i} (r_i^{-1} \Gamma_i \Phi - \hat{\varphi}_i) \end{aligned} \quad (4.57)$$

Applying the norm constraint for the local mode shape, the objective function for the  $i^{th}$  setup is obtained as;

$$J_i(\Phi, \alpha_i, r_i) = L_i(\Phi, r_i) + \alpha_i (\Phi^T \Gamma_i^T \Gamma_i \Phi - r_i^2) \quad (4.58)$$

Taking the first order derivative of Eq. (4.58) with respect to  $r_i$  gives

$$\frac{\partial J_i}{\partial r_i} = r_i^{-2} \Phi^T \Gamma_i^T H_{\hat{\varphi}_i} \hat{\varphi}_i - r_i^{-3} \Phi^T \Gamma_i^T H_{\hat{\varphi}_i} \Gamma_i \Phi - 2\alpha_i r_i = 0 \quad (4.59)$$

Thus, the optimal value of  $\alpha_i$  is obtained as

$$\hat{\alpha}_i = -\frac{r_i^{-4}}{2} \Phi^T \Gamma_i^T H_{\hat{\varphi}_i} \Gamma_i \Phi + \frac{r_i^{-3}}{2} \Phi^T \Gamma_i^T H_{\hat{\varphi}_i} \hat{\varphi}_i \hat{\Phi} \quad (4.60)$$

Finally, the objective function for the global mode vector under norm constraints is written as

$$J(\Phi, \alpha, \beta, r) = \frac{1}{2} \sum_{i=1}^{N_s} (r_i^{-1} \Gamma_i \Phi - \hat{\varphi}_i)^T H_{\hat{\varphi}_i} (r_i^{-1} \Gamma_i \Phi - \hat{\varphi}_i) + \sum_{i=1}^{N_s} \alpha_i (\Phi^T \Gamma_i^T \Gamma_i \Phi - r_i^2) + \beta (1 - \Phi^T \Phi) \quad (4.61)$$

Minimizing Eq. (4.61) with respect to  $\Phi$  leads to the following constrained eigenvalue problem.

$$\begin{aligned} \mathbf{A}\Phi + \mathbf{b} &= \beta\Phi \\ \mathbf{A} &= \frac{1}{2} \sum_{i=1}^{N_s} \Gamma_i^T (r_i^{-2} H_{\hat{\varphi}_i} + 2\hat{\alpha}_i I_{N_i}) \Gamma_i; \quad \mathbf{b} = -\frac{1}{2} \sum_{i=1}^{N_s} r_i^{-1} \Gamma_i^T \hat{H}_{\hat{\varphi}_i} \hat{\varphi}_i \end{aligned} \quad (4.62)$$

The obtained constrained eigenvalue problem is similar to the result by Yan and Katafygiotis (2015b). For this alternative solution, however, Eq. (4.62) is reduced into a standard eigenvalue problem. For this purpose, the components of  $H_{\hat{\varphi}_i}$  can be expressed in terms of the eigenvalue decomposition of its two terms.

$$\begin{aligned} H_{\hat{\varphi}_i} &= -2\hat{\Delta}_i + 2\hat{\lambda}_i I_{N_i} = U\Sigma U^T + 2\hat{\lambda}_i U U^T \\ U &= [u_1 = \hat{\varphi}_i \quad u_2 \quad \dots \quad u_{N_i}] \\ \Sigma &= \text{diag}[\sigma_1 = -2\hat{\lambda}_i \quad \sigma_2 \quad \dots \quad \sigma_{N_i}] \\ |\sigma_1| &= \max(|\sigma_1|, \dots, |\sigma_{N_i}|); \quad U U^T = I_{N_i} \end{aligned} \quad (4.63)$$

Then, the equivalent eigenvalue decomposition of  $H_{\hat{\varphi}_i}$  is written by combining the decomposed terms in Eq. (4.63).

$$\begin{aligned} H_{\hat{\varphi}_i} &= U\bar{\Sigma}U^T \\ U &= [\hat{\varphi}_i \quad u_2 \quad \dots \quad u_{N_i}] \\ \bar{\Sigma} &= \text{diag}\left[0 \quad (\sigma_2 + 2\hat{\lambda}_i) \quad \dots \quad (\sigma_{N_i} + 2\hat{\lambda}_i)\right] \end{aligned} \quad (4.64)$$

In Eq. (4.64),  $H_{\hat{\varphi}_i}$  is semi-positive definite with null vector,  $\hat{\varphi}_i$ , and its eigenvalue that corresponds to  $\hat{\varphi}_i$  is equal to zero. Therefore, the vector of  $b$  will be a zero vector. Thus, Eq. (4.62) leads to the same standard eigenvalue problem that is given in Eq. (4.52).

### 4.4.3. Estimation of the Weights for Individual Setups

In the assembly procedure, local mode shapes that are identified in the individual setups have a contribution to the global mode shape. The Global Least Square approach assumes that all setups are equally weighted, and their contribution is uniform. Bayesian methods, however, considers the weight of each setup incorporating the identification quality (Au and Zhang 2012; Yan and Katafygiotis, 2015b). In this context, Au and Zhang (2012) presents the following asymptotic weighting factor in case of large signal to noise ratio.

$$w_i \propto \frac{r_i^{-2} \bar{\lambda}_i}{S_{ei}} \quad (4.65)$$

in which  $\bar{\lambda}_i$  is the largest eigenvalue of  $\sum_k \text{Re}(F_{ki} F_{ki}^*)$ .

In case of lower signal-to-noise ratio, the weighting of each setup can also be calculated as depending on the data quality. For this purpose, the local Hessian matrix,  $H_{\hat{\varphi}_i}$ , can be rewritten as follows by neglecting the zero-eigenvalue term along the local mode shape direction.

$$H_{\hat{\varphi}_i} \approx \frac{\delta_{\hat{\varphi}_i}}{(N_i - 1)} [I_{N_i} - \hat{\varphi}_i \hat{\varphi}_i^T] \quad (4.66)$$

where  $\delta_{\hat{\varphi}_i}$  = sum of all eigenvalues of  $H_{\hat{\varphi}_i}$ . By using Eq. (4.66), the optimal value of the Lagrange multiplier,  $\alpha_i$ , can be arranged as,

$$\hat{\alpha}_i = \frac{r_i^{-4} \delta_{\hat{\varphi}_i}}{(N_i - 1)} [r_i^{-2} - \Phi^T \Gamma_i^T \hat{\varphi}_i \hat{\varphi}_i^T \Gamma_i \Phi] \quad (4.67)$$

Substituting Eqs. (4.66) and (4.67) into Eq. (4.53) yields,

$$\hat{\mathbf{A}} = \sum_{i=1}^{N_s} \frac{r_i^{-2} \delta_{\hat{\varphi}_i}}{(N_i - 1)} \Gamma_i^T [\bar{\alpha}_i I_{N_i} - \hat{\varphi}_i \hat{\varphi}_i^T] \Gamma_i \quad (4.68)$$

where

$$\bar{\alpha}_i = r_i^{-2} \Phi^T \Gamma_i^T \hat{\varphi}_i \hat{\varphi}_i^T \Gamma_i \Phi \quad (4.69)$$

Thus, the weight of the  $i^{\text{th}}$  setup in the optimal global mode shape can be calculated by the following formula.

$$w_i = \frac{r_i^{-2} \delta_{\hat{\varphi}_i}}{2(N_i - 1)} \quad (4.70)$$

#### 4.4.4. Posterior Uncertainty

The assembled global mode shape vector has identification uncertainty, as well. To define this uncertainty, posterior covariance matrix should be calculated first. To obtain the posterior covariance matrix, the spectrum variables identified at each setup should also be included. Therefore, the Hessian matrix for local spectrum variables and global mode shape vector is obtained as follows

$$\begin{bmatrix} \left[ J^{(\theta_s, \theta_s)} \right]_{N_{\theta_s} \times N_{\theta_s}} & \left[ J^{(\theta_s, \Phi)} \right]_{N_{\theta_s} \times N} \\ \left[ J^{(\Phi, \theta_s)} \right]_{N \times N_{\theta_s}} & \left[ J^{(\Phi, \Phi)} \right]_{N \times N} \end{bmatrix}_{(N_{\theta_s} + N) \times (N_{\theta_s} + N)} \quad (4.71)$$

$$J^{(\theta_s, \theta_s)} = \begin{bmatrix} J^{(\theta_{s1}, \theta_{s1})} & & & \\ & \cdot & & \\ & & \cdot & \\ & & & J^{(\theta_{sN_s}, \theta_{sN_s})} \end{bmatrix} \quad J^{(\theta_s, \Phi)} = \begin{bmatrix} J^{(\theta_{s1}, \Phi)} \\ \cdot \\ \cdot \\ \cdot \\ J^{(\theta_{sN_s}, \Phi)} \end{bmatrix} \quad (4.72)$$

where  $\theta_s = [\theta_{s1}, \dots, \theta_{sN_s}]$ , and  $N_{\theta_s} = \sum_{i=1}^{N_s} N_{\theta_{si}}$ . Before obtaining the derivatives of the objective function, it should be noted that, the Lagrange multiplier of  $\beta$  can be defined as a function of  $\theta_s$ .

$$\beta(\theta_s) = \hat{\Phi}^T \left[ \frac{1}{2} \sum_{i=1}^{N_s} \Gamma_i^T (r_i^{-2} H_{\hat{\phi}_i}(\theta_{si}) + 2\hat{\alpha}_i I_{N_i}) \Gamma_i \right] \hat{\Phi} \quad (4.73)$$

Thus,  $J^{(\hat{\theta}_{si}, \hat{\Phi})}$  is obtained as zero matrix.

$$\begin{aligned} J^{(\hat{\theta}_{si}, \hat{\Phi})} &= \hat{\Phi}^T \frac{\partial}{\partial \theta_{si}} \left[ \sum_{i=1}^{N_s} \Gamma_i^T (r_i^{-2} H_{\hat{\phi}_i}(\theta_{si}) + 2\hat{\alpha}_i I_{N_i}) \Gamma_i \right]_{\theta_{si} = \hat{\theta}_{si}} - 2\hat{\Phi}^T \frac{\partial \beta(\theta_s)}{\partial \theta_{si}} \Big|_{\theta_{si} = \hat{\theta}_{si}} \\ &= \hat{\Phi}^T \frac{\partial}{\partial \theta_{si}} \left[ \sum_{i=1}^{N_s} \Gamma_i^T (r_i^{-2} H_{\hat{\phi}_i}(\theta_{si}) + 2\hat{\alpha}_i I_{N_i}) \Gamma_i \right]_{\theta_{si} = \hat{\theta}_{si}} \left[ I_N - \hat{\Phi} \hat{\Phi}^T \right] \\ &= 0 \end{aligned} \quad (4.74)$$

Note that  $[I_N - \hat{\Phi} \hat{\Phi}^T]$  is a semi-positive definite matrix whose null vector is equal to  $\hat{\Phi}$ . Therefore,  $J^{(\hat{\theta}_{si}, \hat{\Phi})}$  will be a zero matrix. Thus, the Hessian of the objective function will be block diagonal matrix.

$$\begin{bmatrix} H_{\hat{\theta}_s} & 0 \\ 0 & H_{\hat{\Phi}} \end{bmatrix} \quad (4.75)$$

where,  $H_{\hat{\theta}_s} = J^{(\hat{\theta}_s, \hat{\theta}_s)}$  and  $H_{\hat{\Phi}} = J^{(\hat{\Phi}, \hat{\Phi})}$ . Here,  $H_{\hat{\Phi}}$  is obtained as below.

$$H_{\hat{\Phi}} = \sum_{i=1}^{N_s} \Gamma_i^T \left( r_i^{-2} H_{\hat{\phi}_i} + 2\hat{\alpha}_i I_{N_i} \right) \Gamma_i - 2\hat{\beta} I_N \quad (4.76)$$

It is seen that there is no correlation between the local spectrum parameters and global mode shape vector. For this reason, the posterior covariance matrix,  $C_{\hat{\Phi}}$  can be directly obtained by the inverse of Hessian,  $H_{\hat{\Phi}}$ . However, this procedure inevitably causes numerical errors since the minimum eigenvalue of  $H_{\hat{\Phi}}$  might be equal to zero. Instead, pseudo inverse of  $H_{\hat{\Phi}}$  can be taken to calculate  $C_{\hat{\Phi}}$ . Thus, the posterior covariance matrix for multiple setups is obtained as below.

$$\hat{C} = \begin{bmatrix} H_{\hat{\theta}_s}^{-1} & 0 \\ 0 & H_{\hat{\Phi}}^+ \end{bmatrix} \quad (4.77)$$

#### 4.4.5. Summary of Procedure

The proposed modified solution assembles mode shapes by using the probability distributions for local mode shapes centered at the local spectrum variables. For this reason, first, the spectrum variables at  $i^{th}$  setup should be determined. Second, posterior distributions for local mode shapes should be obtained. In the calculation process, the initial guess for  $\bar{S}_i$  and  $S_{ei}$  can be calculated by using Eqs (4.28) and (4.29).

When the local part of  $\hat{\Phi}$  is well matched with the identified local mode shape  $\hat{\phi}_i$  (zero discrepancy), the Lagrange multiplier  $\hat{\alpha}_i$  can be expected to be equal to zero. Thus,  $\hat{A}$  turns into the following form.

$$r_i^{-1} \Gamma_i \Phi \rightarrow \hat{\phi}_i \Rightarrow \hat{\alpha}_i \rightarrow 0; \quad \hat{A} \approx \sum_{i=1}^{N_s} r_i^{-2} \Gamma_i^T H_{\hat{\phi}_i} \Gamma_i \quad (4.78)$$

The initial guess of the global mode shape vector can be taken as the eigenvector of  $\hat{A}$  (corresponding to minimum eigenvalue) in Eq. (4.53) by setting  $r_i=1$ .

The overall procedure of the proposed algorithm is presented in Figure 4.1. The main difference from Au (2017) resides in;

- the application of two-stage BFFTA to multiple setups,
- weighting of each setup by the Hessian matrix for local mode shapes
- the calculation of initial guess, and



- the consideration of possible discrepancy between the local part of the global mode shape and the identified local mode shape.

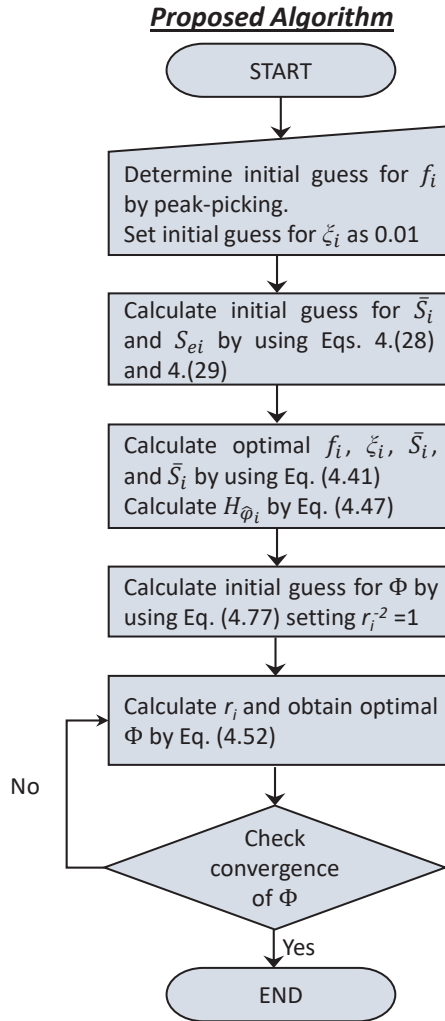


Figure 4.1. Flow chart for the proposed algorithm

The discrepancy is characterized by defining two different norm constraints for local mode shape. First one,  $\hat{\lambda}_i$ , enforces the unit norm for  $\varphi_i$ , and the second one,  $\hat{\alpha}_i$ , enforces that  $r_i = \|\Gamma_i \Phi\|$ . Here, the calculation of optimal  $\varphi_i$  is unnecessary. As the initial guess is close to the optimal value, the convergence speed in the iteration phase is expected to be increased.

Although the theoretical background of the presented methodology is based on the approximation of well-separated modes, it can also be implemented for the closely spaced modes. In case of closely spaced modes, the Hessian matrix for the mode shape vector is also semi-positive definite due to the norm constraint singularity (see Appendix D). Therefore, the presented methodology can be directly applied for closely spaced mode

case. Here, the spectrum variables and the Hessian matrix for local mode shape should be obtained by using the closely spaced mode algorithm at the first stage. In addition, the posterior covariance matrix for the global mode shape vector can be calculated neglecting zero correlation between the global mode shape vectors of closely spaced modes.

## **4.5. Experimental and Numerical Analysis**

In this section, the proposed two-stage mode shape assembly methodology is numerically and experimentally verified. The proposed algorithm is compared to the previous mode shape assembly algorithm by Au (2017). For this purpose, one experimental and one benchmark study is presented. Finally, a field application is presented for global mode shape estimation with closely-spaced modes.

### **4.5.1. Experimental analysis: Laboratory shear frame**

A ten-story shear frame shown in Figure 4.2 is measured with two different multiple setup configurations (see Table 4.2). These cases are considered in order to see the effect of sensor configuration on the assembly procedure. Here, Case-I represents a fixed reference sensor placement, while Case-II represents a roving reference sensor placement configuration. Small amplitude acceleration responses are acquired under ambient excitation for both cases. For comparison purposes, the given shear frame is measured under adequately large amplitude ambient excitation at single setup and the obtained frequencies, damping ratios and modal shape results are used as reference values.

In the laboratory experiments, piezo-electric accelerometers are used which are defined with 1000 mV/g sensitivity and  $11.4 \mu\text{g}/(\text{Hz})^{0.5}$  spectral noise density. The measurement system consists of a laptop computer with a 1.5 GHz single CPU and Linux operating system, a 16 channel USB DUX-Sigma data acquisition box with 24 bit analog to digital conversion, a first order analog lowpass filter with a cut-off frequency at 120 Hz for each channel, and a constant current supply for the accelerometers. The acceleration responses are recorded in the weak direction of the buildings and all measurements of groups are acquired in different times with 1000 Hz. sampling frequency and 5 minutes duration.

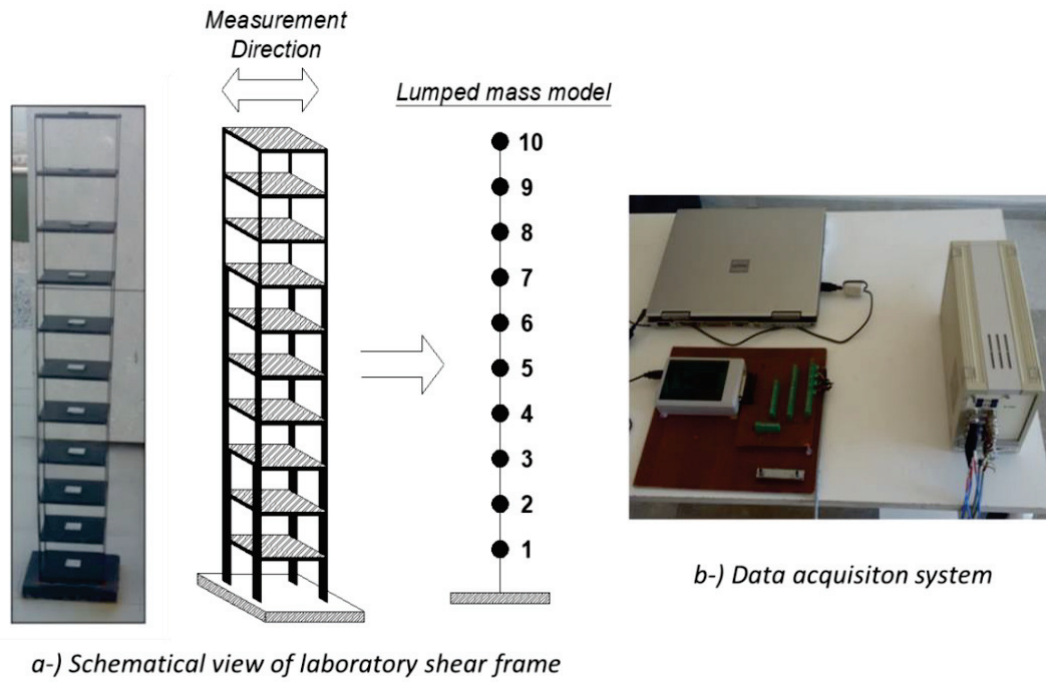


Figure 4.2. Ten story shear frame structure

Table 4.2. Setup configurations for Case-I and Case-II

Setup Number	Measured DOFs	
	Case-I	Case-II
1	1, 2, 3, 10	1, 2, 3, 4
2	1, 4, 5, 10	3, 4, 5, 6
3	1, 6, 7, 10	5, 6, 7, 8
4	1, 8, 9, 10	7, 8, 9, 10

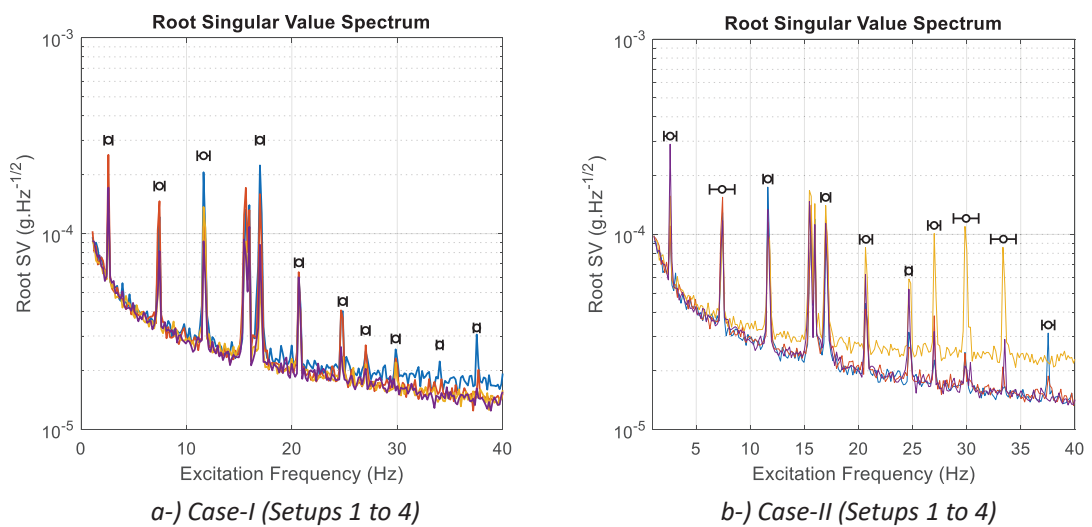


Figure 4.3. Maximum root singular value spectra

Table 4.3. Average MPVs and representative statistics for  $f_i$  and  $\zeta_i$

Mode #	Reference		Case-I				Case-II			
	$f$	$\zeta$	$f$		$\zeta$		$f$		$\zeta$	
	(Hz)	(%)	MPV (Hz)	c.o.v. (%)	MPV (Hz)	c.o.v. (%)	MPV (Hz)	c.o.v. (%)	MPV (Hz)	c.o.v. (%)
1	2.59	0.34	2.62	0.23	0.23	26.77	2.62	0.30	0.23	14.78
2	7.32	0.26	7.38	0.10	0.22	44.30	7.37	0.10	0.22	11.82
3	11.65	0.23	11.71	0.13	0.12	19.72	11.70	0.14	0.11	25.34
4	16.96	0.16	17.03	0.07	0.12	46.93	17.03	0.08	0.14	24.66
5	20.65	0.14	20.72	0.10	0.15	30.62	20.72	0.07	0.14	26.09
6	24.69	0.16	24.75	0.22	0.16	38.27	24.75	0.69	0.14	61.66
7	26.94	0.18	27.07	0.36	0.15	55.43	27.03	0.12	0.14	36.43
8	29.85	0.16	29.95	0.32	0.18	33.86	29.92	0.08	0.15	22.31
9	33.19	0.16	33.23	0.85	0.13	47.23	33.35	0.22	0.16	21.59
10	37.47	0.18	37.53	0.34	0.17	28.18	37.52	0.30	0.15	34.86

A manual selection of the bandwidth for possible modes requires a visual inspection of the frequency response data. For each measurement setup, the maximum root maximum singular value spectrums for Case-I and II are obtained by windowing (with 600 segments), and they are presented in Figure 4.3. The selected bandwidths of possible modes are marked in the figures by lateral error bars.

The average values of the MPV for natural frequencies and damping ratios obtained at each setup together with coefficients of variation are presented in Table 4.3. for Case-I and II. The coefficients of variation for natural frequencies and damping ratios among all setups include setup-to-setup variability and identification uncertainty which is defined as representative statistics by Zhang and Au (2016). According to the results, the maximum c.o.v. remains less than 1% for each case for identified frequencies. For damping ratios, standard deviations show relatively large variations among different setups. These variations are the result of the setup-to-setup variability instead of identification uncertainty. Exact values of natural frequencies and damping ratios are expected to be invariant for each setup. To the contrary, the spectral density of modal excitation and prediction error may show significant variations among different setups due to the possible variations in excitation levels. As a result, a decrease in signal strength is observed for larger modes. To illustrate this case, average modal signal-to-noise ratios and their setup-to-setup variations are presented in Figure 4.4.

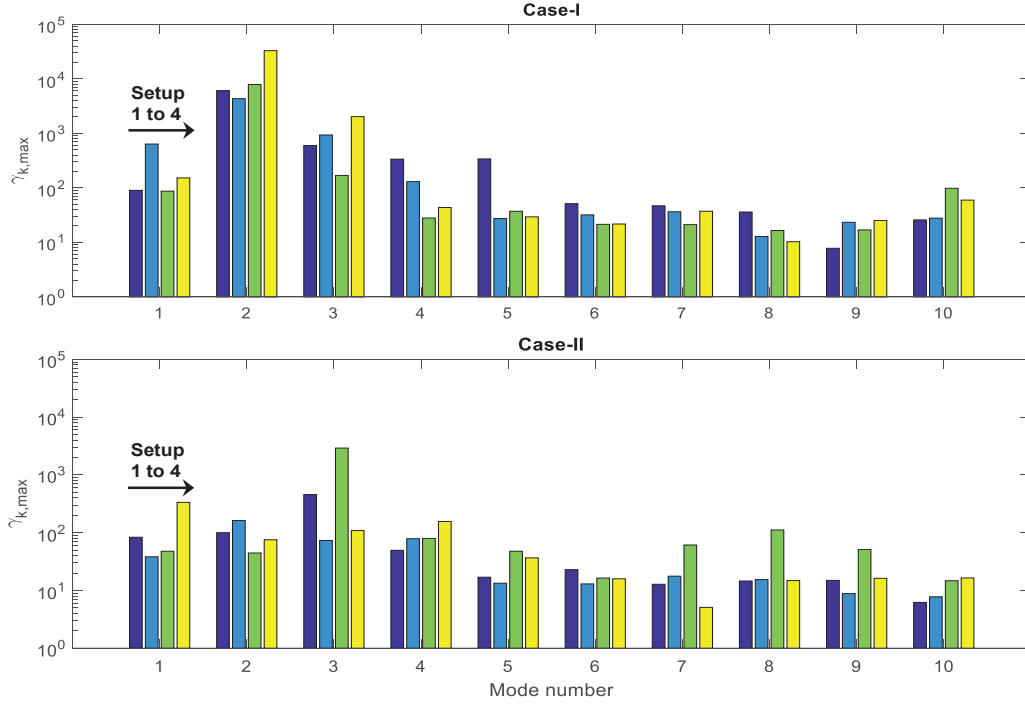


Figure 4.4. Variations in the estimated signal-to-noise ratios

Figure 4.4, the variations in the estimated signal-to-noise ratios,  $\gamma_{ki} = \bar{S}_i D_{ki} / S_{ei}$  are presented. For both cases, setup-to-setup variability of signal-to-noise ratio is remarkably large for all modes. This variability may not affect the identification quality in lower modes due to the relatively higher signal quality. For higher modes (Modes 6 to 10), however, this variability may cause significant errors in the identification process due to the smaller signal-to-noise effect.

Assembled mode shapes for Case-I and II are presented in Figure 4.5 and Figure 4.6, respectively. The iterations of algorithms are stopped as the MAC value between the current and previous steps is larger than 0.9999. According to the results, it is seen that the assembled mode shapes by using the presented methodology are similar for the proposed methodology and the algorithm by Au (2017). The ninth mode obtained by using the algorithm by Au (2017), however, does not meet the reference mode shape. The reason of this fact resides on the initial guess proposed by Au (2017) which is quite far away from the optimal value. The MAC values between the identified and reference mode shapes are presented in Table 4.4. Here, MAC1 and MAC2 indicate the MAC values for the mode shapes obtained by the proposed methodology and the algorithm by Au (2017), respectively, with respect to reference mode shapes. Both procedures give similar results except for the ninth mode.

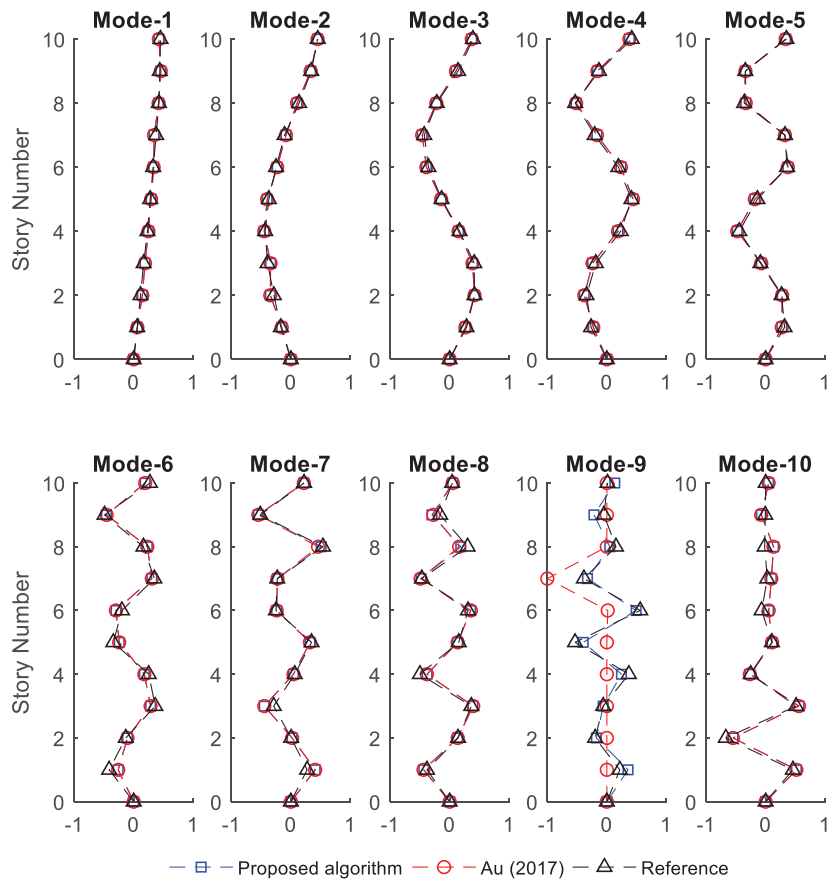


Figure 4.5. Assembled mode shapes for Case-I

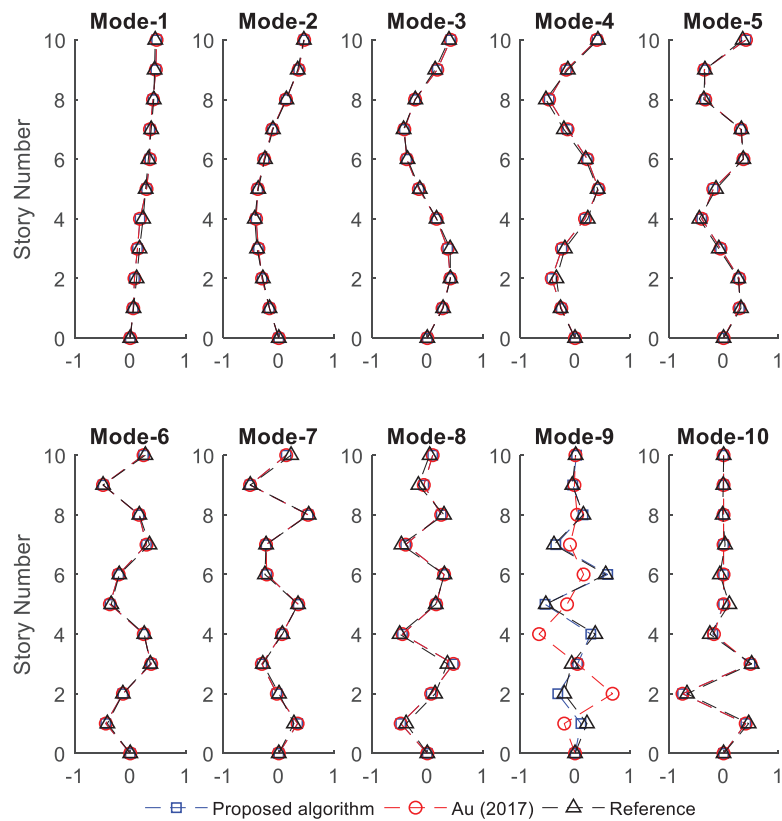


Figure 4.6. Assembled mode shapes for Case-II

Table 4.4. Calculated MAC values for Case I and II

<i>Mode number</i>	<i>Case-I</i>			<i>Case-II</i>		
	<i>MAC1</i>	<i>MAC2</i>	<i>EMAC</i>	<i>MAC1</i>	<i>MAC2</i>	<i>EMAC</i>
1	0.9963	0.9962	0.9998	0.9980	0.9978	0.9991
2	0.9932	0.9934	0.9993	0.9960	0.9954	0.9990
3	0.9915	0.9927	0.9996	0.9986	0.9970	0.9994
4	0.9972	0.9912	0.9992	0.9945	0.9929	0.9993
5	0.9950	0.9933	0.9983	0.9972	0.9967	0.9988
6	0.9801	0.9752	0.9882	0.9852	0.9827	0.9857
7	0.9856	0.9822	0.9906	0.9825	0.9809	0.9860
8	0.9741	0.9695	0.9873	0.9748	0.9737	0.9843
9	0.9665	0.3847	0.9783	0.9763	0.1861	0.9805
10	0.9693	0.9659	0.9935	0.9848	0.9658	0.9835

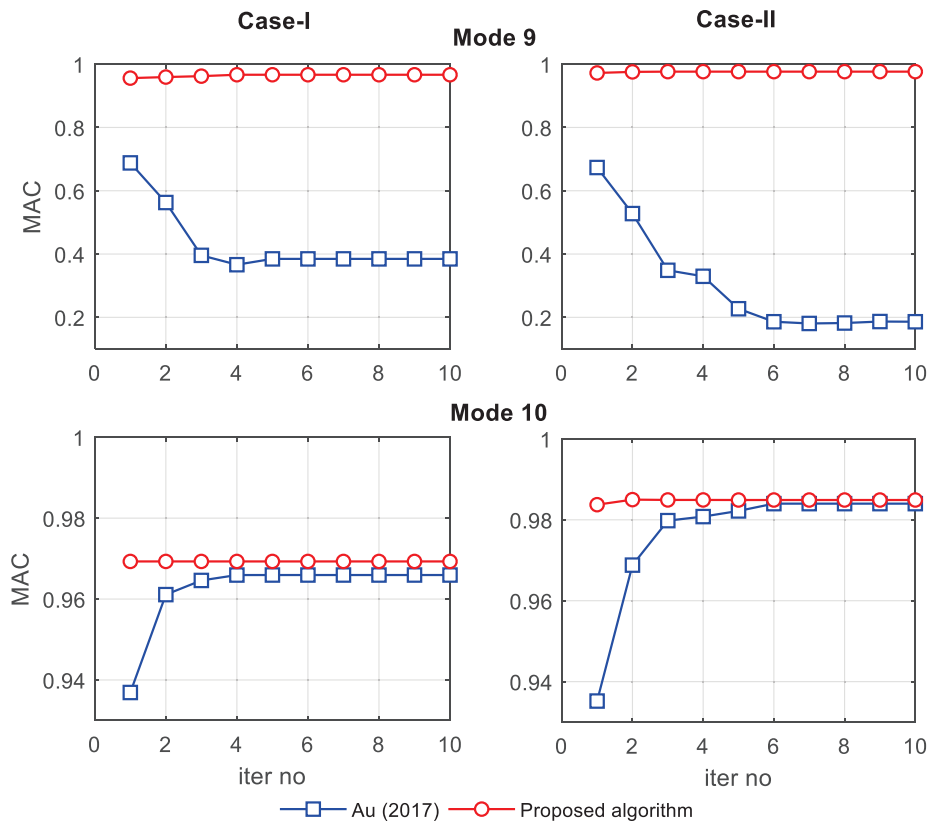


Figure 4.7. Variations in MAC values with respect to reference mode shapes versus the number of iterations

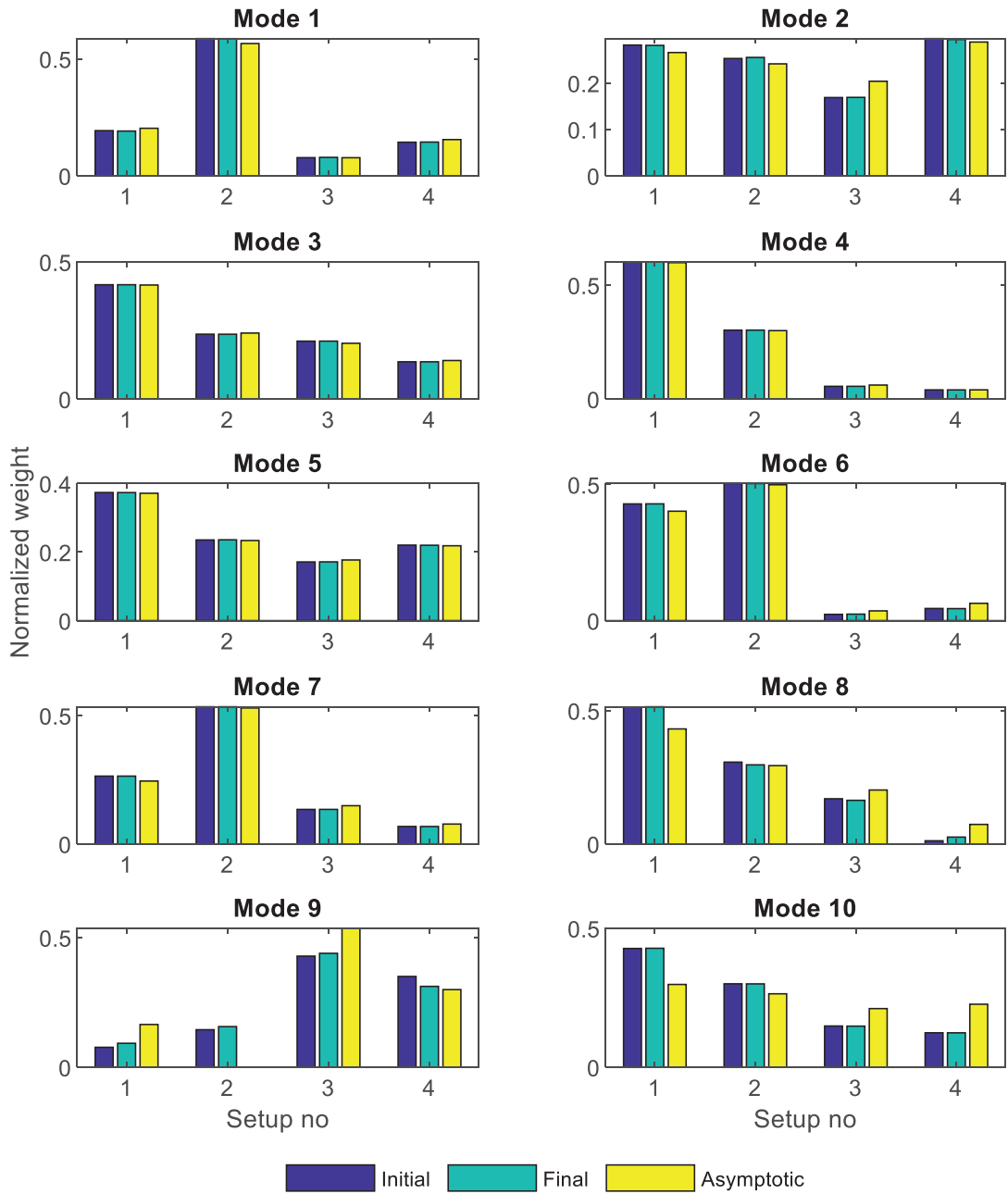


Figure 4.8. Calculated setup weights for Case-I

Figure 4.7 presents the MAC values of the mode shapes that are obtained at each iteration step for Mode 9 and 10 with respect to reference mode shapes. The lower modes show no significant variance, and therefore they are not shown. It is seen that the quality of the initial guess of the proposed algorithm gives more reasonable results when compared to the results of the algorithm by Au (2017). The reason is considered to be caused by the large signal-to-noise asymptotic behavior assumption for the initial guess by Au (2017). Since the higher modes are subjected to less level of excitation, the initial guess by using the large signal-to-noise asymptotic behavior may significantly diverge



from the actual value. Figure 4.8 and Figure 4.9 present the calculated weights for the initial and final mode shapes by the proposed methodology and the asymptotic weight proposed by Au and Zhang (2012). It can be seen that the weights for modes 1 to 8 are in the same range. The asymptotic weights for modes 9 and 10, however, are quite different from the proposed algorithm, which is considered to be the cause of the difference in the ninth mode shape.

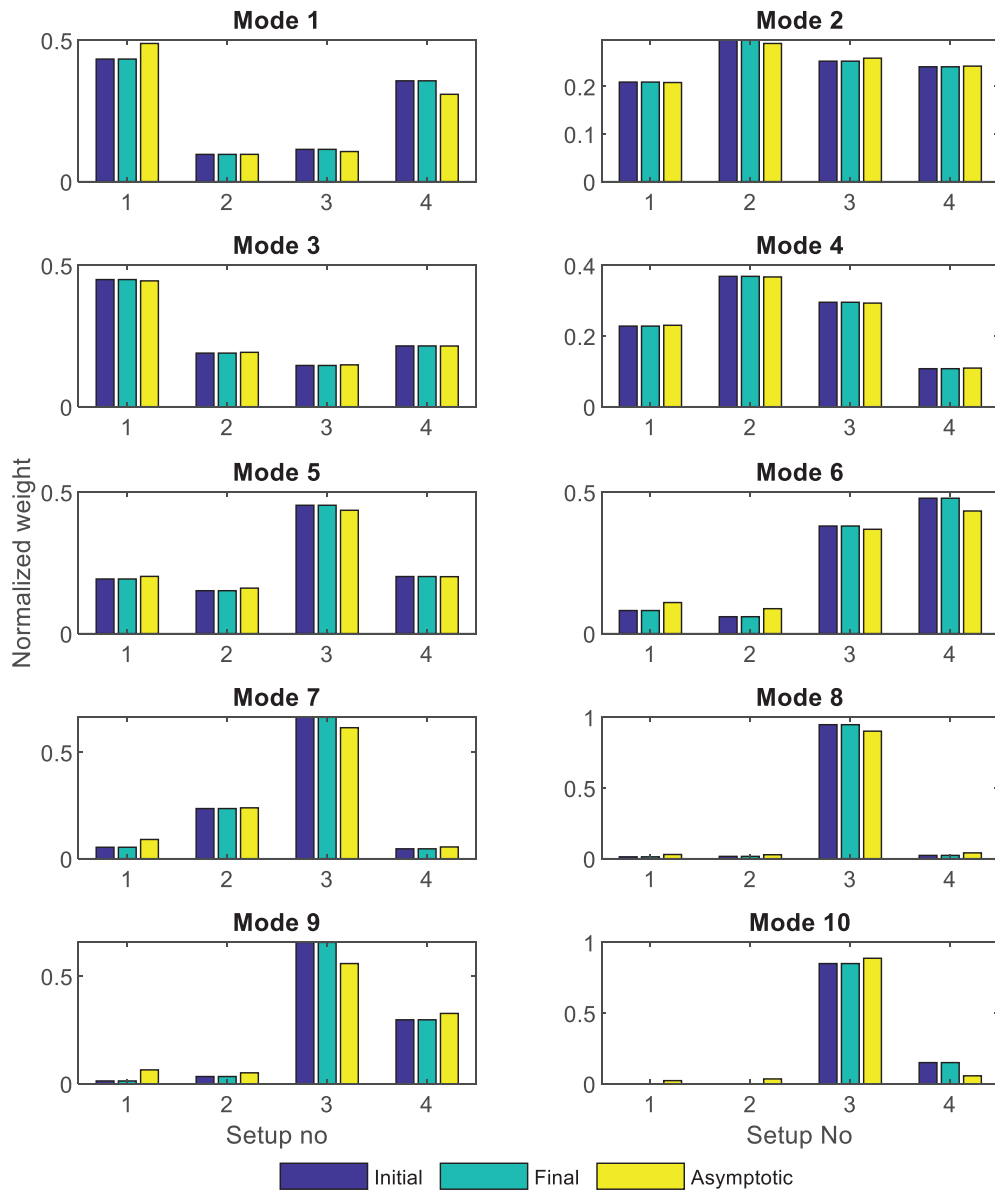


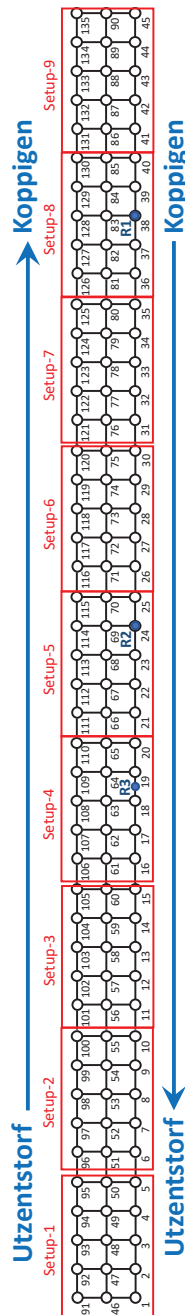
Figure 4.9. Calculated setup weights for Case-II

#### 4.5.2. Benchmark study: Z24 Bridge

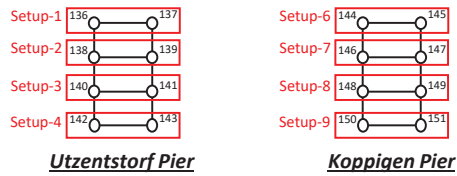
The former Z24 Bridge in Switzerland is investigated in this section. The bridge is used in a benchmark study under the COST-F European Network project (Reynders

and De Roeck, 2008). The bridge passes over the Bern-Zürich highway, and connects the two towns of Utzenstorf and Koppigen. It is composed of three spans with lengths of 14, 30, and 14 meters as it is illustrated in Figure 4.10.

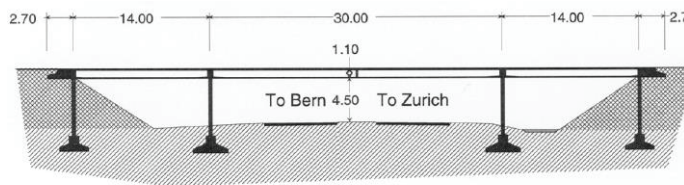
**Sensor locations for deck**



**Sensor locations for piers**



**Elevation view**



**Plan view**

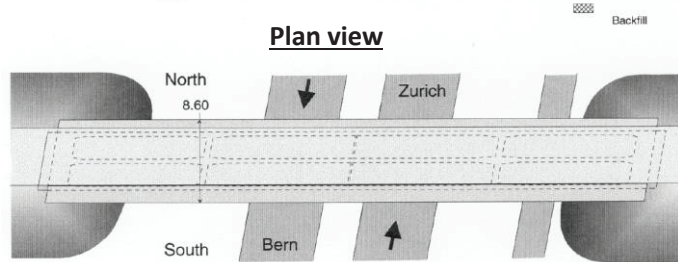


Figure 4.10. Schematic representation of Z24 Bridge and sensor layouts (Reynders et al, 2012; Reynders and Roeck, 2008)

In the benchmark study, the Z24 Bridge is measured at 152 points under ambient and forced vibrations by KU LEUVEN Structural Mechanics division between 1998 and

2000. Nine measurement setups with three reference points are conducted to obtain a complete measurement of the bridge. The schematic representation of the sensor layout for the deck and piers are shown in Figure 4. The collected data for seventeen different cases is available on the website <https://bwk.kuleuven.be/bwm/z24>. Among these, the third reference measurement is considered in this study.

The average root singular value spectrum of reference measurement-2 by using the 13000 windows is presented in Figure 4.11. Here, the first five modes are easily perceptible. The sixth mode is not excited in all setups. It is visible in the second, third and seventh setups, only. In addition, it is seen that the visible modes are well separated. A similar trend is observed in previous studies by Peeters and Ventura (2003), and Reynders et al (2012).

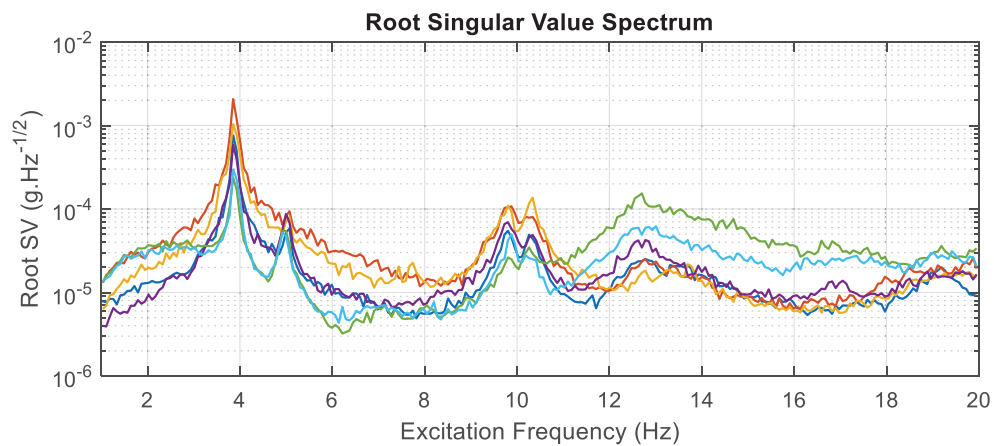


Figure 4.11. Root singular value spectrum for all setups

The calculated natural frequencies and damping ratios are presented in Table 4.5 compared with the results by Peeters and Ventura (2003), and Reynders et al (2012). The identified results are the mean values obtained as the average of the MPVs for all setups. In addition, the posterior coefficient of variations including the setup-to-setup variability and identification are presented in Table 4.5, as well. The calculated MPVs of frequency and damping ratio are compatible with results by the previous studies (Peeters and Ventura, 2003; Reynders et al, 2012) The largest relative difference is less than 1%. Variations in the most probable frequency and damping ratios for the first two modes are presented in Figure 4.12 and Figure 4.13, respectively. Here, error bars show the posterior standard deviations. In addition, due to the large signal-to-noise ratio, the signal quality is observed to be good for all setups according to the results presented in Figure 4.14.

Table 4.5. Calculated frequencies and damping ratios

Mode Number	$f$ (Hz.)				$\xi$ (%)			
	Peeters and Ventura (2003)	Reynders et al (2012)	Present Study	c.o.v. (%)	Peeters and Ventura (2003)	Reynders et al (2012)	Present Study	c.o.v. (%)
1	3.86	3.86	3.85	0.30	0.90	0.80	0.92	24.54
2	4.90	4.90	4.89	0.41	1.40	1.40	1.36	19.34
3	9.77	9.76	9.77	0.25	1.30	1.40	1.19	27.59
4	10.30	10.30	10.32	0.87	1.40	1.30	1.94	54.40
5	12.50	12.42	12.53	1.15	2.50	2.80	3.18	36.84
6	13.20	13.22	13.22	0.86	3.00	3.40	3.05	37.45

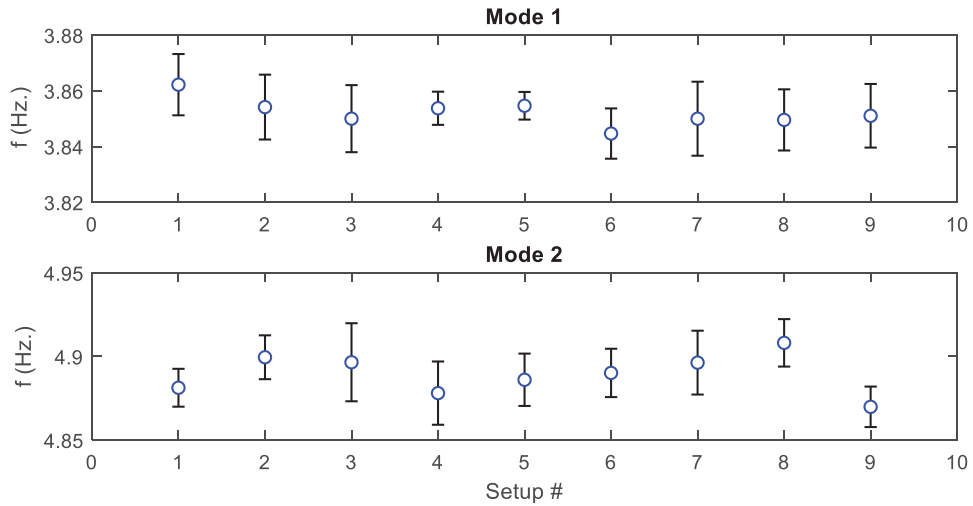


Figure 4.12. Identified frequencies with representative statistics

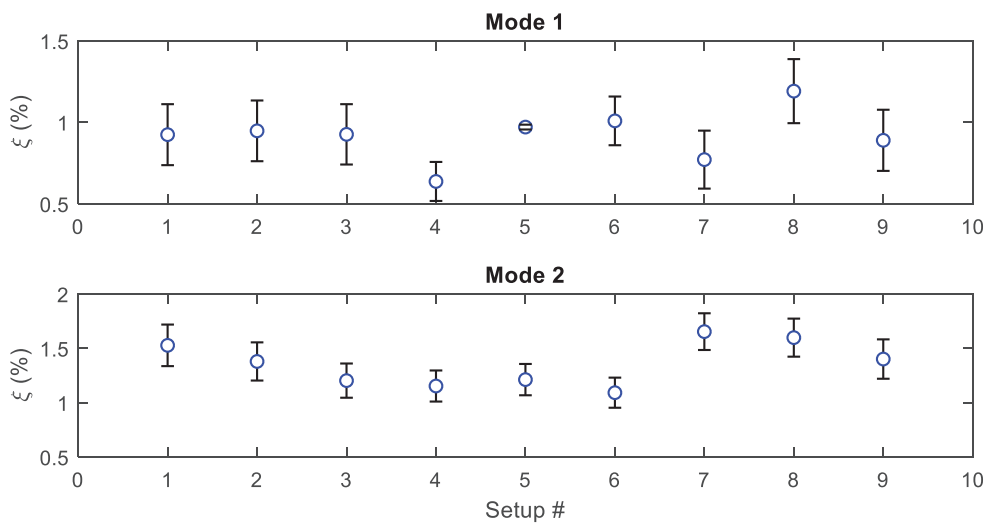


Figure 4.13. Identified damping ratios with representative statistics

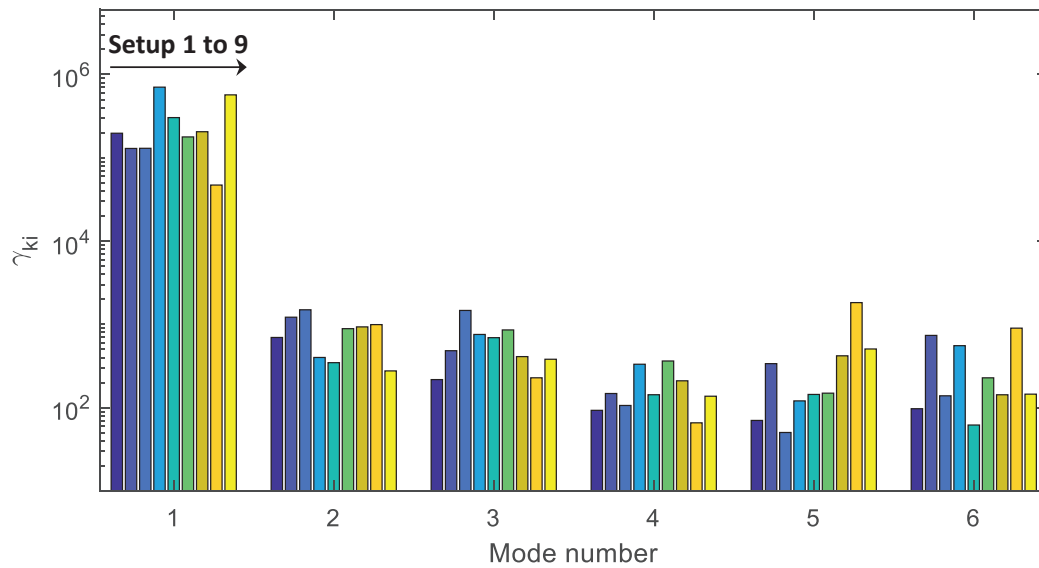


Figure 4.14. Variations in the identified signal-to-noise ratios among different setups

Figure 4.15 presents the assembled global mode shapes by the proposed algorithm. The mode shapes for the first six modes are well identified and seem compatible with previous studies (Peeters and Ventura, 2003; Reynders et al, 2012). The algorithm by Au (2017) gives similar results, and the first three modes are directly identified without iteration. Table 4.6 presents the calculated MAC values between the proposed methodology and the algorithm by Au (2017). Here,  $MAC_{as}$  and  $MAC_{ref}$  represent the MAC values between the final mode shapes by the proposed method, and the initial guess and final mode shapes obtained from the algorithm by Au (2017), respectively. It is seen that the results are similar for both methodologies. The fourth mode, however, shows a difference about 12% between the initial guess by Au (2017) and the final mode shapes.

Table 4.6. MAC values for the estimated mode shapes

<i>Mode number</i>	<i>EMAC</i>	<i>MAC<sub>as</sub></i>	<i>MAC<sub>ref</sub></i>
1	1.0000	1.0000	1.0000
2	1.0000	0.9999	1.0000
3	1.0000	1.0000	1.0000
4	1.0000	0.8826	1.0000
5	1.0000	0.9992	0.9999
6	1.0000	0.9991	1.0000

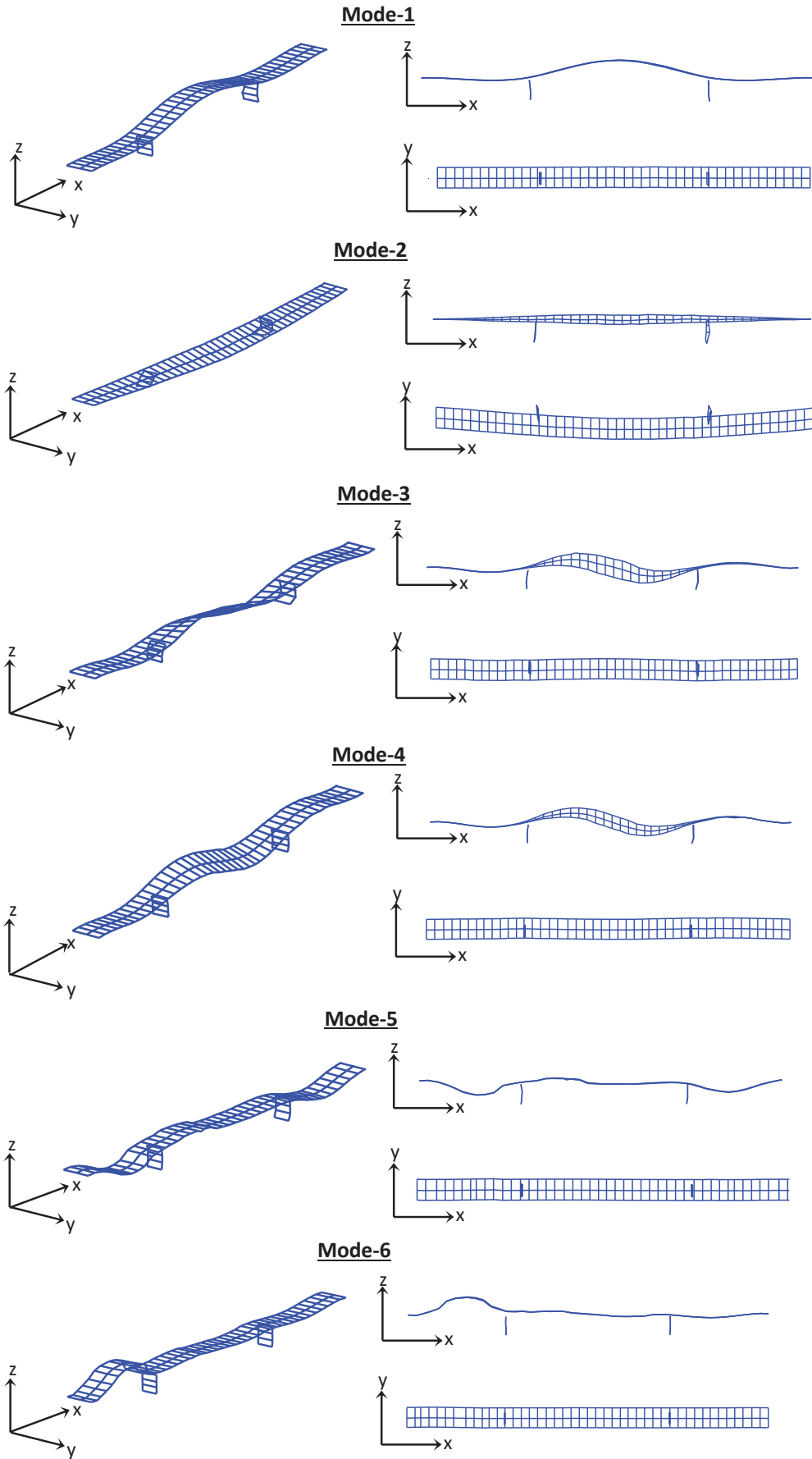


Figure 4.15. Identified mode shapes by the proposed modified algorithm

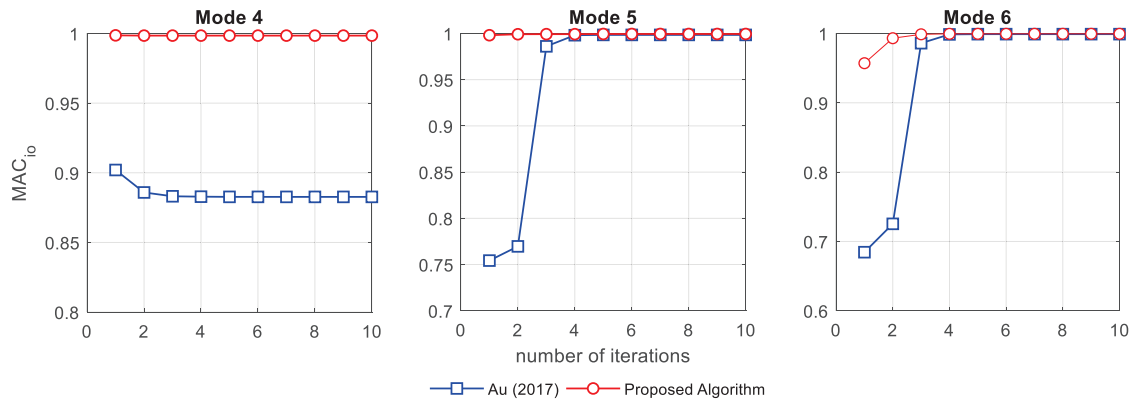


Figure 4.16. Variations in  $MAC_{i,0}$  values with respect to number of iterations

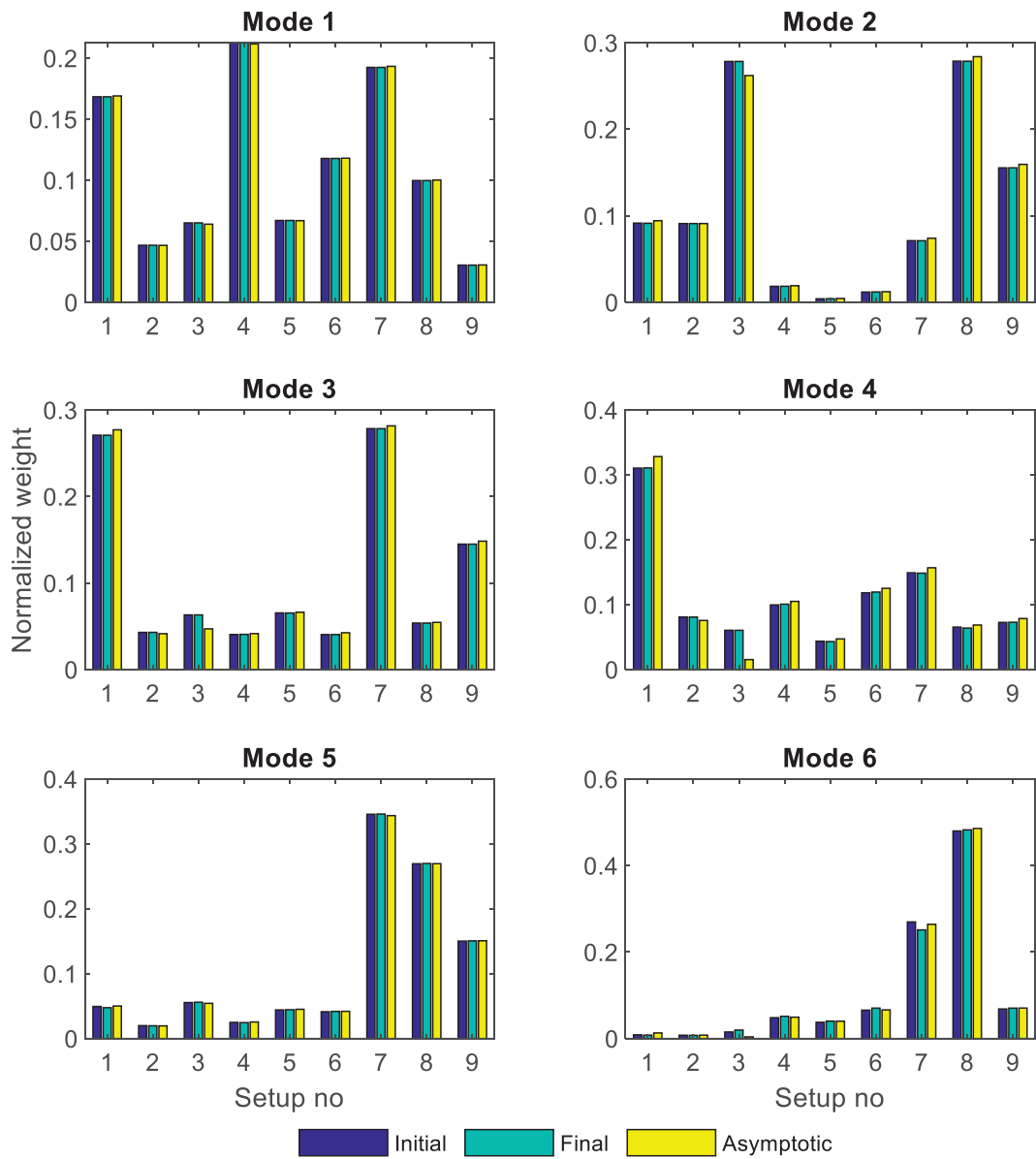


Figure 4.17. Variations in calculated setup weights

Convergence of MAC values with respect to the iteration number is presented in Figure 4.16. Here,  $MAC_{i,0}$  = MAC value between the mode shapes at the  $i^{th}$  iteration and the initial guess of each algorithms. According to Figure 4.16, the estimation of the 4<sup>th</sup> mode shape diverges down to a MAC value of 0.88 from the initial guess with the algorithm by Au (2017). Further, estimations of mode five and six, initially show a significant divergence from the initial guess which is cancelled out in a few numbers of iteration. The MAC values for the proposed algorithm, however, indicates that nearly no change takes place during iteration. The proposed algorithm reaches to this optimal global mode shape without iteration, and therefore it can be concluded that the initial guess of the proposed algorithm is more feasible. The difference between the initial guess by Au (2017) and the proposed algorithm lies in the involvement of spectrum parameters in the calculation of initial guess by the proposed algorithm.

In order to figure out the reason of the divergence in the MAC values, especially for mode 4, the calculated normalized weights of the setups in the global mode shapes are presented in Figure 4.17. For mode 4, it can be seen that the asymptotic weight is much lower than the weights calculated by the proposed methodology at setup 4. This case is not the reason, but it may be considered to be in parallel with the divergence in the MAC value as shown in Figure 4.16.

### 4.5.3. Application for Closely Spaced Modes: One Rincon Tower

The presented method is applied to the measurements acquired from the One Rincon Tower which is previously investigated in Section 2.7.5. The measured data is separated to six setups (see Table 4.7), and first lateral (EW) and translational (NS) mode shapes are identified by using the presented methodology.

Figure 4.18 presents the identified average frequencies and damping ratios with setup-to-setup variability in terms of coefficient of variation. Here, dashed line denotes the most probable values obtained by using the single setup algorithm. Results show that local MPVs reasonably match with the MPVs that are obtained by single mode approach.

Figure 4.19 presents the assembled mode shapes by using the proposed algorithm. At first view, it is seen that the identified mode shapes are reasonable. The MAC values between the mode shapes that are identified by using the closely spaced modes and single



mode algorithms are obtained as 0.9982 and 0.9955, respectively. In addition, EMAC values are obtained as 0.9996 and 0.9996 for closely spaced modes.

Table 4.7. Sensor placements for measurement setups

<i>Setup No</i>	<i>Measured Sensors</i>
1	7, 8, 9 10, 11, 39, 40, 41 42, 43
2	42, 43 50, 51, 52, 12, 13, 14, 44, 45, 53, 54, 55
3	53, 54, 55, 56, 57, 58, 15, 16, 65, 66, 17, 18, 19, 20
4	18, 19, 20, 59, 60, 61, 46, 47, 21, 22,23
5	21, 22, 23, 48, 49, 62, 63, 64, 24, 25, 67, 68, 26, 27, 28, 29
6	27, 28, 29, 69, 30, 70, 71, 72, 31, 32, 33, 35, 36

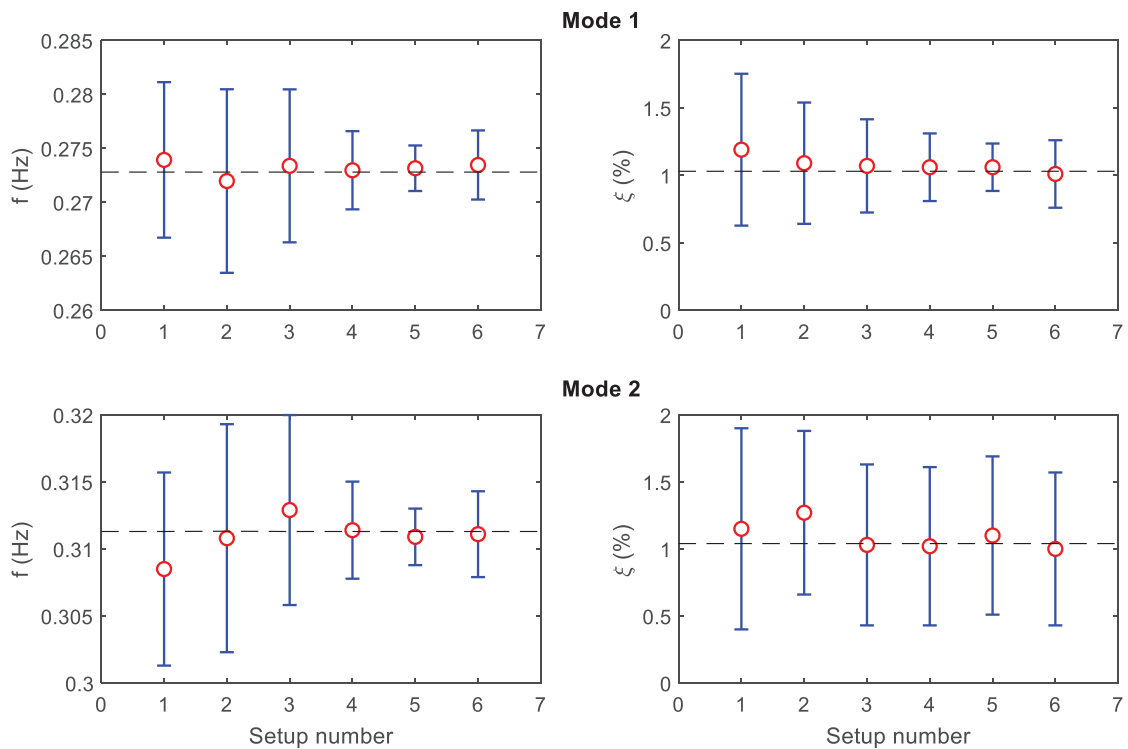


Figure 4.18. Identified natural frequencies and damping ratios with standard deviations

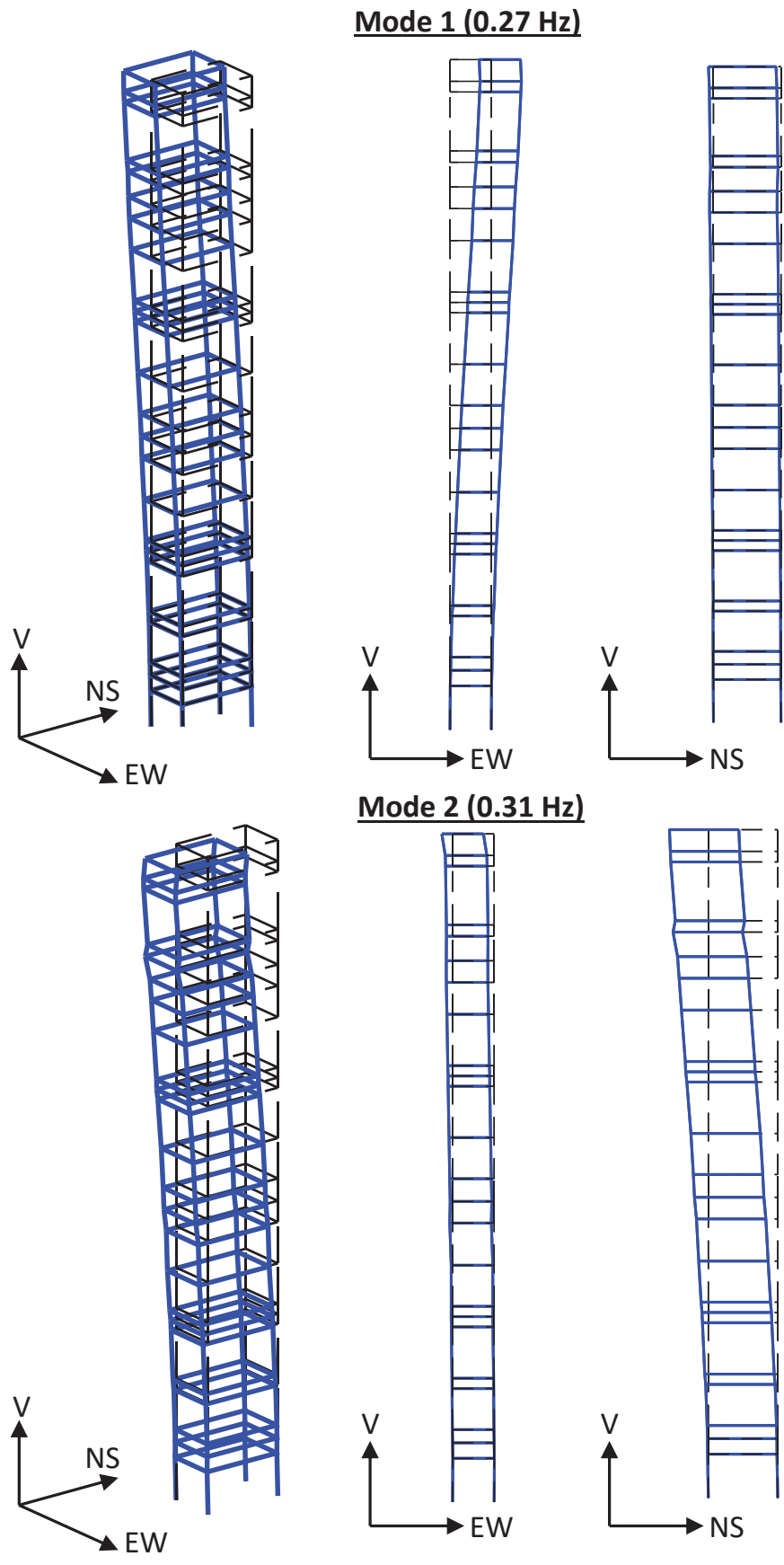


Figure 4.19. Identified mode shapes

#### 4.5.4. Numerical Analysis: A Comparison for Posterior Uncertainty Quantification

The computational time required by the proposed posterior uncertainty quantification methodology for multiple setups is compared to the method by Au and Xie (2017) via an illustrative example. For this purpose, an analytical shear frame model is considered whose fundamental frequency and damping ratio are set to 1 Hz, and 1%, respectively. The number of measurement setups varies from 1 to 100. Only two DOFs are measured at each setup with a single roving reference sensor. An *i.i.d.* Gaussian excitation with modal PSD of  $10 \mu\text{g}^2/\text{Hz}$  is generated as ambient loading with 100 Hz sampling ratio and 300 sec duration, and the measured response is contaminated by a Gaussian white noise with PSD of  $1 \mu\text{g}^2/\text{Hz}$  for each setup. The calculations are carried out by a notebook computer with i7 6700HQ 2.60 GHz processor and 16 GB RAM.

Figure 4.20 presents a comparison of the required computational time versus the number of setups,  $N_s$ , for the proposed methodology and the method by Au and Xie (2017). It is seen that the proposed methodology requires significantly less computational time when  $N_s > 10$ . The reason of this difference lies in the fact that the dimension of the Hessian matrix increases remarkably for larger  $N_s$  values.

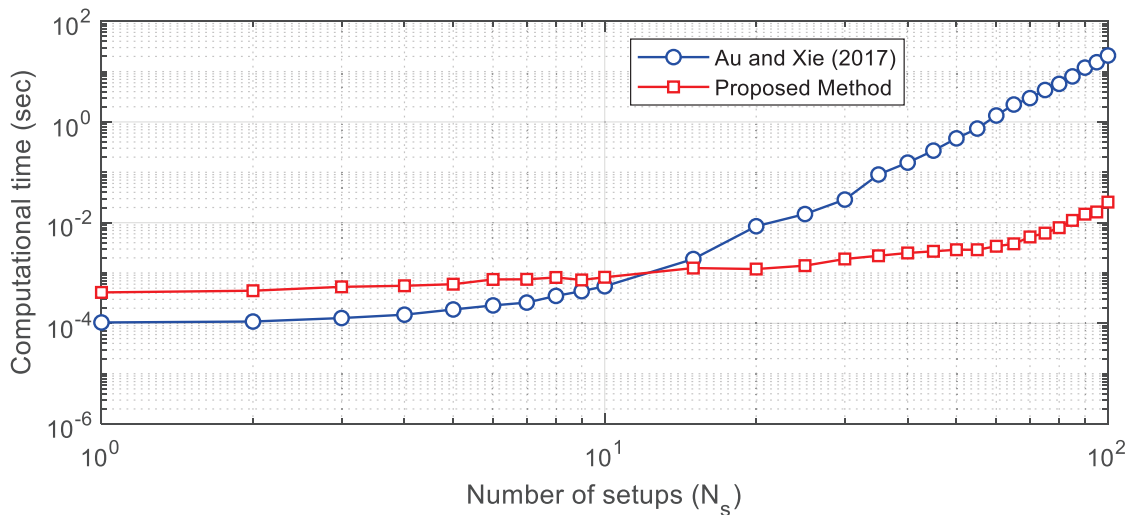


Figure 4.20. Comparison of the computational time required for the calculation of posterior covariance matrix

## 4.6. Concluding Remarks

In this chapter, an alternative mode shape assembly algorithm based on the two-stage BFFTA is presented, and the uniqueness of the solution is verified analytically by using two main methodologies available in the literature. These are based on the direct estimation of the global mode shape vector incorporating the FFT data or assembling the identified local mode shapes by using the Gaussian approximation, respectively. The proposed methodology is implemented to a ten-story laboratory shear frame and a benchmark study, and the obtained results are compared to the algorithm by Au (2017). The general conclusions are summarized below.

- The proposed procedure considers that each setup is weighted by its Hessian matrix (for local mode shape) and the local mode shape information conducted with spectrum parameters is embedded in this matrix. Thus, the global mode shape vector is obtained by assembling the local Hessian matrices and it is not necessary to obtain the optimal local mode shape vectors for each setup.
- In the literature, the initial guess for global mode shape vector assumes large signal-to-noise ratio and neglects the effect of data quality. If the signal-to-noise ratio is not adequately large for all or a few setups, however, the initial guess may significantly diverge from the optimal mode shape. The proposed application, on the other hand, uses the two-stage approach leading to a more reasonable initial guess for global mode shapes which increases the convergence speed during iteration.
- When the data quality is well in each setup, the identified mode shapes shows no significant variance among any method that is being used. According to the results by the ten-story shear frame study, however, it is seen that the quality of identified mode shapes by the proposed algorithm is improved when the signal-to-noise ratio is low.

## CHAPTER 5

# A TWO-STAGE BAYESIAN APPROACH FOR FINITE ELEMENT MODEL UPDATING BY USING ACCELERATION RESPONSE DATA FROM MULTIPLE SETUP MEASUREMENTS

### 5.1. Introduction

Finite element (FE) model updating has great importance in damage detection of structures and calibration of the considered mathematical model with respect to actual effects. For this reason, model updating has received the attention of many researchers over the years. While damage detection is possible with measured vibration response data only, FE model updating might be more effective on the detection of damage location and severity (Yan and Katafygiotis, 2015c). Various FE model updating approaches are available in the literature (Mottershead and Friswell, 1993; Yang and Chen, 2010; Mottershead et al, 2011; Touat et al, 2014). The most generic form of these approaches is based on the determination of system eigenvalues and eigenvectors that are best-fitted with measured (or identified) ones (Yuen, 2010). The problem of obtaining the best-fit between the measured and model parameters can be solved by weighted least-squares. However, some problems inevitable arises in this procedure. The major one of these problems is referred as mode-matching problem (Yuen, 2010; Yan & Katafygiotis, 2015c). For large scale structures, only a few number of lower modes can be determined by modal identification methods. Therefore, the higher modes which dominate the stiffness components are not able to be matched with measured counterparts. In addition, some lower modes may not be identified due to the low ambient excitation level or high level of environmental and/or instrumental noise effects on the measurements. Another problem is existence of incomplete data. When the structure is measured with limited number of sensors, the measured DOF represents only a local part of the whole structure. To solve this problem, the investigated structure may be measured by multiple setups. In this case, the matching of global modal shapes with local parts and FE eigenvectors arises

as another issue. All these issues are also incorporated with a mode matching problem. The solution of this problem is part of the response of how to quantify the parametric uncertainties. For this reason, the FE updating approaches based on stochastic processes have been employed by the researchers within the past decades. Friswell (1989) presented a minimum variance estimator based on the minimization of the expected variance of measurement errors. Here, the basic idea is to consider the effect of measurement noise while matching the measured and modeled parameters. A two-stage covariance minimization method was presented by Govers and Link (2010) incorporating the multiple experimental setups based on a similar idea. At first stage, the expected values and their uncertainties are obtained by taking the sample mean and covariance of experimental parameters among different setups. Second, the model parameter covariance matrix is updated by minimizing the discrepancy between the analytical and experimental results. Various similar stochastic approaches such as perturbation method based on parameter-model variability estimation (Khodaparast et al, 2008; Husain et al, 2012), or robust updating formulation by random matrix theory for uncertain computational models (Soize et al, 2008) are available in the literature.

In previous researches, FE model updating have been also considered based on the probabilistic logic to solve the mode matching problem (Katafygiostis and Beck, 1998; Katafygiostis et al, 1998; Lam et al, 2015; Mustafa and Matsumoto, 2017; Prajapat and Chaudhuri, 2018). In the methodology presented by Beck and Katafygiostis (1998), the optimal (or updated) model parameters are obtained as the most probable value within a chosen class of structural models by Bayesian statistical framework assuming all the models have equally weighted prior distributions. This procedure requires updating the posterior most probable value by integrating the prior distributions over the whole parameter space. This evaluation process is defined as difficult by Beck and Au (2002) due to the large dimension for numerical integration, and a Markov Chain Monte Carlo simulation is employed to reduce the computational effort. A two-stage Bayesian model updating procedure was proposed by Ching and Beck (2004). In this procedure, first, the modal identification procedure is completed, and experimental modal parameters are updated. Second, a prior distribution for stiffness parameters are defined, and finally most probable model parameters are obtained by applying Bayes' theorem. This procedure is applied for both reference (undamaged) and damaged cases, and a damage extent is defined in order to measure the severity of damage level. A similar methodology is introduced by Yuen and Kuok (2011) for modal updating with incomplete measured data

assuming the mass parameters are known. In this methodology, the prior distribution of stiffness parameters is assumed to be Gaussian with large variance so that the prior stiffness parameters are overestimated. Yan and Katafygiotis (2015c) proposed a Bayesian approach for model updating by utilizing the multiple setup measurements. Here, the optimal (most probable) global mode shape is obtained by assembling identified local mode shapes via their prior distributions. Different from the Yuen and Kuok (2011), the eigenvalues are not considered as model parameters to be updated. The formulation considers stiffness, mass and global mode shape uncertainty. Selection of prior distribution is similar with Yuen and Kuok (2011). However, the selection of prior variance for mass parameters is adequately small so that the prior probability for mass parameters is assumed to be well estimated. The assumption of well estimated mass parameters stands on two cases: (i) proper estimation of mass matrix is relatively more possible in comparison with stiffness parameters, (ii) the correlation between the stiffness and mass parameters might make the solution ill-conditioned when both are not considered as well-estimated.

Another major problem in Bayesian FE model updating is the definition of prior distributions for mass and stiffness parameters since they are strictly positive definite. For this reason, using of standard Gaussian distribution becomes unsuccessful to estimate prior probabilities. To solve this problem, the truncated Gaussian distribution (Yan and Katafygiotis, 2015c; Yuen, 2010) or lognormal distribution (Das and Debnath, 2018) may be used. In addition, inverse beta or gamma distributions are also reasonable for prior estimation (Mathai and Moschopoulos, 1997; Furman, 2008).

This chapter presents a Bayesian FE model updating approach utilizing the ambient vibration data from multiple setup measurements. The overall procedure rests on two stages. In the first stage, the MPV of eigenvalues (frequencies) and posterior covariance matrix of eigenvalues and eigenvectors (mode shapes) are obtained by the Bayesian Fast Fourier Transform Approach (BFFTA) and the prior probability distribution of eigenvalues and eigenvectors are estimated by Gaussian approximation of their posterior PDFs. At second stage, the model parameters including eigenvalues, eigenvectors, stiffness and mass parameters are updated by using Bayesian inference. The previous two-stage algorithms (Au and Zhang, 2016; Zhang and Au, 2016; Zhang et al, 2017) consider the posterior covariance matrix for local mode shape as being block diagonal for large values of signal-to-noise ratio. In this study, however, a block diagonal covariance matrix is derived independent from the signal-to-noise ratio. Further, the

modelling error in the eigen equations are considered as a model parameter to be updated. The prior probability distribution for stiffness and mass parameters are assumed as truncated Gaussian. The prior variance of modelling error and measured parameters are considered as soft constraints so that they are updated within the procedure. Further, the effect of soft constraint approximation on the updated parameters and their posterior uncertainties are compared to the rigid constraint (prescribed prior variance) approximation.

## 5.2. Stage I: Modal Identification

Eigenvalues and eigenvectors of the finite element model are expected to represent the whole structure. However, the modal information extracted from measurement data are constrained with the measurement points. In most cases, taking a full-scale measurement may not be possible due to the lack of instruments. The eigenvalues might be obtained with good accuracy by system identification. However, the identified eigenvectors may not represent the system eigenvectors properly when insufficient measurement points are available only. This problem can be confronted by increasing the measurement setups. Thus, the posterior distribution of the modal parameters for each setup can be considered as a proper prior estimation for system eigenvalues and eigenvectors. For this purpose, first BFFTA can be implemented to identify the most probable eigenvalues and eigenvectors, and their posterior uncertainties. Second, their posterior probability distribution can be estimated by Gaussian approximation. According to the fast BFFTA presented by Au (2011a), the negative-likelihood function for modal parameters to be identified, within the resonant frequency band of  $n^{th}$  mode at setup  $i$ , can be defined as follows.

$$\begin{aligned}
L_{ni}(\Theta_{ni}) &= N_i N_{f,ni} \ln \pi + (N_{f,ni} - 1) \ln S_{e,ni} + \sum_k \ln (\bar{S}_{ni} D_{k,ni} + S_{e,ni}) + S_{e,ni}^{-1} \kappa_{ni} \\
&\quad - \varphi_{ni}^T \Delta_{ni} \varphi_{ni} \\
\kappa_{ni} &= \sum_k F_{ki}^* F_{ki}; \quad \Delta_i = \sum_k \frac{\bar{S}_i D_{k,ni} S_{e,ni}^{-1}}{(\bar{S}_{ni} D_{k,ni} + S_{e,ni})} \text{Re}(F_{ki} F_{ki}^*)
\end{aligned} \tag{5.1}$$

In addition,  $L_{ni}(\Theta_{ni})$  should be subjected to the constraint of  $\varphi_{ni}^T \varphi_{ni} = 1$ . Here,  $\Theta_{ni} = [\lambda_{ni}, \zeta_{ni}, \bar{S}_{ni}, S_{e,ni}, \varphi_{ni}]$ , is the set of modal parameters to be identified and comprises the eigenvalue (square of natural angular frequency), damping ratio, spectral density of modal excitation that is scaled with respect to the unit norm for local mode shape, spectral



density of prediction error, and local mode shape vector (with unit norm),  $F_{ki}$  = FFT of acceleration response,  $N_{f,ni}$  = # of data within the selected frequency band, for  $i^{\text{th}}$  setup, respectively. In addition,  $D_{k,ni}$  denotes the dynamic amplification and can be written as,

$$D_{k,ni} = \left[ (1 - \beta_{k,ni})^2 + 4\xi_{ni}^2 \beta_{k,ni} \right]^{-1}; \quad \beta_{k,ni} = \lambda_{ni} / \lambda_k; \quad \lambda_k = 2\pi f_k \quad (5.2)$$

where  $f_k$  = excitation frequency. Minimizing Eq. (4.23) gives the most probable modal parameters for  $i^{\text{th}}$  setup. At the next step, the posterior probability of modal parameters can be well-estimated by Gaussian distribution (Au, 2011a).

$$p(\Theta_{ni} | Z_{ki}) \approx \exp \left[ -\frac{1}{2} (\Theta_{ni} - \hat{\Theta}_{ni})^T H_{\hat{\Theta}_{ni}} (\Theta_{ni} - \hat{\Theta}_{ni}) \right] \quad (5.3)$$

Here,  $Z_{ki} = [\text{Re}(F_{ki}); \text{Im}(F_{ki})] \in \mathfrak{R}$  denotes the augmented FFT vector of the measured response at the  $i^{\text{th}}$  setup, and  $H_{\hat{\Theta}_i}$  = Hessian of Eq. (4.23) under norm constraint at  $\Theta_i = \hat{\Theta}_i$ .  $H_{\hat{\Theta}_i}$  is obtained as a block diagonal matrix and written as below (see Section 2.5.2).

$$H_{\hat{\Theta}_{ni}} = \begin{bmatrix} H_{\hat{\Theta}_{s,ni}} & 0 \\ 0 & H_{\hat{\varphi}_{ni}} \end{bmatrix} \quad (5.4)$$

Here,  $\hat{\Theta}_{s,ni} = [\hat{\lambda}_{ni}, \hat{\xi}_{ni}, \hat{S}_{ni}, \hat{S}_{e,ni}]$ ,  $H_{\hat{\Theta}_{s,ni}} = \nabla^2 L(\hat{\Theta}_{si}, \hat{\Theta}_{si})$ , and  $H_{\hat{\varphi}_{ni}} = \nabla^2 L(\hat{\varphi}_{ni}, \hat{\varphi}_{ni}) + 2\bar{\alpha}_{ni} I_{N_i}$ , ( $\bar{\alpha}_i$  = Lagrange multiplier that enforces the unit norm of  $\hat{\varphi}_{ni}$ ,  $N_i$  = # of measured DOF at  $i^{\text{th}}$  setup). Note that  $H_{\hat{\varphi}_i}$  is a semi positive definite matrix whose null vector corresponds to  $\hat{\varphi}_{ni}$  (see Section 2.4.2).

$$\bar{\alpha}_{ni} = -2\hat{\varphi}_{ni}^T \nabla^2 L \hat{\varphi}_{ni} \Rightarrow \hat{\varphi}_{ni}^T H_{\hat{\varphi}_{ni}} \hat{\varphi}_{ni} = 0 \quad (5.5)$$

### 5.3. Stage II: Model Updating

The prior probability distributions required for FE model updating are defined in this stage. Here, the prior probability distribution of eigenvalues and eigenvectors are modeled by the posterior probability estimation obtained from the modal identification stage. In addition, a prior probability distribution for modelling error in the eigenvalue equations is considered in order to avoid the mode matching problem. Then, the posterior PDF of the model parameters is estimated by using Bayes' theorem. Finally, the FE model is updated by maximum likelihood estimation of the posterior PDF that is obtained by Bayesian inference.

### 5.3.1. Prior Probability Distributions of Eigenvalues and Eigenvectors

The modal parameters to be updated comprise the eigenvalues and eigenvectors with a prediction error for  $i^{th}$  setup. Thus, the eigenvalue and local eigenvector of each setup can be defined by

$$\chi_{ni} = \hat{\chi}_{ni} + \varepsilon_{\chi_{ni}} \quad (5.6)$$

where,  $\chi_{ni} = [\lambda_n, r_{ni}^{-1} \Gamma_{oi} \Phi_n]^T$  denotes the set of system modal parameters,  $\Gamma_{oi}$  = selection matrix that extracts the measured DOFs at  $i^{th}$  setup,  $\hat{\chi}_{ni} = [\hat{\lambda}_{ni}, \hat{\phi}_{ni}]^T$  is the set of most probable local modal parameters obtained at the first stage, and  $\varepsilon_{\chi_{ni}}$  = prediction error, respectively. In addition,  $\lambda_n$  and  $\Phi_n$  denote the  $n^{th}$  mode eigenvalue and eigenvector (global mode shape vector) of the finite element model, respectively. The error term,  $\varepsilon_{\chi_{ni}}$  can be assumed to follow a zero mean Gaussian distribution, and this distribution can be assumed as the posterior of the local eigenvalues and eigenvectors. When  $\varepsilon_{\chi_{ni}}$  is assumed to be linearly independent for each setup, the prior probability distribution of the prediction error can be written as

$$p(\varepsilon_{\chi} | \hat{\Theta}_s) = \prod_{n=1}^{N_m} \prod_{i=1}^{N_s} p(\varepsilon_{\chi_{ni}} | \hat{\Theta}_{sni}) \approx \prod_{n=1}^{N_m} \prod_{i=1}^{N_s} \exp \left\{ -\frac{1}{2} (\chi_n - \hat{\chi}_{ni})^T H_{\hat{\chi}_{ni}} (\chi_n - \hat{\chi}_{ni}) \right\} \quad (5.7)$$

where  $N_s$  = number of measurement setups,  $N_m$  = number of considered modes, and  $\hat{\Theta}_s = [\hat{\Theta}_{s11}, \dots, \hat{\Theta}_{sN_m N_s}]$ . In addition,  $H_{\hat{\chi}_{ni}}$  denotes the Hessian with respect to  $\chi_{ni}$  at  $\chi_{ni} = \hat{\chi}_{ni}$  can be obtained by the BFFTA. Thus,  $H_{\hat{\chi}_{ni}}$  is written as a block diagonal matrix.

$$H_{\hat{\chi}_{ni}} = \begin{bmatrix} H_{\hat{\lambda}_{ni}} & \mathbf{0}_{1 \times N_i} \\ \mathbf{0}_{N_i \times 1} & H_{\hat{\phi}_{ni}} \end{bmatrix} \quad (5.8)$$

### 5.3.2. Estimation of Prior Stiffness and Mass Distributions

The prior probability distribution of mass and stiffness parameters are considered as truncated Gaussian. The mass parameters of civil structures generally can be estimated with high accuracy. Therefore, the mass parameters are assumed to be well-estimated with small prior covariance (Yan and Katafygiotis, 2015c). The prior probability

distributions for mass parameters are assumed to be linearly independent (zero correlation between each mass parameter). Thus, the prior mass distribution can be defined as below.

$$p(\rho) = \prod_{r=1}^{N_\rho} p(\rho_r) \quad (5.9)$$

where,  $\rho = [\rho_1, \rho_2, \dots, \rho_{N_\rho}]$  indicates the set of mass parameters to be updated,  $\rho_r = r^{th}$  mass parameter, and  $N_\rho =$  number of mass parameters. Here,  $p(\rho_r)$  can be defined as below.

$$p(\rho_r) \propto \begin{cases} \exp\left\{-\frac{(\rho_r - \hat{\rho}_{r0})^2}{S_{\hat{\rho}_o}}\right\}, & \text{for } \rho_r > 0 \\ 0, & \text{for } \rho_r \leq 0 \end{cases} \quad (5.10)$$

where  $\hat{\rho}_{r0} =$  prior estimation for  $r^{th}$  mass parameter,  $S_{\hat{\rho}_o} =$  constant prior variance for each mass parameter. The covariance matrix for mass parameters is assumed to be diagonal (as  $S_{\hat{\rho}_o} I_{N_\rho}$ ). Similarly, the prior distribution for stiffness parameters are defined as below.

$$p(\theta) = \prod_{r=1}^{N_\theta} p(\theta_r)$$

$$p(\theta_r) \propto \begin{cases} \exp\left\{-\frac{(\theta_r - \hat{\theta}_{r0})^2}{S_{\hat{\theta}_o}}\right\}, & \text{for } \theta_r > 0 \\ 0, & \text{for } \theta_r \leq 0 \end{cases} \quad (5.11)$$

Here,  $\theta =$  set of stiffness parameters,  $\theta_r = r^{th}$  mass parameter,  $\hat{\theta}_{r0} =$  prior estimation for  $r^{th}$  stiffness parameter,  $S_{\hat{\theta}_o} =$  constant prior variance for each stiffness parameter, and  $N_\theta =$  number of stiffness parameters.

### 5.3.3. Prior Probability Distribution for Modelling Error

Considering a general eigenvalue-eigenvector problem for a particular mode,  $n$ , the following equality can be constructed for a modal updating problem.

$$K\Phi_n = \lambda_n M\Phi_n + \varepsilon_m \quad (5.12)$$

in which  $K$  and  $M$  are the parametric stiffness and mass matrices, respectively. In addition,  $\lambda_n$ ,  $\Phi_n$  and  $\varepsilon_m$  denote the eigenvalue (square of natural angular frequency), eigenvector (mode shape), and modelling error for  $n^{th}$  mode, respectively. Assuming that

$\varepsilon_m$  follows a zero mean Gaussian distribution, the following pdf can be defined for a given set of system modal parameters,  $\chi = [\chi_1, \dots, \chi_{N_m}]$ ,

$$p(\varepsilon_m | \chi) = (2\pi S_{\hat{\varepsilon}})^{-N/2} \exp(\varepsilon_m^T S_{\hat{\varepsilon}}^{-1} \varepsilon_m) \quad (5.13)$$

where  $S_{\hat{\varepsilon}}$  = expected variance of modelling error (assumed to be constant and uniform for each mode), and  $N$  = number of DOFs in the finite element model. The prediction error can be defined in terms of mass and stiffness parameter as below.

$$\varepsilon_m = (K - \lambda_n M) \Phi_n = \Omega_n \Phi_n \quad (5.14)$$

Substituting Eq. (5.14) into Eq. (5.13) leads to the following conditional probability function.

$$p(\varepsilon | \lambda_n, \Phi_n, \theta, \rho) = (2\pi S_{\hat{\varepsilon}})^{-N/2} \exp(\Phi_n^T \Omega_n^T S_{\hat{\varepsilon}}^{-1} \Omega_n \Phi_n) \quad (5.15)$$

Here, the parametric stiffness and mass matrices are defined as follows.

$$K = K_0 + \sum_{r=1}^{N_{\theta}} \theta_r K_r \quad M = M_0 + \sum_{r=1}^{N_{\rho}} \rho_r M_r \quad (5.16)$$

where,  $K_0$  and  $M_0$  are  $N \times N$  sized non-parametric stiffness and mass matrices,  $K_r$ , and  $M_r = N \times N$  sized  $r^{th}$  non-parametric sub-structural stiffness and mass matrices.

### 5.3.4. Posterior Probability Distribution for System Parameters

Applying the Bayes' theorem, the posterior probability distribution for model parameters can be written as follows.

$$p(\theta, \rho, \chi | \varepsilon_{\chi}, \varepsilon_m) = c_0 \times p(\varepsilon_{\chi} | \chi) \times p(\varepsilon_m | \hat{\Theta}_s) \times p(\theta) \times p(\rho) \quad (5.17)$$

where,  $\chi = [\chi_1 \ \dots \ \chi_{N_m}]$ , and  $c_0$  denotes a normalizing constant. The negative-logarithm likelihood function for Eq. (5.17) is obtained as follows by utilizing Eqs. (5.10), (5.11), (5.15), and (5.7).

$$\begin{aligned} L(\theta, \rho, \chi) &= \frac{1}{2} \sum_{n=1}^{N_m} \sum_{i=1}^{N_s} (r_{ni}^{-1} \Gamma_{oi} \Phi_n - \hat{\varphi}_{ni})^T H_{\hat{\varphi}_i} (r_{ni}^{-1} \Gamma_{oi} \Phi_n - \hat{\varphi}_{ni}) + \frac{1}{2} \sum_{n=1}^{N_m} \sum_{i=1}^{N_s} (\lambda_n - \hat{\lambda}_{ni})^2 H_{\hat{\lambda}_{ni}} \\ &+ \frac{1}{2} (\theta - \hat{\theta}_0)^T S_{\hat{\theta}_0}^{-1} (\theta - \hat{\theta}_0) + \frac{1}{2} (\rho - \hat{\rho}_0)^T S_{\hat{\rho}_0}^{-1} (\rho - \hat{\rho}_0) + \frac{1}{2} N_m N \ln 2\pi + \frac{1}{2} N_m N \ln S_{\hat{\varepsilon}} \quad (5.18) \\ &+ \frac{1}{2} \sum_{n=1}^{N_m} \Phi_n^T \Omega_n^T S_{\hat{\varepsilon}}^{-1} \Omega_n \Phi_n \end{aligned}$$

Here, a unit norm constraint should be defined for  $\Gamma_{oi}\Phi_n$  and  $\Phi_n$ , respectively. Thus, Eq. (5.18) leads to a linear optimization problem as below.

$$J(\theta, \rho, \chi, \alpha, \beta) = L(\theta, \rho, \chi) + \sum_{i=1}^{N_s} \alpha_{ni} \left( \Phi_n^T \Gamma_{oi}^T \Gamma_{oi} \Phi_n - r_{ni}^2 \right) + \beta \left( \Phi_n^T \Phi_n - 1 \right) \quad (5.19)$$

where  $\alpha = [\alpha_{11}, \dots, \alpha_{N_m N_s}]$ . MPV of model parameters can be estimated by minimizing Eq. (5.19) with respect to  $\theta, \rho$ , and  $\chi$ .

### 5.3.4.1. MPV of Modal Parameters

Eq. (5.19) defines a set of modal parameters,  $\chi$ , that covers all measurement setups. For this reason, the posterior MPV of  $\chi$  is incorporated with measured response data as well as structural model parameters. Thus, the minimization process performs a posterior modal identification and model updating together. In this context, minimizing Eq. (5.19) with respect to  $\lambda_n$ , and  $\Phi_n$  gives the most probable posterior modal parameters incorporated with structural model parameters.

The first order derivative of Eq. (5.19) with respect to  $\lambda_n$  gives

$$\left. \frac{\partial J}{\partial \lambda_n} \right|_{\lambda_n = \hat{\lambda}_n} = 0 \Rightarrow \hat{\lambda}_n = \left( S_{\hat{\varepsilon}}^{-1} G_{\lambda_n} + \sum_{i=1}^{N_s} H_{\hat{\lambda}_{ni}} \right)^{-1} \times \left( S_{\hat{\varepsilon}}^{-1} g_{\lambda_n} + \sum_{i=1}^{N_s} H_{\hat{\lambda}_{ni}} \hat{\lambda}_{ni} \right) \quad (5.20)$$

Here,  $G_{\lambda_n} = \Phi_n^T M^T M \Phi_n$ , and  $g_{\lambda_n} = \Phi_n^T K^T M \Phi_n$ . If the modelling error is neglected, the MPV of  $\lambda_n$  can be set to the most probable values obtained from the measurements as below;

$$\hat{\lambda}_n = \left( \sum_{i=1}^{N_s} H_{\hat{\lambda}_{ni}} \right)^{-1} \times \sum_{i=1}^{N_s} H_{\hat{\lambda}_{ni}} \hat{\lambda}_{ni} \quad (5.21)$$

Eq. (5.21) can be used as the initial guess for  $\lambda_n$ . Similarly, minimizing Eq. (5.19) with respect to  $\Phi_n$  gives;

$$\begin{aligned} \left. \frac{\partial J}{\partial \Phi_n} \right|_{\Phi_n = \hat{\Phi}_n} &= 0 \\ \Rightarrow \left( \left\{ \sum_{i=1}^{N_s} \Gamma_{oi}^T \left( r_{ni}^{-2} H_{\hat{\varphi}_i} + 2\alpha_{ni} I_{N_i} \right) \Gamma_{oi} \right\} + \Omega_n^T S_{\hat{\varepsilon}}^{-1} \Omega_n \right) \hat{\Phi}_n - 2\beta_n \hat{\Phi}_n + \sum_{i=1}^{N_s} r_{ni}^{-1} \Gamma_{oi}^T H_{\hat{\varphi}_i} \hat{\varphi}_{ni} &= 0 \end{aligned} \quad (5.22)$$

Due to the fact that  $\hat{\varphi}_{ni}$  is the null vector of  $H_{\hat{\varphi}_{ni}}$  ( $H_{\hat{\varphi}_{ni}} \hat{\varphi}_{ni} = 0$ ), Eq. (5.22) leads to the following standard eigenvalue problem.

$$A_n \hat{\Phi}_n = \beta_n \hat{\Phi}_n \quad (5.23)$$

$$A_n = \frac{1}{2} \sum_{i=1}^{N_s} L_{oi}^T \left( r_{ni}^{-2} H_{\hat{\phi}_i} + 2\hat{\alpha}_{ni} I_{N_i} \right) L_{oi} + \frac{1}{2} \Omega_n^T S_{\hat{\varepsilon}}^{-1} \Omega_n \quad (5.24)$$

Thus, the optimal  $\Phi_n$  can be obtained as the eigenvector of  $A_n$  that corresponds to the minimum eigenvalue. When the norm constraint for  $\Phi_n$  is omitted in the solution,  $A_n$  is constrained to be a semi-positive definite matrix. However, this case is possible if and only if modelling and measurement errors are equal to zero. In reality, a zero error may not be obtained and therefore, the norm of  $\Phi_n$  is constrained to be 1 in the presented methodology. On the other hand, an initial estimation for  $\Phi_n$  can be obtained as the eigenvector (for minimum eigenvalue) of the following matrix by assuming zero discrepancy between  $r_{ni}^{-1} \Gamma_{oi} \Phi_n$  and  $\hat{\phi}_{ni}$  and neglecting the modelling error.

$$\sum_{i=1}^{N_s} \Gamma_{oi}^T H_{\hat{\phi}_i} \Gamma_{oi} \quad (5.25)$$

Optimal value of the Lagrange multiplier,  $\alpha_{ni}$  can be obtained by minimizing Eq. (5.19) with respect to  $r_{ni}$ . The first order derivative of Eq. (5.19) leads to the following equation.

$$\left. \frac{\partial J}{\partial r_{ni}} \right|_{r_{ni}=\hat{r}_{ni}, \alpha_{ni}=\hat{\alpha}_{ni}} = -\hat{r}_{ni}^{-3} \Phi_n^T \Gamma_{oi}^T H_{\hat{\phi}_{ni}} - 2\hat{\alpha}_{ni} \hat{r}_{ni} = 0 \quad (5.26)$$

Thus, the optimal  $\alpha_{ni}$  is obtained as follows.

$$\hat{\alpha}_{ni} = -\frac{\hat{r}_{ni}^{-4}}{2} \Phi_n^T \Gamma_{oi}^T H_{\hat{\phi}_{ni}}; \quad \hat{r}_{ni}^2 = \Phi_n^T \Gamma_{oi}^T \Gamma_{oi} \Phi_n \quad (5.27)$$

### 5.3.4.2. MPV of Model Parameters

Taking the first order derivative of Eq. (5.19) with respect to  $\theta$  and solving for optimal  $\hat{\theta}$  yields;

$$\begin{aligned} \left. \frac{\partial J}{\partial \theta} \right|_{\theta=\hat{\theta}} = 0 &\Rightarrow \hat{\theta} S_{\hat{\theta}_o}^{-1} - \hat{\theta}_o S_{\hat{\theta}_o}^{-1} + \sum_{n=1}^{N_m} S_{\varepsilon}^{-1} G_{K_n}^T G_{K_n} \hat{\theta} - \sum_{n=1}^{N_m} S_{\varepsilon}^{-1} G_{K_n}^T \mathbf{g}_{K_n} = 0 \\ \Rightarrow \hat{\theta} &= \left[ S_{\hat{\theta}_o}^{-1} I_{N_\theta} + \sum_{n=1}^{N_m} S_{\varepsilon}^{-1} G_{K_n}^T G_{K_n} \right]^{-1} \times \left[ \hat{\theta}_o S_{\hat{\theta}_o}^{-1} + \sum_{n=1}^{N_m} S_{\varepsilon}^{-1} G_{K_n}^T \mathbf{g}_{K_n} \right] \end{aligned} \quad (5.28)$$

where

$$G_{K_n} = \left[ K_1 \Phi_n \quad \dots \quad K_{N_\theta} \Phi_n \right]_{N \times N_\theta}; \quad \mathbf{g}_{K_n} = \left[ (\lambda_n M(\rho) - K_0) \Phi_n \right]_{N \times 1} \quad (5.29)$$

Similarly, minimizing Eq. (5.19) with respect to  $\rho$  gives the optimal mass parameter vector as below.

$$\begin{aligned}
\left. \frac{\partial J}{\partial \rho} \right|_{\rho=\hat{\rho}} &= 0 \\
\Rightarrow \hat{\rho} S_{\hat{\rho}_0}^{-1} - \hat{\rho}_0 S_{\hat{\rho}_0}^{-1} + \sum_{n=1}^{N_m} S_{\hat{\varepsilon}}^{-1} G_{M_n}^T G_{M_n} \hat{\rho} - \sum_{n=1}^{N_m} S_{\hat{\varepsilon}}^{-1} G_{M_n}^T \mathbf{g}_{M_n} &= 0 \\
\Rightarrow \hat{\rho} &= \left[ S_{\hat{\rho}_0}^{-1} \mathbf{I}_{N_\rho} + \sum_{n=1}^{N_m} S_{\hat{\varepsilon}}^{-1} G_{M_n}^T G_{M_n} \right]^{-1} \times \left[ \hat{\rho}_0 S_{\hat{\rho}_0}^{-1} + \sum_{n=1}^{N_m} S_{\hat{\varepsilon}}^{-1} G_{M_n}^T \mathbf{g}_{M_n} \right]
\end{aligned} \tag{5.30}$$

where

$$\begin{aligned}
G_{M_n} &= \lambda_n \begin{bmatrix} M_1 \Phi_n & \dots & M_{N_\rho} \Phi_n \end{bmatrix}_{N \times N_\rho} \\
\mathbf{g}_{M_n} &= \left[ (K(\theta) - \lambda_n M_0) \Phi_n \right]_{N \times 1}
\end{aligned} \tag{5.31}$$

Finally, the posterior MPV of  $S_\varepsilon$  is obtained as below.

$$\begin{aligned}
\left. \frac{\partial J}{\partial S_\varepsilon} \right|_{S_\varepsilon=S_{\hat{\varepsilon}}} &= 0 \Rightarrow S_{\hat{\varepsilon}}^{-1} N_m N - S_{\hat{\varepsilon}}^{-2} \sum_{n=1}^{N_m} \Phi_n^T \Omega_n^T \Omega_n \Phi_n = 0 \\
\Rightarrow S_{\hat{\varepsilon}} &= \frac{\sum_{n=1}^{N_m} \|\Omega_n \Phi_n\|^2}{N_m N}
\end{aligned} \tag{5.32}$$

#### 5.4. Summary of Procedures

In modal parameter identification by fast BFFTA for individual setups, a norm constraint for local mode shape is necessary. Otherwise the minimization procedure becomes ill-conditioned due to the negative definite Hermitian structure of the Hessian matrix for local mode shape. For mode shape assembly problems, a norm constraint for global mode shape is also required to well match the identified local mode shape and corresponding part of the global mode shape. In Bayesian model updating applications, norm constraint for global mode shape is not used (Yuen 2010, Yan and Katafygiotis 2015c). The presented procedure needs a norm constraint for  $\Phi$  since  $A_n$  might not be a semi-positive definite matrix due to the modelling and measurement error. Otherwise, the solution will be ill-conditioned due to the non-existent null vector search of  $A_n$ .

The flow chart for the proposed procedure is presented in Figure 5.1. First, the local spectrum parameters including eigenvalues (square of most probable natural angular frequency), damping ratio, spectral density of modal excitation and prediction error should be obtained. Second, the Hessian matrix for eigenvalues and eigenvectors (most probable local mode shape) should be obtained by Gaussian approximation. At the

iteration step, the posterior most probable values for model parameters are updated until the prescribed convergence criteria are satisfied.

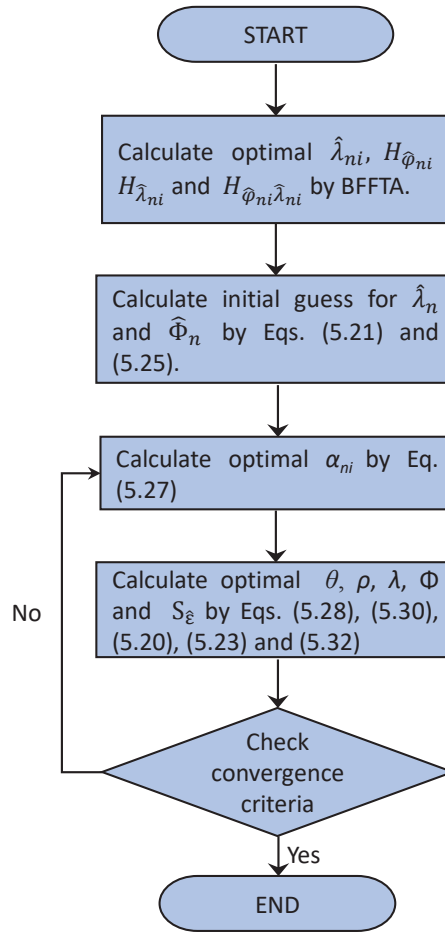


Figure 5.1. Flow chart for the proposed algorithm

## 5.5. Posterior Uncertainty

Posterior statistical parameters in terms of variance, standard deviation, and coefficient of variation can be estimated via the posterior covariance matrix centered at the MPV of system parameters. Using the second order Taylor series expansion, the covariance matrix can be calculated as the inverse of the Hessian matrix. Here, the Hessian matrix centered at the MPV of system parameters is given by

$$\tilde{\mathbf{H}} = \begin{bmatrix} J^{(\theta,\theta)} & J^{(\theta,\rho)} & J^{(\theta,\lambda)} & J^{(\theta,\Phi)} \\ J^{(\rho,\theta)} & J^{(\rho,\rho)} & J^{(\rho,\lambda)} & J^{(\rho,\Phi)} \\ J^{(\lambda,\theta)} & J^{(\lambda,\rho)} & J^{(\lambda,\lambda)} & J^{(\lambda,\Phi)} \\ J^{(\Phi,\theta)} & J^{(\Phi,\rho)} & J^{(\Phi,\lambda)} & J^{(\Phi,\Phi)} \end{bmatrix}_{N_{\Sigma} \times N_{\Sigma}} \quad (5.33)$$



where  $\mathcal{J}^{(\dots)}$  denotes the derivatives of Eq. (5.19) (see Appendix D). In addition,  $N_\Sigma = N_\theta + N_\rho + N_m(N + 1)$ ,  $\lambda = [\lambda_1 \dots \lambda_{N_m}]$ , and  $\Phi = [\Phi_1 \dots \Phi_{N_m}]$ .

## 5.6. Probabilistic Damage Detection

The most probable model parameters and their uncertainties can be obtained by the presented procedure. Here, it should be noted that again, the mass parameters are assumed as initially well-estimated. Using this assumption, the posterior most probable values for stiffness parameters can be estimated well. At the next step, the level of damage for the  $i^{th}$  stiffness parameter can be estimated based on probabilistic logic. By using the Gaussian approximations for marginal distributions, Vanik et al. (2002) defines the probability of exceedance to a certain damage level for the  $i^{th}$  stiffness parameter as follows

$$P_i^{dam}(d_i) = \tilde{\Phi} \left( \frac{(1-d_i)\hat{\theta}_i^{ud} - \hat{\theta}_i^{pd}}{\sqrt{(1-d_i)^2 S_{\hat{\theta}_i^{ud}} + S_{\hat{\theta}_i^{pd}}}} \right) \quad (5.34)$$

where  $d_i \in [0, 1]$  indicates the level of damage (as a threshold),  $\hat{\theta}_i^{ud}$  and  $\hat{\theta}_i^{pd}$  = most probable  $i^{th}$  stiffness parameter that represents the undamaged and damaged case,  $S_{\hat{\theta}_i^{ud}}$  and  $S_{\hat{\theta}_i^{pd}}$  = posterior variance of  $i^{th}$  stiffness parameter for the undamaged and damaged case, and  $\tilde{\Phi}(\cdot)$  = standard normal cumulative distribution function. Thus, the level of damage can be estimated by a probabilistic logic instead of monitoring the change in  $\tilde{\theta}_i$ .

## 5.7. Numerical and Experimental Analysis

In this section, first a numerical analysis is presented to verify the presented procedure. For comparison purposes, the variations in the posterior uncertainties are investigated if the modelling and prediction error is prescribed. Second, an experimental study is presented to see the effect of incomplete data on the results.

### 5.7.1. Numerical analysis: Torsional Shear Frame

A fifteen-story torsional shear frame structure is investigated to validate the proposed methodology. The plan layout of the investigated structure is presented in Figure 5.2. The lateral stiffness in the  $x$ - $x$  and  $y$ - $y$  direction is considered as  $k_{ix} = 1000 \text{ kN/m}$  and  $k_{iy} = 800 \text{ kN/m}$ , respectively. In addition, story mass is  $m = 250 \text{ kg}$  in both directions. Identically distributed and independent Gaussian white noise is generated with 300 second duration and  $100 \text{ Hz}$  sampling frequency, and the spectral density of  $5 \text{ N/Hz}$  in the lateral directions and  $25 \text{ Nm/Hz}$  in the torsional direction, respectively. The rms of measurement error is assumed 20% of the rms of simulated response (without noise) for each channel. The structure is measured with four setups. The sensor layout of the setups is presented in Table 5.1. The acceleration response of the structure is measured at the center in the translational directions. Torsional acceleration measurements are omitted. Therefore, torsional modes are not identified, but they are extracted from the updated finite element model.

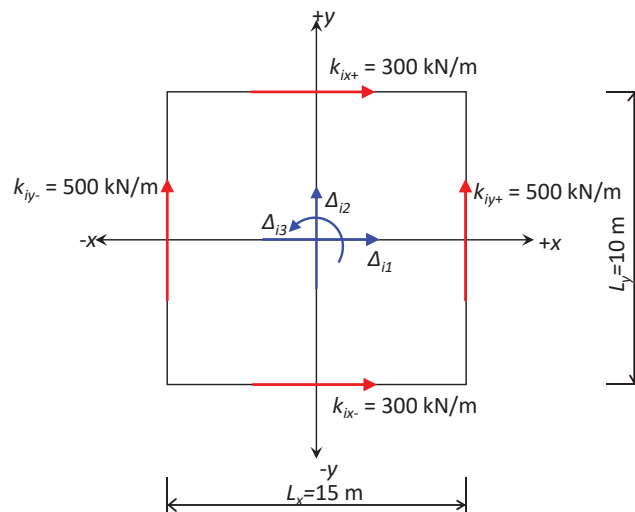


Figure 5.2. Plan view of fifteen story torsional shear frame structure

Table 5.1. Multiple setup configuration

Setup No	Measured DOF
1	1x, 1y, 2x, 2y, 3x, 3y, 4x, 4y, 5x, 5y
2	4x, 4y, 5x, 5y, 6x, 6y, 7x, 7y, 8x, 8y
3	7x, 7y, 8x, 8y, 9x, 9y, 10x, 10y, 11x, 11y, 12x, 12y
4	11x, 11y, 12x, 13y, 13x, 13y, 14x, 15y, 15x, 15y







Table 5.2. Actual and updated natural frequencies with posterior c.o.v.

<i>Mode Number</i>	<i>Undamaged Case</i>				<i>Damaged Case</i>			
	<i>Dir.</i>	<i>Analytical (Hz.)</i>	<i>Updated (Hz.)</i>	<i>c.o.v. (<math>\times 10^{-10}</math>)</i>	<i>Dir.</i>	<i>Analytical (Hz.)</i>	<i>Updated (Hz.)</i>	<i>c.o.v. (<math>\times 10^{-10}</math>)</i>
1	<i>y</i>	0.79	0.79	0.22	<i>y</i>	0.77	0.77	4.68
2	<i>x</i>	1.02	1.02	0.33	<i>x</i>	0.94	0.94	3.48
3	<i>Tors</i>	1.50	1.50*	-	<i>Tors</i>	1.45	1.45*	-
4	<i>y</i>	2.36	2.37	0.15	<i>y</i>	2.36	2.36	2.60
5	<i>x</i>	3.05	3.05	0.26	<i>x</i>	2.91	2.92	2.30
6	<i>y</i>	3.91	3.92	0.08	<i>y</i>	3.87	3.86	1.42
7	<i>Tors</i>	4.49	4.50*	-	<i>x</i>	4.55	4.56	1.10
8	<i>x</i>	5.04	5.04	0.11	<i>Tors</i>	4.42	4.41*	-
9	<i>y</i>	5.42	5.42	0.03	<i>y</i>	5.28	5.28	1.01
10	<i>y</i>	6.87	6.86	0.01	<i>y</i>	6.78	6.78	0.72
11	<i>x</i>	6.99	6.99	0.05	<i>x</i>	6.84	6.84	0.83
12	<i>Tors</i>	7.43	7.43*	-	<i>Tors</i>	7.18	7.18*	-
13	<i>x</i>	8.87	8.87	0.02	<i>x</i>	8.19	8.20	0.61
14	<i>Tors</i>	10.29	10.29*	-	<i>Tors</i>	10.08	10.08*	-
15	<i>Tors</i>	13.06	13.07*	-	<i>Tors</i>	12.61	12.60*	-

Table 5.3. Actual and updated stiffness parameters in the *x-x* direction

<i>Parameter</i>	<i>Undamaged case</i>			<i>Damaged case</i>		
	<i>Actual</i>	<i>Updated</i>	<i>c.o.v. (<math>\times 10^{-14}</math>)</i>	<i>Actual</i>	<i>Updated</i>	<i>c.o.v. (<math>\times 10^{-14}</math>)</i>
$\theta_{x1}$	1.0000	1.0044	1.0214	0.7000	0.7078	8.4405
$\theta_{x2}$	1.0000	1.0114	1.2943	1.0000	1.0107	10.8562
$\theta_{x3}$	1.0000	1.0076	0.8476	1.0000	1.0059	8.6016
$\theta_{x4}$	1.0000	1.0089	1.0702	1.0000	1.0114	8.3922
$\theta_{x5}$	1.0000	1.0089	1.0193	1.0000	1.0062	7.7128
$\theta_{x6}$	1.0000	1.0056	1.0326	1.0000	1.0043	6.9394
$\theta_{x7}$	1.0000	1.0109	1.0056	0.4000	0.4009	2.3786
$\theta_{x8}$	1.0000	1.0010	1.0221	1.0000	1.0076	5.9229
$\theta_{x9}$	1.0000	1.0168	0.9642	1.0000	1.0074	6.5112
$\theta_{x10}$	1.0000	1.0000	0.7876	1.0000	1.0029	8.5295
$\theta_{x11}$	1.0000	1.0057	0.8855	1.0000	1.0037	5.7305
$\theta_{x12}$	1.0000	0.9991	1.0363	1.0000	1.0090	10.6522
$\theta_{x13}$	1.0000	1.0076	1.0826	1.0000	1.0100	7.9952
$\theta_{x14}$	1.0000	1.0125	0.7692	1.0000	1.0016	11.6128
$\theta_{x15}$	1.0000	0.9987	0.9038	1.0000	1.0003	14.9658

Updated natural frequencies for first fifteen modes are presented in Table 5.2. Here, the translational modes indicate the identified most probable values by using the presented algorithm, and torsional modes are obtained from the eigenvalue analysis of

the updated finite element model. It is seen that the identified frequencies match well with their analytical values. In addition, identified stiffness parameters and the corresponding posterior coefficient of variations (c.o.v.) in the  $x$ - $x$  and  $y$ - $y$  direction is presented in Table 5.3 and Table 5.4, respectively. Similarly, it is seen that the stiffness parameters show good convergence to the analytical values for both undamaged and damaged cases.

In the previous studies, the modelling and prediction errors are generally defined as rigid constraints (they are assigned to the selected prescribed values). The presented method, however, defines soft constraints for modelling and prediction error. Therefore, the possible discrepancies due to the modelling and prediction error are calculated at each iteration step. Figure 5.4 presents the cumulative probability density functions of possible damage with respect to the damage level. It is seen that the probabilities of damage show very small (nearly zero) variance around the most probable damage levels. The reason of this fact is thought to be the result of using soft constraints for the modelling and prediction error.

Table 5.4. Actual and updated stiffness parameters in the  $y$ - $y$  direction

<i>Parameter</i>	<i>Undamaged case</i>			<i>Damaged case</i>		
	<i>Actual</i>	<i>Updated</i>	<i>c.o.v</i> ( $\times 10^{-14}$ )	<i>Actual</i>	<i>Updated</i>	<i>c.o.v</i> ( $\times 10^{-14}$ )
$\theta_{y1}$	1.0000	1.0090	1.4566	1.0000	1.0035	11.2068
$\theta_{y2}$	1.0000	1.0105	1.0229	0.9000	0.9089	9.7372
$\theta_{y3}$	1.0000	1.0133	0.9693	1.0000	1.0079	12.1623
$\theta_{y4}$	1.0000	0.9973	0.7562	1.0000	0.9944	15.5966
$\theta_{y5}$	1.0000	1.0085	1.2633	0.7500	0.7521	8.7421
$\theta_{y6}$	1.0000	1.0027	1.0756	1.0000	0.9971	6.4256
$\theta_{y7}$	1.0000	1.0021	1.5264	1.0000	1.0005	5.9322
$\theta_{y8}$	1.0000	1.0105	1.0523	1.0000	1.0014	4.3256
$\theta_{y9}$	1.0000	1.0070	0.9145	1.0000	1.0105	7.1385
$\theta_{y10}$	1.0000	1.0091	1.1580	1.0000	1.0158	9.9661
$\theta_{y11}$	1.0000	1.0137	1.6386	1.0000	1.0144	11.1286
$\theta_{y12}$	1.0000	0.9973	1.1325	1.0000	0.9957	12.5625
$\theta_{y13}$	1.0000	1.0093	1.4086	1.0000	0.9989	8.4346
$\theta_{y14}$	1.0000	0.9982	0.9373	1.0000	1.0085	10.0628
$\theta_{y15}$	1.0000	1.0070	1.1548	1.0000	0.9924	12.0963

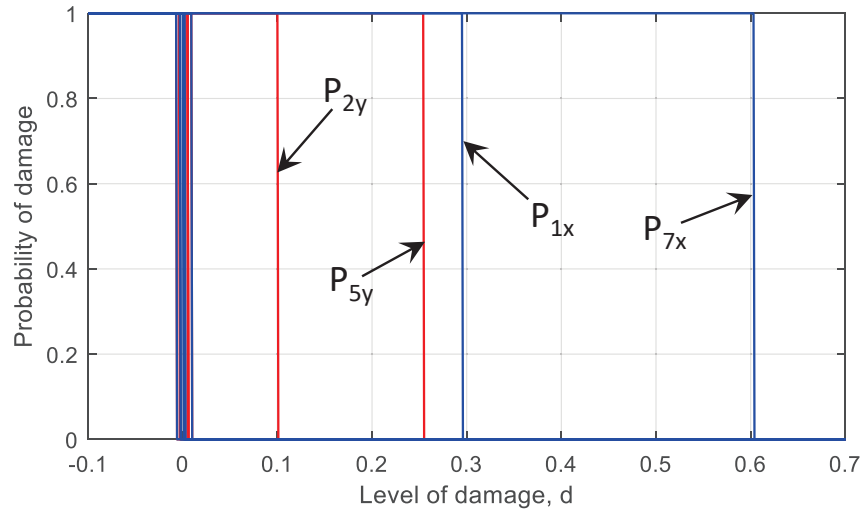


Figure 5.4. Cumulative probability of damage for the stiffness parameters (blue line:  $x$ - $x$  direction, red line:  $y$ - $y$  direction)

Figure 5.5 and Figure 5.6 show the convergence speed of the estimated stiffness parameters to their analytical value and the variation of their posterior c.o.v. with respect to the number of considered modes in the cases of considering the rigid and soft constraints for  $\lambda_{ni}$ , respectively. For the rigid constraint case,  $\lambda_{ni}$  is set to the MPVs that are identified from the measurements. It is seen that the convergence speed of the estimated stiffness parameters to the analytical value is higher in the presented methodology (soft constraint approach) when compared to the rigid constraint approach. In addition, the presented methodology reduces the posterior c.o.v. significantly for the first stiffness parameter when compared to the rigid constraint approach.

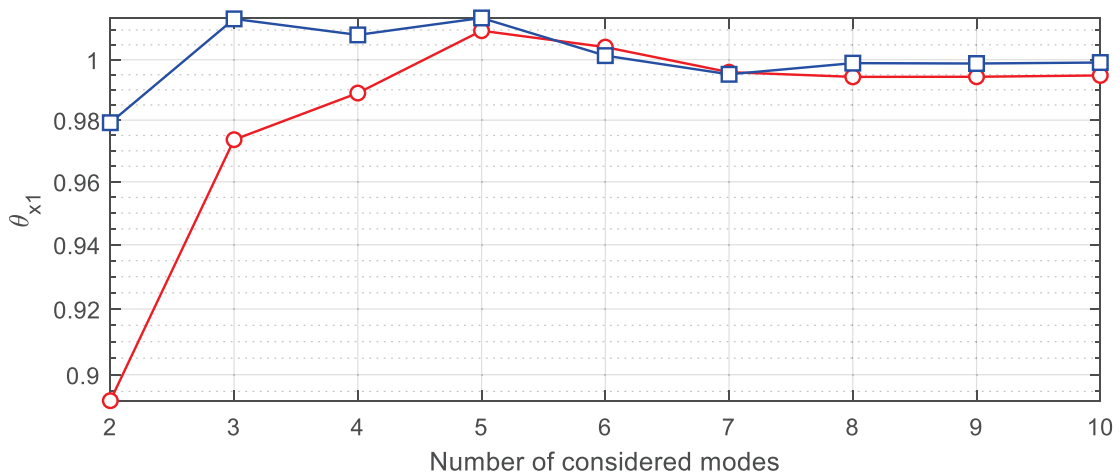


Figure 5.5. Variation of the estimated  $\theta_{x1}$  versus the number of considered modes (red circle: rigid constraint, blue square: soft constraint for eigenvalues)



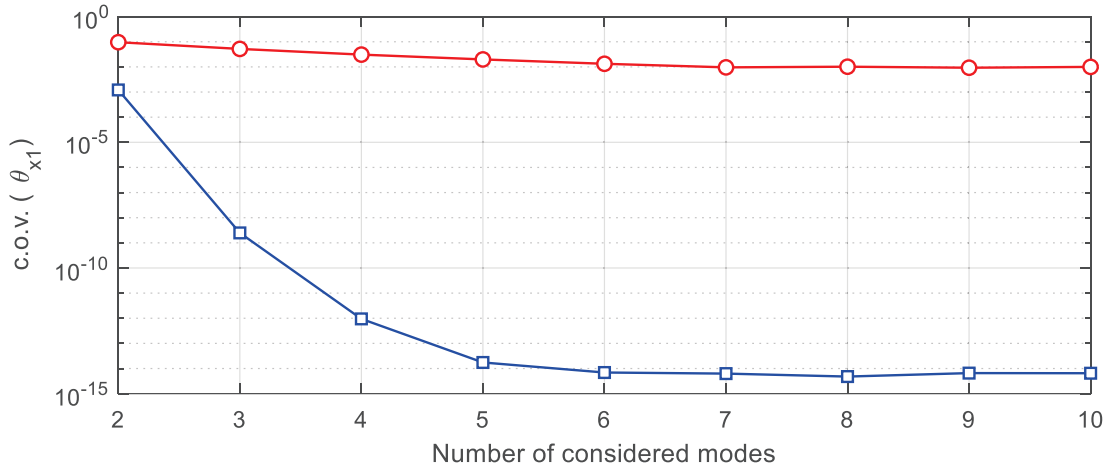


Figure 5.6. Variation of the posterior c.o.v. of  $\theta_{x1}$  versus the number of considered modes (red circle: rigid constraint, blue square: soft constraint for eigenvalues)

Figure 5.7 and Figure 5.8 show the variation of estimated stiffness parameters and their posterior c.o.v. in case of the prescribed variance for modelling and measurement error. Here, the prediction error for eigenvalues and eigenvectors are defined to have a c.o.v. of 1%. The prescribed variance of modelling error is calculated according to the defined prediction error. Results show that the soft constraint approach for modelling and measurement error increases the convergence speed of most probable stiffness parameters and decreases significantly the posterior coefficient of variation.

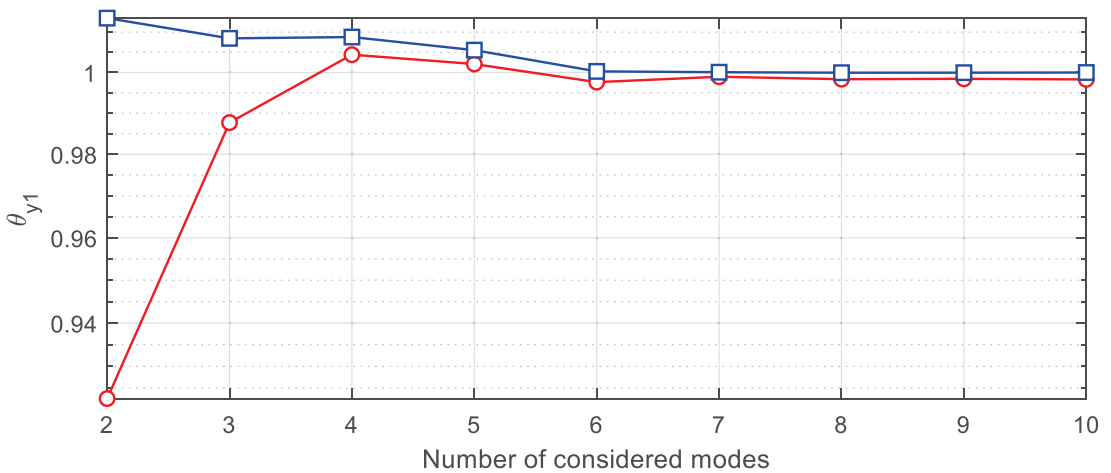


Figure 5.7. Variation of the estimated  $\theta_{y1}$  versus the number of considered modes (red circle: rigid constraint, blue square: soft constraint for modelling and prediction error)

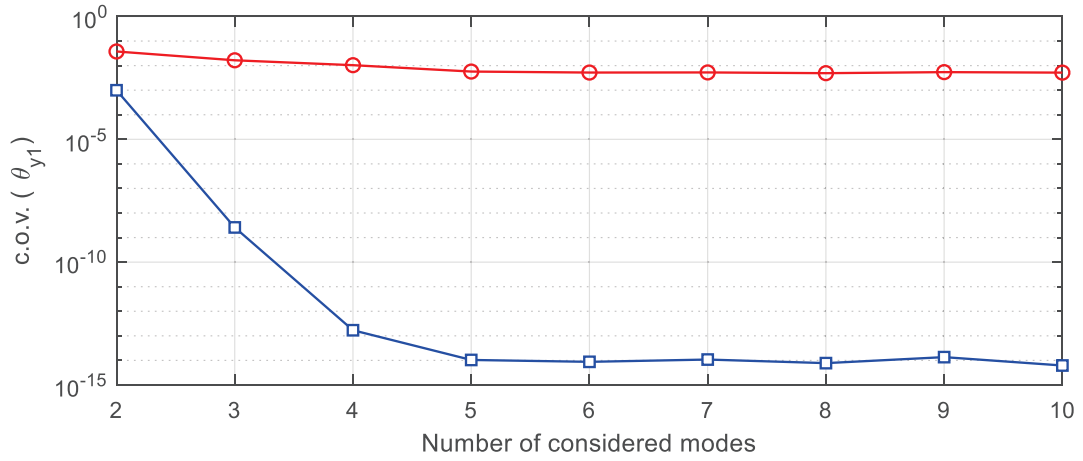


Figure 5.8. Variation of the posterior c.o.v. of  $\theta_{y1}$  versus the number of considered modes (red circle: rigid constraint, blue square: soft constraint for modelling and prediction error)

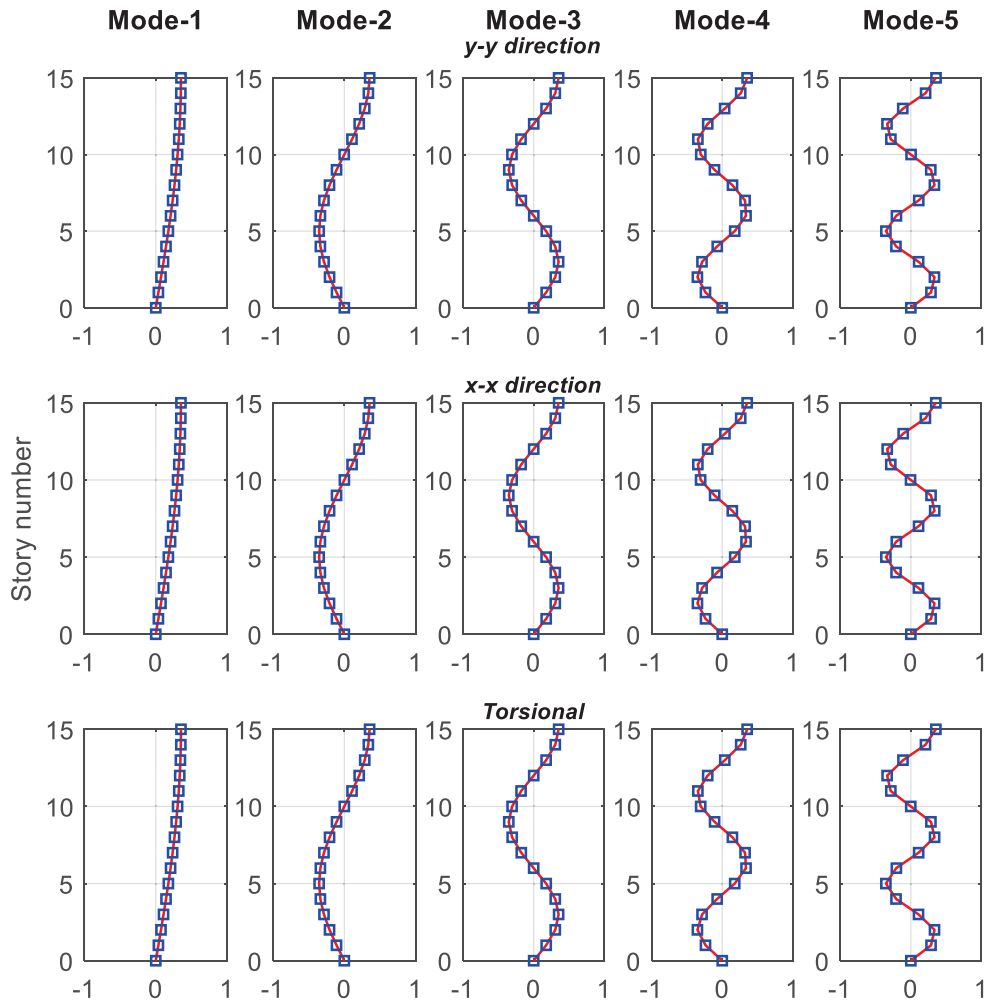


Figure 5.9. Updated mode shapes (blue squares) and analytical values (red line) for undamaged case

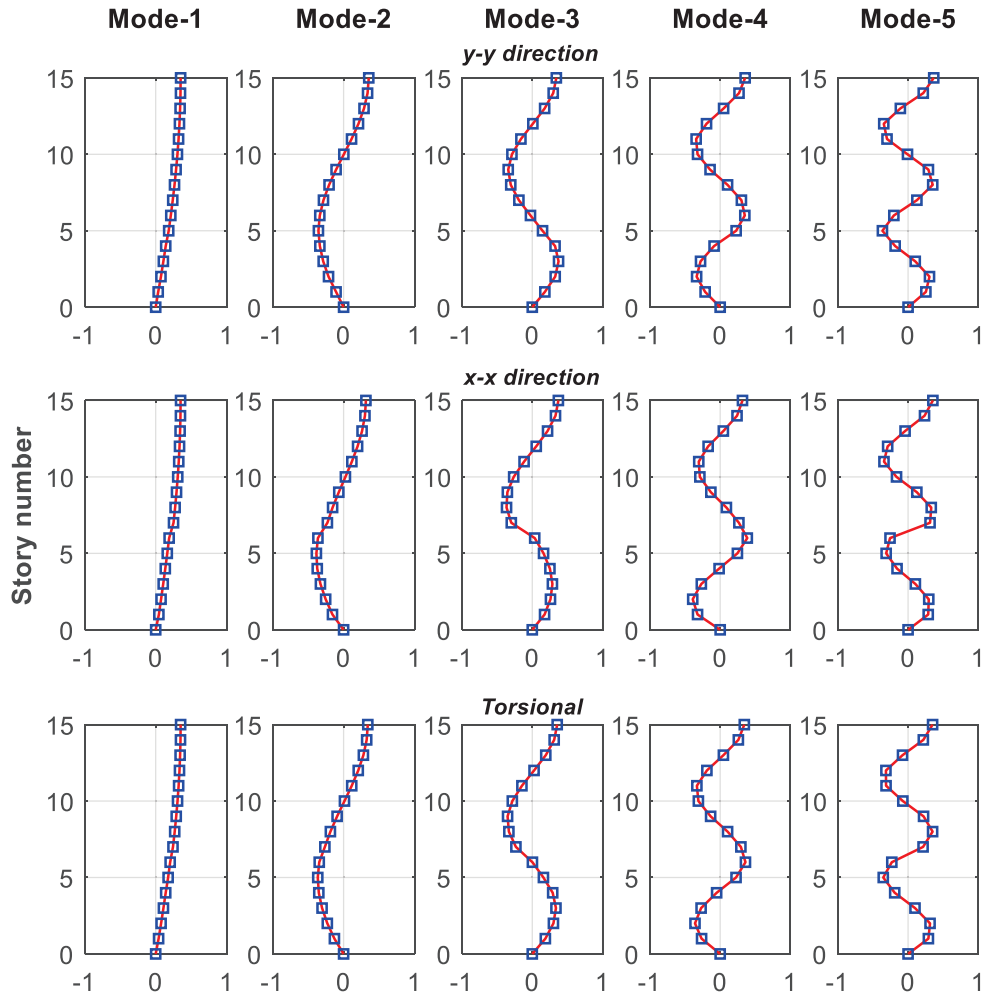


Figure 5.10. Updated mode shapes (blue squares) and analytical values (red line) for damaged case

Figure 5.9 and Figure 5.10 show the updated first fifteen mode shapes for damaged and undamaged cases. Here, torsional mode shapes are estimated from the updated finite element model. The estimated mode shapes (presented by blue squares) match well with the analytical results for both undamaged and damaged cases. In addition, the posterior c.o.v. values for identified mode shapes are presented in Table 5.5.

Table 5.5. Posterior c.o.v. values for mode shapes ( $\times 10^{-12}$ )

<i>Mode number</i>	<i>Undamaged case</i>		<i>Damaged case</i>	
	<i>yy-dir</i>	<i>xx-dir.</i>	<i>yy-dir</i>	<i>xx-dir.</i>
1	3.86	4.25	7.35	9.93
2	5.25	4.92	7.42	11.16
3	5.85	6.04	9.83	13.25
4	7.23	8.23	10.21	13.86
5	9.16	9.95	12.36	15.79

### 5.7.2. Experimental analysis: Ten story shear frame

In this section, the presented methodology is applied to the ten-story shear frame which is investigated in Section 4.5 (see Figure 4.2). The story stiffness of the structure is analytically calculated as [38.67 38.67 38.67 25.78 25.78 25.78 25.78 12.89 12.89 12.89] *KN/m*. In addition, the story mass is calculated as 2.355 kg for each story. For real life applications in which the nominal stiffness parameters are assumed to be well estimated, one may take a prior estimation of 1.00. In this study, however, the prior estimation for stiffness parameters are intentionally considered as overestimated and assigned to 10.0 with a large variance. The mass parameters are selected as 1.00 with small variance (well-estimated). Three different scenarios are considered to see the effect of incomplete measurement data. Sensor configurations for these scenarios are given in Table 5.6.

Table 5.6. Sensor placement configuration for considered measurement scenarios

<i>Setup Number</i>	<i>Measured DOFs</i>		
	<i>Scenario I</i>	<i>Scenario II</i>	<i>Scenario III</i>
1	1, 4	2, 3, 4	1, 2, 3, 4
2	4, 6	4, 5, 6	3, 4, 5, 6
3	6, 8	5, 6, 7	5, 6, 7, 8
4	8, 10	7, 8, 9	7, 8, 9, 10

Table 5.7. MPVs and posterior c.o.v. for natural frequencies (“\*” denotes the MPVs that are identified from the measurements)

<i>Mode #</i>	<i>Scenario I</i>			<i>Scenario II</i>			<i>Scenario III</i>		
	<i>MPV*</i>	<i>MPV</i>	<i>c.o.v (%)</i>	<i>MPV*</i>	<i>MPV</i>	<i>c.o.v (%)</i>	<i>MPV*</i>	<i>MPV</i>	<i>c.o.v (%)</i>
1	2.61	2.62	0.11	2.62	2.62	0.08	2.62	2.62	0.07
2	7.38	7.37	0.06	7.37	7.37	0.05	7.37	7.37	0.05
3	11.67	11.69	0.03	11.69	11.69	0.01	11.70	11.70	0.01
4	17.02	17.03	0.02	17.03	17.03	0.01	17.03	17.03	0.01
5	20.72	20.70	0.02	20.72	20.71	0.01	20.71	20.71	0.01

Table 5.7 presents the identified MPVs of natural frequencies and their posterior c.o.v. values. Here, “*MPV\**” denotes the most probable frequencies identified by BFFTA, and “*MPV*” denotes the most probable frequencies by the presented method. Results show

that the discrepancy between the updated and measured values are very small. In addition, as the number of measured DOF increases, the discrepancy of the MPVs and their posterior c.o.v. values decrease.

Table 5.8. Identified stiffness parameters for considered scenarios

<i>Stiffness</i> <i>Parameter</i>	<i>Scenario I</i>		<i>Scenario II</i>		<i>Scenario III</i>	
	<i>MPV</i>	<i>c.o.v (%)</i>	<i>MPV</i>	<i>c.o.v (%)</i>	<i>MPV</i>	<i>c.o.v (%)</i>
$\theta_1$	0.9055	0.3195	0.9216	0.2927	0.9846	0.1607
$\theta_2$	0.9346	0.5147	0.8632	0.3729	0.8606	0.1700
$\theta_3$	1.1641	0.5701	1.0955	0.1484	0.9162	0.1025
$\theta_4$	1.1868	0.5723	1.0629	0.1512	1.0798	0.1015
$\theta_5$	0.9227	0.6093	0.9929	0.1944	0.9967	0.1288
$\theta_6$	1.1425	0.7114	0.9866	0.2180	1.0205	0.1497
$\theta_7$	1.0547	0.5564	1.1626	0.1774	1.1447	0.1177
$\theta_8$	1.6102	0.7402	1.6051	0.2214	1.5781	0.1311
$\theta_9$	1.4575	0.6004	1.4997	0.2192	1.5269	0.1314
$\theta_{10}$	1.5213	0.5782	1.4805	0.2170	1.5191	0.1343

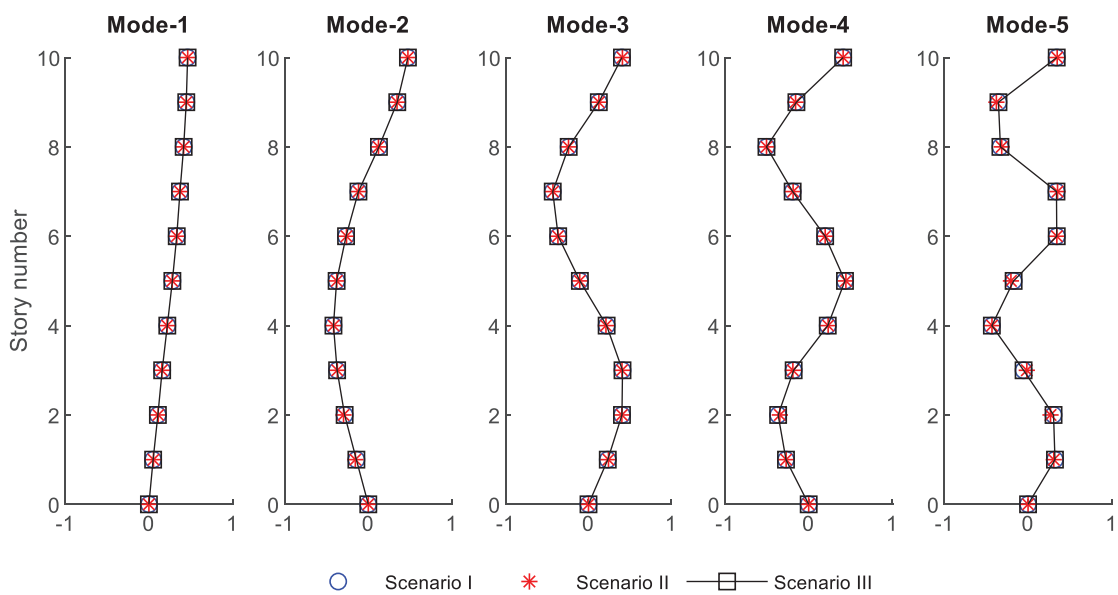


Figure 5.11. Updated mode shapes for considered scenarios

Identified stiffness parameters and their posterior c.o.v. values are presented in Table 5.8. At first view, it is seen that the identified stiffness parameters show a maximum difference of about 10% among the Scenario-I and III. This difference is considered to be caused by the effect of insufficient measurement points in Scenario-I. Here, only the first five modes could be identified by the presented method. The omission of higher modes results in a weaker estimation for stiffness parameters. The results from Scenario II show a small difference from Scenario III, since only the last two modes out of ten are missed. In addition, the posterior c.o.v. shows significant increase in case of incomplete data. Despite the difference in stiffness parameters, the posterior most probable mode shapes are observed to be identical for the considered scenarios (see Figure 5.11).

## 5.8. Concluding Remarks

Motivated from previous research, this study presents a two-stage Bayesian finite element modal updating procedure from the ambient response measurements obtained by multiple setups. The prior estimations for global eigenvalues and eigenvectors are considered by using Gaussian approximation centered at the MPV of local eigenvalues and eigenvectors obtained by BFFTA at each setup. The results are listed below.

- The proposed procedure results in lower posterior uncertainty which makes it less sensitive to the posterior MPV for model parameters. The reason of this fact is considered to stem from using the posterior distribution of local modal parameters obtained by BFFTA at each setup for prior probability distribution of eigenvalues and eigenvectors.
- Some applications in the literature consider the measured eigenvalues as the prescribed (or target) and the possible prediction errors are neglected. In this study, however, the prediction error between the system and measured eigenvalues are considered. According to the results, it is seen that the proposed methodology results in significantly less posterior c.o.v. for stiffness parameters.
- When the modelling error level is prescribed, the posterior uncertainties are affected by the chosen value even if the identified MPVs for model parameters are close to the actual value. The smaller values do not guarantee the smaller posterior c.o.v. for model parameters. This prescribed value should be selected according to the prediction error defined for the eigenvalues and eigenvectors. In

addition, some applications completely neglect the modelling error which may also result in larger posterior uncertainty. In the proposed methodology, however, the modelling error is not constrained, and it is estimated at each iteration step. In the presented numerical analysis, the posterior c.o.v. for model parameters are found significantly smaller from the prescribed modeling error approach.

- Both the stiffness and the mass parameters are considered as model parameters to be updated in the presented methodology. Assuming both parameters are initially not well-estimated does not give reasonable results since an infinite number of sets for most probable stiffness and mass parameters can be found. For this reason, at least one of those parameters should be assumed as well-estimated. The mass is generally much easier to be evaluated, and therefore the mass parameters are assumed to be well-estimated with small prior variance in the numerical examples.

# CHAPTER 6

## CONCLUSIONS

### 6.1. Summary of Results and General Conclusions

In the light of the studies available in the literature, this study presents a Bayesian computational framework starting from the identification of modal properties of the civil engineering structures. The procedure is completed by finite element model updating and damage detection by utilizing the measured acceleration response data. The summary of the general conclusions is presented below.

- The various BAYOMA methods such as BSDA and BFFTA can result in a standard form in terms of the negative logarithm-likelihood function. Only the Bayesian Spectral Trace Approach, which decouples the spectrum variables and mode shapes, presents a different methodology. In this methodology, MPV of spectrum variables are obtained by BSTA at the first stage. The mode shapes are obtained subsequently using the BSDA centered at the MPV of spectrum variables. In this study, however, this approach is considered as ill-conditioned in terms of its theoretical background. The reason of this conclusion lies in the consideration of the distribution of modal parameters by different probabilistic models. Here, the most important conceptual problem arises at the second step in which the most probable mode shapes are determined by assuming the MPV of spectrum variables. This assumption may sound reasonable when the MPV of spectrum variables are well matched with the actual values with zero uncertainty only, because each MPV and its uncertainty is correlated to the selected probability distribution. The identified spectrum parameters at the first stage reflect the MPVs according to the BSTA. Therefore, they cannot be considered as MPVs for BSDA at the second step. Here, assuming the outputs of the first stage as the prior distribution of the spectrum variables becomes more reasonable. Motivated from the previous studies, this study presents a different two-stage approach based on BFFTA. The main difference of the presented study lies in the consideration of the constraint equations for mode shapes. The equality



constraints for mode shapes are defined so that they are satisfied for each trial of spectrum variables. Thus, the posterior uncertainties of spectrum variables and mode shapes can be decoupled.

- The most prominent advantages of BAYOMA is that it provides uncertainty information for the identified values and it is capable of identifying the level of modal excitation and prediction error. When compared to the available OMA methods, BAYOMA does not show remarkable difference in terms of the convergence of identified parameters to actual values. However, the convergence of BAYOMA becomes more reasonable under large noise effect, especially for damping ratio and mode shape vector.
- The available Bayesian formulation for closely spaced modes defines the cross spectral density between different modal excitations in terms of the coherence. Therefore, the norm and phase angle of the coherence are considered as parameters to be identified. This study, however, states that the coherence between the modal excitations can be assumed as a real number when the structure is subjected to *i.i.d.* Gaussian excitation. In addition, numerical results for the burying mode case indicate that the presented methodology is capable of identifying the modal parameters as independent from the location of the burying mode.
- Different from the available Bayesian methods for multiple setups, the proposed Bayesian mode shape assembly technique incorporates the setup weights with Hessian matrix for the local mode shape. Here, the Hessian matrix for the local mode shape is calculated by using the local spectrum variables, only. Therefore, obtaining the local mode shapes becomes unnecessary. Due to the norm constraint singularity, the presented methodology can also be applied for closely spaced modes. The results show that the presented method presents better results in terms of convergence speed due to the high quality of initial estimation. In most cases, the global mode shapes can be identified without iteration. In addition, the presented methodology shows that there is zero correlation between the global mode shape vector and local spectrum parameters in case of well separated modes. This result significantly reduces the computational effort for the posterior uncertainty quantification.

- A new Bayesian finite element model updating methodology is presented incorporating the presented mode shape assembly technique. Here, the posterior distribution of global natural frequencies and mode shape vectors are considered as the prior distribution of the eigenvalues and eigenvector of the finite element model. Therefore, the model parameters could be directly identified from the FFT of measured data. The numerical results indicate that the presented methodology increases the convergence speed and reduces the posterior uncertainty of model parameters significantly. In addition, experimental results show that the presented methodology gives reasonable results in case of incomplete measurement points/data.

## 6.2. Recommendations for Future Works

During the past decade, significant developments have been achieved in regard to solutions of several problems in the applications of BAYOMA and BMU. However, some critical issues that need to be solved still exist.

- In the literature, the effect of modelling error is investigated for a buried mode case in which there is only one buried and one burying mode available. This study extends the possible buried mode cases according to the location of burying modes. However, the presented study is limited to maximum three buried mode cases. There are also a lot of possibilities in regarding to the number of buried and burying mode(s), and their locations. A more general method might be developed.
- Despite the efficiency and high computational speed of frequency domain BAYOMA methods, it needs a manual bandwidth selection. The manual selection also helps to make an inference about the data quality and elimination of spurious (non-structural) modes. However, the computational effort may inevitably increase due to the difficulties on the detection of possible modes in case of low data quality. To solve this problem and to obtain a fully automated BAYOMA application, an automated bandwidth selection should be developed in which the possible modes are efficiently detected without a user interpretation.
- Classical BAYOMA or BMU methods present efficient tools for linear modal analysis under small amplitude ambient vibration effect. A Bayesian approach

might be developed to detect the changes in modal or model parameters in case of non-linear vibration responses during large amplitude earthquake excitations.

## APPENDIX A

### DERIVATIVES OF NEGATIVE-LOGARITHM LIKELIHOOD FUNCTION

Gradients of  $L(\theta)$  with respect to modal parameters are obtained as follows.

- Gradient of  $\nabla^2 L(f, f)$

$$\begin{aligned} \nabla^2 L(f, f) &= \sum_k \left[ SD_k^{(f, f)} (SD_k + S_e)^{-1} - \left\{ SD_k^{(f)} \right\}^2 (SD_k + S_e)^{-2} \right] (1 - \alpha_k S_e^{-1}) \\ &\quad + \sum_k S^2 \left( \left\{ D_k^{(f)} \right\}^2 + D_k D_k^{(f, f)} \right) (SD_k + S_e)^{-2} \alpha_k S_e^{-1} \\ &\quad - 2 \sum_k SD_k \left\{ SD_k^{(f)} \right\}^2 (SD_k + S_e)^{-3} \alpha_k S_e^{-1} \end{aligned} \quad (\text{A.1})$$

- Gradient of  $\nabla^2 L(f, \xi)$

$$\begin{aligned} \nabla^2 L(f, \xi) &= \sum_k \left[ SD_k^{(f, \xi)} (SD_k + S_e)^{-1} - S^2 D_k^{(f)} D_k^{(\xi)} (SD_k + S_e)^{-2} \right] (1 - \alpha_k S_e^{-1}) \\ &\quad + \sum_k S^2 \left( D_k^{(f)} D_k^{(\xi)} + D_k D_k^{(f, \xi)} \right) (SD_k + S_e)^{-2} \alpha_k S_e^{-1} \\ &\quad - 2 \sum_k S^3 D_k D_k^{(f)} D_k^{(\xi)} (SD_k + S_e)^{-3} \alpha_k S_e^{-1} \end{aligned} \quad (\text{A.2})$$

- Gradient of  $\nabla^2 L(f, S)$

$$\begin{aligned} \nabla^2 L(f, S) &= \sum_k \left[ D_k^{(f)} (SD_k + S_e)^{-1} - SD_k D_k^{(f)} (SD_k + S_e)^{-2} \right] \\ &\quad \times \left( 1 - \alpha_k S_e^{-1} SD_k (SD_k + S_e)^{-1} \right) \end{aligned} \quad (\text{A.3})$$

- Gradient of  $\nabla^2 \mathcal{J}(f, S_e)$

$$\begin{aligned} \nabla^2 L(f, S_e) &= \sum_k SD_k^{(f)} (SD_k + S_e)^{-2} \left[ \alpha_k S_e^{-2} - (SD_k + S_e)^{-1} (1 - \alpha_k S_e^{-1}) \right] \\ &\quad - \sum_k S^2 D_k D_k^{(f)} (SD_k + S_e)^{-2} \alpha_k S_e^{-1} \left[ S_e^{-1} + 2(SD_k + S_e)^{-1} \right] \end{aligned} \quad (\text{A.4})$$

- Gradient of  $\nabla^2 L(f, \varphi)$

$$\begin{aligned} \nabla^2 L(f, \varphi) &= \varphi^T \left[ -2 \sum_k S_e^{-1} SD_k^{(f)} (SD_k + S_e)^{-1} \text{Re}(F_k F_k^*) \right. \\ &\quad \left. + 2 \sum_k S_e^{-1} S^2 D_k D_k^{(f)} (SD_k + S_e)^{-2} \text{Re}(F_k F_k^*) \right] \end{aligned} \quad (\text{A.5})$$

- Gradient of  $\nabla^2 L(\xi, \xi)$

$$\begin{aligned}\nabla^2 L(\xi, \xi) &= \sum_k \left[ SD_k^{(\xi, \xi)} (SD_k + S_e)^{-1} - \left\{ SD_k^{(\xi)} \right\}^2 (SD_k + S_e)^{-2} \right] (1 - \alpha_k S_e^{-1}) \\ &\quad + \sum_k S^2 \left( \left\{ D_k^{(\xi)} \right\}^2 + D_k D_k^{(\xi, \xi)} \right) (SD_k + S_e)^{-2} \alpha_k S_e^{-1} \\ &\quad - 2 \sum_k D_k \left\{ SD_k^{(\xi)} \right\}^2 (SD_k + S_e)^{-3} \alpha_k S_e^{-1}\end{aligned}\tag{A.6}$$

- Gradient of  $\nabla^2 L(\xi, S)$

$$\begin{aligned}\nabla^2 L(\xi, S) &= \sum_k \left[ D_k^{(\xi)} (SD_k + S_e)^{-1} - SD_k D_k^{(\xi)} (SD_k + S_e)^{-2} \right] (1 - \alpha_k S_e^{-1}) \\ &\quad + \sum_k 2 SD_k D_k^{(\xi)} (SD_k + S_e)^{-2} \alpha_k S_e^{-1} \left[ 1 - SD_k (SD_k + S_e)^{-1} \right]\end{aligned}\tag{A.7}$$

- Gradient of  $\nabla^2 L(\xi, S_e)$

$$\begin{aligned}\nabla^2 L(\xi, S_e) &= \sum_k SD_k^{(\xi)} (SD_k + S_e)^{-2} \left[ \lambda_k S_e^{-2} - (SD_k + S_e)^{-1} (1 + \alpha_k S_e^{-1}) \right] \\ &\quad + \sum_k S^2 D_k D_k^{(\xi)} (SD_k + S_e)^{-2} \alpha_k S_e^{-1} \left[ S_e^{-1} - 2 (SD_k + S_e)^{-1} \right]\end{aligned}\tag{A.8}$$

- Gradient of  $\nabla^2 L(\xi, \varphi)$

$$\begin{aligned}\nabla^2 L(\xi, \varphi) &= \varphi^T \left[ -2 \sum_k S_e^{-1} SD_k^{(\xi)} (SD_k + S_e)^{-1} \text{Re}(F_k F_k^*) \right. \\ &\quad \left. + 2 \sum_k S_e^{-1} S^2 D_k D_k^{(\xi)} (SD_k + S_e)^{-2} \text{Re}(F_k F_k^*) \right]\end{aligned}\tag{A.9}$$

- Gradient of  $\nabla^2 L(S, S)$

$$\nabla^2 L(S, S) = \sum_k D_k^2 (SD_k + S_e)^{-2} \left[ 2 \alpha_k S_e^{-1} \left\{ 1 - SD_k (SD_k + S_e)^{-1} \right\} - 1 \right]\tag{A.10}$$

- Gradient of  $\nabla^2 L(S, S_e)$

$$\begin{aligned}\nabla^2 L(S, S_e) &= - \sum_k D_k (SD_k + S_e)^{-2} \left[ 1 - \alpha_k S_e^{-1} \left\{ 1 - SD_k (SD_k + S_e)^{-1} \right\} \right] \\ &\quad + \sum_k D_k (SD_k + S_e)^{-1} \left[ \alpha_k S_e^{-2} \left\{ 1 - SD_k (SD_k + S_e)^{-1} \right\} \right. \\ &\quad \left. + \alpha_k S_e^{-1} SD_k (SD_k + S_e)^{-2} \right]\end{aligned}\tag{A.11}$$

- Gradient of  $\nabla^2 L(S, \varphi)$

$$\nabla^2 L(S, \varphi) = \varphi^T \left\{ -2 \sum_k S_e^{-1} D_k (SD_k + S_e)^{-1} \left[ 1 - SD_k (SD_k + S_e)^{-1} \right] \text{Re}(F_k F_k^*) \right\}\tag{A.12}$$

- Gradient of  $\nabla^2 L(S_e, S_e)$

$$\begin{aligned} \nabla^2 L^{(S_e, S_e)} &= -N_f (N-1) S_e^{-2} - \sum_k (SD_k + S_e)^{-2} + 2S_e^{-3} \kappa \\ &\quad - 2 \sum_k SD_k (SD_k + S_e)^{-1} \alpha_k S_e^{-1} \left[ S_e^{-2} + S_e^{-1} (SD_k + S_e)^{-1} + (SD_k + S_e)^{-2} \right] \end{aligned} \quad (\text{A.13})$$

- Gradient of  $\nabla^2 L^{(S_e, \varphi)}$

$$\nabla^2 L^{(S_e, \varphi)} = \left\{ 2 \sum_k SD_k \left[ S_e^{-2} (SD_k + S_e)^{-1} + S_e^{-1} (SD_k + S_e)^{-2} \right] \text{Re}(F_k F_k^*) \right\} \varphi^T \quad (\text{A.14})$$

- Gradient of  $\nabla^2 L^{(\varphi, \varphi)}$

$$L^{(\varphi, \varphi)} = -2\Delta \quad (\text{A.15})$$

In addition, derivatives of  $D_k$  are obtained as below.

- Derivative of  $D_k^{(f)}$

$$D_k^{(f)} = \left[ \frac{2}{f_k} - \frac{2f}{f_k^2} - \frac{8\xi^2 f}{f_k^2} \right] D_k^2 \quad (\text{A.16})$$

- Derivative of  $D_k^{(f, f)}$

$$D_k^{(f, f)} = - \left[ \frac{2}{f_k^2} + \frac{8\xi^2}{f_k^2} \right] D_k^2 + 2 \left[ -\frac{2}{f_k} + \frac{f}{f_k^2} + \frac{8\xi^2 f}{f_k^2} \right]^2 D_k^3 \quad (\text{A.17})$$

- Derivative of  $D_k^{(\xi)}$

$$D_k^{(f)} = -\frac{8\xi f^2}{f_k^2} D_k^2 \quad D_k^{(f)} = -\frac{8\xi f^2}{f_k^2} D_k^2 \quad (\text{A.18})$$

- Derivative of  $D_k^{(\xi, \xi)}$

$$D_k^{(f)} = -\frac{8f^2}{f_k^2} D_k^2 - \frac{128f^2}{f_k^2} D_k^3 \quad (\text{A.19})$$

- Derivative of  $D_k^{(f, \xi)}$

$$D_k^{(f, \xi)} = -\frac{16\xi f}{f_k^2} D_k^2 + 2 \left( -\frac{2}{f_k} + \frac{f}{f_k^2} + \frac{8\xi^2 f}{f_k^2} \right) \left( \frac{8\xi^2 f}{f_k^2} \right) D_k^3 \quad (\text{A.20})$$

## APPENDIX B

### SCALING OF NEGATIVE LOG-LIKELIHOOD FUNCTION FOR UNIT NORM OF MODE SHAPE VECTOR

#### Derivatives of Spectral Density Matrix with Scaled Mode Shape Vector

The expected spectral density of measured response should be written as follows when it is assumed that it always satisfies the unit norm approximation for the mode shape vector.

$$E_k = \varphi \frac{SD_k}{(\varphi^T \varphi)} \varphi^T + S_e I_N \quad (\text{B.1})$$

$E_k^{-1}$  and  $|E_k|$  are obtained as follows by using the matrix inversion and determinant lemma.

$$\begin{aligned} E_k^{-1} &= S_e^{-1} I_N + S_e^{-1} \varphi \left[ \varphi^T S_e^{-1} \varphi + \varphi^T \varphi / SD_k \right]^{-1} \varphi^T S_e^{-1} \\ &= S_e^{-1} I_N + \frac{SD_k / S_e}{(SD_k + S_e)} \varphi \varphi^T (\varphi^T \varphi)^{-1} \end{aligned} \quad (\text{B.2})$$

$$\begin{aligned} |E_k| &= \left| \varphi^T \varphi / SD_k + \varphi^T S_e^{-1} \varphi \right| \left| SD_k / \varphi^T \varphi \right| \left| S_e I_N \right| \\ &= S_e^{N-1} (S_e + SD_k)^{-1} \end{aligned} \quad (\text{B.3})$$

Thus, the negative logarithm-likelihood function can be obtained as follows by making use of Eqs. (B.2) and (B.3).

$$J(\theta) = C + L_s - \frac{\varphi^T \Delta \varphi}{\varphi^T \varphi} \quad (\text{B.4})$$

Derivatives of  $J(\theta)$  are obtained as;

$$J^{(\theta_s)} = L_s^{(\theta_s)} - \frac{\varphi^T \Delta^{(\theta_s)} \varphi}{\varphi^T \varphi} \quad (\text{B.5})$$

$$J^{(\varphi)} = -2 \frac{\varphi^T \Delta}{\varphi^T \varphi} + 2 \frac{\varphi^T \Delta \varphi}{(\varphi^T \varphi)^2} \varphi^T \quad (\text{B.6})$$

$$J^{(\theta_s, \varphi)} = -2 \frac{\varphi^T \Delta^{(\theta_s)}}{\varphi^T \varphi} + 2 \frac{\varphi^T \Delta^{(\theta_s)} \varphi}{(\varphi^T \varphi)^2} \varphi^T \quad (\text{B.7})$$

$$J^{(\varphi, \varphi)} = -2 \frac{\Delta}{\varphi^T \varphi} + 8 \frac{\varphi \varphi^T \Delta}{(\varphi^T \varphi)^2} - 8 \frac{\varphi^T \Delta \varphi}{(\varphi^T \varphi)^3} \varphi \varphi^T + 2 \frac{\varphi^T \Delta \varphi}{(\varphi^T \varphi)^2} I_N \quad (\text{B.8})$$

At  $\theta_s = \hat{\theta}_s$  and  $\varphi = \hat{\varphi}$ ,

$$(\hat{\varphi}^T \hat{\Delta} \hat{\varphi}) \hat{\varphi} = \hat{\Delta} \hat{\varphi} \quad (\text{B.9})$$

$$\begin{aligned} J^{(\hat{\theta}_s, \hat{\varphi})} &= -2 \hat{\varphi}^T \hat{\Delta}^{(\hat{\theta}_s)} + 2 \hat{\varphi}^T \hat{\Delta}^{(\hat{\theta}_s)} \hat{\varphi} \hat{\varphi}^T \\ &= -2 \hat{\varphi}^T \hat{\Delta}^{(\hat{\theta}_s)} (I_N - \hat{\varphi} \hat{\varphi}^T) = 0 \end{aligned} \quad (\text{B.10})$$

$$J^{(\hat{\varphi}, \hat{\varphi})} = -2 \hat{\Delta} + 2 \hat{\varphi}^T \hat{\Delta} \hat{\varphi} I_N \quad (\text{B.11})$$

## Eigen Decomposition of the Derivatives of $\Delta(\theta_s)$

Derivative of  $\Delta(\theta_s)$  with respect to  $\theta_s$  can be obtained as follows.

$$\frac{\partial \Delta(\theta_s)}{\partial \theta_s} = \sum_k \frac{\partial}{\partial \theta_s} \left[ \frac{SD_k}{S_e (SD_k + S_e)} \right] \text{Re}(F_k F_k^*) \quad (\text{B.12})$$

In Eq. (B.12), it is seen that the derivative of  $\Delta(\theta_s)$  is a Hermitian matrix. Therefore, its eigen decomposition should also be Hermitian.

$$\begin{aligned} \Delta(\theta_s) &= \sum_{i=1}^N \lambda_i \rho_i \rho_i^T \\ \frac{\partial \Delta(\theta_s)}{\partial \theta_s} &= \sum_{i=1}^N \frac{\partial \lambda_i}{\partial \theta_s} \rho_i \rho_i^T + \lambda_i \frac{\partial \rho_i}{\partial \theta_s} \rho_i^T + \lambda_i \rho_i \frac{\partial \rho_i^T}{\partial \theta_s} \end{aligned} \quad (\text{B.13})$$

Here,  $\partial \rho_i / \partial \theta_s$  will be orthogonal to  $\rho_i$ . Therefore,  $\partial \rho_i / \partial \theta_s$  should be equal to zero in order to keep Hermitian structure of  $\partial \Delta(\theta_s) / \partial \theta_s$ . Thus, the derivative of  $\Delta(\theta_s)$  is obtained as below.

$$\frac{\partial \Delta(\theta_s)}{\partial \theta_s} = \sum_{i=1}^N \frac{\partial \lambda_i}{\partial \theta_s} \rho_i \rho_i^T = \frac{\partial \alpha(\theta_s)}{\partial \theta_s} \varphi \varphi^T + \sum_{i=2}^N \frac{\partial \lambda_i}{\partial \theta_s} \rho_i \rho_i^T \quad (\text{B.14})$$



## APPENDIX C

### DERIVATION OF COHERENCE BETWEEN TWO DIFFERENT SIGNALS AND CAYLEY TRANSFORMATION

#### The Expected Coherence Between Different Modal Excitations

The expected spectral density matrix of modal excitation can be written as below in case of the considered structure is subjected to independent and identically distributed Gaussian excitations.

$$S = \frac{\Phi^T E [p_k p_k^*] \Phi}{\Phi^T M \Phi} \quad (C.15)$$

where  $\Phi$  = modal shape matrix,  $M$  = mass matrix, and  $p_k$ =nodal force vector (Gaussian). Here, the expected value of the spectral density of nodal forces will equal to a real diagonal matrix due to the zero correlation between different nodes. Thus, the expected spectral density matrix inevitably becomes a real matrix.

$$S = \frac{\Phi^T S_p \Phi}{\Phi^T M \Phi} \in \mathbb{R} \quad (C.16)$$

where  $S_p \in \mathbb{R}$  denotes the expected spectral density of nodal forces. Hence, the coherence between the  $i^{th}$  and  $j^{th}$  modal excitations can be written as below

$$\chi_{12} = \frac{S_{ij}}{\sqrt{S_{ii} S_{jj}}} = \sin(u_{ij}) \in \mathbb{R} \quad (C.17)$$

where  $u_{ij}$  denotes a free parameter.

#### Cayley Transformation

Consider a function a minimization problem with an orthogonality constraint as below.

$$\min_{X \in \mathbb{R}^{n \times m}} \left\{ F(X) + \alpha (X^T X - I_N) \right\} \quad (C.18)$$

where  $F(X)$  is a differentiable function. Using the optimization scheme by Wen and Yin (2013) based on the Cayley transformation - a Crank-Nicholson type updating scheme,

Eq. (C.4) can be minimized by preserving the norm constraint equality of  $(X^T X - I_N)$ . Here,  $X$  can be updated by the Crank-Nicholson like scheme as follows.

$$X_{upd} = X - \frac{\tau}{2} A (X + X_{upd}) \quad (C.19)$$

where

$$A = (\nabla_X F) X^T - X (\nabla_X F) \quad (C.20)$$

and  $\tau$  denotes the step size. Solving Eq. (C.5) for  $X_{upd}$  yields,

$$X_{upd} = \left( I_n + \frac{\tau}{2} A \right)^{-1} \left( I_n - \frac{\tau}{2} A \right) X \quad (C.21)$$

The Barzilai-Borwain step size can be selected for  $\tau$  to accelerate the iteration procedure (Barzilai, 1988). Thus,  $\tau$  can be calculated by using the following equation (Wen and Yin, 2013).

$$\tau = \frac{\left| \text{tr}(\Delta X_{k-1}^T Z_{k-1}) \right|}{\text{tr}(Z_{k-1}^T Z_{k-1})} \quad (C.22)$$

where

$$\begin{aligned} \Delta X_{k-1} &= X_k - X_{k-1} \\ Z_{k-1} &= \nabla_X F(X_k) - \nabla_X F(X_{k-1}) \end{aligned} \quad (C.23)$$

## APPENDIX D

### DERIVATION OF POSTERIOR COVARIANCE MATRIX FOR CLOSELY SPACED MODES

Posterior covariance matrix for closely spaced modes can be obtained by using the fast calculation scheme by Au and Xie (2017). For this purpose, the objective function is defined by

$$J(\theta) = L(\theta) + \sum_{i=1}^{N_m} \alpha_i (\phi_i^T \phi_i - 1) \quad (\text{D.1})$$

where

$$L(\theta) = \sum_k \ln |E_k| + \sum_k \text{tr} [E_k^{-1} F_k F_k^*] \quad (\text{D.2})$$

The second order gradient of  $J(\theta)$  is obtained as below.

$$\nabla^2 J(\theta) = \begin{bmatrix} [J^{(\theta_s, \theta_s)}]_{N_{\theta_s}} & [J^{(\theta_s, \Phi)}]_{N_{\theta_s} \times N_m N} \\ [J^{(\Phi, \theta_s)}]_{N_m N \times N_{\theta_s}} & [J^{(\Phi, \Phi)}]_{N_m N \times N_m N} \end{bmatrix} \quad (\text{D.3})$$

where  $\nabla^2 L(\theta)$  is an  $\{N_{\theta_s} + N_m N\} \times \{N_{\theta_s} + N_m N\}$  size matrix, and  $N_{\theta_s} = (N_m + 1)^2 + O(\{N_m N\}^2)$ . The derivatives of  $J(\theta)$  is given by;

$$J^{(\theta_s, \theta_s)} = L^{(\theta_s, \theta_s)}; \quad J^{(\theta_s, \Phi)} = \begin{bmatrix} L^{(\theta_s, \phi_1)} & & & L^{(\theta_s, \phi_{N_m})} \\ \vdots & & & \vdots \\ \vdots & & & \vdots \\ \vdots & & & \vdots \end{bmatrix}$$

$$J^{(\Phi, \Phi)} = \begin{bmatrix} \{L^{(\phi_1, \phi_1)} + 2\alpha_1 I_N\} & & & \\ & \ddots & & \\ & & \ddots & \\ & & & \ddots \\ & & & & \{L^{(\phi_{N_m}, \phi_{N_m})} + 2\alpha_{N_m} I_N\} \end{bmatrix} \quad (\text{D.4})$$

and the Lagrange multiplier of  $\alpha_i$  is obtained as below.

$$\alpha_i = -\frac{1}{2} L^{(\phi_i)} \phi_i I_N \quad (\text{D.5})$$

Derivatives of  $J(\theta)$ ,

$$L^{(x,y)} = \sum_k \{\ln |E_k|\}^{(x,y)} + \sum_k \{\text{tr} [E_k^{-1} F_k F_k^*]\}^{(x,y)} \quad (\text{D.6})$$

Derivatives of  $\ln |E_k|$  and  $E_k^{-1}$ ;

$$\begin{aligned}
\{\ln|E_k|\}^{(x)} &= \text{tr}\left[E_k^{-1}E_k^{(x)}\right]; \\
\{\ln|E_k|\}^{(x,y)} &= \text{tr}\left[E_k^{-1}E_k^{(x,y)} - E_k^{-1}E_k^{(y)}E_k^{-1}E_k^{(x)}\right] \\
\{E_k^{-1}\}^{(x)} &= -E_k^{-1}E_k^{(x)}E_k^{-1}; \\
\{E_k^{-1}\}^{(x,y)} &= -E_k^{-1}\left[E_k^{(y)}E_k^{-1}E_k^{(x)} - E_k^{(x,y)} + E_k^{(x)}E_k^{-1}E_k^{(y)}\right]
\end{aligned} \tag{D.7}$$

Derivatives of  $E_k$ ;

$$\begin{aligned}
E_k &= \sum_{i=1}^{N_m} \sum_{j=1}^{N_m} \varphi_i H_k(i,j) \varphi_j^T + S_e I_N \\
E_k^{(\bar{\theta}_s)} &= \sum_{i=1}^{N_m} \sum_{j=1}^{N_m} \varphi_i \{H_k(i,j)\}^{(\bar{\theta}_s)} \varphi_j^T + S_e I_N \\
E_k^{(\bar{\theta}_s, \bar{\theta}_s)} &= \sum_{i=1}^{N_m} \sum_{j=1}^{N_m} \varphi_i \{H_k(i,j)\}^{(\bar{\theta}_s, \bar{\theta}_s)} \varphi_j^T + S_e I_N \\
E_k^{(\varphi_i)} &= \sum_{i=1}^{N_m} \sum_{j=1}^{N_m} H_k(i,j) \varphi_j^T; \quad E_k^{(\bar{\theta}_s, \varphi_i)} = \sum_{i=1}^{N_m} \sum_{j=1}^{N_m} H_k(i,j) \{H_k(i,j)\}^{(\bar{\theta}_s, \varphi_i)} \varphi_j^T \\
E_k^{(\varphi_i, \varphi_i)} &= \begin{bmatrix} \sum_{i=1}^{N_m} \sum_{j=1}^{N_m} H_k(i,j) & \text{if } i=j \\ 0 & \text{else} \end{bmatrix} \\
E_k^{(S_e)} &= I_N; \quad E_k^{(\bar{\theta}_s, S_e)} = E_k^{(\varphi_i, S_e)} = 0 \\
\bar{\theta}_s &= [f_i, \zeta_i, S_{ii}, u_{ij}, \dots], \text{ for } i=1 \text{ to } N_m \text{ and } j=1 \text{ to } N_m
\end{aligned} \tag{D.8}$$

First order derivatives of  $H_k$

$$\begin{aligned}
H_k(i,i) &= S_{ii} D_{kii}; \quad H_k(i,j) = (S_{ii} S_{jj})^{1/2} e^{\pm i v_{ij}} h_{ki} h_{kj}^*; \\
\{H_k(i,j)\}^{(f_i)} &= \begin{bmatrix} S_{ii} D_{ki}^{(f_i)} & \text{if } i=j \\ (S_{ii} S_{jj})^{1/2} \sin(u_{ij}) \{h_{ki} h_{kj}^*\}^{(f_i)} & \text{else} \end{bmatrix} \\
\{H_k(i,j)\}^{(\zeta_i)} &= \begin{bmatrix} S_{ii} D_{ki}^{(\zeta_i)} & \text{if } i=j \\ (S_{ii} S_{jj})^{1/2} \sin(u_{ij}) \{h_{ki} h_{kj}^*\}^{(\zeta_i)} & \text{else} \end{bmatrix} \\
\{H_k(i,j)\}^{(S_{ii})} &= \begin{bmatrix} D_{ki}^{(\zeta_i)} & \text{if } i=j \\ \frac{1}{2} S_{ii}^{-1/2} S_{jj}^{1/2} \sin(u_{ij}) h_{ki} h_{kj}^* & \text{else} \end{bmatrix} \\
\{H_k(i,j)\}^{(u_{ij})} &= \begin{bmatrix} 0 & \text{if } i=j \\ (S_{ii} S_{jj})^{1/2} \cos(u_{ij}) h_{ki} h_{kj}^* & \text{else} \end{bmatrix}
\end{aligned} \tag{D.9}$$

Second order derivatives of  $H_k$ ;

$$\begin{aligned}
\{H_k(i, j)\}^{(f_i, f_i)} &= \begin{cases} S_{ii} D_{ki}^{(f_i)} & \text{if } i = j \\ (S_{ii} S_{jj})^{1/2} \sin(u_{ij}) \{h_{ki} h_{kj}^*\}^{(f_i, f_i)} & \text{else} \end{cases} \\
\{H_k(i, j)\}^{(f_i, \xi_i)} &= \begin{cases} S_{ii} D_{ki}^{(\xi_i)} & \text{if } i = j \\ (S_{ii} S_{jj})^{1/2} \sin(u_{ij}) \{h_{ki} h_{kj}^*\}^{(f_i, \xi_i)} & \text{else} \end{cases} \\
\{H_k(i, j)\}^{(f_i, S_{ii})} &= \begin{cases} D_{ki}^{(\xi_i)} & \text{if } i = j \\ \frac{1}{2} S_{ii}^{-1/2} S_{jj}^{1/2} \sin(u_{ij}) \{h_{ki} h_{kj}^*\}^{(f_i)} & \text{else} \end{cases} \\
\{H_k(i, j)\}^{(f_i, u_{ij})} &= \begin{cases} 0 & \text{if } i = j \\ (S_{ii} S_{jj})^{1/2} \cos(u_{ij}) \{h_{ki} h_{kj}^*\}^{(f_i)} & \text{else} \end{cases}
\end{aligned} \tag{D.10}$$

$$\begin{aligned}
\{H_k(i, j)\}^{(\xi_i, \xi_i)} &= \begin{cases} S_{ii} D_{ki}^{(f_i)} & \text{if } i = j \\ (S_{ii} S_{jj})^{1/2} \sin(u_{ij}) \{h_{ki} h_{kj}^*\}^{(\xi_i, \xi_i)} & \text{else} \end{cases} \\
\{H_k(i, j)\}^{(\xi_i, S_{ii})} &= \begin{cases} D_{ki}^{(\xi_i)} & \text{if } i = j \\ \frac{1}{2} S_{ii}^{-1/2} S_{jj}^{1/2} \sin(u_{ij}) \{h_{ki} h_{kj}^*\}^{(\xi_i)} & \text{else} \end{cases} \\
\{H_k(i, j)\}^{(\xi_i, u_{ij})} &= \begin{cases} 0 & \text{if } i = j \\ (S_{ii} S_{jj})^{1/2} \cos(u_{ij}) \{h_{ki} h_{kj}^*\}^{(\xi_i)} & \text{else} \end{cases}
\end{aligned} \tag{D.11}$$

$$\begin{aligned}
\{H_k(i, j)\}^{(S_{ii}, S_{ii})} &= \begin{cases} 0 & \text{if } i = j \\ -\frac{1}{4} S_{ii}^{-3/2} S_{jj}^{1/2} \sin(u_{ij}) h_{ki} h_{kj}^* & \text{else} \end{cases} \\
\{H_k(i, j)\}^{(S_{ii}, u_{ij})} &= \begin{cases} 0 & \text{if } i = j \\ \frac{1}{2} S_{ii}^{-1/2} S_{jj}^{1/2} \cos(u_{ij}) h_{ki} h_{kj}^* & \text{else} \end{cases}
\end{aligned} \tag{D.12}$$

$$\{H_k(i, j)\}^{(u_{ij}, u_{ij})} = \begin{cases} 0 & \text{if } i = j \\ \mp (S_{ii} S_{jj})^{1/2} \sin(u_{ij}) h_{ki} h_{kj}^* & \text{else} \end{cases} \tag{D.13}$$

Derivatives of  $\{h_{ki}h_{kj}^*\}$

$$\begin{aligned}
\{h_{ki}h_{kj}^*\}^{(f_i)} &= \{h_{ki}\}^{(f_i)} h_{kj}^* + h_{ki} \{h_{kj}^*\}^{(f_i)} \\
\{h_{ki}h_{kj}^*\}^{(\xi_i)} &= \{h_{ki}\}^{(f_i)} h_{kj}^* + h_{ki} \{h_{kj}^*\}^{(\xi_i)} \\
\{h_{ki}h_{kj}^*\}^{(f_i, f_i)} &= \{h_{ki}\}^{(f_i, f_i)} h_{kj}^* + 2\{h_{ki}\}^{(f_i)} \{h_{kj}^*\}^{(f_i)} + h_{ki} \{h_{kj}^*\}^{(f_i, f_i)} \\
\{h_{ki}h_{kj}^*\}^{(\xi_i, \xi_i)} &= \{h_{ki}\}^{(\xi_i, \xi_i)} h_{kj}^* + 2\{h_{ki}\}^{(\xi_i)} \{h_{kj}^*\}^{(\xi_i)} + h_{ki} \{h_{kj}^*\}^{(\xi_i, \xi_i)} \\
\{h_{ki}h_{kj}^*\}^{(f_i, \xi_i)} &= \{h_{ki}\}^{(f_i, \xi_i)} h_{kj}^* + \{h_{ki}\}^{(f_i)} \{h_{kj}^*\}^{(\xi_i)} \\
&\quad + h_{ki} \{h_{kj}^*\}^{(f_i, \xi_i)} + \{h_{ki}\}^{(\xi_i)} \{h_{kj}^*\}^{(f_i)}
\end{aligned} \tag{D.14}$$

Derivatives of  $h_{ki}$

$$\begin{aligned}
h_{ki} &= \left(1 - \frac{f_i^2}{f_k^2} - \mathbf{i}2\xi_i \frac{f_i}{f_k}\right)^{1/2}; \quad h_{ki}^* = \left(1 - \frac{f_i^2}{f_k^2} + \mathbf{i}2\xi_i \frac{f_i}{f_k}\right)^{1/2} \\
h_{ki}^{(f_i)} &= \left(-\frac{f_i}{f_k^2} - \mathbf{i}\frac{2\xi_i}{f_k}\right) h_{ki}^{-1}; \quad \{h_{ki}^*\}^{(f_i)} = \left(-\frac{f_i}{f_k^2} + \mathbf{i}\frac{2\xi_i}{f_k}\right) \{h_{ki}^*\}^{-1} \\
h_{ki}^{(\xi_i)} &= -\mathbf{i}\frac{2f_i}{f_k} h_{ki}^{-1}; \quad \{h_{ki}^*\}^{(\xi_i)} = \mathbf{i}\frac{2f_i}{f_k} \{h_{ki}^*\}^{-1} \\
h_{ki}^{(f_i, f_i)} &= -\frac{1}{f_k^2} h_{ki}^{-1} + \left(\frac{f_i}{f_k^2} + \mathbf{i}\frac{2\xi_i}{f_k}\right) h_{ki}^{(f_i)} h_{ki}^{-2}; \\
\{h_{ki}^*\}^{(f_i, f_i)} &= -\frac{1}{f_k^2} \{h_{ki}^*\}^{-1} + \left(\frac{f_i}{f_k^2} - \mathbf{i}\frac{2\xi_i}{f_k}\right) \{h_{ki}^*\}^{(f_i)} \{h_{ki}^*\}^{-2} \\
h_{ki}^{(\xi_i, \xi_i)} &= -\mathbf{i}\frac{2f_i}{f_k} h_{ki}^{(\xi_i)} h_{ki}^{-2}; \quad \{h_{ki}^*\}^{(\xi_i, \xi_i)} = \mathbf{i}\frac{2f_i}{f_k} \{h_{ki}^*\}^{(\xi_i)} \{h_{ki}^*\}^{-2} \\
h_{ki}^{(f_i, \xi_i)} &= -\mathbf{i}\frac{1}{f_k} h_{ki}^{-1} + \mathbf{i}\frac{2f_i}{f_k} h_{ki}^{(f_i)} h_{ki}^{-2} \\
\{h_{ki}^*\}^{(f_i, \xi_i)} &= \mathbf{i}\frac{1}{f_k} h_{ki}^{-1} - \mathbf{i}\frac{2f_i}{f_k} \{h_{ki}^*\}^{(\xi_i)} \{h_{ki}^*\}^{-2}
\end{aligned} \tag{D.15}$$

Thus, the posterior covariance matrix for the modal parameters are obtained as below.

$$C_\theta = \nabla v_c (\nabla^2 J)^+ \nabla v_c^T \tag{D.16}$$

where  $v_c =$  mapping function that always satisfies the equality constraints, and “+” denotes the pseudo inverse.

$$v_c = \left\{ \theta_s^T \quad \varphi_1^T / \|\varphi_1\| \quad \cdot \quad \cdot \quad \cdot \quad \varphi_{N_m}^T / \|\varphi_{N_m}\| \right\}^T \tag{D.17}$$

$$\nabla v_c = \begin{bmatrix} I_{N\theta_s} & & & & & \\ & I_N - \varphi_1 \varphi_1^T & & & & \\ & & \ddots & & & \\ & & & \ddots & & \\ & & & & \ddots & \\ & & & & & I_N - \varphi_{N_m} \varphi_{N_m}^T \end{bmatrix} \quad (\text{D.18})$$

Due to the norm constraint singularity, the null vector of the posterior covariance matrix for  $i^{\text{th}}$  mode shape will be equal to  $\varphi_i$ .

$$\begin{aligned} C_{\varphi_i} &= (I_N - \varphi_i \varphi_i^T) (\nabla_{\varphi_i}^2 J)^+ (I_N - \varphi_i \varphi_i^T) \\ &= \mathbf{0} \times \varphi_i \varphi_i^T + \sum_{j=2}^N \sigma_j \rho_j \rho_j^T \end{aligned} \quad (\text{D.19})$$

Similarly, the null vectors of the  $C_\theta$  will be equal to the corresponding mode shapes.

$$\begin{aligned} C_\theta &= \mathbf{0} \times \begin{bmatrix} \mathbf{0}_{N\theta_s} \\ \varphi_1 \end{bmatrix} \begin{bmatrix} \mathbf{0}_{N\theta_s}^T & \varphi_1^T \end{bmatrix} + \dots + \mathbf{0} \times \begin{bmatrix} \mathbf{0}_{N\theta_s} \\ \varphi_{N_m} \end{bmatrix} \begin{bmatrix} \mathbf{0}_{N\theta_s}^T & \varphi_{N_m}^T \end{bmatrix} \\ &+ \sum_{j=N_m+1}^{N_\theta} \sigma_j \rho_j \rho_j^T \end{aligned} \quad (\text{D.20})$$

## APPENDIX E

### DERIVATION OF HESSIAN MATRIX FOR MODEL PARAMETERS

The derivatives of Eq. (5.19) is obtained as follows.

- Derivative of  $J^{(\theta,\theta)}$

$$J^{(\theta,\theta)} = \frac{\partial^2 J}{\partial \theta^2} \Big|_{\theta=\hat{\theta}, \rho=\hat{\rho}, \chi=\hat{\chi}} = S_{\theta_{ro}}^{-1} \mathbf{I}_{N \times N} + \sum_{n=1}^{N_m} S_{\hat{\epsilon}}^{-1} G_{K_n}^T G_{K_n} \quad (\text{E.1})$$

- Derivative of  $J^{(\theta,\rho)}$

$$J^{(\theta,\rho)} = \{J^{(\rho,\theta)}\}^T = \frac{\partial^2 J}{\partial \theta \partial \rho} \Big|_{\theta=\hat{\theta}, \rho=\hat{\rho}, \chi=\hat{\chi}} = - \sum_{n=1}^{N_m} S_{\hat{\epsilon}}^{-1} G_{K_n}^T G_{M_n} \quad (\text{E.2})$$

- Derivative of  $J^{(\theta,\lambda)}$

$$J^{(\theta,\lambda)} = \{J^{(\lambda,\theta)}\}^T = \frac{\partial^2 J}{\partial \theta \partial \lambda} \Big|_{\theta=\hat{\theta}, \rho=\hat{\rho}, \chi=\hat{\chi}} = \begin{bmatrix} J^{(\theta,\lambda_1)} & \dots & J^{(\theta,\lambda_{N_m})} \end{bmatrix}_{N_\theta \times N_m} \quad (\text{E.3})$$

$$J^{(\theta,\lambda_1)} = -S_{\hat{\epsilon}}^{-1} G_{K_n}^T M(\rho) \Phi_n$$

- Derivative of  $J^{(\theta,\Phi)}$

$$J^{(\theta,\Phi)} = \{J^{(\Phi,\theta)}\}^T = \frac{\partial^2 J}{\partial \theta \partial \Phi} \Big|_{\theta=\hat{\theta}, \rho=\hat{\rho}, \chi=\hat{\chi}} = \begin{bmatrix} J^{(\theta,\Phi_1)} & \dots & J^{(\theta,\Phi_{N_m})} \end{bmatrix}_{N_\theta \times N_m N} \quad (\text{E.4})$$

$$J^{(\theta,\Phi_n)} = \left[ \{J^{(\theta_1,\Phi_n)}\}^T \dots \{J^{(\theta_{N_\theta},\Phi_n)}\}^T \right]_{N \times N_\theta}^T$$

$$J^{(\theta_i,\Phi_n)} = \left[ 2S_{\hat{\epsilon}}^{-1} \hat{\Phi}_n^T \Omega_n K_i (I_N - \hat{\Phi}_n \hat{\Phi}_n^T) \right]_{1 \times N}$$

- Derivative of  $J^{(\rho,\rho)}$

$$J^{(\rho,\rho)} = \frac{\partial^2 J}{\partial \rho^2} \Big|_{\theta=\hat{\theta}, \rho=\hat{\rho}, \chi=\hat{\chi}} = S_{\hat{\rho}_{ro}}^{-1} \mathbf{I}_{N \times N} + \sum_{n=1}^{N_m} S_{\hat{\epsilon}}^{-1} G_{M_n}^T G_{M_n} \quad (\text{E.5})$$

- Derivative of  $J^{(\rho,\lambda)}$

$$J^{(\rho,\lambda)} = \{J^{(\lambda,\rho)}\}^T = \frac{\partial^2 J}{\partial \rho \partial \lambda} \Big|_{\theta=\hat{\theta}, \rho=\hat{\rho}, \chi=\hat{\chi}} = \begin{bmatrix} J^{(\rho,\lambda_1)} & \dots & J^{(\rho,\lambda_{N_m})} \end{bmatrix}_{N_\rho \times N_m} \quad (\text{E.6})$$

$$J^{(\rho,\lambda_n)} = S_{\hat{\epsilon}}^{-1} \left( 2\lambda_n \tilde{G}_{M_n}^T G_{M_n} \hat{\rho} - \tilde{G}_{M_n}^T \mathbf{g}_{M_n} + G_{M_n}^T M_0 \hat{\Phi}_n \right)$$



where

$$\tilde{G}_{M_n} = \begin{bmatrix} M_1 \hat{\Phi}_n & \dots & M_{N_{el}} \hat{\Phi}_n \end{bmatrix}_{N \times N_\rho} \quad (\text{E.7})$$

- Derivative of  $\mathcal{J}^{\rho, \Phi}$

$$\begin{aligned} \mathcal{J}^{(\rho, \Phi)} &= \left\{ \mathcal{J}^{(\Phi, \rho)} \right\}^T = \frac{\partial^2 J}{\partial \theta \partial \lambda} \Bigg|_{\theta=\hat{\theta}, \rho=\hat{\rho}, \chi=\hat{\chi}} = \begin{bmatrix} \mathcal{J}^{(\rho, \Phi_1)} & \dots & \mathcal{J}^{(\rho, \Phi_{N_m})} \end{bmatrix}_{N_\rho \times N_m N} \\ \mathcal{J}^{(\rho, \Phi_n)} &= \begin{bmatrix} \left\{ \mathcal{J}^{(\rho_1, \Phi_n)} \right\}^T & \dots & \left\{ \mathcal{J}^{(\rho_{N_\theta}, \Phi_n)} \right\}^T \end{bmatrix}_{N \times N_\rho} \\ \mathcal{J}^{(\rho_i, \Phi_n)} &= \begin{bmatrix} 2S_{\hat{\varepsilon}}^{-1} \hat{\Phi}_n^T \Omega_n \lambda_n M_i (I_N - \hat{\Phi}_n \hat{\Phi}_n^T) \end{bmatrix}_{1 \times N} \end{aligned} \quad (\text{E.8})$$

- Derivative of  $\mathcal{J}^{(\lambda, \lambda)}$

$$\mathcal{J}^{(\lambda, \lambda)} = \frac{\partial^2 J}{\partial \lambda^2} \Bigg|_{\theta=\hat{\theta}, \rho=\hat{\rho}, \chi=\hat{\chi}} = \begin{bmatrix} \text{diag} \left( S_{\hat{\varepsilon}}^{-1} G_{\lambda_n} + \sum_{i=1}^{N_s} H_{\hat{\lambda}_{ni}} \right) \end{bmatrix}_{N_m \times N_m} \quad (\text{E.9})$$

- Derivative of  $\mathcal{J}^{(\lambda, \Phi)}$

$$\begin{aligned} \mathcal{J}^{(\lambda, \Phi)} &= \left\{ \mathcal{J}^{(\Phi, \lambda)} \right\}^T = \frac{\partial^2 J}{\partial \Phi \partial \lambda} \Bigg|_{\theta=\hat{\theta}, \rho=\hat{\rho}, \chi=\hat{\chi}} = \begin{bmatrix} \mathcal{J}^{(\lambda, \Phi_1)} & \dots & \mathcal{J}^{(\lambda, \Phi_{N_m})} \end{bmatrix}_{N \times N_m N} \\ \mathcal{J}^{(\lambda, \Phi_n)} &= \begin{bmatrix} \left\{ \mathcal{J}^{(\lambda_1, \Phi_n)} \right\}^T & \dots & \left\{ \mathcal{J}^{(\lambda_{N_m}, \Phi_n)} \right\}^T \end{bmatrix}_{N_m N \times N} \\ \mathcal{J}^{(\lambda_m, \Phi_n)} &= \begin{cases} \begin{bmatrix} -2\hat{S}_{\hat{\varepsilon}_n}^{-1} \hat{\Phi}_n^T \Omega_n M(\rho) (I_N - \hat{\Phi}_n \hat{\Phi}_n^T) \end{bmatrix}_{1 \times N} & \text{if } n = m \\ \mathbf{0}_{1 \times N} & \text{otherwise} \end{cases} \end{aligned} \quad (\text{E.10})$$

- Derivative of  $\mathcal{J}^{(\Phi, \Phi)}$

$$\begin{aligned} \mathcal{J}^{(\Phi, \Phi)} &= \frac{\partial^2 J}{\partial \Phi^2} \Bigg|_{\theta=\hat{\theta}, \rho=\hat{\rho}, \chi=\hat{\chi}} = \text{diag} \left[ \mathcal{J}^{(\Phi_1, \Phi_1)} \quad \dots \quad \mathcal{J}^{(\Phi_{N_m}, \Phi_{N_m})} \right]_{N_m N \times N_m N} \\ \mathcal{J}^{(\Phi_n, \Phi_n)} &= \left\{ \sum_{i=1}^{N_s} \Gamma_{oi}^T \left( r_{ni}^{-2} H_{\hat{\rho}_i} + 2\alpha_{ni} I_{N_i} \right) \Gamma_{oi} \right\} + \Omega_n^T S_{\hat{\varepsilon}_n}^{-1} \Omega_n - 2\beta_n \mathbf{I}_n \end{aligned} \quad (\text{E.11})$$

## REFERENCES

- Abu Husain, N., Khodaparast, H. H., and Ouyang, H. (2012). Parameter selection and stochastic model updating using perturbation methods with parameter weighting matrix assignment. *Mechanical Systems and Signal Processing*, 32, 135–152.
- Au, S. K., and Zhang, F. L. (2011). On assessing the posterior mode shape uncertainty in ambient modal identification. *Probabilistic Engineering Mechanics*, 26(3), 427–434.
- Au, S. K. (2011a). Fast Bayesian FFT method for ambient modal identification with separated modes. *Journal of Engineering Mechanics*, 137(3), 214–226.
- Au, S. K. (2011b). Assembling mode shapes by least squares. *Mechanical Systems and Signal Processing*, 25(1), 163–179.
- Au, S. K. (2012a). Connecting Bayesian and frequentist quantification of parameter uncertainty in system identification. *Mechanical Systems and Signal Processing*, 29, 328–342.
- Au, S. K. (2012b). Fast Bayesian ambient modal identification in the frequency domain, Part I: Posterior most probable value. *Mechanical Systems and Signal Processing*, 26(1), 60–75.
- Au, S. K. (2012c). Fast Bayesian ambient modal identification in the frequency domain, Part II: Posterior uncertainty. *Mechanical Systems and Signal Processing*, 26(1), 76–90.
- Au, S. K., and Zhang, F. L. (2012). Ambient modal identification of a primary-secondary structure by Fast Bayesian FFT method. *Mechanical Systems and Signal Processing*, 28, 280–296.
- Au, S. K., and Zhang, F. L. (2012). Fast Bayesian ambient modal identification incorporating multiple setups. *Journal of Engineering Mechanics*, 138(7), 800–815.
- Au, S. K., Zhang, F. L., and Ni, Y. C. (2013). Bayesian operational modal analysis: Theory, computation, practice. *Computers and Structures*, 126(1), 3–14.
- Au, S. K. (2014a). Uncertainty law in ambient modal identification - Part I: Theory. *Mechanical Systems and Signal Processing*, 48(1–2), 15–33.
- Au, S. K. (2014b). Uncertainty law in ambient modal identification - -Part II: Implication and field verification. *Mechanical Systems and Signal Processing*, 48(1–2), 34–48.
- Au, S.-K., and Zhang, F.-L. (2016). Fundamental two-stage formulation for Bayesian system identification, Part I: General theory. *Mechanical Systems and Signal Processing*, 66–67, 31–42.

- Au, S. K. (2016a). Insights on the Bayesian spectral density method for operational modal analysis. *Mechanical Systems and Signal Processing*, 66–67, 1–12.
- Au, S. K. (2016b). Model validity and frequency band selection in operational modal analysis. *Mechanical Systems and Signal Processing*, 81, 339–359.
- Au, S. K. (2017). *Operational modal analysis: Modeling, Bayesian inference, uncertainty laws*. Springer Nature Singapore Pte Ltd.
- Au, S. K., and Xie, Y. L. (2017). Calculation of Hessian under constraints with applications to Bayesian system identification. *Computer Methods in Applied Mechanics and Engineering*, 323, 373–388.
- Barzilai, J. (1988). Two-Point Step Size Gradient Methods. *IMA Journal of Numerical Analysis*, 8(1), 141–148.
- Beck, J. L., and Au, S.-K. (2002). Bayesian updating of structural models and reliability using Markov Chain Monte Carlo simulation. *Journal of Engineering Mechanics*, 128(4), 380–391.
- Beck, J. L., and Katafygiostis, L. S. (1998). Updating models and their uncertainties I: Bayesian statistical frameworks. *Journal of Engineering Mechanics*, 124(4), 455–461.
- Brincker, R., Zhang, L., and Andersen, P. (2001). Modal identification of output-only systems using frequency domain decomposition. *Smart Materials and Structures*, 10(3), 441–445.
- Caicedo, J. M. (2011). Practical guidelines for the natural excitation technique (NExT) and the eigensystem realization algorithm (ERA) for modal identification using ambient vibration. *Experimental Techniques*, 35(4), 52–58.
- Center of Engineering Strong Motion Data (CESMD), [www.strongmotioncenter.org](http://www.strongmotioncenter.org), Accessed 07 July 2018.
- Çelebi, M. (2016). Responses of a 58 story RC dual core shear wall and outrigger frame building inferred from two earthquakes Responses of a 58 story RC dual core shear wall and outrigger frame building inferred from two earthquakes. *Earthquake Spectra*, 32(4), 2449–2471.
- Çelebi, M., Huang, M., Shakal, A., Hooper, J., and Klemencic, R. (2013). Ambient response of a unique performance-based design tall building with dynamic response modification features. *The Structural Design of Tall and Special Structures*, 22, 816–829.
- Ching, J., and Beck, J. L. (2004). New Bayesian model updating algorithm applied to a structural health monitoring benchmark. *Structural Health Monitoring*, 3(4), 313–332.
- Ching, J., Muto, M., and Beck, J. L. (2006). Structural model updating and health monitoring with incomplete modal data using Gibbs sampler. *Computer-Aided Civil and Infrastructure Engineering*, 21(4), 242–257.

- Das, A., and Debnath, N. (2018). A Bayesian finite element model updating with combined normal and lognormal probability distributions using modal measurements. *Applied Mathematical Modelling*, 61, 457–483.
- Döhler, M., Reynders, E., Magalhães, F., Mevel, L., De Roeck, G., and Cunha, Á. (2011). *Pre- and Post-identification Merging for Multi-Setup OMA with Covariance-Driven SSI*. In: Dynamics of Bridges, Volume 5. Conference Proceedings of the Society for Experimental Mechanics Series, Springer, New York, NY 57–70.
- Friswell, M. I. (1989). The adjustment of structural parameters using a minimum variance estimator. *Mechanical Systems and Signal Processing*, 3(2), 143–155.
- Furman, E. (2008). On a multivariate gamma distribution. *Statistics and Probability Letters*, 78(15), 2353–2360.
- Govers, Y., and Link, M. (2010). Stochastic model updating-covariance matrix adjustment from uncertain experimental modal data. *Mechanical Systems and Signal Processing*, 24(3), 696–706.
- Ibrahim, S. R. (1999). Fundamentals of time domain modal identification. In *Modal Analysis and Testing* (Vol. 241, pp. 241–250).
- Katafygiostis, L. S., and Beck, J. L. (1998). Updating models and their uncertainties II: Model identifiability. *Journal of Engineering Mechanics*, 124(4), 463–467.
- Katafygiostis, L. S., Papadimitriou, C., and Lam, H. F. (1998). A probabilistic approach to structural model updating. *Soil Dynamics and Earthquake Engineering*, 17, 495–507.
- Katafygiotis, L. S., and Yuen, K. V. (2001). Bayesian spectral density approach for modal updating using ambient data. *Earthquake Engineering and Structural Dynamics*, 30(8), 1103–1123.
- Khodaparast, H. H., Mottershead, J. E., and Friswell, M. I. (2008). Perturbation methods for the estimation of parameter variability in stochastic model updating. *Mechanical Systems and Signal Processing*, 22(8), 1751–1773.
- Lam, H. F., Yang, J., and Au, S. K. (2015). Bayesian model updating of a coupled-slab system using field test data utilizing an enhanced Markov chain Monte Carlo simulation algorithm. *Engineering Structures*, 102, 144–155.
- Lam, H. F., Zhang, F. L., Ni, Y. C., and Hu, J. (2017). Operational modal identification of a boat-shaped building by a Bayesian approach. *Engineering Structures*, 138, 381–393.
- Malekjafarian, A., Brincker, R., Ashory, R. M., and Khatibi, M. M. (2012). *Modified Ibrahim time domain method for identification of closely Spaced Modes: Experimental Results*. Topics on the Dynamics of Civil Structures, Volume 1, Conference Proceedings of the Society for Experimental Mechanics Series. Springer, New York, NY.

- Mathai, A. M., and Moschopoulos, P. G. (1997). A multivariate inverted beta model. *Statistica LVII*, 4, 189–197.
- MATLAB 2018b. *Computer software*. MathWorks, Natick, MA.
- Mottershead, J. E., and Friswell, M. I. (1993). Model updating in structural dynamics: A Survey. *Journal of Sound and Vibration*, 167(2), 347–375.
- Mottershead, J. E., Link, M., and Friswell, M. I. (2011). The sensitivity method in finite element model updating: A tutorial. *Mechanical Systems and Signal Processing*, 25(7), 2275–2296.
- Mustafa, S., and Matsumoto, Y. (2017). Bayesian model updating and its limitations for detecting local damage of an existing truss bridge. *Journal of Bridge Engineering*, 22(7), 04017019.
- Ni, Y.-C., and Zhang, F.-L. (2015). Bayesian operational modal analysis of a pedestrian bridge using a field test with multiple setups. *International Journal of Structural Stability and Dynamics*, 16(08), 1550052.
- Ni, Y. C., Zhang, F. L., Lam, H. F., and Au, S. K. (2016). Fast Bayesian approach for modal identification using free vibration data, Part II - Posterior uncertainty and application. *Mechanical Systems and Signal Processing*, 70–71, 221–244.
- Ni, Y. Q., Zhang, F. L., Xia, Y. X., and Au, S. K. (2015). Operational modal analysis of a long-span suspension bridge under different earthquake events. *Earthquake and Structures*, 8(4), 859–887.
- Orlowitz, E., and Brandt, A. (2017). Comparison of experimental and operational modal analysis on a laboratory test plate. *Measurement: Journal of the International Measurement Confederation*, 102, 121–130.
- Overschee, P. Van, and Moor, B. De. (1993). Subspace algorithms for the stochastic identification problem. *Automatica*, 29(3), 649–660.
- Peeters, B., and De Roeck, G. (2000). Reference based stochastic subspace identification in Civil Engineering. *Inverse Problems in Engineering*, 8(1), 47–74.
- Peeters, B., and Ventura, C. E. (2003). Comparative study of modal analysis techniques for bridge dynamic characteristics. *Mechanical Systems and Signal Processing*, 17, 965–988.
- Prajapat, K., and Ray-Chaudhuri, S. (2018). Detection of multiple damages employing best achievable eigenvectors under Bayesian inference. *Journal of Sound and Vibration*, 422, 237–263.
- Reynders, E., and Roeck, G. De. (2008). Reference-based combined deterministic – stochastic subspace identification for experimental and operational modal analysis. *Mechanical Systems and Signal Processing*, 22, 617–637.
- Reynders, E., Houbrechts, J., and De Roeck, G. (2012). Fully automated (operational) modal analysis. *Mechanical Systems and Signal Processing*, 29, 228–250.

- Harville, D. A. (1997). *Matrix algebra from a statistician's perspective*. Springer, New York.
- Soize, C., Capiez-Lernout, E., and Ohayon, R. (2008). Robust Updating of Uncertain Computational Models Using Experimental Modal Analysis. *AIAA Journal*, 46(11), 2955–2965.
- Touat, N., Benseddiq, N., Ghoul, A., and Rechak, S. (2014). An accelerated pseudo-genetic algorithm for dynamic finite element model updating. *Engineering Optimization*, 46(3), 340–360.
- Wen, Z., and Yin, W. (2013). A feasible method for optimization with orthogonality constraints. *Mathematical Programming*, 142(1–2), 397–434.
- Yan, W. J., and Katafygiotis, L. S. (2015a). A two-stage fast Bayesian spectral density approach for ambient modal analysis. Part I: Posterior most probable value and uncertainty. *Mechanical Systems and Signal Processing*, 54, 139–155.
- Yan, W. J., and Katafygiotis, L. S. (2015b). A two-stage fast Bayesian spectral density approach for ambient modal analysis. Part II: Mode shape assembly and case studies. *Mechanical Systems and Signal Processing*, 54, 156–171.
- Yan, W. J., and Katafygiotis, L. S. (2015c). A novel Bayesian approach for structural model updating utilizing statistical modal information from multiple setups. *Structural Safety*, 52, 260–271.
- Yang, Y. B., and Chen, Y. J. (2010). Direct versus iterative model updating methods for mass and stiffness matrices. *International Journal of Structural Stability Dynamics*, 10, 165–186.
- Yuen, K.-V., and Kuok, S.-C. (2011). Bayesian methods for updating dynamic models. *Applied Mechanics Reviews*, 64(1), 010802.
- Yuen, K. (2010). *Bayesian methods for structural dynamics and civil engineering*. John Wiley and Sons (Asia) Pte Ltd.
- Yuen, K., and Katafygiotis, L. S. (2003). Bayesian fast fourier transform approach for modal updating using ambient data. *Advances in Structural Engineering*, 6(2), 81–95.
- Yuen, K. V., and Katafygiotis, L. S. (2001). Bayesian time-domain approach for modal updating using ambient data. *Probabilistic Engineering Mechanics*, 16, 219–231.
- Zhang, F. (2012). Bayesian Ambient Modal Identification Incorporating Multiple Setups. Dissertation, City University of Hong Kong.
- Zhang, F. L., and Au, S. K. (2016). Fundamental two-stage formulation for Bayesian system identification, Part II: Application to ambient vibration data. *Mechanical Systems and Signal Processing*, 66–67, 43–61.
- Zhang, F. L., and Au, S. K. (2016). Probabilistic model for modal properties based on operational modal analysis. *ASCE-ASME Journal of Risk and Uncertainty in*

- Engineering Systems, Part A: Civil Engineering*, 2(3), 1–12.
- Zhang, F. L., Ni, Y. C., and Lam, H. F. (2017). Bayesian structural model updating using ambient vibration data collected by multiple setups. *Structural Control and Health Monitoring*, 24(12), 1–18.
- Zhu, Y. C., Au, S. K., and Brownjohn, J. M. W. (2019). Bayesian operational modal analysis with buried modes. *Mechanical Systems and Signal Processing*, 121, 246–263.

# VITA

## PERSONAL INFORMATION:

**Name & Surname:** Çağlayan HIZAL

**Date and Place of Birth:** 03/09/1986, Rize/Turkey

## EDUCATION:

<u>Degree</u>	<u>Institution</u>	<u>Graduation Year</u>
PhD.	Izmir Institute of Technology	2019
MSc.	Dokuz Eylul University	2012
BSc.	Dokuz Eylul University	2010

## PUBLISHED ARTICLES:

Hızal, Ç., and Çatal, H.H. (2019). Rotary inertia and higher modes effect on the dynamic response of Timoshenko beams on two-parameter foundation. *Teknik Dergi*, 30(4), 9289-9308.

Hızal, Ç., and Turan, G. (2019). Analysis of multi story frames subjected to multiple support excitation by using displacement loading. *Teknik Dergi*, 30 (3), 9053-9071.

Hızal, Ç., and Turan, G. (2018). Effect of seismic wave velocity on the dynamic response of multi-story structures on elastic foundation. *Soil Dynamics and Earthquake Engineering*, 113, 432-441.

Hızal, Ç., and Turan, G. (2017). Importance of static correction and damping in the analysis of a cable-stayed bridge subjected to displacement loading. *Journal of Bridge Engineering*, 22(6), 04017009.

Hızal, Ç., and Çatal, H.H. (2016). Comparative dynamic analysis of axially loaded beams on modified Vlasov foundation. *Structural Engineering and Mechanics*, 57(6), 969-988.

## SUBMITTED ARTICLES:

Hızal, Ç., Turan, G., Aktaş, E. and Ceylan, H. (2019). A mode shape assembly algorithm by using two-stage Bayesian Fast Fourier Transform approach. *Mechanical Systems and Signal Processing* (Under Review).

Hızal, Ç., and Turan, G. (2019). A two-stage Bayesian algorithm for finite element modal updating by using response data from multiple measurement setups. *Journal of Sound and Vibration* (Under Review).